Astronomy Reports, Vol. 49, No. 9, 2005, pp. 671–677. Translated from Astronomicheskiĭ Zhurnal, Vol. 82, No. 9, 2005, pp. 755–762.

Redetermination of the Helium Abundances in HII Regions in Blue Compact Dwarf Galaxies

V. V. Holovatyi and B. Ya. Melekh

Chair of Astrophysics, Ivan Franko L'vov National University, ul. Kyryla i Mefodiya 8, L'vov, 79005 Ukraine

Received August 1, 2004; in final form, February 17, 2005

Abstract—The He/H abundances in HII regions in Blue Compact Dwarf Galaxies are redetermined using the new recombination coefficients of Benjamin *et al.* The electron number density n_e in the He^+ region, optical depth τ_{3889} in the HeI λ3889 Å line, and coefficient of underlying stellar absorption a_{HeI} are determined using the self-consistent method of Olive and Skillman. The primordial helium abundance and its enrichment are found using the helium abundances obtained in this paper and heavy-element abundances from our recent paper I: $Y_p = 0.244 \pm 0.004$ and $dY/dZ = 8.8 \pm 4.6$. © *2005 Pleiades Publishing, Inc.*

1. INTRODUCTION

Blue Compact Dwarf Galaxies (BCDGs) are characterized by active star formation; giant HII regions are observed near the sites hosting these processes. These have low metallicity and have evolved from material that has not yet taken part in stellar evolution. Therefore, they are important objects for determining the primordial helium abundance Y_p and the rate of its enrichment dY/dZ during the chemical evolution of the stellar material in our Metagalaxy.

In our previous paper [1], we determined the chemical compositions of HII regions in BCDGs using new ionization correction factors derived from a calculated grid of photoionization models for the emission [2]. The observations used for this purpose were spectra of the HII regions obtained by Izotov *et al.* [3, 4]. Based on the chemical compositions obtained, we determined the primordial helium abundance, $Y_p = 0.244 \pm 0.002$, and rate of its enrichment, $dY/dZ = -4.02 \pm 2.46$. These values of Y_p and dY/dZ were obtained using the recombination coefficients of Smits [5] and the collisional coefficients of Kingdon and Ferland [6] for the HeI lines. However, the value of dY/dZ turned out to be negative, in basic contradiction to the theory of the chemical evolution of stellar material, according to which the helium abundance should increase, not decrease, with time.

Recently Benjamin *et al.* [7, 8] published new approximate expressions for the recombination coefficients of He^+, which self-consistently take into account the collisional excitation of He^+ ions and radiative transfer in HeI lines. Given the importance of determining He/H, we decided to rederive this ratio and, accordingly, revise our previous values of Y_p and dY/dZ.

We report here the results of redetermining the He/H abundance taking into account the above factors.

2. TECHNIQUE FOR DETERMINING THE HELIUM ABUNDANCE

The traditional method for determining the He/H abundance ratio is based on using the helium ion content He^+/H^+ and He^{++}/H^+ together with the ionization-correction factors for He, which take into account unobserved H and He atoms. The results of [1, 3, 4] demonstrate that the He^+/H^+ ratios found using the recombination coefficients of Brocklehurst [9] and Smits [5] differ systematically. Using different coefficients for the collisional excitation of HeI lines also affects the results; however, the main role in determining He/H is played by the recombination coefficients. Though the data of Smits [5] are considered to be more correct, they (as well as the data of Brocklehurst [9]) do not take into account radiative transfer in HeI lines.

In two recent papers, Benjamin *et al.* [7, 8] (BSS) present new expressions for the recombination coefficients taking into account radiative transfer and collisional excitation of the HeI lines. The results of [8] show that the He/H values obtained in [3, 4] can substantially change when radiative transfer in HeI lines is taken into account. Accordingly, we decided to redetermine the He^+/H^+ and He^{++}/H^+ ratios using the BSS recombination coefficients.

As a rule, two unknown parameters are involved when determining the He^+/H^+ ratio: the electron density n_e(HeI) in the HeI region and the optical depth τ_{3889} in the HeI λ3889 Å line, which characterizes the radiative transfer in the HeI lines. When

1063-7729/05/4909-0671$26.00

Values of n_e(HeI), τ_{3889}, $a_{\rm HeI}$ and, accordingly, y^+, y^{++} for four cases including different numbers of HeI lines. (The He/H abundances were obtained using our ionization-correction factors from [2].)

Included lines	n_e, cm^{-3}	τ_{3889}	$a_{\rm HeI}$	$y^+_{\rm aver}$	y^{++}	He/H	$\chi^2_{\rm min}$
1	2	3	4	5	6	7	8
Object: 0723+692A							
3 lines	140 ± 130	0.0 ± 3.0	0.3 ± 0.2	0.0830 ± 0.0008	0.00078 ± 0.00009	0.0838 ± 0.0048	0.002
4 lines	117 ± 110	1.3 ± 0.5	0.3 ± 0.2	0.0831 ± 0.0017	0.00078 ± 0.00009	0.0839 ± 0.0051	0.006
5 lines	110 ± 120	1.3 ± 0.5	0.6 ± 0.1	0.0844 ± 0.0015	0.00078 ± 0.00009	0.0852 ± 0.0051	1.690
6 lines	300 ± 5	0.5 ± 0.1	0.3 ± 0.1	0.0782 ± 0.0007	0.00078 ± 0.00009	0.0790 ± 0.0045	135
Object: 0723+692B							
3 lines	10 ± 66	0.0 ± 2.5	1.1 ± 0.2	0.0905 ± 0.0025	0.0012 ± 0.0004	0.0915 ± 0.0030	4.23
4 lines	10 ± 4	0.0 ± 0.0	1.2 ± 0.2	0.0885 ± 0.0015	0.0012 ± 0.0004	0.0895 ± 0.0022	19.8
5 lines*	10 ± 4	0.0 ± 0.0	1.2 ± 0.1	0.0886 ± 0.0015	0.0012 ± 0.0004	0.0896 ± 0.0022	20.5
Object: 0741+535							
3 lines	10 ± 290	0.0 ± 3.0	0.1 ± 0.2	0.0850 ± 0.0060	0 ± 0	0.0821 ± 0.0063	0.300
4 lines	10 ± 97	0.0 ± 0.4	0.1 ± 0.2	0.0846 ± 0.0060	0 ± 0	0.0817 ± 0.0062	0.361
5 lines*	10 ± 95	0.0 ± 0.3	0.0 ± 0.1	0.0793 ± 0.0026	0 ± 0	0.0766 ± 0.0034	9.32
Object: 0907+543							
3 lines	10 ± 190	0.0 ± 3.0	0.1 ± 0.8	0.0947 ± 0.0051	0.0025 ± 0.0001	0.0966 ± 0.0058	4.16
4 lines	10 ± 97	0.1 ± 0.4	0.1 ± 0.8	0.0949 ± 0.0043	0.0025 ± 0.0001	0.0968 ± 0.0051	4.18
5 lines	10 ± 120	0.3 ± 0.3	0.6 ± 0.1	0.0978 ± 0.0022	0.0025 ± 0.0001	0.0997 ± 0.0036	4.61
6 lines	87 ± 86	0.0 ± 0.6	0.5 ± 0.1	0.0943 ± 0.0039	0.0025 ± 0.0001	0.0962 ± 0.0047	9.26
Object: 0917+527							
3 lines	10 ± 220	0 ± 3	0.1 ± 0.1	0.0834 ± 0.0017	0.0020 ± 0.0003	0.0850 ± 0.0022	0.079
4 lines	10 ± 8	0 ± 0	0.2 ± 0.1	0.0833 ± 0.0020	0.0020 ± 0.0003	0.0848 ± 0.0025	5.90
5 lines	10 ± 7	0 ± 0	0.1 ± 0.0	0.0814 ± 0.0000	0.0020 ± 0.0003	0.0829 ± 0.0015	6.49
6 lines	10 ± 7	0 ± 0	0.1 ± 0.0	0.0812 ± 0.0000	0.0020 ± 0.0003	0.0827 ± 0.0015	7.50
Object: 0926+606							
3 lines	10 ± 43	0.0 ± 1.4	0.8 ± 0.1	0.0882 ± 0.0022	0.0014 ± 0.0002	0.0870 ± 0.0033	12.0
4 lines	10 ± 47	0.6 ± 0.2	0.8 ± 0.1	0.0880 ± 0.0011	0.0014 ± 0.0002	0.0869 ± 0.0027	12.4
5 lines	11 ± 66	0.6 ± 0.3	0.6 ± 0.0	0.0854 ± 0.0018	0.0014 ± 0.0002	0.0843 ± 0.0029	13.9
6 lines	10 ± 41	0.6 ± 0.2	0.6 ± 0.0	0.0855 ± 0.0012	0.0014 ± 0.0002	0.0845 ± 0.0027	17.5
Object: 0940+544N							
3 lines	236 ± 190	2.9 ± 2.9	0.4 ± 0.5	0.0820 ± 0.0034	0 ± 0	0.0803 ± 0.0036	1×10^{-7}
4 lines	199 ± 130	0.0 ± 0.8	0.4 ± 0.5	0.0828 ± 0.0038	0 ± 0	0.0811 ± 0.0041	0.203
5 lines	10 ± 44	1.1 ± 0.4	0.0 ± 0.0	0.0856 ± 0.0007	0 ± 0	0.0839 ± 0.0017	16.9
6 lines	10 ± 53	1.1 ± 0.5	0.0 ± 0.0	0.0854 ± 0.0009	0 ± 0	0.0837 ± 0.0018	18.1
3 lines	300 ± 200	3.0 ± 3.0	0.0 ± 0.1	0.0796 ± 0.0011	0.0014 ± 0.0001	0.0798 ± 0.0025	0.488
4 lines	290 ± 170	0.0 ± 0.5	0.0 ± 0.1	0.0799 ± 0.0021	0.0014 ± 0.0001	0.0800 ± 0.0030	0.949
5 lines	277 ± 160	0.0 ± 0.7	0.5 ± 0.1	0.0870 ± 0.0033	0.0014 ± 0.0001	0.0870 ± 0.0040	7.510
6 lines	277 ± 160	0.0 ± 0.5	0.5 ± 0.1	0.0870 ± 0.0030	0.0014 ± 0.0001	0.0870 ± 0.0038	7.510

Table. (Contd.)

1	2	3	4	5	6	7	8
Object: 0948+532							
3 lines	300 ± 200	3.0 ± 3.0	0.0 ± 0.3	0.0799 ± 0.0026	0.0008 ± 0.0001	0.0808 ± 0.0036	1.20
4 lines	300 ± 190	0.6 ± 0.7	0.0 ± 0.3	0.0800 ± 0.0031	0.0008 ± 0.0001	0.0808 ± 0.0040	1.54
5 lines	300 ± 150	0.5 ± 0.6	0.8 ± 0.0	0.0876 ± 0.0009	0.0008 ± 0.0001	0.0884 ± 0.0028	5.97
6 lines	293 ± 250	0.6 ± 0.9	0.8 ± 0.0	0.0878 ± 0.0014	0.0008 ± 0.0001	0.0886 ± 0.0030	8.28
Object: 1030+583							
3 lines	10 ± 28	0.0 ± 1.1	0.6 ± 0.1	0.0867 ± 0.0014	0.0021 ± 0.0002	0.0888 ± 0.0021	7.17
4 lines	10 ± 34	0.7 ± 0.2	0.6 ± 0.1	0.0866 ± 0.0012	0.0021 ± 0.0002	0.0886 ± 0.0020	7.79
5 lines	10 ± 60	0.7 ± 0.3	0.2 ± 0.0	0.0803 ± 0.0012	0.0021 ± 0.0002	0.0824 ± 0.0019	17.8
6 lines	25 ± 110	0.6 ± 0.5	0.2 ± 0.0	0.0801 ± 0.0019	0.0021 ± 0.0002	0.0821 ± 0.0024	21.7
Object: 1054+365							
3 lines	300 ± 290	3.0 ± 3.0	0.1 ± 0.3	0.0803 ± 0.0034	0 ± 0	0.0796 ± 0.0040	0.026
4 lines	106 ± 96	0.0 ± 0.5	0.3 ± 0.3	0.0846 ± 0.0029	0 ± 0	0.0839 ± 0.0037	0.596
5 lines	122 ± 110	0.0 ± 0.6	0.4 ± 0.1	0.0853 ± 0.0028	0 ± 0	0.0846 ± 0.0037	1.41
6 lines	134 ± 71	0.0 ± 0.2	0.4 ± 0.1	0.0845 ± 0.0014	0 ± 0	0.0838 ± 0.0027	7.96
Object: 1116+583B							
3 lines	231 ± 220	3.0 ± 3.0	0.0 ± 0.8	0.0766 ± 0.0011	0.0022 ± 0.0009	0.0784 ± 0.0110	0.004
4 lines	253 ± 240	0.0 ± 1.9	0.0 ± 0.8	0.0766 ± 0.0097	0.0022 ± 0.0009	0.0784 ± 0.0098	0.007
5 lines	10 ± 290	1.8 ± 1.6	0.0 ± 0.6	0.0796 ± 0.0074	0.0022 ± 0.0009	0.0814 ± 0.0076	14.1
Object: 1124+792							
3 lines	10 ± 36	0.0 ± 1.4	0.1 ± 0.2	0.0820 ± 0.0017	0 ± 0	0.0804 ± 0.0022	5.14
4 lines	10 ± 1	0.0 ± 0.0	0.0 ± 0.1	0.0783 ± 0.0009	0 ± 0	0.0768 ± 0.0016	33.9
5 lines	10 ± 1	0.0 ± 0.0	1.1 ± 0.1	0.0875 ± 0.0011	0 ± 0	0.0858 ± 0.0019	75.9
6 lines	10 ± 1	0.0 ± 0.0	1.0 ± 0.1	0.0862 ± 0.0011	0 ± 0	0.0845 ± 0.0019	79.8
Object: 1128+573							
3 lines	300 ± 290	3.0 ± 3.0	0.2 ± 0.4	0.0740 ± 0.0074	0 ± 0	0.0740 ± 0.0090	0.384
4 lines	10 ± 27	0.0 ± 0.1	0.0 ± 0.3	0.0684 ± 0.0052	0 ± 0	0.0684 ± 0.0070	9.17
5 lines	10 ± 27	0.0 ± 0.1	0.0 ± 0.3	0.0684 ± 0.0050	0 ± 0	0.0684 ± 0.0069	9.18
Object: 1135+581							
3 lines	300 ± 64	3.0 ± 1.9	0.4 ± 0.1	0.0815 ± 0.0013	0.0016 ± 0.0001	0.0807 ± 0.0026	2.97
4 lines	228 ± 50	0.0 ± 0.1	0.4 ± 0.1	0.0821 ± 0.0011	0.0016 ± 0.0001	0.0813 ± 0.0025	6.18
5 lines	211 ± 140	0.0 ± 0.5	0.0 ± 0.0	0.0772 ± 0.0012	0.0016 ± 0.0001	0.0766 ± 0.0025	21.8
6 lines	213 ± 90	0.0 ± 0.3	0.0 ± 0.0	0.0771 ± 0.0008	0.0016 ± 0.0001	0.0765 ± 0.0023	23.7
Object: 1152+579							
3 lines	300 ± 43	3.0 ± 2.3	0.2 ± 0.2	0.0803 ± 0.0011	0.0010 ± 0.0001	0.0813 ± 0.0061	2.12
4 lines	300 ± 40	1.3 ± 0.2	0.2 ± 0.2	0.0804 ± 0.0012	0.0010 ± 0.0001	0.0815 ± 0.0061	2.83
5 lines	300 ± 46	1.3 ± 0.3	0.0 ± 0.0	0.0793 ± 0.0003	0.0010 ± 0.0001	0.0804 ± 0.0059	4.02
6 lines	300 ± 40	1.3 ± 0.2	0.0 ± 0.0	0.0792 ± 0.0002	0.0010 ± 0.0001	0.0803 ± 0.0059	5.58

Table. (Contd.)

1	2	3	4	5	6	7	8
Object: 1159+545							
3 lines	300 ± 83	3.0 ± 3.0	0.0 ± 0.4	0.0708 ± 0.0023	0.0007 ± 0.0001	0.0701 ± 0.0026	1.23
4 lines	202 ± 82	0.0 ± 0.3	0.0 ± 0.4	0.0719 ± 0.0021	0.0007 ± 0.0001	0.0712 ± 0.0025	3.55
5 lines	216 ± 92	0.0 ± 0.3	0.1 ± 0.1	0.0719 ± 0.0017	0.0007 ± 0.0001	0.0712 ± 0.0021	3.84
6 lines	223 ± 120	0.0 ± 0.4	0.1 ± 0.1	0.0720 ± 0.0018	0.0007 ± 0.0001	0.0713 ± 0.0022	5.77
Object: 1205+557							
3 lines	10 ± 290	0.0 ± 3.0	0.0 ± 0.2	0.0813 ± 0.0045	0.0016 ± 0.0006	0.0790 ± 0.0049	0.445
4 lines	10 ± 9	0.0 ± 0.0	0.6 ± 0.2	0.0898 ± 0.0058	0.0016 ± 0.0006	0.0871 ± 0.0061	20.6
5 lines	10 ± 9	0.0 ± 0.0	0.2 ± 0.0	0.0793 ± 0.0000	0.0016 ± 0.0006	0.0771 ± 0.0023	25.9
6 lines	10 ± 9	0.0 ± 0.0	0.2 ± 0.0	0.0787 ± 0.0000	0.0016 ± 0.0006	0.0766 ± 0.0023	27.4
Object: 1211+540							
3 lines	10 ± 160	0.0 ± 3.0	0.4 ± 0.1	0.0829 ± 0.0011	0.0023 ± 0.0001	0.0848 ± 0.0026	0.038
4 lines	13 ± 140	0.6 ± 0.6	0.4 ± 0.1	0.0828 ± 0.0022	0.0023 ± 0.0001	0.0847 ± 0.0026	0.084
5 lines	54 ± 95	0.4 ± 0.4	0.5 ± 0.0	0.0830 ± 0.0009	0.0023 ± 0.0001	0.0849 ± 0.0018	1.21
6 lines	87 ± 77	0.2 ± 0.5	0.5 ± 0.0	0.0825 ± 0.0011	0.0023 ± 0.0001	0.0844 ± 0.0019	2.49
Object: 1222+614							
3 lines	300 ± 180	3.0 ± 3.0	0.0 ± 0.0	0.0743 ± 0.0002	0.0015 ± 0.0002	0.0751 ± 0.0021	1.01
4 lines	20 ± 24	0.0 ± 0.1	0.0 ± 0.0	0.0764 ± 0.0005	0.0015 ± 0.0002	0.0772 ± 0.0022	4.79
5 lines	29 ± 22	0.0 ± 0.1	0.2 ± 0.0	0.0796 ± 0.0004	0.0015 ± 0.0002	0.0804 ± 0.0023	9.32
6 lines	33 ± 23	0.0 ± 0.1	0.2 ± 0.0	0.0793 ± 0.0004	0.0015 ± 0.0002	0.0801 ± 0.0023	11.8
Object: 1223+487							
3 lines	10 ± 18	0.0 ± 0.7	0.7 ± 0.1	0.0854 ± 0.0006	0.0010 ± 0.0001	0.0864 ± 0.0016	7.88
4 lines	10 ± 22	0.5 ± 0.1	0.7 ± 0.1	0.0854 ± 0.0006	0.0010 ± 0.0001	0.0865 ± 0.0016	8.74
5 lines	10 ± 14	0.5 ± 0.1	0.4 ± 0.0	0.0837 ± 0.0002	0.0010 ± 0.0001	0.0847 ± 0.0015	13.7
6 lines	95 ± 56	0.1 ± 0.3	0.3 ± 0.0	0.0813 ± 0.0008	0.0010 ± 0.0001	0.0823 ± 0.0016	19.4
Object: 1256+351							
3 lines	10 ± 32	0.0 ± 0.9	0.6 ± 0.1	0.0858 ± 0.0008	0.0009 ± 0.0001	0.0859 ± 0.0025	5.16
4 lines	10 ± 42	1.5 ± 0.2	0.6 ± 0.1	0.0855 ± 0.0010	0.0009 ± 0.0001	0.0855 ± 0.0026	6.90
5 lines	10 ± 70	1.5 ± 0.3	0.7 ± 0.0	0.0861 ± 0.0007	0.0009 ± 0.0001	0.0861 ± 0.0025	11.5
6 lines	120 ± 90	1.0 ± 0.4	0.7 ± 0.0	0.0852 ± 0.0010	0.0009 ± 0.0001	0.0853 ± 0.0026	18.9
Object: 1319+579A							
3 lines	10 ± 29	0.0 ± 0.7	0.2 ± 0.0	0.1010 ± 0.0001	0.0007 ± 0.0001	0.1010 ± 0.0028	14.0
4 lines	243 ± 42	3.0 ± 0.1	0.1 ± 0.0	0.0885 ± 0.0003	0.0007 ± 0.0001	0.0887 ± 0.0025	40.3
5 lines	298 ± 68	1.7 ± 0.2	0.0 ± 0.0	0.0766 ± 0.0004	0.0007 ± 0.0001	0.0768 ± 0.0022	105
6 lines	300 ± 11	1.6 ± 0.1	0.0 ± 0.0	0.0756 ± 0.0002	0.0007 ± 0.0001	0.0759 ± 0.0021	200
Object: 1319+579C							
3 lines	10 ± 290	0.0 ± 3.0	0.0 ± 0.1	0.0807 ± 0.0019	0.0012 ± 0.0003	0.0779 ± 0.0020	0.701
4 lines	10 ± 7	0.0 ± 0.0	0.3 ± 0.1	0.0840 ± 0.0024	0.0012 ± 0.0003	0.0809 ± 0.0025	18.9
5 lines*	10 ± 6	0.0 ± 0.0	0.3 ± 0.1	0.0842 ± 0.0024	0.0012 ± 0.0003	0.0812 ± 0.0025	20.2

Table. (Contd.)

1	2	3	4	5	6	7	8
Object: 1331+493N							
3 lines	300 ± 240	3.0 ± 3.0	0.4 ± 0.3	0.0790 ± 0.0024	0 ± 0	0.0790 ± 0.0029	0.017
4 lines	26 ± 39	0.0 ± 0.2	0.5 ± 0.3	0.0837 ± 0.0020	0 ± 0	0.0837 ± 0.0026	2.11
5 lines	38 ± 36	0.0 ± 0.2	0.2 ± 0.1	0.0804 ± 0.0018	0 ± 0	0.0804 ± 0.0024	2.94
6 lines	39 ± 36	0.0 ± 0.2	0.2 ± 0.1	0.0802 ± 0.0018	0 ± 0	0.0802 ± 0.0024	3.59
Object: 1437+370							
3 lines	10 ± 240	0.0 ± 3.0	0.3 ± 0.3	0.0840 ± 0.0035	0.0025 ± 0.0002	0.0848 ± 0.0042	0.306
4 lines	10 ± 11	0.0 ± 0.2	0.5 ± 0.2	0.0851 ± 0.0029	0.0025 ± 0.0002	0.0859 ± 0.0038	4.08
5 lines	10 ± 3	0.0 ± 0.0	0.0 ± 0.0	0.0833 ± 0.0000	0.0025 ± 0.0002	0.0841 ± 0.0024	175
6 lines	10 ± 3	0.0 ± 0.0	0.0 ± 0.0	0.0837 ± 0.0000	0.0025 ± 0.0002	0.0845 ± 0.0024	181
Object: 1533+574A							
3 lines	10 ± 290	0.0 ± 3.0	0.1 ± 0.1	0.0840 ± 0.0055	0 ± 0	0.0827 ± 0.0056	0.273
4 lines	10 ± 39	0.0 ± 0.1	0.1 ± 0.0	0.0832 ± 0.0003	0 ± 0	0.0819 ± 0.0015	0.747
5 lines*	10 ± 42	0.0 ± 0.1	0.1 ± 0.0	0.0829 ± 0.0003	0 ± 0	0.0816 ± 0.0015	2.59
Object: 1533+574B							
3 lines	10 ± 290	2.6 ± 2.6	0.1 ± 0.1	0.0828 ± 0.0017	0.0009 ± 0.0002	0.0822 ± 0.002	0.035
4 lines	54 ± 250	1.5 ± 1.0	0.1 ± 0.1	0.0827 ± 0.0039	0.0009 ± 0.0002	0.0821 ± 0.0044	0.036
5 lines	300 ± 290	0.6 ± 1.1	0.4 ± 0.0	0.0864 ± 0.0033	0.0009 ± 0.0002	0.0858 ± 0.0041	6.40
6 lines	300 ± 66	0.7 ± 0.2	0.4 ± 0.0	0.0850 ± 0.0007	0.0009 ± 0.0002	0.0843 ± 0.0025	39.3

* The HeI λ4026 Å line is absent; we have taken instead the HeI λ3889 Å line.

the effect of the radiative transfer is included, the intensity of the HeI λ3889 Å line decreases, while the intensities of most of the remaining HeI lines increase. There is also a third important parameter for HII regions in BCDGs: $a_{\rm HeI}$, which characterizes the so-called underlying stellar absorption. This effect arises because observations of HII regions in BCDGs measure the integrated spectrum, which is a superposition of the emission spectrum from the HII region and the stellar absorption spectra. If this contribution is important, the observed intensities of the HeI lines are lower than the "pure" intensities; this results, in turn, in underestimated He abundances for the HII regions. We took the underlying stellar absorption into account using equivalent widths in HeI lines of the HII regions, EW(λ), kindly supplied to us by Yu.I. Izotov. The general expression for determining the ion content $y^+ \equiv {\rm He}^+/{\rm H}^+$ from the intensity of an HeI line $I(\lambda)$ is [10]

$$y^+(\lambda) = \frac{I(\lambda)}{I({\rm H}_\beta)} \frac{F(n_e, T_e)}{f(n_e, T_e, \tau_{3889})} \frac{{\rm EW}(\lambda) + a_{\rm HeI}}{{\rm EW}(\lambda)}, \quad (1)$$

where $I(\lambda)/I({\rm H}_\beta)$ is the relative intensity in a HeI line, and $F(n_e, T_e)$ and $f(n_e, T_e, \tau_{3889})$ are the approximation functions of BSS for the recombination coefficients and for taking into account the radiative transfer in HeI lines, respectively. The electron temperature T_e in the HeII region was taken to be equal to the electron temperature in the [OIII] region [3, 4]. The electron density n_e in the HeII region, optical depth τ_{3889}, and underlying stellar-absorption factor $a_{\rm HeI}$ were taken to be unknown. We estimated these quantitites using the technique of Olive and Skillman [10], which is based on finding the mean weighted abundance

$$y^+_{\rm aver} = \frac{\sum_\lambda \frac{y^+(\lambda)}{\sigma(\lambda)^2}}{\sum_\lambda \frac{1}{\sigma(\lambda)^2}}, \quad (2)$$

where we have used the errors in the relative intensities of the observed lines for $\sigma(\lambda)$, and the $y^+(\lambda)$ values were calculated using (1) for different HeI

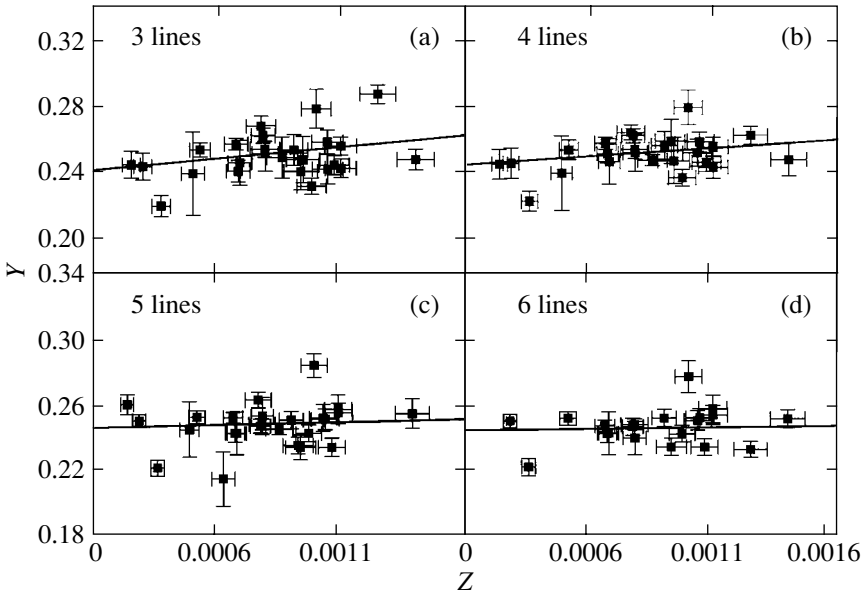

Fig. 1. $Y-Z$ relationships found for cases including (a) three, (b) four, (c) five, and (d) six HeI lines when determining He^+/H^+.

lines. Searching for the most probable values of n_e, τ_{3889}, and a_{HeI} reduces to finding the minimum of the χ^2 function

$$\chi^2 = \sum_{\lambda} \frac{(y^+(\lambda) - y^+_{aver})^2}{\sigma(\lambda)^2}. \qquad (3)$$

3. RESULTS AND DISCUSSION

The table lists the values of n_e, τ_{3889}, a_{HeI}, and y^+, y^{++} we obtained, together with the corresponding value of χ^2_{min}, for the objects that were used in [4] to derive the primordial helium abundance. Like Olive and Skillman [10], we considered four types of HeI line combinations: (1) the three lines λ4471, λ5876, λ6678, (2) the four lines λ4471, λ5876, λ6678, λ7065, (3) the five lines λ4026, λ4471, λ5876, λ6678, λ7065, and (4) the six lines λ3889, λ4026, λ4471, λ5876, λ6678, λ7065. The expressions needed to determine He/H with the He ionization-correction factors we obtained from photoionization-model calculations are given in [2].

The resulting He/H ratios in the studied HII regions and their standard deviations Δ(He/H) are presented in the table for each of the four HeI line combinations noted above.

We determined Y_p and dY/dZ using a $Y-Z$ relationship, where Y and Z are the mass abundances of helium and heavy elements (see formulas (5) in [1]). We described the procedure used to derive Y_p and dY/dZ in [1]. We obtained the following approximation relationships for the various cases for determining He^+/H^+ (see above):

Including three HeI lines:

$$Z = 15.11\ O/H + 4.72 \times 10^{-5}. \qquad (4)$$

Including four HeI lines:

$$Z = 15.22\ O/H + 3.55 \times 10^{-5}. \qquad (5)$$

Including five HeI lines:

$$Z = 15.35\ O/H + 3.01 \times 10^{-5}. \qquad (6)$$

Including six HeI lines:

$$Z = 15.55\ O/H + 2.20 \times 10^{-5}. \qquad (7)$$

Thus, having the O/H abundance, which is always determined most firmly, we can find Z using expressions (4)–(7). We have plotted the resulting $Y-Z$ relationships (Fig. 1) for the objects considered for all the cases noted above. Linear approximations to each of these relations, weighted with the standard deviations of the corresponding values, yield

Including three HeI lines:

$$Y = 0.241(\pm 0.004) + 12.2(\pm 4.2)Z. \qquad (8)$$

Including four HeI lines:

$$Y = 0.244(\pm 0.004) + 8.8(\pm 4.6)Z. \qquad (9)$$

Including five HeI lines:

$$Y = 0.247(\pm 0.003) + 2.7(\pm 3.8)Z. \qquad (10)$$

Including six HeI lines:

$$Y = 0.245(\pm 0.003) + 1.3(\pm 3.5)Z. \qquad (11)$$

4. CONCLUSIONS

We have redetermined the He/H abundance ratios for 23 HII regions in BCDGs using the new recombination coefficients of [8]. When finding this ratio, we took into account the parameters of the HeI region, such as n_e, τ_{3889}, and $a_{\rm HeI}$. We used the heavy-element abundances from [1] to analyze the $Y-Z$ relation, and have revised our previous values for the primordial helium abundance, Y_p, and the rate of its enrichment, dY/dZ.

Our results demonstrate that the new Y_p and dY/dZ values coincide with those obtained by Izotov *et al.* [4, 11] within 1σ. In cases when three and four HeI lines were used, we can derive two dY/dZ values, and, in the cases of five and six lines, another pair of dY/dZ values; the former are greater than the latter values. This discrepancy could be due to inaccuracy in the intensities of the HeI λ4026 Å and λ3889 Å lines. For instance, the λ3889 Å line is blended with the H8 line. As in [4], we took the H8 intensity to be 0.106. However, there is no guarantee that it is, in fact, equal to this value. The HeI λ4026 Å line is characterized by a very small equivalent width, which makes this line extremely sensitive to effects such as underlying stellar absorption. In addition, the faint intensity of this line gives rise to a lower signal-to-noise ratio than for the other lines. Therefore, the HeI λ4026 Å line cannot be considered a reliable indicator of the He/H content. Thus, we consider the result obtained using four HeI lines (9) to be the most reliable; i.e., $Y_p = 0.244 \pm 0.004$ and $dY/dZ = 8.8 \pm 4.6$.

ACKNOWLEDGMENTS

The authors are grateful to Yu.I. Izotov (Main Astronomical Observatory, Ukrainian National Academy of Sciences) for supplying us with the equivalent widths of the HeI lines in the BCDGs HII regions and for useful discussions.

REFERENCES

1. V. V. Holovatyi and B. Ya. Melekh, Astron. Zh. **79**, 668 (2002) [Astron. Rep. **46**, 779 (2002)].
2. V. V. Holovatyi and B. Ya. Melekh, Kin. Fiz. Neb. Tel **18** (4), 362 (2002).
3. Yu. I. Izotov, T. X. Thuan, and V. A. Lipovetsky, Astrophys. J. **435**, 647 (1994).
4. Yu. I. Izotov, T. X. Thuan, and V. A. Lipovetsky, Astrophys. J., Suppl. Ser. **108**, 1 (1997).
5. D. P. Smits, Mon. Not. R. Astron. Soc. **278**, 683 (1996).
6. J. Kingdon and G. J. Ferland, Astrophys. J. **442**, 714 (1995).
7. R. A. Benjamin, E. D. Skillman, and D. P. Smits, Astrophys. J. **514**, 307 (1999).
8. R. A. Benjamin, E. D. Skillman, and D. P. Smits, astro-ph/0202227.
9. M. Brocklehurst, Mon. Not. R. Astron. Soc. **153**, 211 (1972).
10. K. A. Olive and E. D. Skillman, astro-ph/0007081.
11. Yu. I. Izotov and T. X. Thuan, Astrophys. J. **511**, 639 (1999).

Translated by G. Rudnitskiĭ

Astronomy Reports, Vol. 49, No. 9, 2005, pp. 678–692. Translated from Astronomicheskiĭ Zhurnal, Vol. 82, No. 9, 2005, pp. 763–778.

Acceleration of Spatial Motions of Stars by Close-Binary Supermassive Black Holes in Galactic Nuclei

A. V. Tutukov and A. V. Fedorova

Institute of Astronomy, Russian Academy of Sciences, ul. Pyatnitskaya 48, Moscow, 109017 Russia

Received February 5, 2005; in final form, February 17, 2005

Abstract—The conditions for the acceleration of the spatial motions of stars by close-binary supermassive black holes (SMBHs) in galactic nuclei are analyzed in order to derive the velocity distribution for stars ejected from galaxies by such black holes. A close binary system consisting of two SMBHs in circular orbits was subject to a spherically symmetrical "barrage" of solar-mass stars with various initial velocities. The SMBHs were treated as point objects with Newtonian gravitational fields. Models with binary component-mass ratios of 1, 0.1, 0.01, and 0.001 were studied. The results demonstrate the possibility of accelerating neutron stars, stellar-mass black holes, and degenerate dwarfs to velocities comparable to the relative orbital velocities of the binary-SMBH components. In the stage when the binary components are merging due to the action of gravitational-wave radiation, this velocity can approach the speed of light. The most massive binary black-holes ($M \gtrsim 10^9\,M_\odot$) can also accelerate main-sequence stars with solar or subsolar masses to such velocities. © *2005 Pleiades Publishing, Inc.*

1. INTRODUCTION

The rotational space velocities of most stars belonging to the disk component of our Galaxy and the velocities of spherical-component stars are both 200–300 km/s. Essentially, these velocities were reached due to the acceleration of gas and stars during the initial collapse of the Galaxy. Other mechanisms for the acceleration of single and binary stars are also known, such as the disruption of unstable triple stellar systems. In order to be stable, a triple system must have a hierarchical structure, in which two stars form a binary and the third rotates about this binary. According to the observations of [1], the ratio of the rotational period of the third star and the orbital period of the binary must exceed some critical value, which is close to eight and depends on the component-mass ratio of the system. This period ratio corresponds to a ratio of the system semimajor axes that is close to four. It is obvious that closer triple stars will be disrupted due to instability, forming binaries and, as a rule, ejecting the lower-mass component with a velocity of the order of the orbital velocity of the remaining binary components. For the closest binaries that remain bound, the velocity of the ejected star can reach 100–200 km/s. Stars of any mass, from $0.1\,M_\odot$ to $100\,M_\odot$, can be accelerated in this way.

Another way in which single stars can be accelerated by binaries is during collisions between single and close binary stars. Hill [2, 3] was the first to consider this case; these studies were later continued by Hut [4–6]. The main goal of these investigations was to determine the conditions for the acceleration of single stars in globular clusters due to interactions with close binaries.

Extensive calculations of the evolution of globular clusters in the framework of the N-body problem carried out by Baumgardt *et al.* [7] showed that, due to collisions (close passages) of single stars, more than half the stars leaving the parent cluster gain velocities of the order of the velocity dispersion of the cluster stars. As a rule, the simulated characteristic velocities gained by the stars reach several tens of km/s, which is sufficient for a star to leave the cluster.

Another means of acceleration that is possible for the most massive single and binary stars is provided by supernova explosions in the closest binaries [8]. These supernovae are of types Ib,c, whose precursors are helium stars—products of mass transfer in close binaries with similar initial component masses. As a result, so-called "runaway" stars are formed [8]. This mechanism is potentially very efficient, and the products of such disrupted systems can gain velocities of up to 1000 km/s, as is exemplified by radio pulsars that are the products of type-Ib,c supernovae in closest binaries. The mechanism can also efficiently accelerate low-mass main-sequence (MS) stars. For example, let us suppose that an initial binary consists of a helium star with mass $10\,M_\odot$ (sufficient to provide the formation of a neutron star with a mass of $1.3\,M_\odot$ after the supernova) and a MS star with a mass below $\sim 1.5\,M_\odot$. The radii of MS stars of such masses are related to their masses

as $R/R_\odot \approx M/M_\odot$. To estimate the highest possible orbital velocity of a MS star, let us assume that it fills its Roche lobe. In this case, its orbital velocity will be $\sim 600(M/M_\odot)^{-1/3}$ km/s. A solar-type "runaway" star leaving the Galaxy with a velocity of ~700 km/s was recently detected by Brown *et al.* [9]; the distance to this star is ~50 Kpc, and its velocity appreciably exceeds the escape velocity from the Galaxy at this distance, ~300 km/s. Thus, close binaries may form a kind of "wind" consisting of MS stars, neutron stars, and stellar-mass black holes that are leaving their parent galaxies and populating intergalactic space.

Observations show that the intergalactic space in clusters of galaxies contains 10–20% of all the stars [10]. Some of these stars display velocities corresponding to the escape velocities from the halo of our own Galaxy [11]. There is no doubt that most of these stars have ended up in intergalactic space due to collisions between galaxies, with their partial disruption in dense clusters of galaxies. In such clusters, galaxies move with velocities of up to 500–1000 km/s [12], and their collisions fill the intergalactic space (and the galaxies themselves) with rapidly moving stars with velocities comparable to those of their parent galaxies. Thus, collisions between galaxies, which are very frequent in dense clusters of galaxies, represent another, and possibly the most likely, means to produce stars with velocities reaching ~1000 km/s. This primarily refers to long-lived MS stars with subsolar masses, and also to degenerate dwarfs, neutron stars, and black holes (BHs).

Another interesting implication of the existence of high-velocity stars follows from the fact that the Universe contains clusters of galaxies with masses of up to $\sim 10^{15}\ M_\odot$ at distances ~80 Mpc [7]. Assuming a Hubble constant of ~70 km/s Mpc, adjacent clusters move apart with velocities of ~5000–6000 km/s. Hence, the most rapid objects originating in galaxies will be able to fill the intercluster space, "overcoming" cosmological expansion, so that adjacent clusters of galaxies, as we shall see later, can even "exchange" their fastest stars.

The above acceleration mechanisms are not able to yield stellar velocities higher than ~1000 km/s. However, neutron stars and stellar BHs can potentially gain even higher velocities. If the ejection of neutrino energy during a supernova explosion that gives rise to a neutron star or BH is asymmetrical, the neutron star or BH can acquire a "kick," which is potentially capable of accelerating them to ~30 000 km/s. On the other hand, the currently observed velocities of radio pulsars are no higher than ~1000 km/s. Such velocities can be explained by the disruption of close binaries in the second supernova in the binary [13]. Therefore, the role of the "kick" in the acceleration of neutron stars remains unclear.

For completeness, we should point out another mechanism for accelerating compact objects to high velocities, which can occur only around a single supermassive black hole (SMBH, which are probably common in galactic nuclei). This mechanism is related to binary "collisions" (close passages) of two single, unrelated stars, or of a very close binary in the vicinity of a SMBH. The essence of the mechanism is that the energy of the forming connection between the SMBH and the more massive of the two stars is transformed into kinetic energy of the less massive star. Let $M_{\rm BH}$ be the BH mass, and M and m the masses of the more massive and less massive star. When the initial semimajor orbital axes of the colliding stars are large, their initial energy can be neglected if the orbits have a sufficiently high eccentricity. Let us assume that, after the collision, the more massive star acquires a circular orbit at a distance A around the BH. The law of energy conservation can then be written

$$\frac{GMM_{\rm BH}}{2A} = \frac{GmM_{\rm BH}}{A} + \frac{mv^2}{2}, \qquad (1)$$

where v is the velocity of the runaway star at infinity. Hence, this velocity can be estimated:

$$v = \left[\frac{GM_{\rm BH}}{A}\left(\frac{M}{m} - 2\right)\right]^{1/2}. \qquad (2)$$

A can be of the order of the gravitational radius of the BH, which for $M > 2m$ provides a nearly relativistic velocity v for a point-like mass. In reality, however, the velocities will be restricted to their parabolic values on the surfaces of the colliding stars. Therefore, only degenerate dwarfs, neutron stars, and stellar-mass BHs, which are relatively rare (10^{-3}–10^{-2}) but natural for a stellar population surrounding an SMBH at the center of a galaxy, can be accelerated to nearly relativistic velocities. Degenerate dwarfs bound to the same dwarfs, neutron stars, or BHs can be accelerated to ~4000 km/s, and neutron stars or stellar-mass BHs to ~100 000 km/s. Specially designed modeling that takes into account the diffusion of stars in the space around an SMBH and the variation of their velocity distribution with time is needed to estimate the contribution of this mechanism.

In collisions with SMBHs, MS stars (not to mention red giants) will be disrupted by tidal forces while crossing the boundary of the Roche lobe of the SMBH, preventing them from being accelerated to higher velocities. In ordinary galaxies with central BHs with masses of 10^6–$10^8\ M_\odot$, the frequency of such events is 10^{-4}–10^{-5}/year [14]. There has been

little observational evidence for such events; however, it is important that they are seen as optical and X-ray flares lasting from months to years [15–19]. After an MS star is disrupted, the SMBH accretes part of its matter over several months or years. It is likely that some fraction of the disrupted star is evaporated by X-ray radiation originating during the accretion of the disk formed from the star (polar jets may be seen in this case). If stars of a galactic nucleus possess angular momentum, some of the matter of the disrupted stars may form a stationary compact gaseous disk around the central SMBH. If this disk is dense enough, star formation may even occur in it. Some evidence for this is provided, for example, by the detection of massive young stars around the BH in the nucleus of our Galaxy [20].

Finally, we consider another possible mechanism: the acceleration of stars by a close binary SMBH in the nucleus of the product of a galaxy merger [21, 22]. Here, we study the interaction of stars in a galactic nucleus with a central close-binary SMBH. We wish to obtain the velocity spectrum of the stars that are accelerated as a result of this interaction under these conditions. We also consider the distribution of the incoming and outgoing regions occupied by the accelerated stars on the sky as a function of their final velocity. In particular, we pay special attention to the closeness of approach of the components of the binary SMBH by the accelerated stars, in order to estimate the role of tidal forces, which are capable of disrupting these stars under certain conditions. These stars may provide an important source of matter accreted by the BH, despite the fact that a disrupted star is excluded from the stars that can be accelerated.

2. ACCELERATION OF STARS BY BINARY SMBHs IN GALACTIC NUCLEI

2.1. Formation and Evolution of Binary SMBHs

Close-binary SMBHs originate in collisions between galaxies containing SMBHs in each of their nuclei [22]. The stellar components of the galaxies integrate, forming an elliptical galaxy, which is generally free of gas, while the SMBHs are tidally decelerated by the stellar component of the merger product, forming a close-binary SMBH.

Such binary SMBHs are indeed observed in galactic nuclei; some examples are presented by Komossa [23]. Binary nuclei were detected in 5 of 77 elliptical galaxies studied by Lauer *et al.* [11]. The nucleus of the galaxy Mkn 501 contains two BHs with masses of $10^8\,M_\odot$ and $10^9\,M_\odot$ [24]. A binary BH with component masses $\sim 7\times 10^8\,M_\odot$, semimajor axes $\sim$0.33 pc, and an orbital period of $\sim$480 yr was suspected in the nucleus of the galaxy 3C 345 [25]. The orbital velocities of the components of this system are $\sim$1000 km/s. Even among the most nearby galaxies, merging galaxies with two [26, 27] and even three [28] nuclei are observed. Binary quasars with SMBHs separated by only $\sim$20 kpc [29] and even $\sim$8 kpc at $z = 2.24$ [30] are known. These facts present additional arguments in support of studies of the behavior of stars in the gravitational field of close-binary SMBHs. The very fact that quasars originated when the age of the Universe was as small as $\sim 10^9$ yr underlines the efficiency of collisions of galaxies in dense clusters [31]. Another possible way for a close-binary SMBH with a large component-mass ratio to form in a galactic nucleus is when a globular cluster of a galaxy merges with the SMBH at its center. This mechanism may represent the main way in which the masses of SMBHs in galactic nuclei grow [22].

At late stages in the evolution of a close-binary BH, its components merge due to the loss of momentum from the system via gravitational-wave radiation. The characteristic time for the approach of two BHs with masses M_1 and M_2 and an orbital semimajor axis A is given by the expression

$$\tau_{\rm GWR} \approx 10^8 \left(\frac{A}{R_\odot}\right)^4 \frac{M_\odot^3}{M_1 M_2 (M_1+M_2)}\ \text{yrs}. \quad (3)$$

Assuming for simplicity that the components have the same mass M and $\tau_{\rm GWR} = 1.3\times 10^{10}$ yr, we can find the size of systems that coalesce over the Hubble time and the minimum orbital velocities of their components. The minimum semimajor axis is equal to $A_{\rm min} \approx 3.4(M/M_\odot)^{3/4}\,R_\odot$, while the relative orbital velocity of the components is $V_{\rm orb} \approx 240(M/M_\odot)^{1/8}$ km/s. It is obvious that, if the time for the components to merge is smaller than the Hubble time, the orbital velocities of the components will increase to values close to the speed of light as the orbital semimajor axis decreases.

2.2. The Velocity Distribution for Ejected Stars

The observed masses of BHs in galactic nuclei are confined to the interval 10^4–$10^{10}\,M_\odot$ [32]. As we will see below, the orbital velocities of the components of close-binary SMBHs are the same as the characteristic velocities of the stars accelerated by them. Therefore, based on general reasoning, we conclude from the last expression that the characteristic velocities gained by accelerated stars from close-binary SMBH components that coalesce over the Hubble time should be confined to the interval 600–4000 km/s. Both the upper and lower limits exceed the velocity needed for a star to escape from the parent

galaxy. Naturally, the approach of the binary components under the action of gravitational radiation decreases the lifetime of the system [formula (3)]; it also gradually increases the velocities of the ejected stars.

Let us estimate the velocity spectrum of stars ejected due to interactions with close-binary SMBHs. We will assume that a binary SMBH with mass M is immersed in a cluster of solar-mass stars with density n and velocity v. The radius of gravitational capture of stars by the binary SMBH will be $r = GM/v^2$, where G is the gravitational constant. The number of accelerated stars N will then be

$$N = \pi r^2 n v \tau_{\rm GWR} \sim \left(\frac{M}{M_\odot}\right)^3 \frac{n}{V_{\rm orb}^8 v^3}. \qquad (4)$$

This expression yields the conditions for the acceleration of stars by a binary SMBH. The number of accelerated stars increases with increasing mass of the binary components and with decreasing velocity dispersion of the stars surrounding the system. It is natural that increasing the density of field stars also increases the number of accelerated stars. The main property of the velocity spectrum (4) is its strong dependence on the orbital velocity of the binary SMBH. This is due to the rapid decrease of the time for the merger of the close-binary SMBH components, together with the decreasing distance between them [see formula (3)].

2.3. Tidal Disruption of Stars around SMBHs

Tidal forces from the components of close-binary SMBHs may disrupt stars interacting with them. Tidal disruption is also possible in the gravitational field of a single SMBH. Let us estimate the conditions for the disruption of various types of stars in the gravitational field of such a BH. A star undergoes tidal disruption when it enters a region where the average density determined by the BH exceeds that of the star. This average density is specified by $\bar{\rho} = 3M_{\rm BH}/4\pi R^3$, where R is the distance from the star to the BH and $M_{\rm BH}$ the mass of the BH. The average density of low-mass MS stars (below $1{-}5\,M_\odot$) is $\rho_* \approx (M_*/M_\odot)^{-2}$ g/cm^3, for degenerate dwarfs it is $\rho_* \approx 10^6 (M_*/M_\odot)^2$ g/cm^3, and for neutron stars it is $\rho_* \approx 10^{15}$ g/cm^3. The radius of the BH is given by the formula $R_{\rm BH} = 2GM_{\rm BH}/c^2$ or $R_{\rm BH}/R_\odot \approx 10^{-6}\, M_{\rm BH}/M_\odot$.

We can now estimate the limiting distance for a star to approach an SMBH, denoting $K = R/R_{\rm BH}$, where $K > 1$. The preservation of an MS star requires that $M_{\rm BH}/M_\odot > (10^9/K^{3/2})(M_*/M_\odot)$. This means that solar-mass MS stars can approach the surface of an SMBH; hence, their interaction with a close-binary SMBH can accelerate them to velocities comparable to the speed of light, if the mass of the components exceeds $\sim 10^9\, M_\odot$. The preservation condition for degenerate dwarfs is weaker: $M_{\rm BH}/M_\odot > (10^6/K^{3/2})(M_\odot/M_*)$. Therefore, solar-mass degenerate dwarfs will also be accelerated to very high velocities during interactions with close-binary SMBHs with masses of $\sim 10^6\, M_\odot$. The preservation condition for a neutron star is $M_{\rm BH} > 30\, M_\odot/K^{3/2}$. Thus, even a stellar-mass BH can accelerate a neutron star to relativistic velocities.

Summarizing the estimates made in this Section, we conclude that neutron stars/stellar-mass BHs, white dwarfs, and solar or subsolar-mass MS stars and planets can be efficiently accelerated without tidal disruption during interactions with close-binary SMBHs with masses exceeding $\sim 100\, M_\odot$, $\sim 10^6\, M_\odot$, and $\sim 10^9\, M_\odot$, respectively. BHs with such masses are observed in galactic nuclei [32]. However, some fraction of the accelerated stars, primarily MS stars, will undoubtedly be disrupted by tidal forces and their matter partially merged with the SMBH through an accretion–decretion disk. Such a scenario is described by de Vries *et al.* [33], who analyzed observations of 3791 quasars with redshifts $0 < z < 4.5$ on time scales from several months to 50 yr in order to search for transient events in a "mean" quasar on long time scales. The transient events took the form of bursts lasting several years, which occurred after $\sim$200 yr. These bursts can be explained by variability of the accretion rate due to some kind of instability of the accretion disk; however, they could also be associated with the tidal disruption of MS stars in the gravitational field of a BH with a characteristic mass of $\sim 10^7\, M_\odot$. Further detailed comprehensive studies of the observed bursts are needed to identify their true origin.

3. THE MODEL

In order to study the motion of stars in the gravitational field of a close-binary SMBH, we considered a binary SMBH in which one of the components (the primary) has a mass of $10^6\, M_\odot$ and the other (the secondary) has a mass of either $10^6, 10^5, 10^4$, or $10^3\, M_\odot$. This variation of the secondary mass was introduced to study the dependence of the acceleration and velocity spectrum of the ejected stars on the binary component-mass ratio. The SMBHs were treated as point objects, and their gravitational fields taken to be Newtonian. We assumed that the binary orbit was circular and fixed. In most of the computations, the orbital semimajor axis was taken to be $10^5\, R_\odot$. For component-mass ratios $q = 1.0, 0.1, 0.01, 0.001$, the orbital periods of the close-binary SMBH are equal to

7.10, 9.57, 9.99, and 10.03 yr, and the relative orbital velocities of the binary SMBH components are 1.95, 1.45, 1.39, and 1.38 thousand km/s, respectively. For $q = 1$, the time for the binary components to merge due to gravitational radiation is 7.6 billion yr, while the merger time scale exceeds the Hubble time for the other q values.

To derive the velocity spectrum for the stars ejected due to gravitational acceleration, we initially placed these stars uniformly on the celestial sphere, with the close-binary SMBH at the center of this distribution. In most of the models, the initial velocities of the stars were assumed to be directed towards the center of mass of the binary SMBH. To display the incoming and outgoing directions of these stars on the celestial sphere, we used a planar projection with an area equal to that of the sphere. This projection was constructed by transforming the latitude ϕ and longitude l (in radians) into planar coordinates X and Y using the formulas $Y = \phi$, $X = l\cos\phi$ for $l < \pi$ and $X = (l - 2\pi)\cos\phi$ for $l > \pi$. This yields a planar figure (see Figs. 1–9 below) whose area is equal to that of the sphere, with the coordinates varying in the ranges X from $-\pi$ to π, Y from $-\pi/2$ to $\pi/2$. The inverse transformation is also simple: $\phi = Y, l = X/\cos\phi$ for $X > 0$ and $l = 2\pi + X/\cos\phi$ for $X < 0$. This coordinate transformation enables us to easily specify a uniform distribution of incoming stars over the celestial sphere (via a uniform distribution in the planar figure) and to conveniently display the directions of incoming and outgoing stars accelerated by the close-binary SMBH.

The meridian that contains the radius vector from the primary to the secondary at the initial time was taken as the initial meridian of the sphere (which is transformed to the vertical axis of the planar figure). The opposite meridian is transformed into two boundary curves of the planar figure. The distribution of incoming directions for the stars was specified by dividing the X axis of the planar figure into 100 sections and the Y axis into 50 sections. Points located at the centers of the formed squares and lying within the planar figure (the projection of the sphere onto the plane) corresponded to the directions of the incoming stars. This procedure provides a uniform, spherically symmetrical distribution of incoming directions of stars. The number of test stars (directions) was 3192.

We computed the motion of a star in the region of the binary SMBH in a nonrotating coordinate system X, Y, Z with its origin at the center of mass of the binary and the XY plane coinciding with the orbital plane of the binary. The binary components were assumed to be located on the X axis at the initial time, with the coordinate of the primary being negative. The three-dimensional motion of a star in the gravitational field of the binary BH was computed by solving the classical equations

$$\frac{d^2X}{dt^2} = -\frac{GM_1}{R_1^3}(X - X_1) - \frac{GM_2}{R_2^3}(X - X_2), \quad (5)$$

$$\frac{d^2Y}{dt^2} = -\frac{GM_1}{R_1^3}(Y - Y_1) - \frac{GM_2}{R_2^3}(Y - Y_2), \quad (6)$$

$$\frac{d^2Z}{dt^2} = -\frac{GM_1}{R_1^3}(Z - Z_1) - \frac{GM_2}{R_2^3}(Z - Z_2). \quad (7)$$

Here, X, Y, Z are the coordinates of the star, X_1, Y_1, Z_1 the coordinates of the binary primary, X_2, Y_2, Z_2 the coordinates of the secondary, and R_1 and R_2 the distances from the star to the corresponding binary components.

The components of the binary SMBH rotate in circular orbits about their center of mass in the XY plane. The radii of the primary and secondary orbits are $A_1 = Aq/(1 + q)$ and $A_2 = A/(1 + q)$, respectively, where A is the orbital semimajor axis of the binary SMBH. The rotation angle of the system at time t is equal to $\phi = 2\pi t/P_{\rm orb}$, where $P_{\rm orb}$ is the orbital period of the binary. As a result, the coordinates of the components at time t are specified by the expressions

$$X_1 = -A_1\cos\phi, \quad (8)$$

$$Y_1 = -A_1\sin\phi, \quad (9)$$

$$Z_1 = 0, \quad (10)$$

$$X_2 = A_2\cos\phi, \quad (11)$$

$$Y_2 = A_2\sin\phi, \quad (12)$$

$$Z_2 = 0. \quad (13)$$

This system of equations was solved using the Kutte–Merson method. The relative accuracy of the integration was on the order of 10^{-8}.

We estimated the applicability of the technique by computing the trajectory of a star that "falls" in the polar direction towards the center of mass of a binary with equal component masses. In the absence of any perturbations, such a star should become a "pendulum" oscillating with a constant amplitude along the rotational axis of the system, which goes through the center of mass and is perpendicular to the orbital plane. The test computation showed that such oscillations along the rotational axis of the system indeed occurred during approximately 160 orbital periods of the binary (about ten periods of the pendulum); later, however, the accumulation of numerical errors results in a deviation of the trajectory of the pendulum from the axis. This causes the type of motion to change

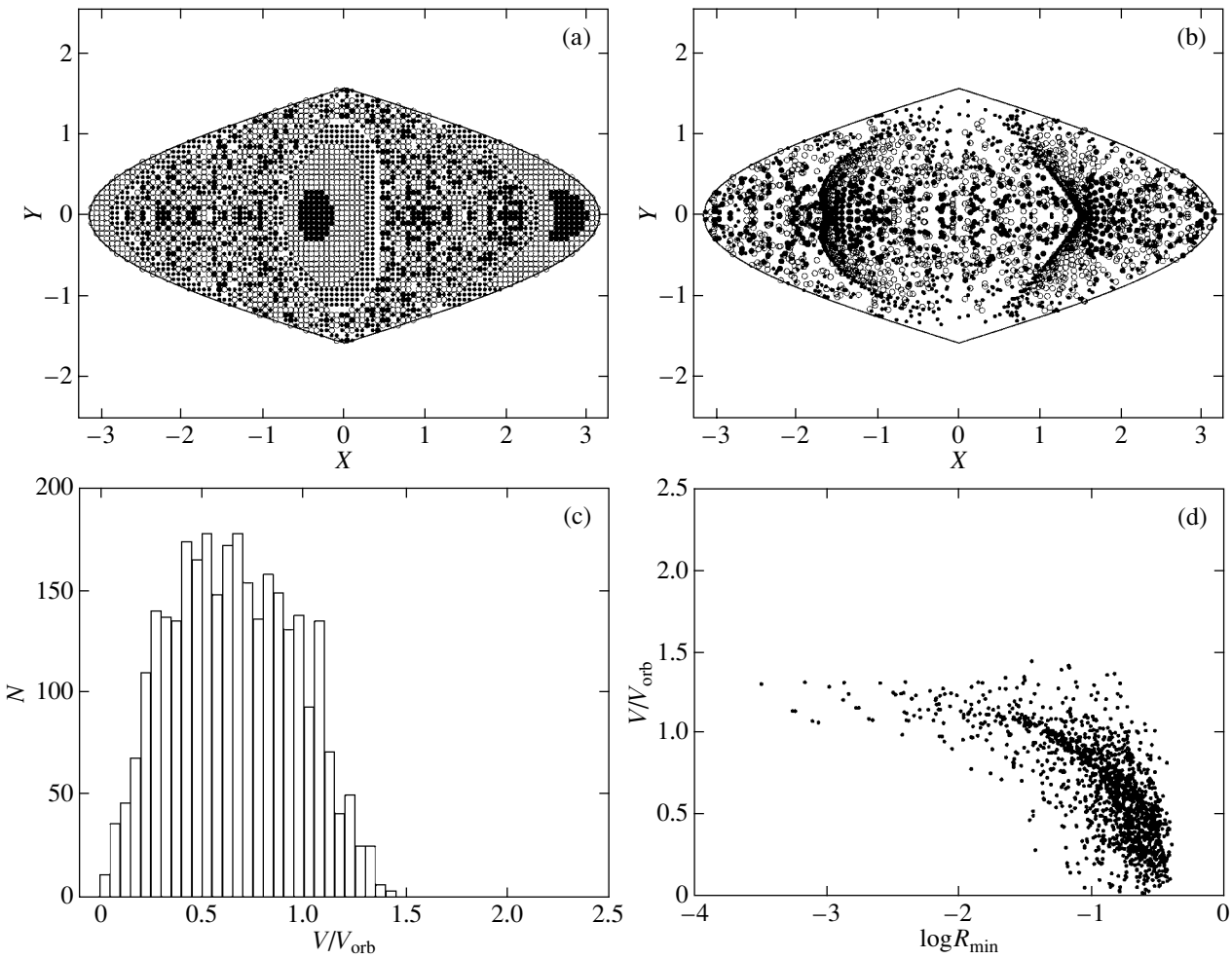

Fig. 1. Computation results for $q = 1$, $V_0 = 0$, $R_0 = 10\,A$. (a) Direction distribution for stars incoming towards the close-binary SMBH on the projection plane of the celestial sphere; (b) direction distribution for stars leaving the close-binary SMBH. Different symbols denote stars with different final velocities V. Large filled circles correspond to $V > V_{orb}$, hollow circles to $0.5\,V_{orb} < V < V_{orb}$, and small filled circles to $0 < V < 0.5\,V_{orb}$, where V_{orb} is the relative orbital velocity of the close-binary SMBH component. (c) Numbers of stars with different ratios of the final velocity and the relative orbital velocity of the binary SMBH components. (d) Final velocity of outgoing stars as a function of the logarithm of the minimum distance to the binary SMBH components R_{min} (in units of A).

rapidly (on the orbital time scale), and the pendulum is ejected from the system. Increasing the relative accuracy of integration to 10^{-10} does not affect the calculated orbit of the pendulum. Therefore, we conclude that the computation method used yields satisfactory results during at least two hundred orbital periods of the binary.

To study the stability of the results, in addition to varying the binary component-mass ratio, we also varied the initial velocity of a star V_0 and its initial distance to the binary center of mass R_0. We adopted values for R_0 of 10 and 100 A, where A is the orbital semimajor axis of the binary, while V_0 was assigned values of 0 and 1000 km/s. In most of the computations, the initial velocity of the star was directed towards the center of mass of the system. For $q = 1$, we also considered the case where the initial velocity is directed towards the point where one of the binary components was located at the initial time. It is obvious that these V_0 and R_0 do not exhaust the possible range of parameters of stars moving in the vicinity of a galactic nucleus. However, we restricted our consideration to these values, since we were essentially interested in demonstrating the fundamental possibility of efficiently accelerating stars via their interaction with a close-binary SMBH.

We present the results of our computations using four plots (Figs. 1–9). Plot (a) presents the direction distribution for stars incoming toward the close-binary SMBH on the projection plane of the celestial sphere. Only stars that leave the binary are shown. Various symbols are used to indicate the incoming

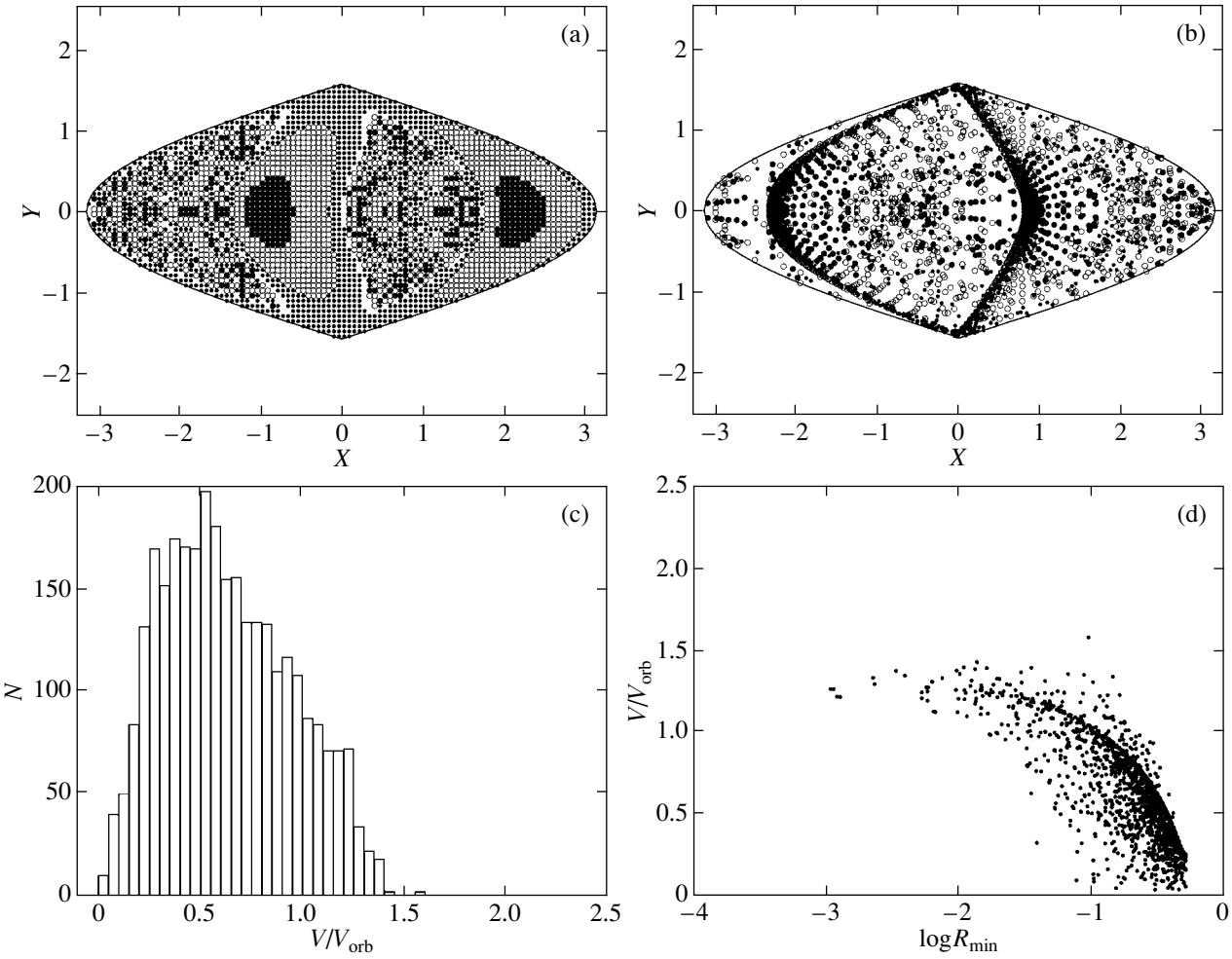

Fig. 2. Same as Fig. 1 for $q = 1$, $V_0 = 1000$ km/s, and $R_0 = 10\,A$.

directions, depending on the final velocity of the star leaving the system. Thus, darker regions in the plot correspond to incoming directions for stars achieving the highest velocities. Plot (b) presents the direction distribution for stars leaving the close-binary SMBH on the projection plane of the celestial sphere. The final velocities of the stars are denoted using the same symbols as in (a). Thus, the darkest regions of plot (b) correspond to directions into which most stars accelerated to highest velocities go.

Plot (c) displays the distribution of the velocity at infinity for stars leaving the system, measured in units of the relative orbital velocity of the close-binary SMBH components. Plot (d) presents the correlation between the outgoing velocity of a star and the minimum distance of approach of the binary components.

We present here results of computations of the motion of a star over 200 (for $R_0 = 10\,A$) or 400 (for $R_0 = 100\,A$) orbital periods of the binary SMBH. In the latter case, the computation time was increased, since the time when the star reaches the vicinity of the close-binary SMBH is already close to 200 periods. We also carried out test computations of the motion of a star during 10^4 periods. The main difference is that more stars are accelerated over the longer time, since they have more opportunities to come into the close vicinity of one of the components of the close-binary SMBH. However, the accumulation of numerical errors makes the details of such computations unreliable.

4. RESULTS OF THE SIMULATIONS

4.1. Mechanism for the Acceleration of the Stars

The acceleration of the motion of a star interacting with a close-binary SMBH is due to the "slingshot effect." A star that has closely approached a rapidly moving close-binary SMBH component is "captured," and thus accelerated. Detailed studies of this mechanism make it clear that the "throw"

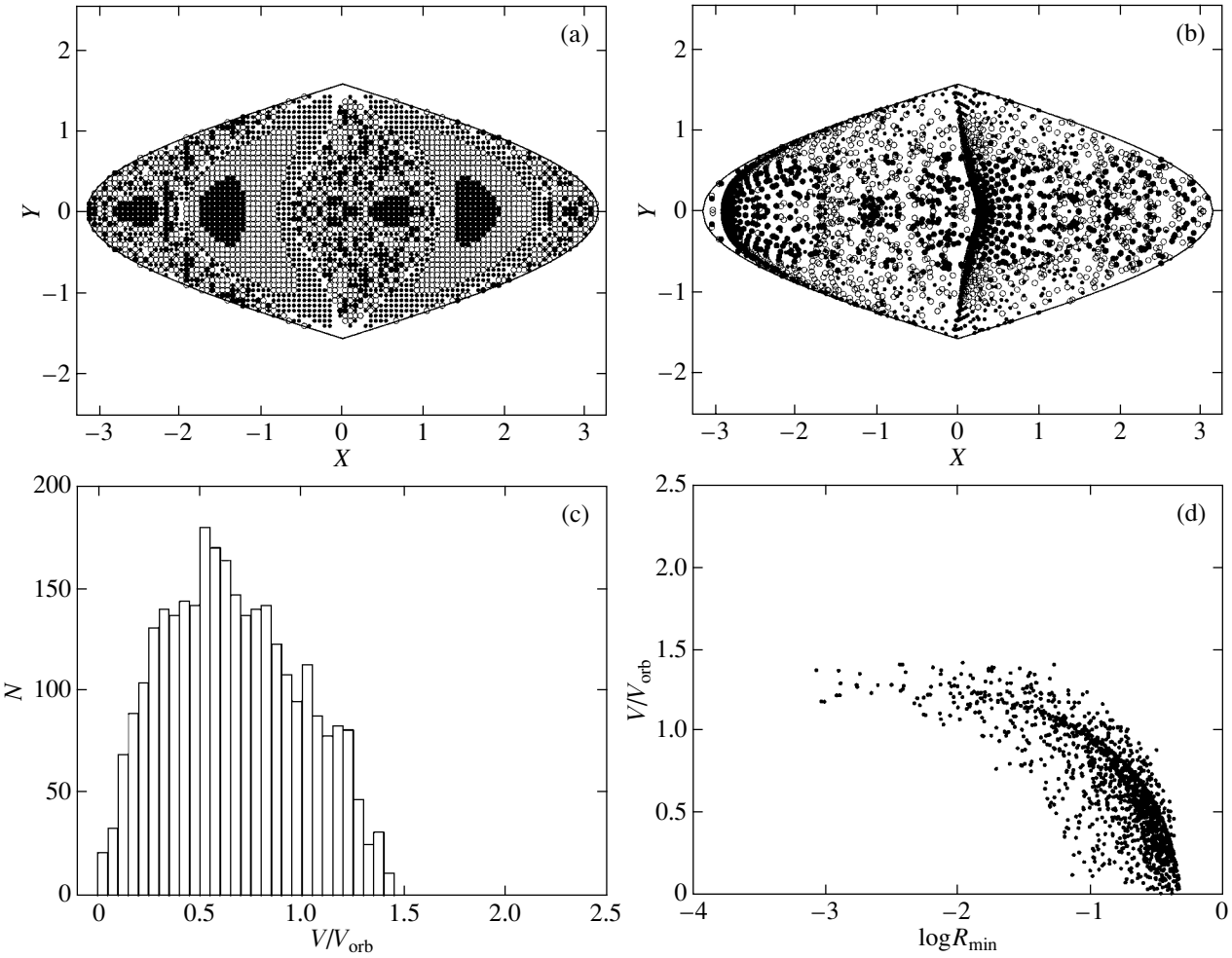

Fig. 3. Same as Fig. 1 for $q = 1$, $V_0 = 0$, and $R_0 = 100\,A$.

always occurs at the same phase of the motion of an unstable triple system, when all the components lie almost precisely along a straight line and rotate in the same direction. In the case of equal component masses, the force of the "throw" is determined by the proximity to the accelerating component of the close-binary SMBH (Fig. 1d). The closer the accelerated star is to the accelerating BH, the larger the velocity at infinity it reaches (Fig. 1d). This dependence displays a large scatter, probably due to the phase of the secondary component of the close-binary SMBH and the direction of the velocity of the accelerated star. The situation is different for $q = 0.1$ (Fig. 4d). The acceleration gained in the interaction with the lower-mass component, which has higher orbital velocity, enables the star to reach a higher outgoing velocity; however, such approaches occur less frequently, partly due to our assumption that the initial velocity of the star is directed towards the center of mass of the close-binary SMBH, which is located substantially closer to the secondary. Due to its low orbital velocity, the more massive component is unable to accelerate an ejected star to a high velocity. Therefore, the correlation is less pronounced in Fig. 4d. Finally, for $q = 0.01$ (Fig. 7d), the highest velocities are gained by the still rarer stars that are accelerated by the lower-mass component, while the correlation between the closeness of approach and the velocity essentially disappears for small final velocities.

4.2. Computation Results for $q = 1$

Figures 1–3 present our computation results for $q = 1$. Figure 1 shows that the incoming directions for stars accelerated to the highest velocities are primarily concentrated in two "spots" that are symmetrically located on the equator of the close-binary SMBH, while the outgoing directions for these stars are concentrated on two symmetrical meridians. Essentially no stars are ejected along the polar directions. Stars incoming from some directions are not

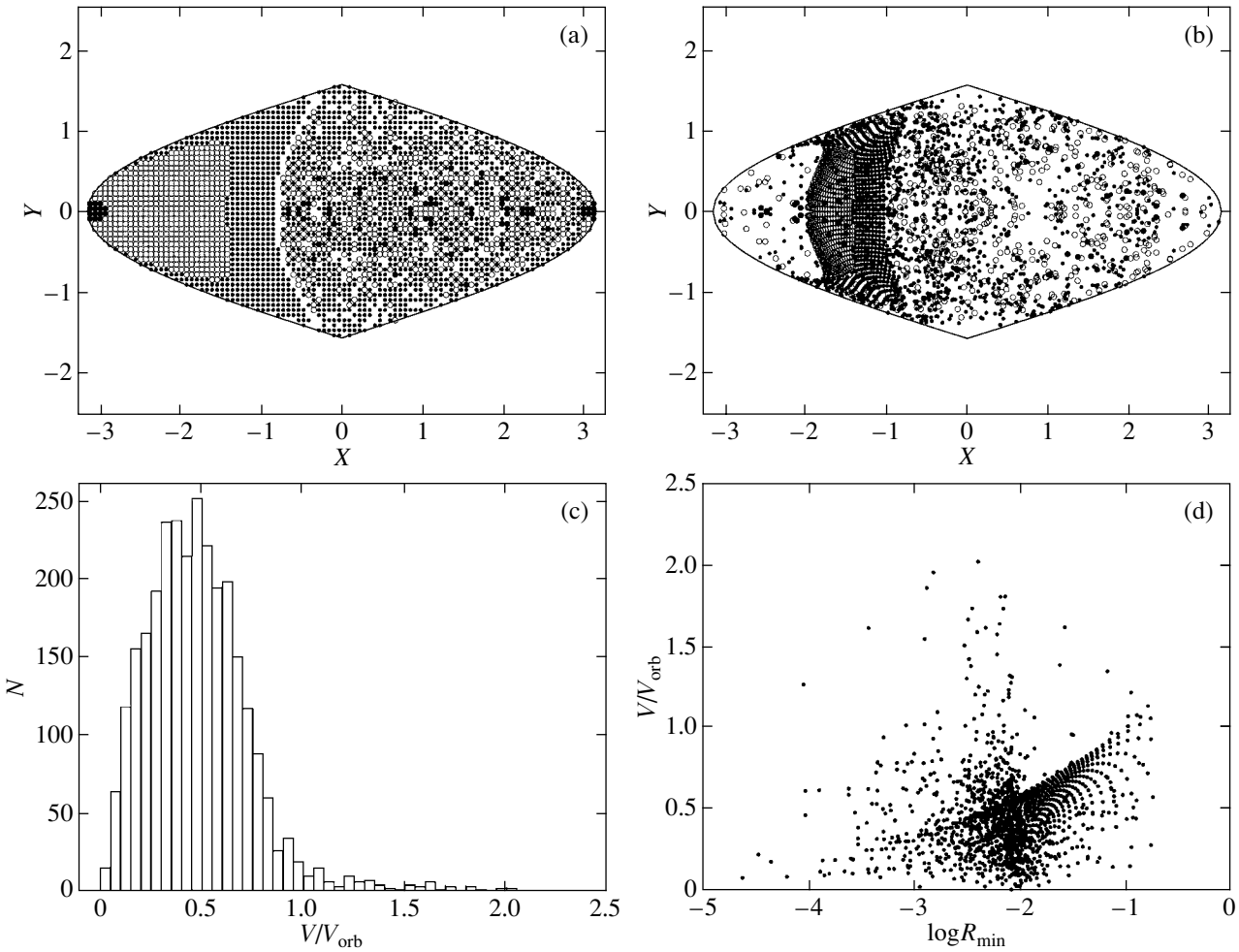

Fig. 4. Same as Fig. 1 for $q = 0.1$, $V_0 = 0$, and $R_0 = 10\,A$.

ejected from the system over the computed time interval, but are instead captured in quasi-stable orbits around one of the components. These directions correspond to "gaps" in the planar projection, indicating the directions of these incoming stars (Fig. 1a). Our modeling showed that the number of stars captured in this way increases with the component-mass ratio of the binary SMBH (Figs. 1–9). We should bear mind, however, that if the components of the binary SMBH coalesce over the Hubble time, these stars will also be ejected from the system with velocities comparable to the orbital velocity of the components, since the semimajor axis of the system will gradually contract. In addition, they may be tidally disrupted by the components of the binary SMBH.

A comparison of Figs. 1 and 2 shows the influence of the initial velocity of the star. Figure 1 corresponds to zero initial velocity and Fig. 2 to an initial velocity of 1000 km/s, which is comparable to the absolute orbital velocity of the close-binary SMBH components. A comparison of Figs. 1 and 3 shows the effect of an order-of-magnitude (from $10\,A$ to $100\,A$) increase of the initial distance from the star to the center of mass of the close-binary SMBH. As we can see, varying V_0 and R_0 does not substantially affect our main result for the velocity distribution for the outgoing stars [plots (c)]. Only details of this distribution vary within the overall dispersion ($N^{1/2}$), while the maximum velocities remain approximately the same. The ratio of these velocities and the relative orbital velocity of the close-binary SMBH components is close to 1.5, while their ratio to the absolute orbital velocity of the components is close to 3. We therefore conclude that, within a broad range of initial parameters for stars approaching a close-binary SMBH, some fraction of these stars can be accelerated to velocities exceeding the orbital velocity of the components of the SMBH by a factor of two to three. For $q = 1$, we also considered the case when the initial velocity of the star is directed towards the point where one of the binary components is located at the initial time, rather than towards the binary center of mass. However,

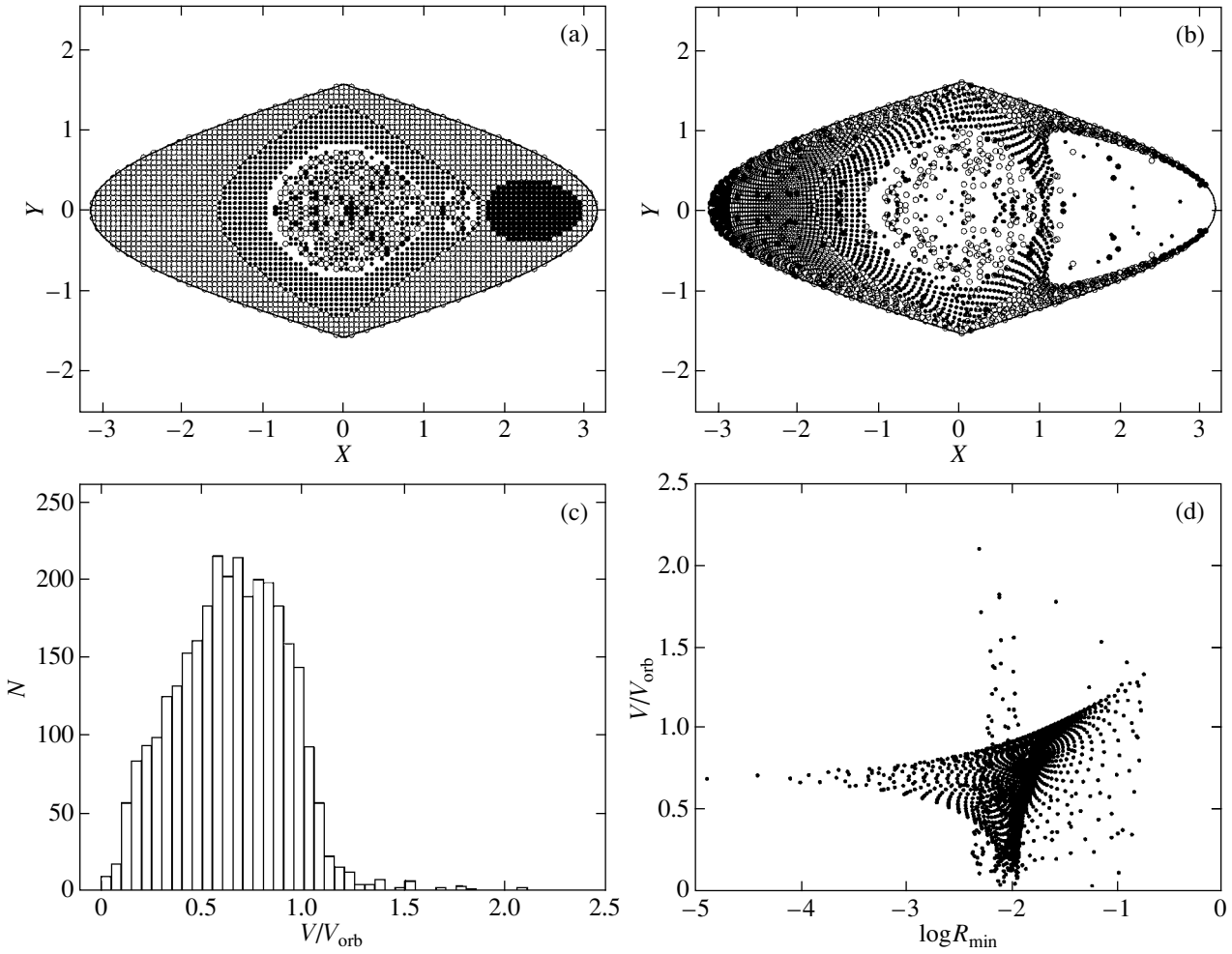

Fig. 5. Same as Fig. 1 for $q = 0.1$, $V_0 = 1000$ km/s, and $R_0 = 10\,A$.

this likewise did not appreciably change the velocity distribution for the outgoing stars; the only variations were essentially in the distribution of stars leaving the system on the celestial sphere.

The main result of our modeling is the possibility for compact stars—primarily, stellar BHs and neutron stars—to be accelerated to velocities of the order of the orbital velocities of the components of close-binary SMBHs, which can reach the speed of light over the time scale for the merging of the components. This implies that acceleration by a SMBH is able to produce neutron stars and stellar BHs with velocities approaching the speed of light. Obviously, the number of such rapidly moving compact stars cannot be large [see (2)], and we have only made the first steps towards understanding such stars. During their acceleration, some of the stars that are accelerated to high velocities approach the BH to distances of $\sim 10^{-3}$–10^{-7} of the semimajor axis of the system. It is obvious that tidal disruption or merging of these stars with the BH restricts the maximum velocity of the accelerated stars to $\sim cR_{\min}^{1/2}$, where c is the speed of light and $R_{\min}$ the minimum distance to the close-binary SMBH components in units of the semimajor axis. Therefore, only binary BHs with comparable component masses can accelerate compact stars to relativistic velocities. To obtain the actual velocity spectrum, this problem must be treated in the framework of general relativity and the approach of the close-binary SMBH components under the action of gravitational radiation in the acceleration phase must be taken into account.

4.3. Computation Results for $q = 0.1$

Figures 4–6 present our computation results for $q = 0.1$. In these figures, the distribution of initial parameters is the same as for $q = 1$. In this case, the maximum initial velocity of a star (1000 km/s) is equal to 0.76 of the absolute orbital velocity of the close-binary SMBH secondary, which is 1320 km/s.

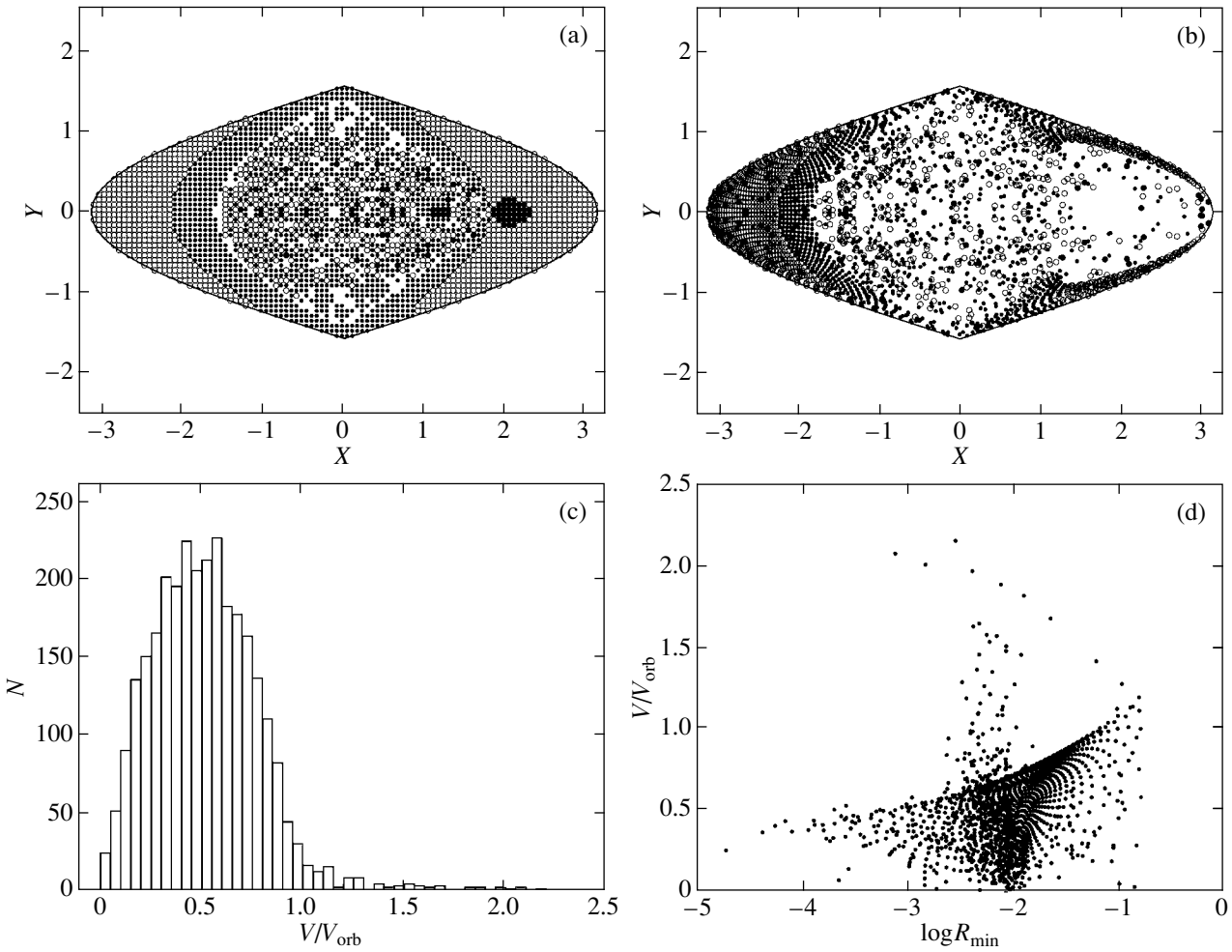

Fig. 6. Same as Fig. 1 for $q = 0.1$, $V_0 = 0$, and $R_0 = 100\,A$.

The main difference between the results for $q = 0.1$ and $q = 1.0$ is the final velocity distribution for the outgoing stars [plot (c)]. In this case, the relative number of stars accelerated to high velocities decreases, since the main accelerating component of the close-binary SMBH is the more massive component. Some 99% of stars approach the more massive component, whose orbital velocity is, naturally, comparatively small. Note that the maximum velocities of the accelerated stars exceed the orbital velocity of the secondary by almost a factor of two. Here, the dependence on V_0 is pronounced more strongly than for close-binary SMBHs with equal-mass components.

When $q = 0.1$, the direction distributions for the incoming and outgoing stars on the projection plane of the celestial sphere become more nonsymmetrical, which can naturally be explained as an effect of the different masses of the close-binary SMBH components and the advantage of the less massive component as an efficient accelerator.

4.4. Computation Results for $q = 0.01$

Figures 7–9 present the computation results for $q = 0.01$. In this case, the maximum initial velocity of a star (1000 km/s) is 0.73 of the absolute orbital velocity of the close-binary SMBH secondary, 1370 km/s. The most important difference from previous results is that, in the case of low initial velocities of the incoming stars, a substantial number remain in the binary rather than leaving it, due to their very close approach to the more massive binary component. Such stars are captured into comparatively stable orbits around this component. When $q = 1$, the fraction of stars remaining in the system (for a computation time of about two hundred orbital periods of the close-binary SMBH) was around 6% for small V_0, rising to 10% for $q = 0.1$. However, this fraction increases appreciably when $q = 0.01$, reaching 94% for $R_0 = 10\,A$ and 60% for $R_0 = 100\,A$ when $V_0 = 0$. Only for $V_0 = 1000$ km/s do all the stars leave the close-binary SMBH.

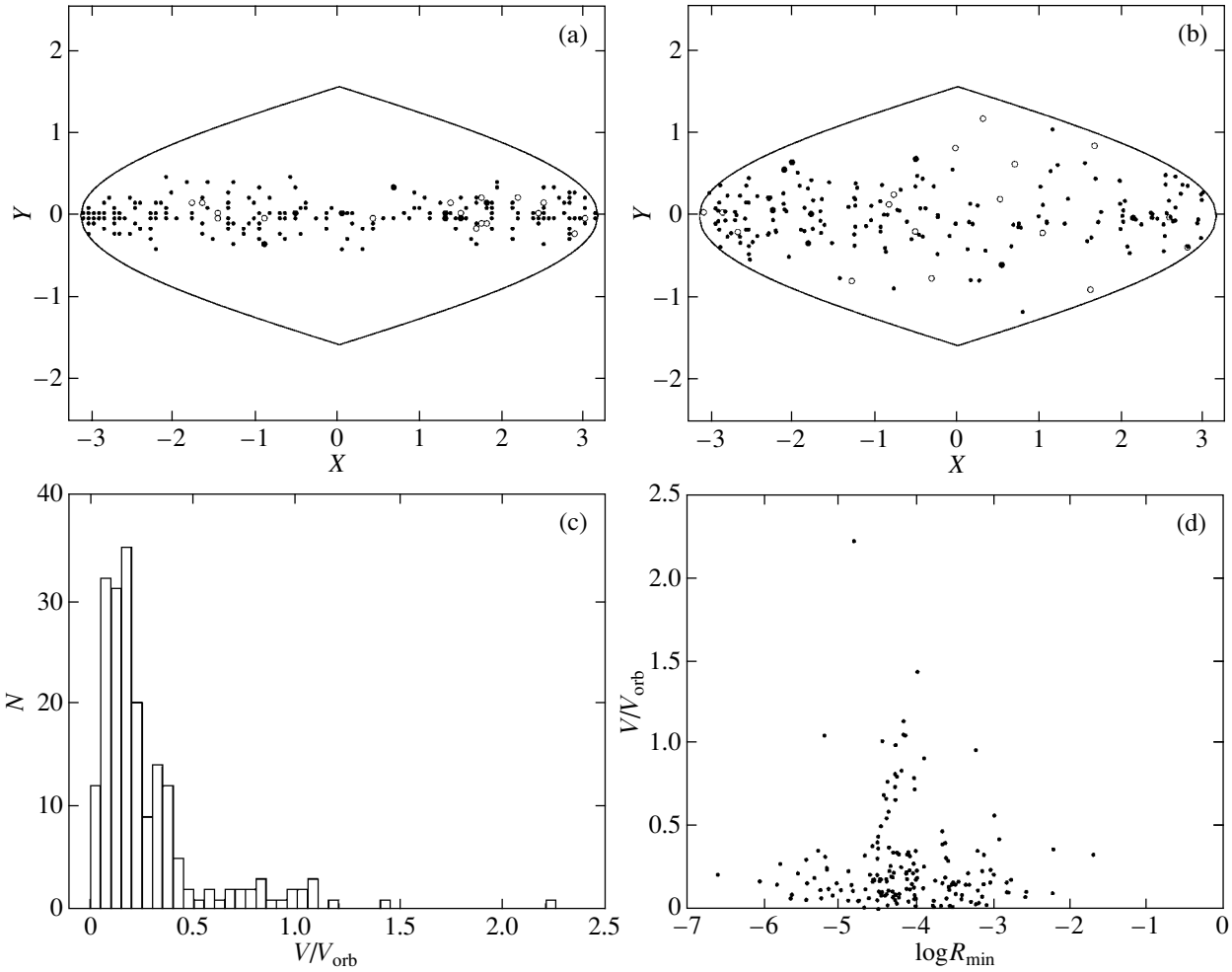

Fig. 7. Same as Fig. 1 for $q = 0.01$, $V_0 = 0$, and $R_0 = 10\,A$.

The decrease in the number of outgoing stars appreciably affects their velocity distributions (Figs. 7d, 8d). In addition, the number of stars accelerated to velocities comparable with the orbital velocity of the less massive binary component decreases dramatically. As a result of our assumption that the initial velocity of a star is directed towards the center of mass of the system (which for $q = 0.01$ essentially coincides with the direction towards the primary), stars essentially end up in the vicinity of the more massive component of the close-binary SMBH; this favors their capture by this component, while only a few approach the less massive component, which is the efficient accelerator. Recall that the "captured" stars will also eventually either be ejected from the SMBH, if this binary coalesces over the Hubble time, or be disrupted by tidal forces from the SMBH.

4.5. Computation Results for $q = 0.001$

Let us briefly describe what makes this case qualitatively different from the previous one. As the close-binary SMBH component-mass ratio decreases further, stars end up even closer to the massive component. As a result, the number of stars leaving the binary decreases even more dramatically. Their minimum distance from the primary becomes approximately 10^{-5}–10^{-8} of the orbital semimajor axis, so that they are very likely to be distupted. The average velocity of the stars leaving the system decreases; however, when $R_0 = 100\,A$, individual stars can be accelerated to velocities a factor of four to five greater than the relative orbital velocities of the close-binary SMBH components, which was not the case for large q. In this case, a SMBH coalescing over the Hubble time will either disrupt the "captured" stars or eject them from the system with velocities comparable to the orbital velocity of the SMBH components.

5. CONCLUSION

We have modeled a close-binary SMBH formed in the nucleus of two merged galaxies that accelerates

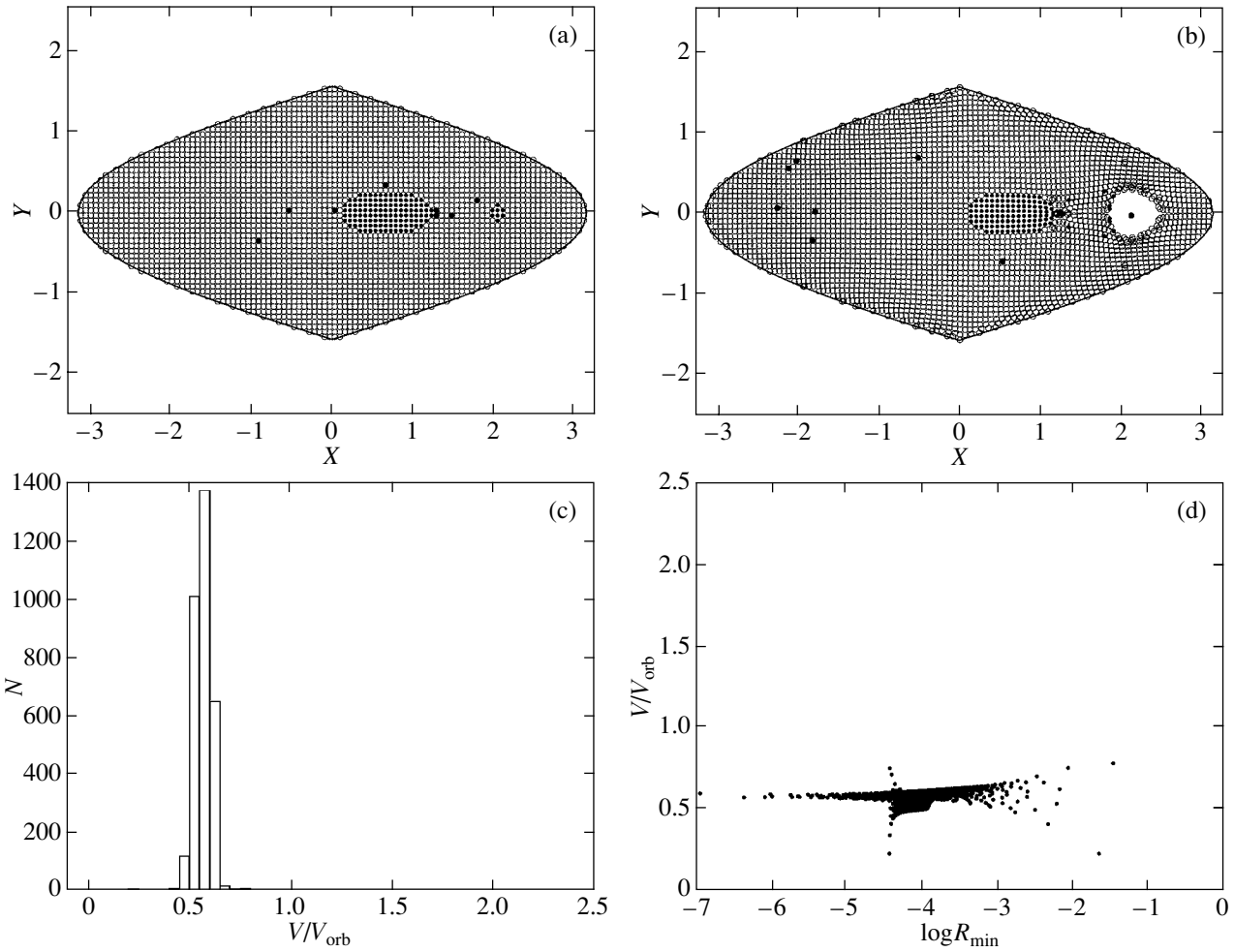

Fig. 8. Same as Fig. 1 for $q = 0.01$, $V_0 = 1000$ km/s, and $R_0 = 10\,A$.

MS stars, degenerate dwarfs, neutron stars, and stellar BHs in the nucleus. Our calculations indicate that, within a broad interval of component-mass ratios of the close-binary SMBH, the SMBH acts as an efficient accelerator of stars that end up within the sphere of its gravitational influence. In the case of comparable component masses for the close-binary SMBH, the characteristic velocities of the accelerated stars at infinity are of the order of the orbital velocities of the binary components. As the mass of the close-binary SMBH secondary decreases, the mean velocity of the ejected stars also decreases. This is partly due to the decrease in the total mass of the system, and hence of the component velocities. In addition, in the case of small component-mass ratios, the more massive component, in whose vicinity more stars end up, becomes the main (though less efficient) accelerator. Thus, as a result of the acceleration, compact neutron stars and stellar-mass BHs can acquire velocities comparable to the orbital velocity of the close-binary SMBH components. Just before the components merge, this orbital velocity can reach the speed of light. Therefore this mechanism can accelerate neutron stars, stellar BHs, degenerate dwarfs, and, if $M_{BH} \gtrsim 10^9\,M_\odot$, MS stars to relativistic velocities. To derive a more accurate velocity spectrum for the stars ejected by coalescing close-binary SMBH components, this problem must be solved taking into account general-relativistic effects and the merging of the components under the action of gravitational radiation by the system during the acceleration of the ejected stars.

The characteristic relative orbital velocities of equal-mass close-binary SMBH components that coalesce over the Hubble time [formula (3)] are $\sim 250(M_{BH}/M_\odot)^{1/8}$ km/s. Since, according to the Tully–Fisher relation [34], the stellar escape velocity from a galaxy with mass M_G is $v_{esc} \sim 0.7(M_G/M_\odot)^{1/4}$ km/s, while $M_{BH} \sim 0.001\,M_G$ [35], nearly all the stars that are accelerated by a binary BH will be ejected from their parent galaxies, increasing the stellar population of the intergalactic medium.

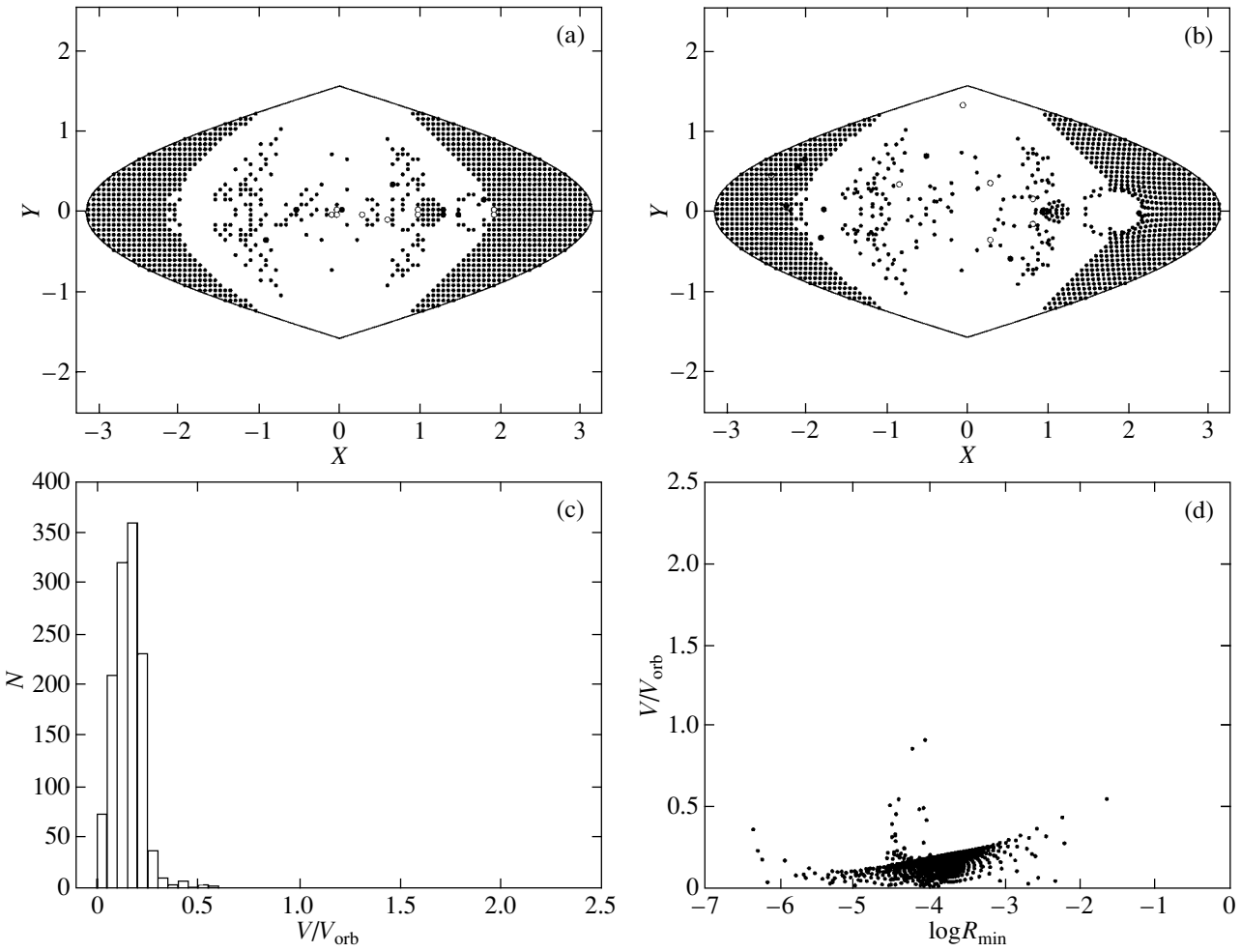

Fig. 9. Same as Fig. 1 for $q = 0.01$, $V_0 = 0$, and $R_0 = 100\,A$.

The phase of BH merging in the nuclei of merging galaxies can be divided into two main stages. In the first, for $A > 10^{-7}(M_{BH}/M_\odot)^{3/4}$ pc, the relative velocities of the BHs are low, and they decelerate to velocities lower than the escape velocity, primarily due to tidal forces and the acceleration of field stars. This process increases the galactic-bulge population. In the second stage, when the BH orbital velocities reach 200–500 km/s, the binary nucleus begins to eject stars from the galaxy, forming a corona with a power-law decrease in the stellar density, as is seen for the Andromeda Galaxy [36, 37], as well as an intergalactic stellar population [10]. The detection of this latter population requires studies of the radial velocities of its brightest members—(super)giants and planetary nebulae, whose radial velocities can be determined in a large volume of space.

Our study of the acceleration of stars by close-binary SMBHs with high component-mass ratios demonstrates the possible appearance of a large number of stars with high orbital eccentricities. This mechanism may explain the presence in the nucleus of our Galaxy of stars rotating about the central SMBH with orbital velocities of several thousands of km/s and orbital eccentricities of 0.5–0.98 [38]. These stars could have been accelerated by one of the close binary SMBHs that may originate from time to time in the nucleus of our Galaxy due to the merging of globular clusters located close to the Galactic center and containing intermediate-mass BHs with the Galactic bulge during the formation of the central supermassive black hole [22]. Some of the accelerated stars were ejected from the nucleus, while others remained in the currently observed eccentric orbits.

ACKNOWLEDGMENTS

This work was supported by the Program of Support for Leading Scientific Schools of the Russian Federation (grant no. NSh-162.2003.2), the Federal Science and Technology Program in Astronomy, the

program of the Presidium of the Russian Academy of Sciences "Nonstationary Phenomena in Astronomy," and the Russian Foundation for Basic Research (project no. 03-02-16254).

REFERENCES

1. A. Tokovinin, Astron. Astrophys. **124**, 75 (1997).
2. J. Hills, Astron. J. **80**, 809 (1975).
3. J. Hills, Astron. J. **102**, 704 (1991).
4. P. Hut, Astrophys. J. **268**, 342 (1983).
5. P. Hut, Celest. Mech. **45**, 713 (1989).
6. P. Hut, Astrophys. J. **403**, 256 (1993).
7. H. Baumgardt, P. Hut, and D. Heggie, Mon. Not. R. Astron. Soc. **336**, 1069 (2002).
8. A. Blaaw, Annu. Rev. Astron. Astrophys. **2**, 213 (1964).
9. W. Brown, M. Geller, S. Kenyon, *et al.*, astro-ph/0501177 (2005).
10. R. Mendez, M. Guerrero, K. Freeman, *et al.*, Astrophys. J. Lett. **491**, L23 (1997).
11. T. Lauer, S. Faber, K. Gebhardt, *et al.*, astro-ph/0412040 (2004).
12. M. Mozi, ASP Conf. Ser. **222**, 359 (2001).
13. I. Iben, Jr., A. Tutukov, and L. Yungelson, Astrophys. J., Suppl. Ser. **100**, 233 (1995).
14. T. Bogdanovic, M. Eracleons, S. Mahadevan, *et al.*, Astrophys. J. **610**, 707 (2004).
15. D. Stern, P. van Dokkum, P. Nugent, *et al.*, Astrophys. J. **612**, 690 (2004).
16. L. Li, R. Narayan, and K. Menou, Astrophys. J. **576**, 753 (2002).
17. A. Renzini, Nature **378**, 39 (1995).
18. A. Komossa and N. Bade, Astron. Astrophys. **343**, 775 (1999).
19. A. Komossa and J. Greiner, Astron. Astrophys. **349**, L45 (1999).
20. Y. Levin, A. S. P. Wu, and E. W. Thommes, astro-ph/0502143 (2005).
21. Q. Yu and S. Tremaine, Astrophys. J. **599**, 1129 (2003).
22. A. V. Tutukov, Astron. Zh. **82**, 1 (2005) [Astron. Rep. **49**, 13 (2005)].
23. S. Komossa, Am. Inst. Phys. Conf. Proc. **686**, 161 (2003).
24. R. Rieger and K. Maunheim, Astron. Astrophys. **397**, 121 (2003).
25. A. Lobanov and J. Roland, astro-ph/0411417 (2004).
26. J. Gerssen, Astron. J. **127**, 75 (2004).
27. F. Liu, X. Wu, and S. Cao, Mon. Not. R. Astron. Soc. **340**, L411 (2003).
28. M. Seigar, Mon. Not. R. Astron. Soc. **344**, 110 (2003).
29. H. Zhou, T. Wang, X. Zhang, *et al.*, Astrophys. J. Lett. **604**, L33 (2004).
30. N. Morgan, G. Burley, E. Costa, *et al.*, Astron. J. **119**, 1083 (2000).
31. G. Voit, astro-ph/0410173 (2004).
32. T. Ho, Astrophys. J. **564**, 120 (2002).
33. W. de Vries, R. Becker, and R. White, Astron. J. **126**, 1217 (2003).
34. R. B. Tully and J. R. Fisher, Astron. Astrophys. **54**, 661 (1977).
35. M. Elvis, G. Risaliti, and G. Zamorani, Astrophys. J. Lett. **565**, L75 (2002).
36. C. Zier and P. L. Bierman, Astron. Astrophys. **377**, 23 (2001).
37. P. Guhathakurta, J. Ostheimer, K. Gilbert, *et al.*, astro-ph/0502366 (2005).
38. M. Davies and A. King, astro-ph/0503441 (2005).

Translated by K. Maslennikov

Astronomy Reports, Vol. 49, No. 9, 2005, pp. 693–700. Translated from Astronomicheskiĭ Zhurnal, Vol. 82, No. 9, 2005, pp. 779–787.

Kinematics of Stars in the Old Open Cluster M67

A. V. Loktin

Astronomical Observatory, Ural State University, Leninskiĭ pr. 51, Yekaterinburg, 620083 Russia

Received July 12, 2004; in final form, February 17, 2005

Abstract—We report an analysis of the kinematic properties of stars in the old open cluster M67 based on proper motions taken from a master catalog made up of nine different catalogs containing proper motions of stars in the cluster field. A modified Sanders method is used to identify 511 probable cluster members. The dependence of the mean radial components of the proper motions of cluster members on clustercentric radius indicates that the cluster core is expanding with a velocity of 0.4 km/s. The radial dependence of the mean tangential components of the proper motions suggests the possible rotation of the cluster core. The dispersions of the velocity components of the cluster members show no evidence for the dominance of elongated stellar orbits in the cluster. The kinetic energy of the cluster stars depends strongly on their mass.

1. INTRODUCTION

Proper motions of stars in an open star cluster bear important information about the kinematics of the cluster members. Many independent proper-motion determinations for extensive samples of stars are now available for a large number of clusters; if reduced to a single system, these data can be used to determine high-accuracy proper motions for further analysis. The available proper-motion measurements for a large number of stars in rich open clusters provide extensive samples for analyses of the kinematic properties of open clusters, making it possible to study the systematic motions of the cluster stars and the behavior of the residual velocity dispersion as a function of stellar mass and the coordinates in the cluster. We decided to perform the first such analysis for stars in the open cluster M67. We chose M67 for our first attempt of a detailed proper-motion analysis of the kinematics of its members for several reasons. First, M67 is a well-studied cluster, for which several independent catalogs of relative proper motions are available. Second, it is a rich cluster, so that sufficiently trustworthy statistical estimates can be obtained for its dynamical and kinematic parameters. Third, M67 is a fairly distant cluster, so that we can estimate the current limits for analyses based on proper motions, which are the most extensive source of stellar data. Fourth, M67 is an old open cluster, which is very likely to be in an almost dynamically stable state, so that the kinematics of its stars should not be too confused by group motions.

Until now, only a few authors have analyzed the kinematics of stars in open clusters, most notably stellar motions in the Coma [1], Hyades [2], and Pleiades [3] clusters. However, even studies of clusters located in the nearby solar neighborhood were limited in practice to determining the velocity dispersion of the entire cluster, with only the first steps taken toward analyzing the behavior of these quantities in relation to the properties of stellar orbits in the clusters. It was the need to further develop the observational base for analyses of the dynamics of open clusters that stimulated this research.

2. INITIAL DATA

To analyze stellar motions in a cluster, we must have high-accuracy proper motions, which can be calculated by reducing the data provided by various catalogs of absolute and relative stellar proper motions in the cluster field to a single system. A description of the technique used to combine the data for different catalogs is described in [4]. Below, we briefly review the underlying ideas of such a compilation. To produce a master catalog, we first choose one of the proper-motion catalogs used as a reference to which we reduce the proper-motion systems of all the other catalogs. We adopted the Tycho-2 catalog as this reference catalog. We reduced the proper motions of each catalog to the Tycho-2 system using linear transformations of the form

$$\begin{cases} \mu_{x1} = a_x\mu_{x2} + b_x\mu_{y2} + c_xV + d_x, \\ \mu_{y1} = a_y\mu_{x2} + b_y\mu_{y2} + c_yV + d_y. \end{cases} \quad (1)$$

We determined the transformation coefficients for (1) via a least-squares fit. The coefficients a_x, b_x, a_y, and b_y describe the rotation and contraction or expansion of the system of proper motions, d_x and d_y describe the offset, and c_x and c_y are responsible for the

1063-7729/05/4909-0693$26.00

Table 1. Proper-motion sources and their weights

Source	σ_x, mas/yr	σ_y, mas/yr	Weight
Ebbighausen [6]	2.60	2.75	0.14
van Maanen [7]	1.70	1.41	0.21
Murrey and Clements [8]	1.78	1.54	0.36
Tycho-2	3.24	2.68	0.12
Sanders [9]	1.33	0.98	0.25
Murray and Clements [10]	2.25	2.12	0.21
Girard *et al.* [11]	1.21	1.09	0.76
Zhao *et al.* [12]	2.12	1.91	0.25
Frolov and Anan'evskaya [13]	2.10	2.19	0.22

eventual magnitude equation. We ignored the color equation, since the magnitudes of stars in cluster fields are tightly correlated with their colors.

The use of (1) poses the following problems [4]. First, the least-squares estimates of the coefficients in the transformation equations are biased due to the appreciable random errors in the proper motions, which appear on both the right-hand and left-hand sides of (1), with the magnitude of the bias depending primarily on the ratio of the variances for the errors on the right- and left-hand sides of the equations. In addition, the observational errors broaden the distributions of the proper motions, resulting in overestimated mean proper motions. This effect shows up as an additional deviation from unity of the determinant of the matrix of the transformation coefficients, in addition to the eventual deviation due to the expansion or contraction of the system of proper motions. The latter may affect both the estimated stellar-velocity dispersion and the analysis of the eventual expansion or contraction of the cluster.

To minimize the effect of the above factors, Loktin [4] suggested a technique for the iterative reduction of catalogs. At the first stage, the second catalog is reduced to the system of the chosen reference catalog, after which the proper motions of the two catalogs are averaged with weights inversely proportional to the catalog-averaged errors in the proper motions. The resulting catalog is then used as the new reference catalog to reduce the next independent catalog, etc. The reduction of the last catalog yields a first approximation for the master catalog. This first-approximation catalog is then again reduced to the system of the reference catalog. The reduction of the first approximation for the master catalog to the proper-motion system of the reference catalog yields more reliable results, since the random errors of the proper motions in the first-approximation master catalog are smaller. The magnitude equation for the resulting catalog is checked, which, in the case of sufficiently rich open clusters, can easily be done using $\mu_x - V$ and $\mu_y - V$ plots, where V is the apparent magnitude. The procedure for reducing each catalog is then repeated using the first-approximation catalog as the reference catalog: the small random errors in the proper motions in this catalog simplify the correction for the effect of the errors on the least-squares estimates. The reduction of the systems of the individual catalogs to the system of the first-approximation catalog is based on the maximum number of common stars, thereby minimizing the errors in the estimated coefficients of transformation (1). The weights of the individual catalogs are calculated from the standard deviations of the corresponding reduction formulas.

We analyzed the kinematic parameters of the open cluster M67 based on data from the master proper-motion catalog for stars in the cluster field compiled by Loktin [5] from various published data. We added several sources to the data of this catalog to produce a new master catalog. All the data sources are listed in Table 1. We specified the weights of the individual catalogs to be inversely proportional to the dispersions (standard deviations) from the linear reductions of the catalogs to the first-approximation catalog with the magnitude-equation term included. These dispersions, σ_x and σ_y, and the adopted weights of the catalogs are listed in columns 2–4 in Table 1, respectively. Here and below, the proper motions and their errors are in arcs/1000 yr. It is obvious from the table that the mean errors σ_x somewhat exceed the mean errors σ_y for almost all catalogs. However, the ratio of these quantities is close to unity, and we decided to use the same weights for both components of the proper motion.

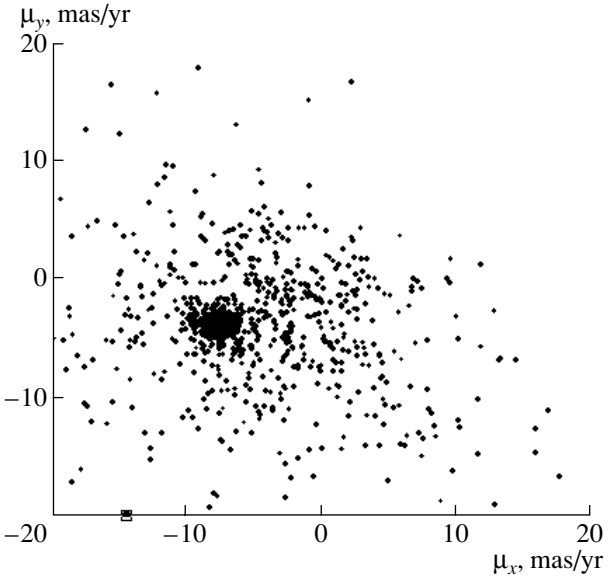

Fig. 1. Vector diagram of the stellar proper motions in the field of the open cluster M67.

The master prop-motion catalog for stars in the field of M67 contains a total of 1212 stars, each appearing in at least two initial catalogs. We did not use the stars appearing in only one catalog, due to the low accuracy of their proper motions and the high probability of spurious identification. We calculated the weighted averages of the proper-motion components and the associated standard errors for the remaining stars.

Our next step was to identify cluster members. We excluded from the resulting catalog 33 stars with the largest estimated errors in the total proper motions $s = \sqrt{s_x^2 + s_y^2}$, where s_x and s_y are the errors of the proper-motion components in right ascension and declination, respectively. Such stars should be excluded, due to the uncertainty of the membership of stars with large proper-motion errors.

Figure 1 shows a vector diagram of the proper motions of stars included in the resulting master catalog. This figure shows a well-defined concentration of cluster stars. It is obvious that cluster stars can be identified quite reliably. We used Loktin's [5] modification of the Sanders method to identify 511 stars as probable cluster members (with membership probabilities of more than 50%). The central coordinates of the concentration of cluster stars on the vector diagram (Fig. 1) obtained by estimating the parameters of a corresponding approximating normal distribution are $\mu_{xc} = -7.48$ and $\mu_{yc} = -3.83$. The number of cluster members noted also provides an estimate of the corresponding parameter. Obviously, these estimates are functions of the proper-motion errors, and

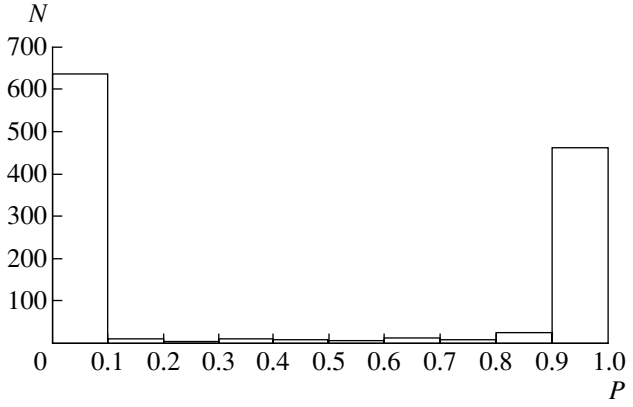

Fig. 2. Frequency distribution of the estimated membership probabilities P for stars in the field of M67.

depend on the adequacy of the fitting of the proper-motion distribution using a superposition of two normal distributions, since any errors that change the parameters of the distribution of data points in Fig. 1 bias the parameters of the approximating distribution.

Figure 2 shows the frequency distribution for the membership probabilities of the cluster stars. As expected, cluster stars can be confidently distinguished from field stars. However, a few objects have membership probabilities from 0.1 to 0.9, probably due to the inhomogeneity of the resulting master catalog in terms of random errors.

The mean errors in the proper-motion components of the identified cluster members are $\langle s_x \rangle = 0.58$ and $\langle s_y \rangle = 0.59$, which corresponds to 2.5 km/s for the adopted heliocentric distance of the cluster, 908 pc [14]. Figure 3 shows the frequency distributions of the errors of the x and y proper-motion components for the identified cluster members. The solid and dashed lines in the figure show the error distributions for the x and y components, respectively. It is clear that the overwhelming majority of stars in the sample to be used for analyzing the kinematics of M67 have proper-motion errors of less than $0.001''$/yr. Note that the error distributions for the two proper-motion components are almost identical. Recall that most of the measurements used to determine the relative proper motions were made in the central part of the cluster, while the proper motions derived for stars at the cluster periphery may have lower accuracy. Figure 4 illustrates this effect for the stars in our sample. It is evident from Fig. 4 that the increase in the errors with clustercentric distance is only slightly visible out to an angular distance of 0.3° and is very weak out to 0.6°. This indicates, in particular, that the sample is complete out to this latter distance—even at the periphery of the cluster, the data are based on a sufficiently large number of catalogs for the radial increase of the errors to be small.

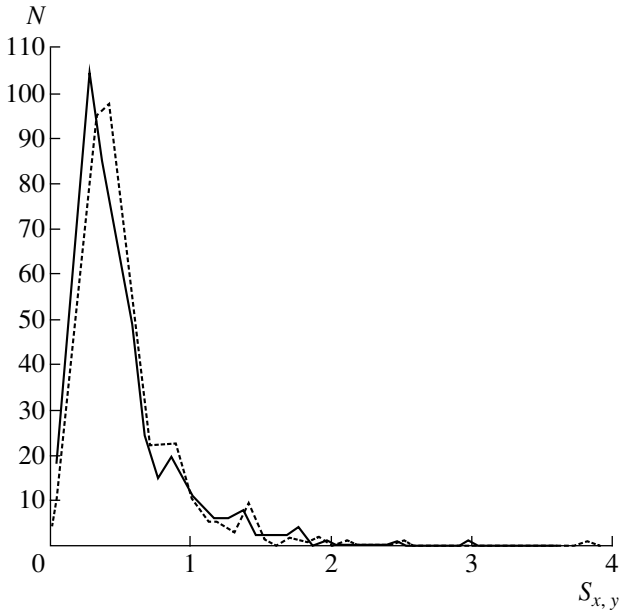

Fig. 3. Frequency distribution of the estimated rms errors of the proper-motion components of the M67 cluster members in right ascension s_x (solid line) and declination s_y (dashed line).

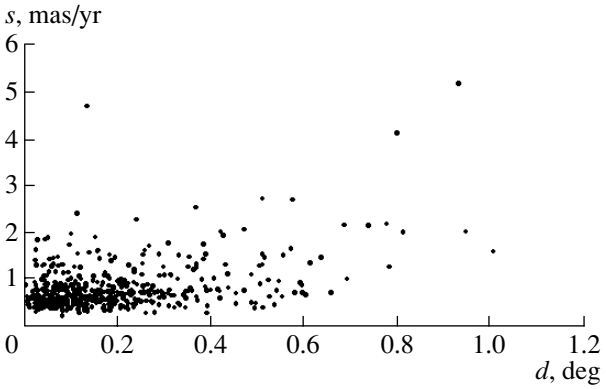

Fig. 4. Dependence of the errors of the proper motions of the M67 members on clustercentric distance d.

We calculated the angular clustercentric distances using the equatorial coordinates $\alpha_c = 132.825^\circ = 8^{\rm h}49^{\rm m}30^{\rm s}$ and $\delta_c = +11.796^\circ = +11^\circ47'46''$ for the cluster center, calculated as the modes of the right-ascension and declination distributions for the probable cluster members.

To verify that the proper-motion components of the sample stars contain no magnitude equation, let us consider the magnitude dependence of the proper motions of probable cluster members (Fig. 5). It is clear from plots (a) and (b) of Fig. 5 that neither of the proper-motion components shows evidence for a significant magnitude equation.

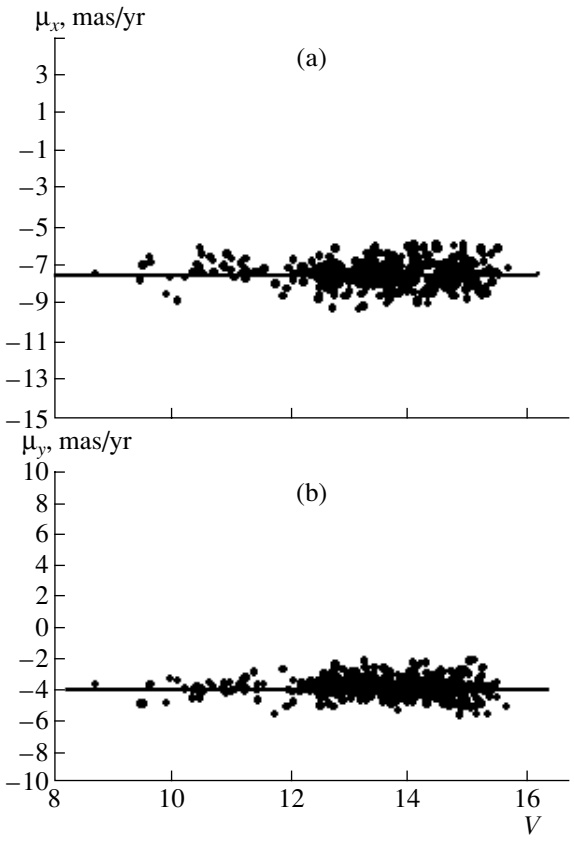

Fig. 5. Apparent-magnitude dependence of the proper motions of the M67 cluster members.

3. MEAN VELOCITIES OF STARS IN THE CLUSTER

To analyze the properties of the dispersion of the residual velocities of the stars, we must eliminate all possible sources of systematic motions with any origin: both real motions, such as expansion or contraction of the cluster or parts of the cluster or rotation of the cluster, and fictitious motions, such as residual systematic errors or the geometric effect of the convergence toward the radiant.

To analyze the motions of stars in a cluster based on the proper motions of its members, we subtracted the motion of the cluster as a whole. We determined the components of this mean cluster motion by calculating the modes of the distributions of the proper-motion components in two coordinates for 200 cluster members located within $7'$ of the cluster center. We set the angular radius of the cluster equal to $7'$ based on the radial distribution of the space density of its members. The components of the mean proper motion are $\langle\mu_x\rangle = -7.32 \pm 0.02$ and $\langle\mu_y\rangle = -3.76 \pm 0.02$ in the units of $0.001''$/yr. We then decomposed the total residual proper motions of the stars into components directed radially (μ_R) and tangentially (μ_θ) relative to the cluster center. We

Table 2. Average residual proper motions of the M67 cluster members

No.	Interval of r, pc	$\langle d \rangle$, arcmin	N	$\langle \mu_R \rangle$, mas/yr	$\langle \mu_\theta \rangle$, mas/yr
1	0–0.71	1.85	57	$+0.064 \pm 0.060$	$+0.026 \pm 0.047$
2	0.72–1.18	3.60	57	$+0.109 \pm 0.057$	-0.041 ± 0.051
3	1.18–1.56	5.15	57	$+0.028 \pm 0.060$	-0.011 ± 0.062
4	1.57–2.09	6.96	57	$+0.070 \pm 0.063$	-0.095 ± 0.059
5	2.13–2.75	9.07	58	$+0.108 \pm 0.070$	-0.098 ± 0.058
6	2.76–3.46	11.76	58	-0.015 ± 0.069	-0.157 ± 0.063
7	3.46–4.62	15.04	58	-0.011 ± 0.070	$+0.021 \pm 0.084$
8	4.63–7.23	21.33	59	-0.133 ± 0.080	-0.017 ± 0.085
9	7.24–12.92	33.55	46	-0.095 ± 0.138	-0.224 ± 0.113

then averaged the resulting residual proper motions within nine groups of clustercentric distance.

The results of this averaging are listed in Table 2 and shown in Figs. 6 and 7. The columns of Table 2 give (1) the running number of the interval, (2) the interval of clustercentric distances in pc, calculating using the adopted heliocentric distance of the cluster, (3) the weighted average of the clustercentric distances of the stars in the group, (4) the number of stars in the group, (5), (6) the weighted averages of the proper-motion components (in mas/yr) and their standard errors. Recall that 1 mas/yr corresponds to 4.3 km/s at the adopted distance of the cluster. For convenience, Figs. 6 and 7 also show the radial dependences of the mean proper motions.

Consider now the clustercentric-distance dependence of the radial component of the mean proper motion, which is related to the expansion/contraction velocity of the cluster (Fig. 6). When analyzing this dependence, we must take into account the convergence of the proper motions of the cluster members toward the radiant, since M67 has a significant radial velocity. According to the published data we have compiled, the mean radial velocity of the cluster is $+33.6$ km/s. The component of the proper motion responsible for the convergence effect can easily be calculated using the formula

$$\mu_R = -0.4602 v_R \tan(d/2)/r, \qquad (2)$$

where v_R is the radial velocity of the cluster as a whole (in km/s), d the angular clustercentric distance (in arcmin), and r the heliocentric distance of the cluster. Formula (2) for the geometric estimation of the heliocentric distance of the cluster without determining the position of the radiant can be easily derived

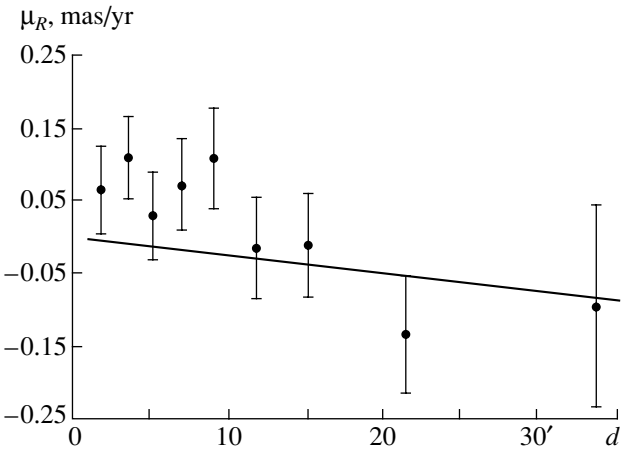

Fig. 6. Dependence of the mean radial components of the residual proper motions of M67 members on angular clustercentric distance.

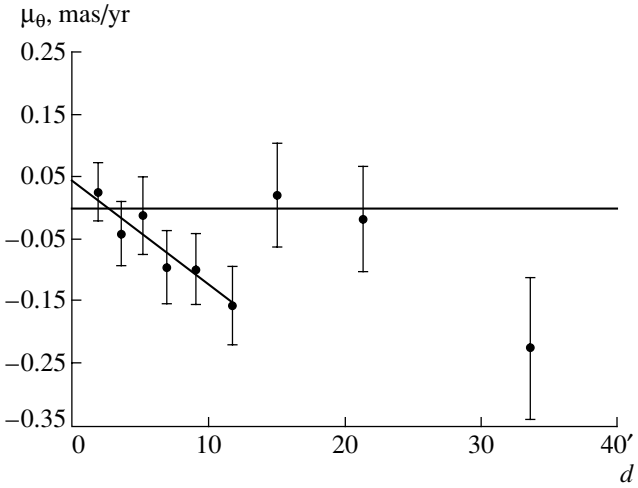

Fig. 7. Same as Fig. 6 for the mean tangential components.

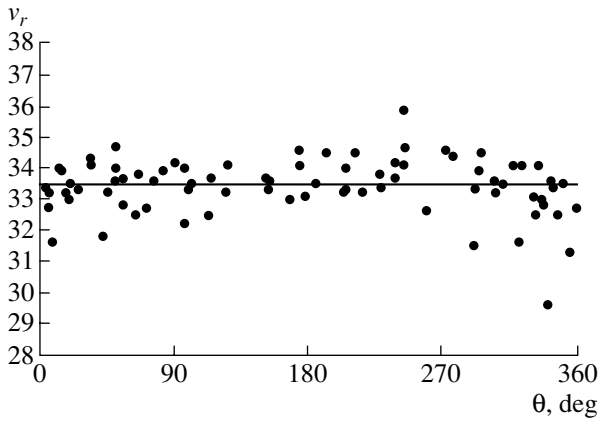

Fig. 8. Azimuthal dependence of the radial velocities of M67 members.

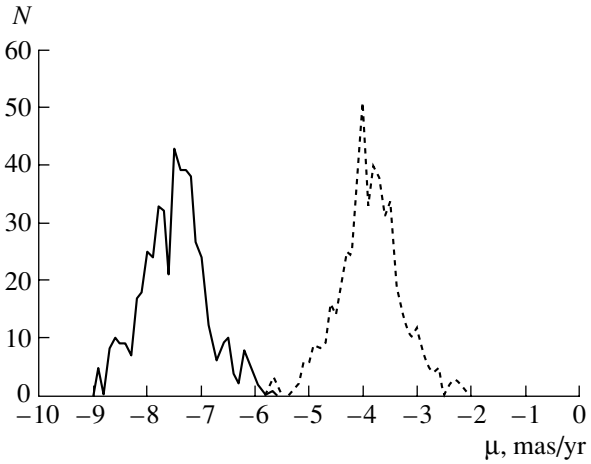

Fig. 9. Frequency distributions of the proper-motion components of M67 members.

from elementary geometric considerations, as is done by Loktin and Matkin [15].

The solid line in Fig. 6 shows the dependence (2) for M67. On the whole, the points in this figure follow the slanting curve. However, all the stars in the vicinity of the cluster (the five leftmost points in the figure) clearly lie above this curve, which may indicate the expansion of the cluster core with a mean velocity of about 0.38 ± 0.07 km/s. We calculated this velocity by converting the average excess proper motion of the five leftmost points in Fig. 6 above the curve to linear units. Recall that most, but not all, the sample stars are located near the plane of the sky, so that the contraction velocity noted above is only an underestimate of the actual value. The remaining four points in the figure do not deviate significantly from the solid curve, implying that the cluster halo exhibits no significant expansion/contraction within the errors determined from the actual accuracy of the proper motions.

Consider now the tangential components of the residual proper motions (Fig. 7). It is clear that the points corresponding to the inner parts of the cluster exhibit a well-defined systematic trend, which may indicate rotation of the cluster core. A linear least-squares fit to these data points yields the formula $v_t = 0.21 - 0.05d$ for the linear rotational velocity, where v_t and d are in km/s and arcmin, respectively. The standard errors of the coefficients are 0.09 and 0.01 km/s, respectively. Thus, this trend is statistically significant, and the linear rotational velocity reaches 0.7 km/s at the core periphery. Except for the outermost, least reliable data point, the data points lying outside the cluster core appear to exhibit no signs of rotation.

The calculations of all the mean residual proper motions considered above are affected by the extent of the cluster along the line of sight: on average, the nearest stars have larger proper motions than the most distant stars. This effect is insignificant if the cluster is spherically symmetrical; thus, the above qualitative conclusions remain valid if the cluster is spherically symmetrical. Note also that the line-of-sight extent at M67 has little effect on the proper motions at the adopted heliocentric distance—the difference between the nearest and the furthest cluster stars is less than 4%.

If the cluster rotational axis does not coincide with the line of sight, the effect of rotation should also be manifest in the stellar radial velocities. Figure 8 shows the radial velocities of probable cluster members adopted from Mathieu *et al.* [16] as a function of the position angle in the cluster. In the case of appreciable rotation, the plot should display one period of a sine curve; however, we can see that it shows a virtually uniform distribution. This leads us to conclude that the cluster shows no visible rotation around any axis lying near the plane of the sky.

The residual proper motions, which, in our case, yield estimates of the core rotational and expansion velocities, are very small, and we cannot be sure that they are not due to some local distortions of the proper-motion field. Increasing the firmness of the results obtained, new high-precision proper motions are required for the stars in a field that is at least 1° in size and centered on M67. Note, however, that our results agree fully with the preliminary results published in [17], where we did not use the additional three catalogs of relative proper motions that we employed in the current study.

4. DISPERSIONS OF THE RESIDUAL VELOCITIES

The chief difficulty in calculating the velocity dispersions of the cluster stars from the proper motions

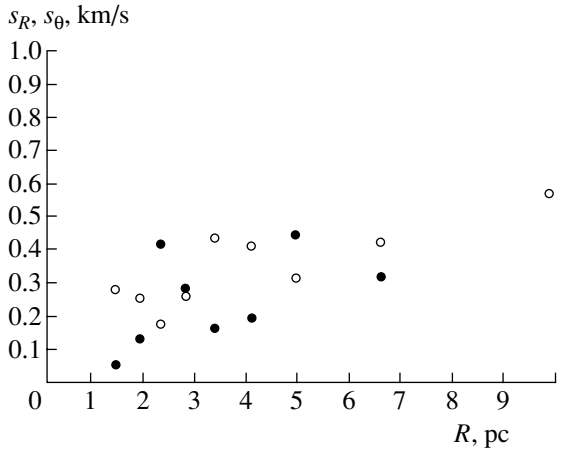

Fig. 10. Dependences of the dispersions of the radial (open circles) and tangential (filled circles) residual velocities on clustercentric distance.

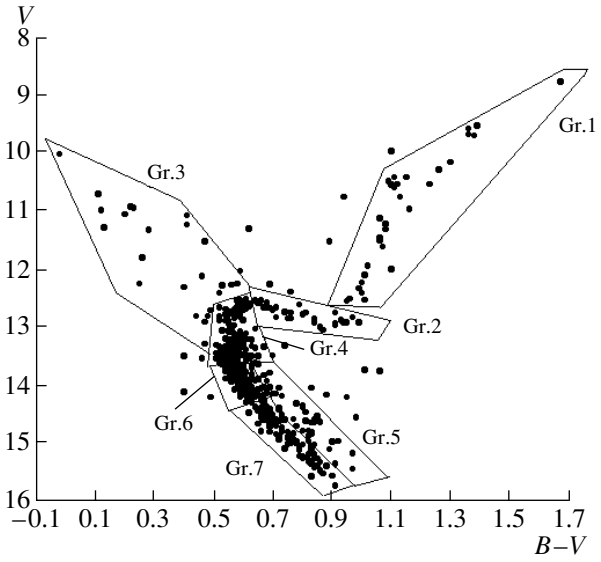

Fig. 11. Color–apparent magnitude diagram for identified members of M67 (with seven groups of stars marked).

is the unequal accuracies of the latter, associated with both the measurements of the stellar positions and the process of combining the various proper-motion catalogs into a single catalog. The estimated velocity dispersions must therefore be treated with caution. The dispersion ratios are a different matter, since the above errors cancel each other out to some extent in this case.

Figure 9 shows frequency-distribution polygons for the proper-motion components of identified members of M67. It is clear that the shapes of the two distributions differ little, as do the dispersions of the residual velocities, indicating that the distribution of the residual velocities of the cluster as a whole is almost spherically symmetric.

Let us now consider the radial variations of the components of the residual-velocity dispersions. Figure 10 shows the dispersions of the residual velocities in the radial (open circles) and tangential (filled circles) directions as a function of clustercentric distance in parsecs. To allow for the effect of proper-motion errors, we subtracted the mean square of the proper-motion errors for the group of stars considered from the calculated squares of the residual-velocity dispersions. The velocity dispersions are in km/s. There is a slight increase in the velocity dispersion with clustercentric distance, probably due to mass segregation. On average, the ratio of the radial and tangential velocity dispersions is close to unity. In the case of purely radial orbits, the radial motions should dominate the tangential motions, making the above ratio significantly higher than unity. This casts doubt on the hypothesis that some open-cluster stars have strongly elongated orbits.

To analyze the dependences of the velocity dispersion of the cluster stars on their masses, we subdivided the cluster stars into seven groups according to their location in the color–magnitude diagram (HR diagram). These groups are separated by broken lines in Fig. 11, which shows the HR diagram for the probable cluster members we have identified. It is clear that group 1 corresponds to red giants, group 2 to subgiants, group 3 to blue stragglers, group 5 to main-sequence (MS) binaries, groups 6 and 7 mostly to single MS stars, and group 4 to the region of the MS turnoff, where the sequences of single and binary stars merge. Table 3 gives the estimated radial and tangential dispersions of the stellar velocity components, together with a measure of the characteristic mean kinetic energy of the stars for each group.

The columns of table give the number of the group, the number for stars used to estimate the velocity dispersions, the average stellar mass (in solar masses)

Table 3. Velocity-dispersion estimates for groups of stars in M67

Group	N	$m, M_\odot$	σ_R, km/s	σ_θ, km/s	mW^2
1	31	1.47	0.84 ± 0.47	0.77 ± 0.41	0.953
2	26	1.45	1.08 ± 0.36	0.83 ± 0.38	1.322
3	17	–	0.20 ± 0.36	–	–
4	135	–	1.01 ± 0.18	1.04 ± 0.18	–
5	46	–	1.77 ± 0.48	1.34 ± 0.39	–
6	99	1.14	1.45 ± 0.27	1.36 ± 0.24	2.250
7	85	1.01	1.26 ± 0.33	1.26 ± 1.89	2.505

calculated from the evolutionary tracks of [18], and the estimated radial and tangential velocity dispersions in km/s corrected for the average velocity errors along the corresponding axis. The last column of the table gives the square of the velocity dispersion averaged over the two directions, $W^2 = \sigma_R^2 + \sigma_\theta^2$, multiplied by the mass, as a characteristic measure of the average kinetic energy of the stars of a given group. We did not estimate the average masses for groups 4 and 5, since these groups include both single and binary stars, and their mean masses cannot be estimated without knowing the essentially unknown fraction of binary stars in this part of the HR diagram and the distribution of binaries in terms of their component-mass ratios. We can make the crude assumption that the mean mass in these parts of the HR diagram is one and a half times higher than in the adjacent regions. We likewise do not give an average mass for the blue stragglers, since the masses of these stars are unknown. The small size of the sample prevented us from determining the velocity dispersion for the blue stragglers: one of the velocity components differed only insignificantly from zero, and we could not estimate the other component, since the square of the velocity dispersion was smaller than the square of the standard error for the stars of this group.

The velocity-dispersion estimates listed in Table 3 lead to the following conclusions. The velocity dispersions for the single (groups 6 and 7) and binary (group 5) MS stars are virtually the same, although we might expect single and binary stars to interact with other stars with different degrees of "elasticity." The average kinetic energy appears to increase somewhat with decreasing mass; in any case, according to the estimates in Table 3, on average, single MS stars have twice the kinetic energy of the somewhat more massive red giants and subgiants (groups 1 and 2). This could be due to mass segregation in the cluster, when the more massive stars are concentrated toward the cluster center and do not move far from the center during their orbital motions. Note that groups 1 and 2 include single stars, whereas our numerical simulations of the structure of the HR diagram of M67 (which we describe in another paper) show that the regions occupied by giants and subgiants in Fig. 11 contain virtually no binaries.

5. CONCLUSIONS

Combining catalogs of relative and absolute proper motions into a single master catalog has enabled us to obtain an extensive sample of high-precision proper motions for stars in the field of the open cluster M67. This has made it possible to confidently identify probable cluster members and analyze their motions. Our experience leads us to conclude that even old proper-motion measurements have sufficient accuracy to be used along with modern catalogs. Objects with heliocentric distances within 1 kpc can be used to analyze the kinematics of stars in open clusters.

Unfortunately, the very narrow interval of observed stellar masses in such old clusters as M67 make it impossible to confidently analyze the dependence of the average kinetic energy of the stars on their mass. We plan to carry out a similar analysis for stars of the younger Pleiades and Praesepe clusters in the future.

It is clear from our results that analyses of the phase-density functions of open clusters must take into account various large-scale motions, such as the expansion/contraction of the cluster as a whole or of parts of the cluster (core and halo) and rotation of the cluster.

Some of the conclusions we have drawn here are at the limit of statistical significance. It would be highly desirable to obtain at least one more independent set of stellar proper motions down to a limiting magnitude of at least $V \approx 15^m$ in a $2^\circ \times 2^\circ$ field centered on M67, in order to refine our conclusions.

REFERENCES

1. M. Odenkirchen, C. Soubiran, and J. Colin, New Astron. **3**, 583 (1998).
2. M. A. C. Perryman, A. A. Brown, Y. Lebreton, *et al.*, Astron. Astrophys. **331**, 81 (1998).
3. B. F. Jones, Astron. J. **75**, 563 (1970).
4. A. V. Loktin, Astron. Astrophys. Trans. **23**, 61 (2004).
5. A. V. Loktin, Astron. Astrophys. Trans. **23**, 117 (2004).
6. E. G. Ebbighausen, Astrophys. J. **91**, 244 (1940).
7. A. van Maanen, Astrophys. J. **96**, 382 (1942).
8. C. A. Murray and E. D. Clements, R. Obs. Bull., No. 139, 309 (1968).
9. W. L. Sanders, Astron. Astrophys., Suppl. Ser. **27**, 89 (1977).
10. C. A. Murray, R. Obs. Bull., No. 141, 339 (1968).
11. T. M. Girard, W. M. Grundy, C. E. Lopez, *et al.*, Astron. J. **98**, 227 (1989).
12. J.-L. Zhao, K.-P. Tian, Z.-H. Xu, *et al.*, Chin. Astron. **6**, 344 (1982).
13. V. N. Frolov and I. K. Anan'evskaya, Astron. Tsirk, No. 1432, 4 (1986).
14. A. V. Loktin, T. P. Gerasimenko, and L. K. Malysheva, Astron. Astrophys. Trans. **20**, 607 (2001).
15. A. V. Loktin and N. V. Matkin, Kin. Fiz. Neb. Tel **4**, 59 (1988).
16. R. D. Mathieu, D. W. Latham, R. F. Griffin, and J. E. Gunn, Astron. J. **92**, 1100 (1986).
17. A. V. Loktin, in *Order and Chaos in Stellar and Planetary Systems* (St. Petersburg, 2003), p. 34.
18. G. Schaller, D. Scaerer, G. Meynet, *et al.*, Astron. Astrophys., Suppl. Ser. **96**, 269 (1992).

Translated by A. Dambis

Astronomy Reports, Vol. 49, No. 9, 2005, pp. 701–708. Translated from Astronomicheskiĭ Zhurnal, Vol. 82, No. 9, 2005, pp. 788–796.

The Possible Nature of Dips in the Light Curves of Semidetached Binaries with Stationary Disks

D. V. Bisikalo[1], P. V. Kaigorodov[1], A. A. Boyarchuk[1], and O. A. Kuznetsov[1,2]

[1] *Institute of Astronomy, Russian Academy of Sciences, ul. Pyatnitskaya 48, Moscow, 119017 Russia*

[2] *Keldysh Institute of Applied Mathematics, Russian Academy of Sciences, Miusskaya pl. 4, Moscow, 125047 Russia*

Received February 2, 2005; in final form, February 17, 2005

Abstract—A thickening at the outer edge of the accretion disk is usually invoked to explain the dips in the light curves of cataclysmic variables with stationary disks at phases ∼0.7. The noncollisional interaction between the stream and the disk in the stationary solution raises the question of why matter appears at a considerable height above the accretion disk in such systems. Our three-dimensional numerical modeling demonstrates that a thickening of the halo above the disk can appear even in the absence of a direct collision between the stream and the disk. In the gas-dynamical flow pattern described with the "hot-line" model, a considerable fraction of the matter is accelerated in the vertical direction during the flow's interaction with the circumdisk halo. The vertical motion of the gas due to the presence of the z component of the velocity leads to a gradual thickening of the circumdisk halo. The computations reveal the strongest thickening of the halo above the outer edge of the disk at phases ∼0.7, in agreement with observations for stationary-disk cataclysmic variables. This supports the hot-line model suggested earlier as a description of the pattern of the matter flows in semidetached binaries and presents new possibilities for interpreting the light curves of such systems. © *2005 Pleiades Publishing, Inc.*

1. INTRODUCTION

Observations of low-mass X-ray binaries (LMXBs) have revealed dips in the X-ray light curves for several systems. Explanations of these dips have hypothesized the presence of a thickening at the accretion disk's outer edge at phase ∼0.8, which corresponds to the position of this feature in the light curves ([1, 2] and references therein). The presence of matter surrounding the X-ray source at a considerable height above the system's orbital plane, along with the matter's uneven distribution in azimuth, can be explained in terms of either the companion's gravitational action on the accretion disk or the interaction between the stream of matter from the inner Lagrangian point (L_1) and the disk. The coincidence of the phase of the observed dips with the assumed position where the stream from L_1 approaches the outer edge of the disk, has tended to focus study on this particular region. Beginning with [3–5], numerical studies of variations of the disk's scale height due to its interaction with the stream were initiated. Currently, the idea that the stream ricochets off the disk's outer edge is considered the best way to explain the presence of matter at heights considerably exceeding the disk thickness. The possibility that the stream flows around the edge of the disk was first discussed in [6–9]; in 1996, the gas-dynamical computations of Armitage and Livio [10] showed that a considerable fraction of the stream's matter can ricochet off the edge of the accretion disk. In their model, after colliding with the disk edge, some of the matter in the stream rises to a considerable height (compared to the disk thickness), forming a stream towards the inner parts of the disk. The computations of [10] demonstrated that this stream of matter could explain the presence of the dips observed in LMXB light curves.

It is easiest to identify dips due to the presence of matter located high above the disk in LMXBs, since they contain a very compact source at the center of the disk. However, similar light-curve features in various wavelength ranges have also been recorded for a number of cataclysmic binaries in outburst, such as U Gem [11, 12], OY Car [13, 14], and Z Cha [15]. Further observations showed that light-curve dips can also appear when a system is in a stationary state. Studies of the ultraviolet light curves of the eclipsing novalike cataclysmic binaries UX UMa and RW Tri [16] confirmed this result and suggested that this phenomenon was universal in semidetached binaries with accretion disks. As an example, Fig. 1 presents the observed light curves for UX UMa (left panel) and RW Tri (right panel) from [16]. It is interesting that, in contrast to the cataclysmic systems,

1063-7729/05/4909-0701$26.00

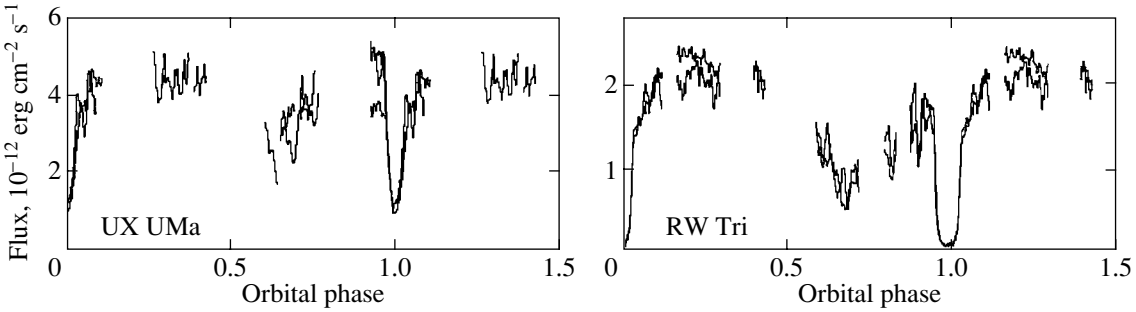

Fig. 1. Light curves of the UX UMa (left) and RW Tri (right) systems in the ultraviolet (1415–1433 Å), according to [16].

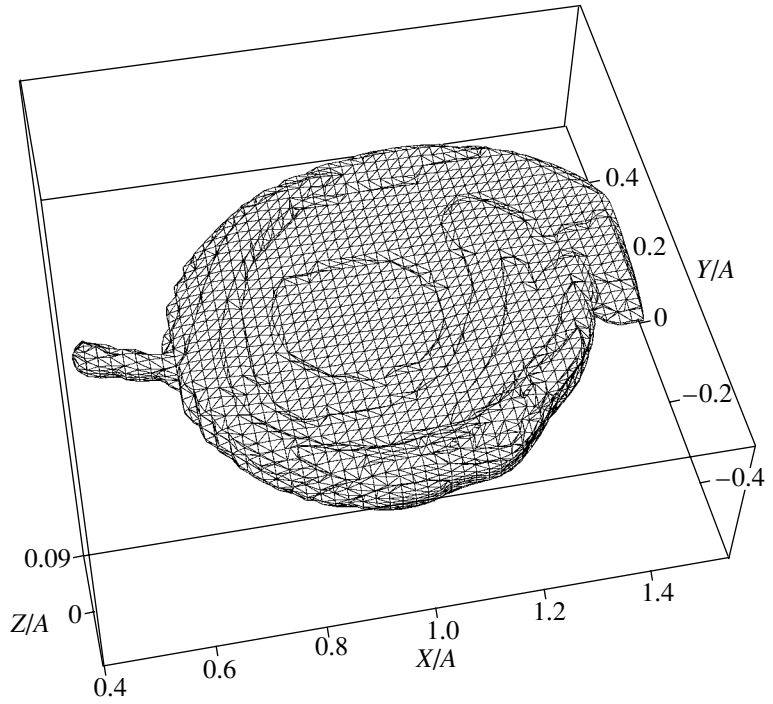

Fig. 2. Three-dimensional surface of constant density $\rho = 5 \times 10^{-11}$ g/cm^3.

systems with stationary disks display preeclipse dips at much earlier phases,[1] 0.6–0.7 [16, 17] (Fig. 1).

This raises the question of what leads to the presence of matter at considerable heights above the accretion disk in the case of a stationary interaction between the stream and the disk. Gasdynamical studies of the terminal flow pattern in semidetached binaries demonstrate that the interaction between the stream and the disk is collisionless in this case [18–24]. In contrast to the hot-spot model, which assumes that the stream impacts the edge of the accretion disk, the stream interacts with gas of the circumdisk halo in the stationary case, forming an extended region of enhanced energy release, or so-called "hot line." This means that there will be no ricochet of the stream in the steady-state mode, and hence this model cannot explain the dips in the light curves of binaries with stationary disks.

Our aim here is to study possible ways of thickening the halo above a disk, ways that give rise to eclipses of the central source and the presence of dips in the light curves during the stationary flow of matter in semidetached binaries. Our three-dimensional modeling of the flow structure demonstrates that, during the stream's interaction with the circumdisk halo, a considerable fraction of the matter is accelerated in the vertical direction and rises to heights appreciably exceeding the disk scale height. The strongest thickening of the halo above the outer

[1] As usual in the analysis of observational data, the phase angle, ϕ, is measured from the line connecting the centers of the two stars, with the phase increasing in the direction opposite to the system's rotation.

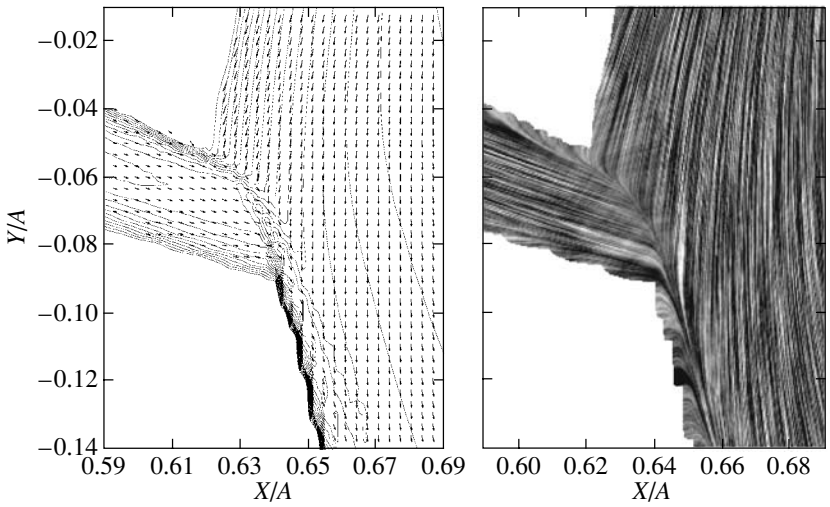

Fig. 3. Contours of constant density and velocity vectors (left panel) and a visualization of the velocity field (right panel) in the region of interaction between the stream and the circumdisk halo, in the system's equatorial plane. This figure was first published in [22].

edge of the disk occurs at phase ∼0.7, in agreement with observations of systems with a continuous accretion regime. This provides new possibilities for interpreting the light curves of such systems.

2. THE MODEL

We used the model of [22] in our numerical study of the gas dynamics of the matter flows in a semidetached binary. We described the flow pattern using a three-dimensional system of gravitational gasdynamical equations including the effects of radiative heating and cooling of the gas:

$$\begin{cases} \dfrac{\partial \rho}{\partial t} + \mathrm{div}\rho\mathbf{v} = 0, \\ \dfrac{\partial \rho\mathbf{v}}{\partial t} + \mathrm{div}(\rho\mathbf{v}\otimes\mathbf{v}) + \mathrm{grad}P \\ = -\rho\mathrm{grad}\Phi - 2[\boldsymbol{\Omega}\times\mathbf{v}]\rho, \\ \dfrac{\partial \rho(\varepsilon + |\mathbf{v}|^2/2)}{\partial t} + \mathrm{div}\rho\mathbf{v}(\varepsilon + P/\rho + |\mathbf{v}|^2/2) \\ = -\rho\mathbf{v}\mathrm{grad}\Phi + \rho^2 m_p^{-2}\left(\Gamma(T, T_{wd}) - \Lambda(T)\right). \end{cases} \quad (1)$$

Here, ρ is the density, $\mathbf{v} = (u, v, w)$ is the velocity vector, P is the pressure, ε is the internal energy, Φ is the Roche potential, m_p is the proton mass, and $\Gamma(T, T_{wd})$ and $\Lambda(T)$ are the radiative heating and cooling functions, respectively. The system of gasdynamical equations was closed with the equation of state for an ideal gas, $P = (\gamma - 1)\rho\varepsilon$, where γ is the adiabatic index. The parameter γ was taken to be 5/3.

We solved this system of equations using the Roe–Osher technique [21, 25, 26] adapted for multiprocessor computers. The modeling was carried out in a noninertial frame of reference rotating with the binary, in Cartesian coordinates, on a rectangular three-dimensional grid. Since the problem is symmetric about the equatorial plane, we modeled only half of the space occupied by the disk. The size of the modeled region, $1.12\,A \times 1.14\,A \times 0.17\,A$ (where A is the distance between the system's components), was chosen to completely include the disk and the stream of matter from the point L_1. The computational grid had $121 \times 121 \times 62$ cells distributed among 81 processors forming a 9×9 two-dimensional array. The grid was made denser in the region of interaction between the stream and the disk in order to improve the accuracy of the solution in this region. The grid was also denser near the equatorial plane, providing good resolution of the disk's vertical structure.

The solution obtained for the model without cooling was used for the initial conditions [27]. Before the solution converged, the model with cooling was computed for ≈5 orbital periods of the system as a whole. The total computation time was ≈1000 hours at the MVS 1000A computer of the Joint Supercomputer Center (JSCC).

A free boundary condition with constant density $\rho_b = 10^{-8}\rho_{L_1}$, a temperature of 13 600 K, and zero velocity was imposed at the outer boundaries of the computational region (except near L_1), where ρ_{L_1} is the matter density at L_1. The accretor was taken to be a sphere of radius $10^{-2}\,A$. All the matter entering the accretor cells was assumed to fall onto the star. The stream was specified as a boundary condition:

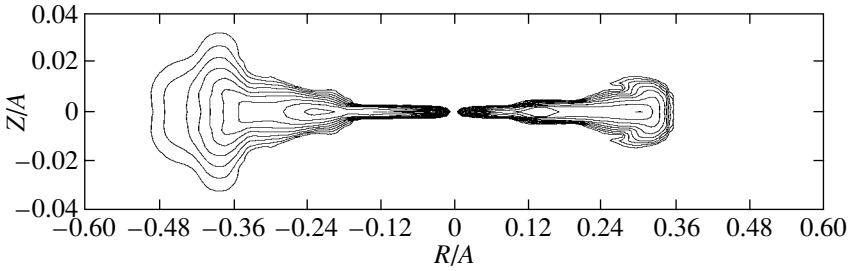

Fig. 4. Contours of constant density in the section of the flow structure perpendicular to the equatorial plane and passing through the accretor and the region of the halo's maximum thickening ($\phi = 0.7$).

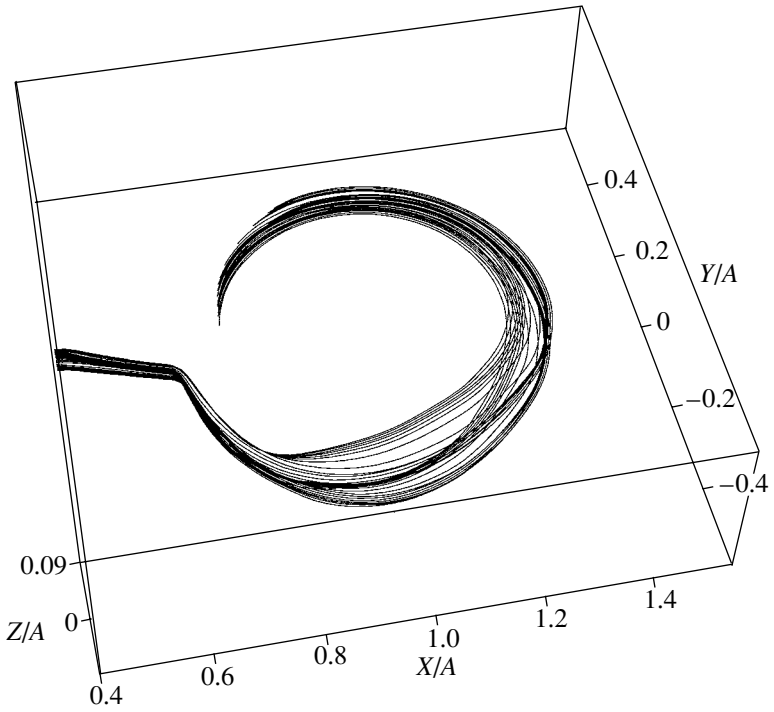

Fig. 5. Fragments of streamlines emerging from the neighborhood of L_1.

matter with a temperature of 5800 K, density of $\rho_{L_1} = 1.6 \times 10^{-8}$ g/cm^3, and velocity along the x axis $v_x = 6.3$ km/s was injected into a region of radius $0.014\,A$ around L_1.

We considered a semidetached binary consisting of a donor with mass M_2 that fills its Roche lobe and an accretor with mass M_1. The following parameters were adopted for the system: $M_1 = 1.02\,M_\odot$, $M_2 = 0.5\,M_\odot$, and $A = 1.42\,R_\odot$, corresponding to $P_{\rm orb} = 3.79^{\rm h}$. The disk in the model had a temperature of 13 600 K. For the specified rate of matter entering the system, the corresponding accretion rate in the model was $\approx 10^{-10}\,M_\odot$/yr.

3. RESULTS OF COMPUTATIONS

We described the morphology of the matter flows in a semidetached binary with a stationary, cool ($T =$ 13 600 K) disk in [22]. Let us briefly summarize the main features of the computed flow structure. Figure 2 shows a three-dimensional surface of constant density of $\rho = 5 \times 10^{-11}$ g/cm^3. The region of the interaction between the stream and circumdisk halo is shown enlarged in Fig. 3 [22, Figs. 7, 8]. The left panel of Fig. 3 displays contours of constant density and velocity vectors, while the right panel of Fig. 3 is the so-called texture: a visualization of the velocity field by means of numerous tracks of test particles.

The results presented demonstrate that the interaction between the circumdisk halo and the stream possesses all the characteristic features of an oblique collision of two flows. The resulting structure of two shock waves with a tangential discontinuity between them is clearly visible in Fig. 3. The region of the shock interaction between the stream and halo has a complex shape. The parts of the halo far from the

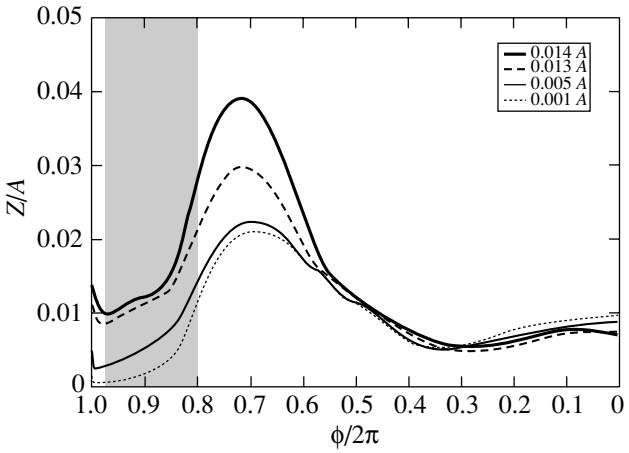

Fig. 6. $z(\phi)$ relation for four streamlines. The streamlines originate in the vicinity of L_1 and have the coordinates $(x_{L_1}, 0, z_0)$. The z_0 values for each streamline are indicated in the plot. The shaded area corresponds to the region where v_z increases.

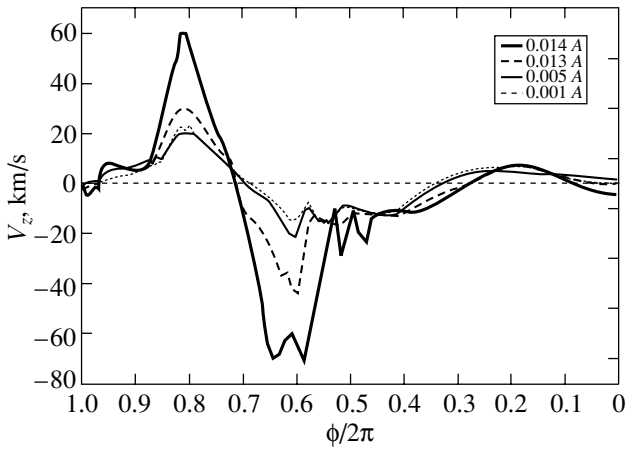

Fig. 7. $V_z(\phi)$ relation along the same four streamlines as in Fig. 6.

disk have low density, and the shock due to their interaction with the stream lies along the edge of the stream. The shock bends as the gas density in the halo increases, finally assuming a position along the edge of the disk. Note that the solution for the cool case has the same qualitative features as the solution for hot outer parts of the disk [27]: the interaction between the stream and the disk is collisionless; the region of enhanced energy release is due to the interaction between the gas in the circumdisk halo and in the stream and is located outside the disk; and the resulting system of shocks is extended and can be considered as a hot line.

It follows from the above general features of the flow pattern that, at the interaction zone, the halo gas and stream gas pass through the shocks corresponding to their own flows, are mixed, and then move along the tangential discontinuity between the two shocks. Subsequently, the disk itself, halo, and intercomponent envelope are formed of precisely this matter. The jump in the gas parameters after the passage of the shock leads to the increase of density and temperature in the region between the shocks and, consequently, to the appearance of a pressure gradient along the z axis, perpendicular to the system's plane of rotation. As a result, the gas begins to expand vertically, increasing the z component of the velocity, until the pressure gradient is balanced by the gravitational force.

The vertical gas pressure due to the presence of the z component of the velocity, together with the motion of the gas along the tangential discontinuity at the disk's outer edge, lead to a gradual increase of the thickening of the circumdisk halo (along the z axis). This thickening of the halo along the outer edge of the accretion disk is clearly visible in the three-dimensional constant-density surface shown in Fig. 2, as well as in Fig. 4, which displays constant-density curves in the section of the flow structure that is perpendicular to the equatorial plane and drawn through the accretor and the maximum thickening of the halo ($\phi = 0.7$). An additional illustration of the halo thickening above the disk is provided by Fig. 5, which shows fragments of computed streamlines emerging from the vicinity of L_1. We can see that the streamlines diverge after acquiring a vertical acceleration in the region between the shocks, then converge again toward the system's equatorial plane. The region of vertical acceleration is restricted to the hot-line zone. After passing this region, the gas has a large vertical velocity component that makes it climb higher, until its store of kinetic energy is exhausted. The point where the upward motion ceases corresponds to the maximum height, which is reached at phase $\sim$0.7, i.e., already considerably outside the hot line.

To quantitatively analyze the thickening of the halo above the disk, let us consider the behavior of the streamlines and the distributions of the gas parameters along them. In a cylindrical coordinate system with its origin coincident with the accretor $(x = A, y = 0.0, z = 0.0)$ and the angle ϕ measured from the point L_1 opposite to the direction of rotation of the matter (coincident with the system's direction of rotation), each point of the streamline is described by the coordinates (r, ϕ, z). The $z(\phi)$ relations for four streamlines originating at points in the neighborhood of L_1 are presented in Fig. 6. We can see that, after entering the hot-line region (phase $\sim$0.975), the streamlines begin to climb due to the increase of the velocity's z component. The phase relation of the vertical velocity for the same four streamlines is

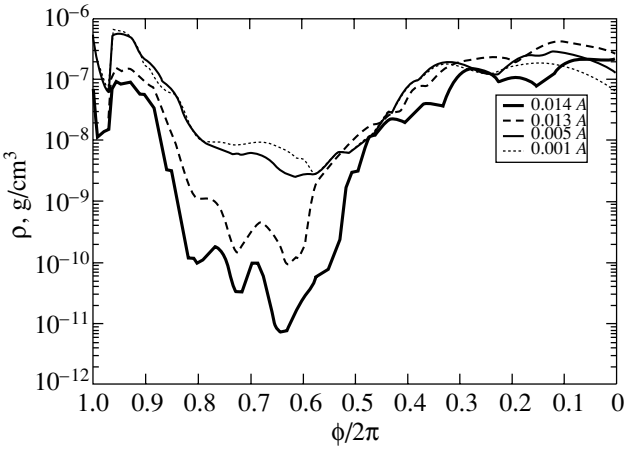

Fig. 8. The density relation $\rho(\phi)$ along the same four streamlines as in Fig. 6.

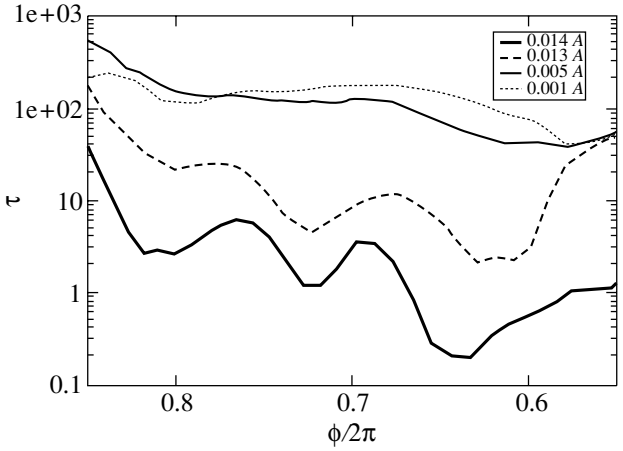

Fig. 9. The optical depth relation, $\tau(\phi)$, near the thickening ($\phi = 0.55$–0.85) along the same four streamlines as in Fig. 6.

displayed in Fig. 7. When the gas emerges from the hot line (phase $\sim$0.8), the force due to the pressure jump behind the shocks disappears, and the gas simply moves in the accretor's gravitational field. The vertical velocity of the gas becomes zero at phase $\sim$0.7, corresponding to the maximum ascent of the streamlines. The height of the halo at this position reaches $\sim 0.04\,A$.

In addition to the primary maximum, the system also exhibits a minimum height at phase $\sim$0.3, when $z \sim (0.005$–$0.006)\,A$, and a secondary maximum at phase $\sim$0.1, when the height of the halo is $\sim 0.01\,A$. Due to the effects of viscous dissipation, the minimum and secondary maximum are considerably less pronounced than the primary maximum. Eventually, viscosity leads to complete damping of the vertical velocity oscillations, so that the gas no longer possesses a significant vertical velocity when it next approaches the region of the interaction with the stream.

Figure 8 is the phase dependence of the density for the same four streamlines as in Fig. 6. The densities correspond to the mass-exchange rate in the RW Tri system ($\sim 10^{-8}\,M_\odot$/yr [28]). We can see from these results that a strong density decrease is observed in the region of maximum ascent of the streamlines. This behavior of the density can lead to a displacement of the light-curve dips towards regions of higher ρ; i.e., towards higher phases. This should be manifest most strongly in short-wavelength observations, since higher densities are required to absorb harder radiation. It is also interesting that the gas density is much higher near the secondary maximum, at phases $\sim$0.1, than near the first thickening.

To evaluate whether the central source can be eclipsed by the thickening of the halo, we computed the optical depth of the halo matter, τ. The optical depth is the product of the density, the layer's geometrical depth, and the absorption coefficient: $\tau = \rho l \kappa$. To estimate τ near the region of thickening, let us use the densities presented in Fig. 8, taking the characteristic linear size of the thickening to be its half-height (Fig. 6). We estimate the absorption coefficient using the approximation formulas from [29] with a temperature of $\sim$13 600 K and a characteristic density corresponding to the value at the thickening's half maximum. Our estimates of τ are presented in Fig. 9, which shows the relations between the optical depth and the phase, $\tau(\phi)$, along the same four streamlines as in Fig. 6. An analysis of these estimates of τ shows that the thickening is optically thick, even at its greatest heights, and the value of τ at the half maximum can reach $\sim 10^2$. This means that the halo thickening is capable of eclipsing the central source, giving rise to the dips observed in the light curves of semidetached binaries with stationary disks.

Obviously, in stationary systems, when there is no collision between the stream and the outer edge of the disk, there can be no ricochet and no transfer of a substantial fraction of the stream's matter into the inner parts of the disk. However, the momentum of the stream matter is lower than that of the halo gas, so that some of the stream gas at great heights can slide down into inner orbits, appearing as if the stream is flowing around the outer edge of the disk. This sliding-down can take place only in the hot-line region, where the momenta of the matter in the stream and in the halo have not yet become equalized. Indeed, when considering the streamlines that reach high heights from the stream's center (Fig. 10), we can see that some of them leave the interaction region of the stream and halo, envelop the disk from the upper side, and get into its inner regions. The results

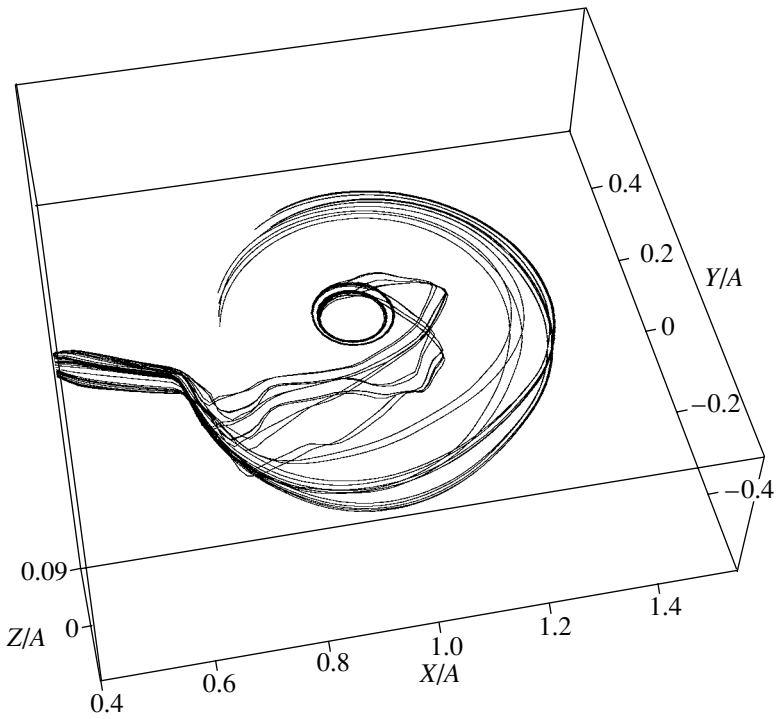

Fig. 10. Same as Fig. 5, also showing fragments of the streamlines emerging from a wider vicinity of L_1.

of our computations demonstrate that the total flux of matter associated with this effect is small, and apparently cannot significantly influence the visibility of the central object.

4. CONCLUSIONS

Observations of semidetached binaries with stationary accretion disks reveal dips in their light curves at phase ∼0.7. These dips are usually explained by invoking the presence of a thickening at the outer edge of the accretion disk, without explaining how matter appears at considerable heights above the accretion disk in the case of a stationary interaction between the stream and disk. It is important to resolve the problem of the formation of this thickening of the halo above a stationary disk if we wish to correctly interpret the observations and more fully understand the nature of matter-exchange processes in these stars.

The results of our three-dimensional numerical modeling of the matter-flow structure in semidetached binaries with stationary disks confirm our earlier conclusions [21, 22, 27] that the interaction between the stream and disk is collisionless, the region of increased energy release is due to the interaction between the gas in the circumdisk halo and the stream and is located outside the disk, and the system of shocks that forms is extended and can be considered as "hot line." The interaction between the circumdisk halo and the stream possesses all the characteristic features of an oblique collision of two flows that results in the formation of a structure consisting of two shock waves and a tangential discontinuity.

In the hot-line region, the halo and stream gases pass through the shocks corresponding to their own flows, are mixed, and then move along the tangential discontinuity between the two shocks. During the interaction between the stream and the circumdisk halo, a considerable fraction of the matter acquires a vertical acceleration. The vertical motion of the gas due to the z component of the velocity, together with its motion along the tangential discontinuity at the outer edge of the disk, results in a gradual growth of the thickness of the circumdisk halo. The region of vertical acceleration is restricted to the hot-line zone, and its angular size does not exceed ∼65°. However, once it has passed this region, the gas has a sufficiently large vertical velocity component to rise until its store of kinetic energy is exhausted. The point where the upward motion ceases corresponds to the maximum height, which is reached at phase ∼0.7, already considerably outside the hot line. The thickening extends appreciably higher than the scale height of the disk, reaching values of $\sim 0.04\,A$ (this corresponds to a ratio of the thickening's height to the distance to the accretor of >0.1), and its angular size exceeds ∼130°. Our computations also show that, in addition to the primary maximum, the system also displays a height minimum at phase ∼0.3, when $z \sim$

(0.005–0.006) A, and a secondary maximum at phase ~0.1, when the height of the halo is ~0.01 A.

Our analysis of these results leads us to conclude that the dips in the light curves of semidetached binaries with stationary disks (i.e., in the absence of a collisional interaction between the stream and disk), can be explained by the formation of a thickening of the halo above the outer edge of the disk. The origin of this thickening is described well by the hot-line model, and its quantitative features are consistent with observations. The proposed model can be applied to both semidetached systems (LMXBs, cataclysmic variables) in their stationary state and to dwarf novae in outburst, provided that the outer parts of the disk are not strongly distorted in the outburst.

ACKNOWLEDGMENTS

This study was supported by the Russian Foundation for Basic Research (project nos. 03-02-16622, 03-01-00311, 05-02-16123, 05-02-17070, and 05-02-17874), the Program for Support of Leading Scientific Schools of Russia (grant no. NSh-162.2003.2), and the basic research programs "Mathematical Modeling and Intellectual Systems" and "Unstable Phenomena in Astronomy" of the Presidium of the Russian Academy of Sciences.

REFERENCES

1. N. E. White and S. S. Holt, Astrophys. J. **257**, 318 (1982).
2. K. O. Mason, in *Two Topics in X-ray Astronomy*, Vol. 1: *X-ray Binaries* (1989), ESA SP-296, p. 113.
3. M. Livio, N. Soker, and R. Dgani, Astrophys. J. **305**, 267 (1986).
4. R. Dgani, M. Livio, and N. Soker, Astrophys. J. **336**, 350 (1989).
5. M. Hirose, Y. Osaki, and S. Mineshige, Publ. Astron. Soc. Jpn. **43**, 809 (1991).
6. S. H. Lubow and F. H. Shu, Astrophys. J. Lett. **198**, 383 (1975).
7. S. H. Lubow and F. H. Shu, Astrophys. J. Lett. **207**, L53 (1976).
8. S. H. Lubow, Astrophys. J. **340**, 1064 (1989).
9. J. Frank, A. R. King, and J.-P. Lasota, Astron. Astrophys. **178**, 137 (1987).
10. P. J. Armitage and M. Livio, Astrophys. J. **470**, 1024 (1996).
11. K. O. Mason, F. A. Cordova, M. G. Watson, and A. R. King, Mon. Not. R. Astron. Soc. **232**, 779 (1988).
12. K. S. Long, C. W. Mauche, J. C. Raymond, *et al.*, Astrophys. J. **469**, 841 (1996).
13. T. Naylor, G. T. Bath, P. A. Charles, *et al.*, Mon. Not. R. Astron. Soc. **231**, 237 (1988).
14. I. Billington, T. R. Marsh, K. Horne, *et al.*, Mon. Not. R. Astron. Soc. **279**, 1274 (1996).
15. E. T. Harlaftis, B. J. M. Hassall, T. Naylor, *et al.*, Mon. Not. R. Astron. Soc. **257**, 607 (1992).
16. K. O. Mason, J. E. Drew, and C. Knigge, Mon. Not. R. Astron. Soc. **290**, L23 (1997).
17. C. S. Froning, K. S. Long, and C. Knigge, Astrophys. J. **584**, 433 (2003).
18. D. V. Bisikalo, A. A. Boyarchuk, O. A. Kuznetsov, and V. M. Chechetkin, Astron. Zh. **74**, 880 (1997) [Astron. Rep. **41**, 786 (1997)].
19. D. V. Bisikalo, A. A. Boyarchuk, O. A. Kuznetsov, *et al.*, Astron. Zh. **75**, 40 (1998) [Astron. Rep. **42**, 33 (1998)].
20. D. V. Bisikalo, A. A. Boyarchuk, V. M. Chechetkin, *et al.*, Mon. Not. R. Astron. Soc. **300**, 39 (1998).
21. A. A. Boyarchuk, D. V. Bisikalo, O. A. Kuznetsov, and V. M. Chechetkin, *Mass Transfer in Close Binary Stars* (Taylor and Francis, London, 2002).
22. D. V. Bisikalo, A. A. Boyarchuk, P. V. Kaigorodov, and O. A. Kuznetsov, Astron. Zh. **80**, 879 (2003) [Astron. Rep. **47**, 809 (2003)].
23. M. Makita, K. Miyawaki, and T. Matsuda, Mon. Not. R. Astron. Soc. **316**, 906 (2000).
24. K. Sawada and T. Matsuda, Mon. Not. R. Astron. Soc. **255**, 17P (1992).
25. P. L. Roe, Annu. Rev. Fluid Mech. **18**, 337 (1986).
26. S. R. Chakravarthy and S. Osher, in *Proceedings of the 23rd Aerospace Sci. Meeting* (1985), AIAA-85-0363, p. 363.
27. O. A. Kuznetsov, D. V. Bisikalo, A. A. Boyarchuk, *et al.*, Astron. Zh. **78**, 997 (2001) [Astron. Rep. **45**, 872 (2001)].
28. P. J. Groot, R. G. M. Rutten, and J. van Paradijs, Astron. Astrophys. **417**, 283 (2004).
29. K. R. Bell and D. N. C. Lin, Astrophys. J. **427**, 987 (1994).

Translated by N. Samus'

Astronomy Reports, Vol. 49, No. 9, 2005, pp. 709–713. Translated from Astronomicheskiĭ Zhurnal, Vol. 82, No. 9, 2005, pp. 797–802.

Modeling the Wind of the Be Star SS 2883

A. I. Bogomazov

Moscow State University, Moscow, Russia

Received January 20, 2005; in final form, February 17, 2005

Abstract—Observations of eclipses of the radio pulsar B1259-63 by the disk of its Be-star companion SS 2883 provide an excellent opportunity to study the winds of stars of this type. The eclipses lead to variations in the radio flux (due to variations in the free–free absorption), dispersion measure, rotation measure, and linear polarization of the pulsar. We have carried out numerical modeling of the parameters of the Be-star wind and compared the results with observations. The analysis assumes that the Be-star wind has two components: a disk wind in the equatorial plane of the Be star with a power-law fall-off in the electron density n_e with distance from the center of the star ρ ($n_e \sim \rho^{-\beta_0}$), and a spherical wind above the poles. The parameters for a disk model of the wind are estimated. The disk is thin (opening angle 7.5°) and dense (electron density at the stellar surface $n_{0e} \sim 10^{12}$ cm^{-3}, $\beta_0 = 2.55$). The spherical wind is weak ($n_{0e} \lesssim 10^9$ cm^{-3}, $\beta_0 = 2$). This is the first comparison of calculated and observed fluxes of the pulsating radio emission. © *2005 Pleiades Publishing, Inc.*

1. INTRODUCTION

The first binary system consisting of a radio pulsar and a Be star was discovered more than ten years ago using the Parkes radio telescope [1, 2]. This is the B1259-63 system, in which the pulsar moves along a very elongated orbit ($e \geq 0.87$) around its companion—the 10^m Be star SS 2883.

The first theoretical estimates of the number of such systems, carried out in 1983–1987 using the so-called "scenario machine" [3–6], showed that approximately one in 700 observed radio pulsars should have an OB companion. The detection of the B1259-63 system not only confirmed the possibility of the evolutionary scenario obtained by the authors of [3–6], but also provided a powerful tool for studies of the associated stellar wind, as was also predicted in these studies. Currently, ≈1500 radio pulsars are known, of which at least two are in binary systems with OB companions (B1259-63 and J0045-7319), consistent with the above estimate.

In 1997–1998, possible evolutionary tracks for the B1259-63 and J0045-7319 systems were computed using the scenario machine [7]. These computations were based on an evolutionary scenario that predicts the existence of systems consisting of a radio pulsar and a massive optical component. The high eccentricity of the orbit is explained as an effect of the "kick" given by the anisotropic supernova explosion that gave rise to the pulsar. Possible magnitudes and the direction of the kick velocity in the B1259-63 system were also derived [8].

In 2003, the scenario machine was used to estimate the number of such systems in which the orbital plane of the pulsar and the equatorial plane of the Be star do not coincide [9]. For characteristic anisotropic kick velocities of 50–200 km/s, these two planes should be inclined relative to one another by several tens of degrees in more than half of these systems.

A Be star is a main-sequence star of spectral class B which has one or more Balmer emission lines in its spectrum, with these lines usually displaying two peaks. Struve proposed in 1931 that this spectral characteristic could be explained as radiation from a rotating disk associated with the Be star. These disks have now been observed in the optical, infrared, and radio. They are comprised of dense, slowly rotating material that is located in or near the equatorial plane of the Be star. In addition, Be stars produce winds with low density and high velocity.

Observations of the transit of PSR B1259-63 provide a unique opportunity for studying the characteristics of the disk of the Be star based on the observed variations of the radio flux, linear polarization, rotation measure, and pulse delay. This is possible because the disk of SS 2883 is inclined relative to the orbital plane of its companion, so that the pulsar is sometimes eclipsed by the disk.

Attempts were undertaken to construct a model for the Be-star wind and compare the calculated parameters with the observed dispersion measure, rotation measure, and pulse delay time. A disk model with an exponential fall-off of the electron density with distance from the Be star and with height above the plane of the disk was considered in [10].

1063-7729/05/4909-0709$26.00

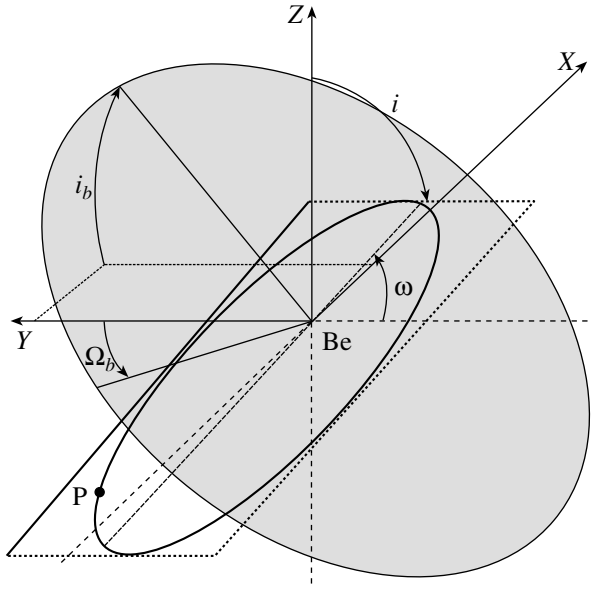

Fig. 1. Schematic model for a system consisting of a radio pulsar and a Be star. The X axis is directed along the line of sight toward the observer. ω is the longitude of the ascending node, i is the orbital inclination (the angle between the plane of the sky YZ and the orbital plane of the pulsar), P indicates the pulsar and Be the Be star, i_b is the angle between the XY plane and the plane of the Be-star disk, and Ω_b is the angle between the Y axis and the line corresponding to the intersection of the XY plane and the disk of the Be star.

A model with a power-law fall-off of the density in the disk is more physically justified, however [11]; with some parameters, this model was able to explain the observed variations in the dispersion measure near periastron. A model with a clumpy disk wind from the Be star has also been developed [12, 13] (in addition to, not replacing, the power-law disk). Rapidly moving bubbles (velocities of ≈2000 km/s) with electron densities that differ from the value in the surrounding region ($n_e \sim 10^6$ cm^{-3} and dimensions $<10^{10}$ cm at a distance of 20–50 stellar radii) give rise to appreciable fluctuations in the electron density along the line of sight, and thereby to fluctuations in the flux, dispersion measure, and rotation measure.

An attempt to establish the position of the orbital plane of PSR B1259-63 relative to the equatorial plane of SS 2883 was made using timing measurements for the pulsar [14, 15]. However, it proved impossible to construct a unique model for the system due to the noise level and the prolonged eclipses of the pulsating radio emission.

A disk model for the Be-star wind is also considered, for example, in [16, 17], where the ratio N of the densities of the outflowing material in the equatorial plane and at the poles is derived. If the Be star rotates with a velocity v that is 90% of the critical velocity v_{crit}, then $N = 150$; slower rotation lowers this value (when $v = 0.70\,v_{crit}$, $N \approx 15$–20). According to [18], the rotational velocity of SS 2883 is approximately 70% of the critical velocity.

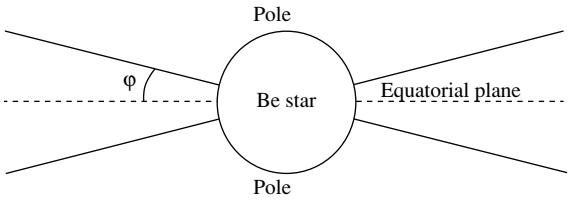

Fig. 2. Model Be-star wind. There is a disk wind with a power-law fall-off in the electron density in the equatorial plane and a spherical wind above the poles.

We consider here the absorption of the radio emission in a model with a power-law disk wind in the equatorial plane and a spherical wind above the poles of the Be star (without including the effect of clumpiness). In contrast to previous studies, we compare the calculated and observed fluxes of pulsating radio emission. The derived parameters of the wind differ from those presented in [11]. The available rotation-measure data are sufficient only to derive order-of-magnitude estimates of the magnetic-field strength in the wind (in particular, in bubbles), as was done in [11–13]. Accordingly, we will consider further only the radio flux and dispersion measure.

2. MODEL Be-STAR WIND

Figure 1 depicts a schematic model of a binary system consisting of a radio pulsar and a Be star. In this figure, ω is the longitude of the ascending node, i is the orbital inclination (the angle between the plane of the sky YZ and the orbital plane of the pulsar), P indicates the pulsar and Be the Be star, i_b is the angle between the XY plane and the plane of the Be-star disk, and Ω_b is the angle between the Y axis and the line corresponding to the intersection of the XY plane and the disk of the Be star. The X axis is oriented along the line of sight toward the observer.

The calculated model for the wind of SS 2883 is presented in Fig. 2. There is a disk wind with opening angle φ in the equatorial plane, and a spherical wind above the poles, which we take here to be isothermal and to have a constant radial speed. We assume that the outflowing gas is fully ionized.

The electron density n_e a distance ρ from the star is calculated using the formula

$$n_e = n_{0e}\,(\rho_0/\rho)^{\beta_0}\,. \qquad (1)$$

Here, n_{0e} is the electron density at the stellar surface (i.e., at a distance ρ_0 from its center). For the spherical

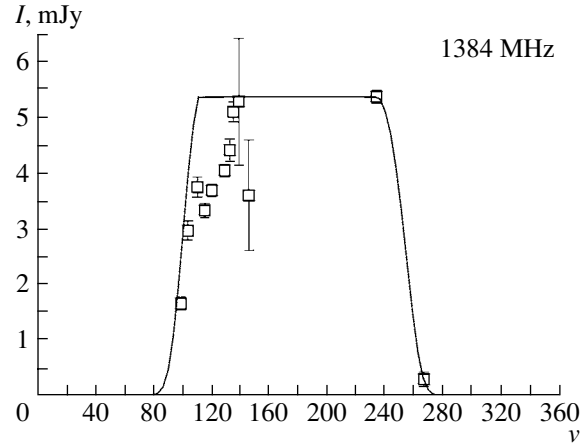

Fig. 3. Dependence of the 1384 MHz radio flux of B1259-63 on the position of the pulsar relative to SS 2883; v is the true anomaly. The hollow squares show the observational data with their errors. The solid curve denotes the calculated model.

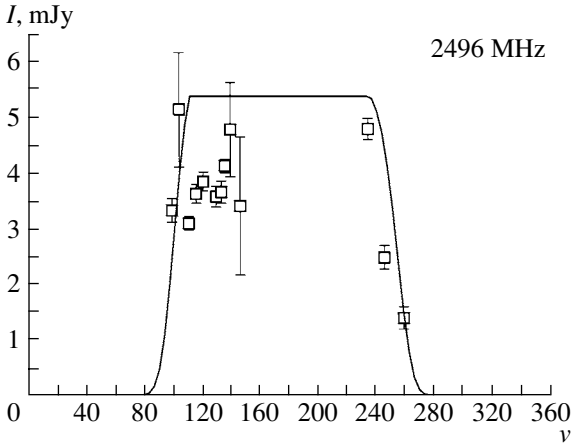

Fig. 4. Same as Fig. 3 for 2496 MHz.

wind, $\beta_0 = 2$; this is a free parameter for the disk wind, whose value is one of the parameters we seek.

We also assumed that the temperature of the disk wind can be determined by the power-law relation

$$T = T_0 \, (\rho_0/\rho)^{\beta_1} \, . \qquad (2)$$

Here, T is the temperature of the plasma a distance ρ from the star and T_0 is the temperature at the stellar surface.

The optical depth to radio emission can be calculated using the formula [19]

$$\tau = 0.34 \left(\frac{1\ \mathrm{GHz}}{\nu}\right)^{2.1} \left(\frac{10^4\ \mathrm{K}}{T}\right)^{1.35} \frac{\mathrm{EM}}{10^6\ \mathrm{pc\ cm^{-6}}}. \qquad (3)$$

Here, ν is the frequency of the radio emission, T the temperature of the wind (2), and EM the emission measure, which is defined to be

$$\mathrm{EM} = \int n_e^2 dl. \qquad (4)$$

The dispersion measure is given by the formula

$$\mathrm{DM} = \int n_e dl. \qquad (5)$$

The quantity n_e in (4) and (5) is calculated using (1).

3. RESULTS

We carried out theoretical calculations of the flux and dispersion measure of the radio emission of the B1259-63 pulsar as a function of its position relative to its companion—the Be star SS 2883. These calculated values were compared with the observations.

The observational data on the radio fluxes were taken from Table 2 of [13], and on the dispersion measures from Table 1 of [10], Table 2 of [11], and Table 3 of [13]. The longitude of the ascending node of the pulsar orbit in the B1259-63 system is $\omega = 138°$, the orbital inclination is $i = 36°$, the characteristic radius of the star is $\rho_0 = 6\,R_\odot$, the mass of the optical star is $M = 10\,M_\odot$, and the projection of the semimajor axis onto the line of sight is $a \sin i =$ 1295.98 light seconds [2]. The interstellar contribution to the dispersion measure of the B1259-63 pulsar is 146.8 pc/cm^3 [13].

The velocity of the Be-star wind at infinity is $V_\infty = 1000{-}1300$ km/s in the equatorial plane and $V_\infty \approx 2300$ km/s at the poles [17] (the characteristic wind velocity at infinity for SS 2883 is $\approx 1350 \pm$ 200 km/s [20]). The radial outflow velocity of the disk material at the Be-star surface is 5–10 km/s [21].

To check the resulting parameters of the stellar wind, we must compare the mass-loss rate in the model obtained with the characteristic values for Be stars. The rate at which matter flows from the star can be found from the expression

$$\dot{M} = \Omega \rho^2 n m_i V, \qquad (6)$$

where ρ is the distance from the star; n, the particle density of the wind at the distance ρ, which is calculated using (1); m_i, the mean mass of the ions in the wind; V, the wind velocity at the distance ρ; and Ω, the solid angle into which the given type of wind (spherical or disk) flows.

The mass loss of Be stars was investigated in detail in [22]. A Be star with an initial mass of $10\,M_\odot$ loses mass at the rate $\dot{M} = 3 \times 10^{-9}\,M_\odot$/yr.

We carried out numerical computations in order to determine the best-fit orientation of the disk of the Be star SS 2883 relative to the orbital plane of

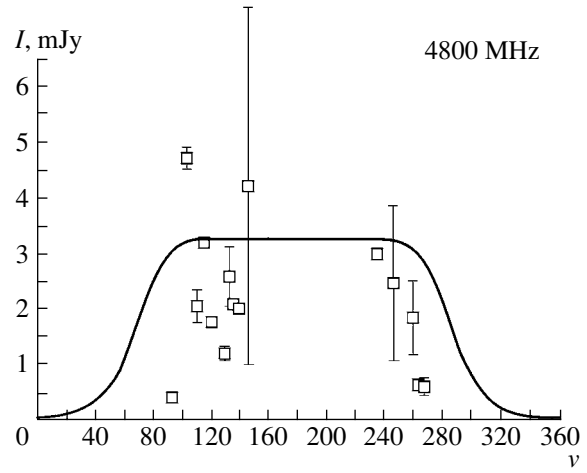

Fig. 5. Same as Fig. 3 for 4800 MHz.

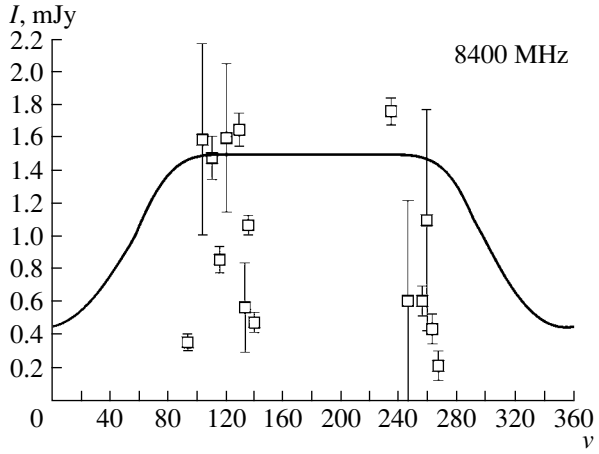

Fig. 6. Same as Fig. 3 for 8400 MHz.

PSR B1259-63, which is given by the parameters Ω_b and i_b (Fig. 1). We also wished to determine the best-fit values of β_0 for the disk wind and the electron density at the stellar surface n_0 for both the disk and spherical winds ($\beta_0 = 2$ for the spherical wind). We constructed theoretical light curves for the pulsar at 1384, 2496, 4800, and 8400 MHz together with the dependence of the dispersion measure of the pulsar radio emission on the position of the pulsar relative to its companion.

The results of the numerical simulations are shown in Figs. 3–7 together with the observational data. The criterion used to evaluate the correctness of a model is the closeness of the computed curves to the observational data. In addition, the model should not contradict our understanding of the matter outflow rate in Be stars.

The computations yielded the following best-fit parameters for the disk model. The disk opening angle was $\varphi = 7.5°$, the electron density in the disk at the stellar surface was $n_{0e} \approx 10^{12}$ cm^{-3}, and $\beta_0 = 2.55$. The spherical wind was weak ($n_{0e} \lesssim 10^9$ cm^{-3}, $\beta_0 = 2$). The orientation of the SS 2883 disk relative to the orbital plane is described by the parameters Ω_b and i_b (Fig. 1), which have the values $\Omega_b = 12°$ and $i_b = 67°$ in the best-fit model. The disappearance of the pulsating emission of B1259-63 near periastron is due to eclipses of the pulsar by the Be-star disk. The weak spherical wind does not make an appreciable contribution to either the decrease in the radio flux or the increase in the dispersion measure. The model mass-loss rate via the SS 2883 wind estimated using (6) is consistent with our current understanding of the mass-loss rates of Be stars: $\dot{M} \approx 3 \times 10^{-9} M_\odot$/yr, in good agreement with the results of [22].

Although we have assumed that the temperature of the wind may depend on the distance from the Be star (2), the best-fit model was obtained for a constant temperature, equal to 10^4 K. Substituting (1) and (2) into (3), we can see that the behavior of the light curve will not change if $2\beta_0 - 1.35\beta_1 = 5.1$, if we suppose that $\beta_1 \neq 0$ (so that consequently $\beta_0 \neq 2.55$). However, the variations of β_0 must not be in contradiction with the observed dispersion measures, and cannot be large.

Figure 3 clearly displays a secondary minimum of the light curve at values of the true anomaly v from 100° to 120°. Our model for the wind is not able to fit this observational feature. The computations yielded a model with $\Omega_b \approx -55°$ that can fit this secondary minimum, whose presence is then explained by the absorption of the radio emission in the disk. However, in this case, the pulsar and observer are located on the same side of the disk at periastron, and we must introduce a strong spherical wind in order to fit the decrease in the radio flux. This led to an implausibly high mass-loss rate ($\dot{M} \approx 3 \times 10^{-7} M_\odot$/yr). In addition, a strong spherical wind would make an appreciable contribution to the dispersion measure, so that it would be necessary to appreciably lower the interstellar dispersion measure (from 146.8 pc/cm^3 to 135–140 pc/cm^3). We, accordingly, rejected this second model.

The parameters of the best-fit model presented here differ substantially from the results of [11], where, in particular, it was found that $\beta_0 = 4.2$ in the disk and that the mass-loss rate of the optical star is $\dot{M} = 5 \times 10^{-8} M_\odot$/yr.

4. CONCLUSIONS

Our computations have yielded the following best-fit parameters for the disk model used. The opening

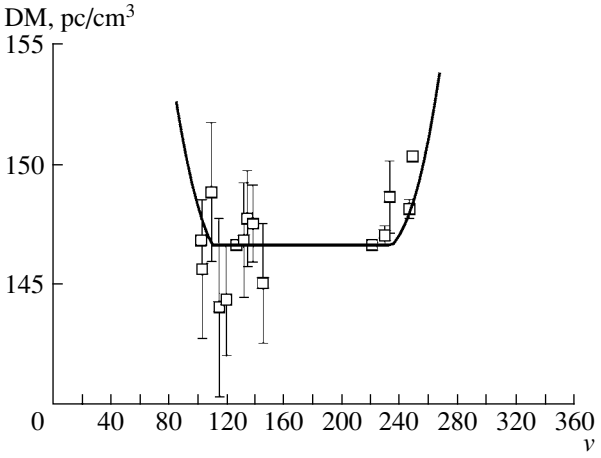

Fig. 7. Dependence of the dispersion measure on the true anomaly v of the B1259-63 pulsar. The hollow squares indicate the observational data with their errors. The solid curve denotes the model with a thin and dense disk wind and a negligibly small spherical wind (we took the interstellar contribution to the dispersion measure to be 146.8 pc/cm^3).

angle of the disk is $\varphi = 7.5°$, the electron density in the disk at the stellar surface is $n_{0e} \approx 10^{12}$ cm^{-3}, and $\beta_0 = 2.55$. The spherical wind is weak ($n_{0e} \lesssim 10^9$ cm^{-3}, $\beta_0 = 2$), and cannot make a significant contribution to either the decrease in the radio flux or the increase in the dispersion measure near periastron. The orientation of the SS 2883 disk relative to the pulsar's orbital plane is fit by the parameters $\Omega_b = 12°$ and $i_b = 67°$ (Fig. 1). The mass-loss rate in the SS 2883 wind estimated using (6) is consistent with current thinking about the mass-loss rates of Be stars: $\dot{M} \approx 3 \times 10^{-9}\, M_\odot$/yr, in good agreement with the results of [22]. The disappearance of the pulsating radio emission of B1259-63 near periastron is due to eclipsing of the pulsar by the dense disk of the Be star.

ACKNOWLEDGMENTS

The author thanks the anonymous referee for useful comments.

REFERENCES

1. S. Johnston, R. N. Manchester, A. G. Lyne, *et al.*, Astrophys. J. Lett. **387**, L37 (1992).
2. S. Johnston, R. N. Manchester, A. G. Lyne, *et al.*, Mon. Not. R. Astron. Soc. **268**, 430 (1994).
3. V. G. Kornilov and V. M. Lipunov, Astron. Zh. **60**, 284 (1983) [Sov. Astron. **27**, 163 (1983)].
4. V. G. Kornilov and V. M. Lipunov, Astron. Zh. **60**, 574 (1983) [Sov. Astron. **27**, 334 (1983)].
5. V. G. Kornilov and V. M. Lipunov, Astron. Zh. **61**, 686 (1984) [Sov. Astron. **28**, 402 (1984)].
6. V. M. Lipunov and M. E. Prokhorov, Astron. Zh. **74**, 1189 (1997) [Astron. Rep. **41** (1997)].
7. N. V. Raguzova and V. M. Lipunov, Astron. Zh. **75**, 857 (1998) [Astron. Rep. **42**, 757 (1998)].
8. M. E. Prokhorov and K. A. Postnov, Pis'ma Astron. Zh. **23**, 503 (1997) [Astron. Lett. **23**, 439 (1997)].
9. A. I. Bogomazov, Astron. Astrophys. Trans. **23**, 71 (2004).
10. A. Melatos, S. Johnston, and D. B. Melrose, Mon. Not. R. Astron. Soc. **275**, 381 (1995).
11. S. Johnston, R. N. Manchester, A. G. Lyne, *et al.*, Mon. Not. R. Astron. Soc. **279**, 1026 (1996).
12. S. Johnston, N. Wex, L. Nicastro, *et al.*, Mon. Not. R. Astron. Soc. **326**, 643 (2001).
13. T. W. Connors, S. Johnston, R. N. Manchester, and D. McConnell, Mon. Not. R. Astron. Soc. **336**, 1201 (2002).
14. N. Wex, S. Johnston, R. N. Manchester, *et al.*, Mon. Not. R. Astron. Soc. **298**, 997 (1998).
15. N. Wang, S. Johnston, and R. N. Manchester, Mon. Not. R. Astron. Soc. **351**, 599 (2004).
16. F. X. de Araujo and J. A. de Freitas Pacheco, Mon. Not. R. Astron. Soc. **241**, 543 (1989).
17. F. X. de Araujo, J. A. de Freitas Pacheco, and D. Petrini, Mon. Not. R. Astron. Soc. **267**, 501 (1994).
18. J. M. Porter, Mon. Not. R. Astron. Soc. **280**, 31 (2001).
19. S. A. Kaplan and S. B. Pikel'ner, *Physics of the Interstellar Medium* (Nauka, Moscow, 1979) [in Russian].
20. B. McCollum, Bull. Am. Astron. Soc. **25**, 1321 (1993).
21. L. B. F. M. Waters, J. Cote, and H. J. G. L. M. Lamers, Astron. Astrophys. **185**, 206 (1987).
22. A. V. Tutukov and A. V. Fedorova, Astron. Zh. **80**, 896 (2003) [Astron. Rep. **47**, 826 (2003)].

Translated by D. Gabuzda

Astronomy Reports, Vol. 49, No. 9, 2005, pp. 714–723. Translated from Astronomicheskiĭ Zhurnal, Vol. 82, No. 9, 2005, pp. 803–813.

Abundances of Carbon, Nitrogen, Oxygen, and Other Elements in the Atmospheres of the Giants 25 Mon and HR 7389

T. M. Rachkovskaya

Crimean Astrophysical Observatory, Nauchnyĭ, Ukraine

Received December 20, 2004; in final form, February 17, 2005

Abstract—An analysis of high-resolution CCD spectra of the giant 25 Mon, which shows signs of metallicity, and the normal giant HR 7389 is presented. The derived effective temperatures, gravitational accelerations, and microturbulence velocities are $T_{\rm eff} = 6700$ K, $\log g = 3.24$, and $\xi_t = 3.1$ km/s for 25 Mon and $T_{\rm eff} = 6630$ K, $\log g = 3.71$, and $\xi_t = 2.6$ km/s for HR 7389. The abundances ($\log \varepsilon$) of nine elements are determined: carbon, nitrogen, oxygen, sodium, silicon, calcium, iron, nickel, and barium. The derived excess carbon abundances are 0.23 dex for 25 Mon and 0.16 dex for HR 7389. 25 Mon displays a modest (0.08 dex) oxygen excess, with the oxygen excess for HR 7389 being somewhat higher (0.15 dex). The nitrogen abundance is probably no lower than the solar value for both stars. The abundances of iron, sodium, calcium (for HR 7389), barium, and nickel exceed the solar values by 0.22–0.40 dex for both stars. The highest excess (0.62 dex) is exhibited by the calcium abundance for 25 Mon. Silicon displays a nearly solar abundance in both stars—small deficits of −0.03 dex and −0.07 dex for 25 Mon and HR 7389, respectively. No fundamental differences in the elemental abundances were found in the atmospheres of 25 Mon and HR 7389. Based on their $T_{\rm eff}$ and $\log g$ values, as well as theoretical calculations, A. Claret estimated the masses, radii, luminosities, and ages of 25 Mon ($M/M_\odot = 2.45$, $\log(R/R_\odot) = 0.79$, $\log(L/L_\odot) = 1.85$, $t = 5.3 \times 10^8$ yr) and HR 7389 ($M/M_\odot = 2.36$, $\log(R/R_\odot) = 0.50$, $\log(L/L_\odot) = 1.24$, $t = 4.6 \times 10^8$ yr), and also of the stars 20 Peg ($M/M_\odot = 2.36$, $\log(R/R_\odot) = 0.73$, $\log(L/L_\odot) = 1.79$, $t = 4.9 \times 10^8$ yr) and 30 LMi ($M/M_\odot = 2.47$, $\log(R/R_\odot) = 0.73$, $\log(L/L_\odot) = 1.88$, $t = 4.8 \times 10^8$ yr) studied by the author earlier. © *2005 Pleiades Publishing, Inc.*

1. INTRODUCTION

Various stars with peculiar chemical compositions are observed among star of spectral types A–F on the Hertzsprung–Russell diagram. Classical Am stars, whose distinguishing characteristic is an increase in the abundances of elements with growth in their atomic number and underabundances of calcium and scandium, are concentrated near the main sequence. A qualitatively similar pattern of abundance anomalies is observed for pulsating δ Sct stars, but with only some of them displaying a slightly underabundance of calcium and scandium (see, for example, [1]). Kurtz [2] concluded that δ Sct stars are evolved Am stars. Analysis of the spectra of eight A–F giants that show signs of metallicity according to the photometric observations of Hauck [5] led Berthet [3, 4] to conclude that they displayed abundance anomalies similar to δ Sct stars. Later, taking into consideration the results of [3–5], Berthet [6] proposed that, during their evolution, classical Am stars lose their deficiencies of calcium and scandium and enter a δ Sct stage, then a stage in which they become A–F giants with some characteristics of Am stars. Kunzli and North [7] criticize this hypothesis, since Am stars and A–F giants should then have the same frequency of binarity and similar distributions of their rotational velocities $v \sin i$, which is not the case. In their comparative study of the elemental abundances of 18 A–F giants with signs of metallicity and 17 normal giants, Erspamer and North [8] found that the former display somewhat higher abundances of at least eight elements: Al, Ca, Ti, Cr, Mn, Fe, Ni, and Ba.

In two previous papers, we present results of studies of the atmospheric abundances of C, N, O, and some other elements in the giants 20 Peg [9] and 30 LMi [10], which were also considered earlier by Berthet [3, 4]. In contrast to Berthet, our estimates displayed only small differences between the abundances of these elements in these stars and in the Sun.

The main goal of the present work is similar to that of these previous studies. We present results of spectral analyses for 25 Mon and HR 7389. According to Hauck [5], 25 Mon is a giant that displays some characteristics of an Am star, while HR 7389 is a normal giant. Some data about these stars are presented in Table 1. The parameters presented in columns (1)–(6) are taken from the catalog [11],

Table 1. Some parameters of 25 Mon and HR 7389

HR	HD	Name	m_v	Sp	$v \sin i$, km/s	β	c_1	$b-y$	$[c_1]$
2927	61064	25 Mon	5.12	F6III	25	2.675	0.643	0.284	0.586
7389	182900		5.74	F6III	30	2.659	0.541	0.302	0.481

and those from columns (8) and (9) from Hauck and Mermilliod [12].

2. OBSERVATIONAL MATERIAL

The observations were obtained on the 2.6-m reflector of the Crimean Astrophysical Observatory using a 1024×256 EEV15–11 American CCD array mounted at the Coude focus. 25 Mon was observed episodically from February 1998 through December 2003, and HD 7389 from August–September 2003. All the spectra were recorded in the second order of the diffraction grating, and encompassed an interval of about 70 Å. The inverse linear dispersion of the spectra is 3 Å/mm, with a spectral resolution of 30 000. The signal-to-noise ratios are in the range $S/N = 50$–150. The spectra were reduced using standard techniques (see, for example, [13]). As earlier, with the aim of estimating the C, N, and O abundances, we recorded spectral intervals centered on the CI λ 5052, NI λ 8683, and OI λ 6156 lines. However, since we were not able to find enough unblended lines in these intervals for 25 Mon and HD 7389 to estimate the microturbulence velocities, we carried out additional observations in other spectral intervals as well. In oriented our choice of these intervals first and foremost toward FeI lines, which are most numerous in the spectra of these stars. The centers of the chosen wavelength intervals are $\lambda\lambda$ 6065, 6096, 6265, 6380, 6425, 6484, and 6810. We also obtained observations of Hα and Hβ in order to determine the parameters of the stellar atmospheres.

When possible, the abundance estimates were derived from the equivalent widths W_λ of lines free from blending, and otherwise via fitting of synthetic spectra.

3. EQUIVALENT WIDTHS. OSCILLATOR STRENGTHS

We used the line list of the Vienna spectroscopic database [14] to identify the lines in the spectra of 25 Mon and HR 7389; a list of the lines used is presented in Table 2. The first three columns present the wavelengths λ, excitation potentials for the lower level χ, and oscillator strengths $\log gf$ for the lines, in accordance with [14]. Oscillator strengths for CI from other sources are also given. The fourth and fifth columns present the line equivalent widths W_λ, and the sixth and seventh the elemental abundances $\log \varepsilon$ found from individual lines. If no equivalent widths are given in the fourth and fifth columns, the abundance derived from that line is based on a fitted synthetic spectrum. Oxygen abundances $\log \varepsilon$ were obtained for several values of the oscillator strengths.

4. ATMOSPHERIC PARAMETERS

The **effective temperatures and gravitational accelerations** for 25 Mon and HR 7389 were determined by comparing the observed and theoretical parameters corresponding to a model of Kurucz [17]. The parameters used were (1) the equivalent widths W_λ of the Hα and Hβ Balmer lines; (2) the photometric index $[c_1] = c_1 - 0.2(b-y)$ (Table 1) in a four-color system, which is known to be free from interstellar absorption; and (3) the photometric index β (Table 1). The corresponding theoretical parameters are presented by Kurucz [17]. The values of c_1 and $b-y$ for the calculation of $[c_1]$ and β were taken from Hauck and Mermilliod [12] and are presented in Table 1. Since the CCD array we used did not enable us to obtain a full profile of the hydrogen lines, complete with the line wings and surrounding intervals required for correct construction of the continuum level, we applied the method described by us in [9] to measure the equivalent widths W_λ for the Hα and Hβ lines; the essence of this method is comparing the observed "truncated" hydrogen-line profile with a theoretical profile based on a Kurucz model in order to calculate the total equivalent width. The resulting equivalent widths were $W(\mathrm{H}\alpha) = 6.00$ Å and $W(\mathrm{H}\beta) = 8.30$ Å for 25 Mon and $W(\mathrm{H}\alpha = 6.10$ Å and $W(\mathrm{H}\beta) = 7.60$ Å for HR 7389. These W_λ values were used to determine the models.

The effective temperatures T_{eff} and gravitational accelerations $\log g$ were found by averaging the parameters corresponding to points of intersection of the β, Hα, and Hβ curves with the $[c_1]$ curve (Fig. 1). The chosen models for 25 Mon and HR 7389 are denoted by the points in Fig. 1. The results obtained are collected in Table 3; the presented errors in the temperature and gravitational acceleration estimates are formal. We can see that 25 Mon and HR 7389 have similar temperatures. We also present in Table 3 values of T_{eff} and $\log g$ derived by other authors.

Table 2. Studied lines in the spectra of 25 Mon and HR 7389

Line λ, Å	χ, eV	log gf	W_λ, mÅ		log ε	
			25 Mon	HR 7389	25 Mon	HR 7389
CI						
5052.17	7.68	−1.65			8.70	8.75
		−1.49[15]			8.65	8.60
		−1.30[16]			8.50	8.30
NI						
8683.40	10.33	+0.09	47	20	8.14	7.74
OI						
6155.98	10.74	−0.66			8.75	8.80
6156.77	10.74	−0.48			8.75	8.85
6158.18	10.74	−0.31			8.80	8.85
NaI						
6154.23	2.10	−1.56			6.55	6.50
SiI						
6125.02	5.61	−0.93	38	35	7.40	7.29
6145.02	5.62	−0.82	49	47	7.45	7.37
6155.13	5.62	−0.40			7.40	7.40
6155.69	5.62	−1.69			7.35	7.65
6237.32	5.61	−0.53		64		7.32
6244.13	5.62	−0.69		56		7.36
SiII						
6371.37	8.12	−0.00	137	109	7.94	7.88
CaI						
6122.22	1.89	−0.39	200	170	7.14	6.85
6166.44	2.52	−1.16	77		6.86	
6439.08	2.53	+0.39	212	173	7.02	6.58
6471.66	2.53	−0.65	120	86	6.86	6.44
6499.65	2.52	−0.72	121	96	6.93	6.63
FeI						
5044.21	2.85	−2.04	67	61	7.77	7.64
5049.82	2.28	−1.36	159	138	7.82	7.65
5051.28	4.22	−1.19			7.70	7.70
5051.63	0.92	−2.80			7.60	7.70
6056.00	4.73	−0.46	82	77	7.91	7.86
6065.48	2.61	−1.53	133	108	7.79	7.53
6096.66	3.98	−1.93		30		8.00
6127.91	4.14	−1.40	44	34	7.89	7.69
6136.62	2.45	−1.40			7.65	7.70

Table 2. (Contd.)

Line λ, Å	χ, eV	log gf	W_λ, mÅ		log ε	
			25 Mon	HR 7389	25 Mon	HR 7389
6136.99	2.20	−2.95			7.65	7.70
6137.27	4.58	−1.94			7.65	7.60
6141.71	3.60	−1.46			7.70	7.75
6147.83	4.08	−1.67			7.65	7.75
6151.62	2.18	−3.30		34		7.89
6157.73	4.08	−1.26			7.70	7.85
6230.72	2.56	−1.28	148		7.68	
6232.64	3.65	−1.22	72		7.62	
6252.56	2.40	−1.69	128	130	7.69	7.80
6265.13	2.18	−2.55	76	86	7.74	7.84
6380.74	4.19	−1.38	45		7.91	
6393.60	2.43	−1.43	141	137	7.68	7.61
6411.65	3.65	−0.60	132	123	7.67	7.73
6419.95	4.73	−0.24	91	94	7.79	7.86
6421.35	2.28	−2.03	114	109	7.73	7.71
6430.85	2.18	−2.00	113	116	7.71	7.61
6810.26	4.61	−0.99	36	37	7.76	7.71
7780.55	4.47	−0.25	119		7.86	
FeII						
6147.74	3.89	−2.72			7.65	7.75
6149.26	3.89	−2.72			7.60	7.75
NiI						
6108.11	1.68	−2.45	42	57	6.47	6.56
6111.07	4.09	−0.87	30	33	6.73	6.69
7788.94	1.95	−2.42	67		6.85	
7797.59	3.90	−0.26	72		6.44	
BaII						
6141.73	0.70	−0.08			2.50	2.40

Table 3. Atmospheric parameters for 25 Mon and HR 7389

Star	$T_{\rm eff}$, K	log g	ξ_t, km/s	Reference
25 Mon	6700 ± 250	3.24 ± 0.37	3.1	This work
	6360	3.10	2.4	[3]
HR 7389	6630 ± 100	3.71 ± 0.15	2.6	This work
	6338	3.73	1.5	[8]

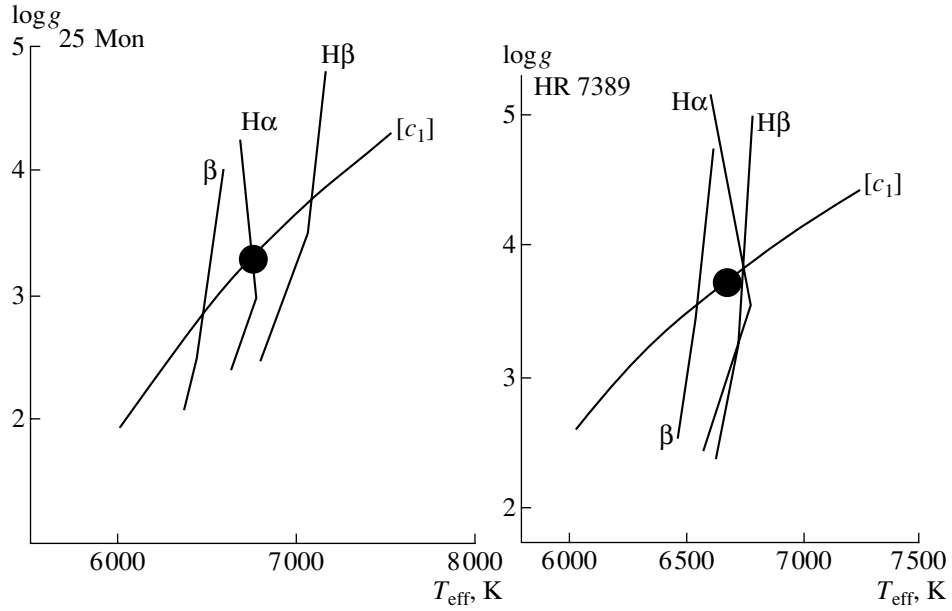

Fig. 1. Diagram for determining the temperatures $T_{\rm eff}$ and gravitational accelerations $\log g$ for 25 Mon and HR 7389. The points correspond to the adopted models.

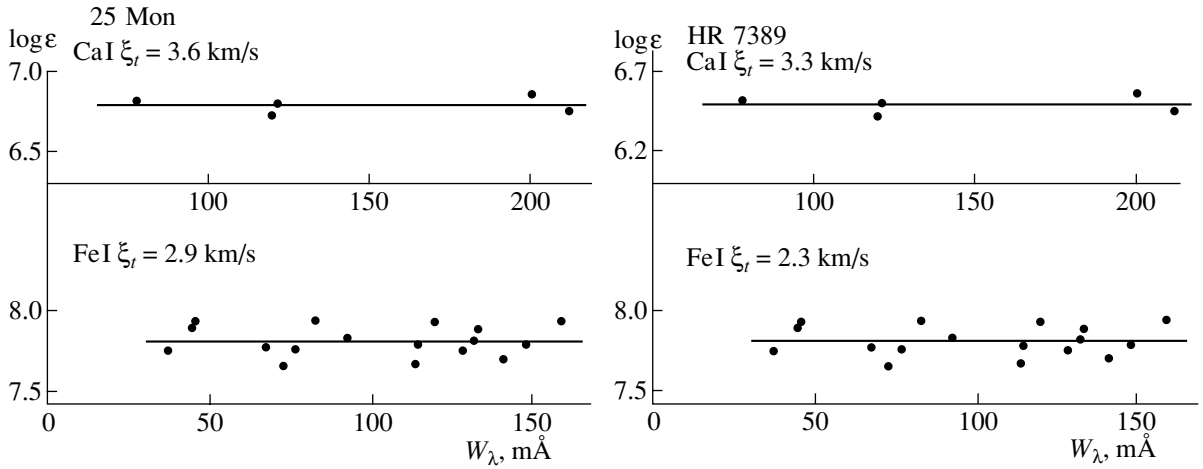

Fig. 2. Abundances $\log \varepsilon$ derived from CaI and FeI as a function of the equivalent widths W_λ for $\xi_t = 3.6$ km/s and $\xi_t = 2.9$ km/s for 25 Mon and $\xi_t = 3.3$ km/s and $\xi_t = 2.3$ km/s for HR 7389.

The **microturbulence velocity** ξ_t is an important parameter that must be known when analyzing elemental abundances in stellar atmospheres. It is especially important to determine ξ_t as reliably as possible if strong lines are used to estimate $\log \varepsilon$, since these are especially sensitive to microturbulence; otherwise, it is possible to derive erroneous values of $\log \varepsilon$. The quantity ξ_t is determined from the condition that the abundance of an element $\log \varepsilon$ calculated based on lines of a certain ion does not display any systematic variations with increasing equivalent width W_λ. This requires that the lines be sufficiently numerous and that their equivalent widths cover a sufficiently large interval. We used FeI lines to calculate ξ_t for both stars, as well as CaI lines, which are not as numerous as the FeI lines but whose equivalent widths can be determined with confidence from the observations. Figure 2 shows that there is no correlation with equivalent width for 25 Mon for the FeI lines when $\xi_t = 2.9$ km/s, and for the CaI lines when $\xi_t = 3.6$ km/s; the corresponding values for HR 7389 are $\xi_t = 2.3$ km/s for the FeI lines and $\xi_t = 3.3$ km/s for the CaI lines. Assigning weights in accordance with the numbers of FeI and CaI lines used yielded the values $\xi_t = 3.1$ km/s for 25 Mon and $\xi_t = 2.6$ km/s

Table 4. Elemental abundance in the atmosphere of 25 Mon and HR 7389

	25 Mon			HR 7389		
Element	$\log\varepsilon$	σ	$[X]$	$\log\varepsilon$	σ	$[X]$
CI	8.62(1)		+0.23	8.55(1)		+0.16
NI	8.14(1)		+0.31	7.74(1)		−0.09
OI	8.77(3)	0.02	+0.08	8.84(3)	0.02	+0.15
NaI	6.55(1)		+0.25	6.50(1)		+0.20
SiI	7.40(4)	0.04		7.40(6)	0.12	
SiII	7.94(1)			7.88(1)		
Si	7.51(5)		−0.03	7.47(7)		−0.07
CaI	6.96(5)	0.11	+0.62	6.62(4)	0.15	+0.28
FeI	7.73(25)	0.09		7.73(23)	0.11	
FeII	7.62(2)	0.02		7.75(2)	0.00	
Fe	7.72(27)		+0.25	7.73(25)		+0.26
NiI	6.62(4)	0.17	+0.40	6.62(2)	0.06	+0.40
BaII	2.50(1)		+0.32	2.40(1)		+0.22

for HR 7389, which are presented in Table 3. We used these values for our final abundance calculations. Berthet [3] obtained the value $\xi_t = 2.4$ km/s using the FeI lines for 25 Mon using the same method as we did, while Erspamer and North [8] obtained $\xi_t = 1.5$ km/s via synthetic spectra calculations. Table 3 shows that our estimates of ξ_t for both stars are slightly higher than the values of these other authors [3, 8].

5. CHEMICAL COMPOSITION

The elemental abundances $\log\varepsilon(\mathrm{El}) = \log[\mathrm{N(El)/N(H)}] + 12$ (the abundance of hydrogen is $\log\varepsilon(\mathrm{H}) = 12$ on this scale) were estimated using the parameter values $T_{\mathrm{eff}} = 6700$ K, $\log g = 3.24$, $\xi_t = 3.1$ km/s for 25 Mon and $T_{\mathrm{eff}} = 6630$ K, $\log g = 3.71$, $\xi_t = 2.6$ km/s for HR 7389. The calculations assumed LTE. The abundances calculating using individual lines for 25 Mon and HR 7389 are given in the sixth and sevenths columns of Table 2. If no equivalent width is given for a particular line in the fourth and fifth columns, this indicates that $\log\varepsilon(\mathrm{El})$ was derived by fitting a synthetic spectrum. Our synthetic spectrum calculations yielded rotational velocities of $v\sin i = 27$ km/s for 25 Mon and $v\sin i = 28$ km/s for HR 7389, which are 2 km/s higher and 2 km/s lower, respectively, than the corresponding values of [11] presented in Table 1.

The values of $\log\varepsilon$ averaged over the results for various ions are presented in the second (25 Mon) and fifth (HR 7389) columns of Table 4, with the number of lines used in the average indicated in parentheses. The third and sixth columns of this table give the rms deviation from the mean abundances, σ. The fourth and seventh columns give the difference between our abundances estimates and those of Lodders [18] for the Sun, $[X] = \log\varepsilon(\mathrm{El})_* - \log\varepsilon(\mathrm{El})_\odot$, where we have used the mean weighted value $\log\varepsilon(\mathrm{El})$ for the stars if an element was observed in various ionization states. We will now consider our results for each element separately, comparing our results with those obtained in other studies of 25 Mon and HR 7389. Note that there are no previously published nitrogen abundances for these stars.

Carbon. We observed one line of this element, CI λ5052.17, which is blended with FeI λ5051.63 line in the spectra of 25 Mon and HR 7389. Accordingly, we derived the carbon abundance using a calculated synthetic spectrum. Since various published oscillator strengths for CI λ5052.17 differ strongly (Table 2), we calculated carbon abundances for each of three values of $\log gf$, which are presented in the sixth and seventh columns of Table 2. The differences between the maximum and minimum abundances $\log\varepsilon(\mathrm{C})$ are 0.20 dex for 25 Mon and 0.45 dex for HR 7389. The mean values $\log\varepsilon(\mathrm{C}) = 8.60$ for 25 Mon and $\log\varepsilon(\mathrm{C}) = 8.52$ for HR 7389 are presented in Table 4. According to Rentzsch-Holm [19], the non-LTE corrections to the carbon abundances of 25 Mon and HR 7389 comprise approximately −0.1 dex, which is smaller than the scatter in the carbon abundances

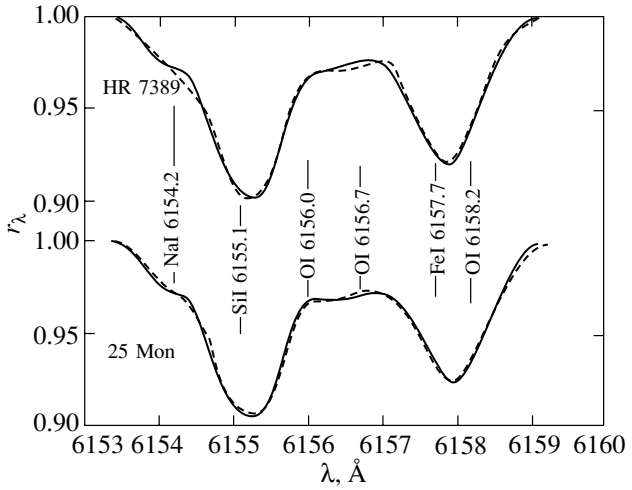

Fig. 3. Comparison of the synthetic (solid) and observed (dashed) spectra near λ 6156.

due to the uncertainty in the oscillator strengths. The abundance $\log\varepsilon(\mathrm{C}) = 9.41$ for 25 Mon was estimated by Berthet [3] based on three lines in the ultraviolet. According to [14], one of these three lines is a blend; however, if we take into account only the two other lines used by Berthet [3], the resulting abundance is still 0.8 dex lower than our own estimate. The carbon abundance of 25 Mon indicated by our estimates is 0.23 dex higher than to the solar value (Table 4, column 4). Our $\log\varepsilon(\mathrm{C})$ estimate for HR 7389 is 0.16 dex higher than the solar value. Erspamer and North [8] found $\log\varepsilon(\mathrm{C})$ for HR 7389 to be 0.22 dex higher then the solar value.

Nitrogen. We were able to estimate the nitrogen abundances only using the NI λ8683.40 line, which yielded $\log\varepsilon(\mathrm{N}) = 8.14$ for 25 Mon and $\log\varepsilon(\mathrm{N}) = 7.74$ for HR 7389, with the accuracy of these estimates being only modest. Nevertheless, comparing with the solar value (Table 4), we can assert that the nitrogen abundance of 25 Mon is at least not lower than the solar value, while the nitrogen abundance of HR 7389 is consistent with the solar value.

Oxygen. The oxygen abundances derived using three lines and synthetic spectra differ only slightly for each star (Table 2), with the corresponding mean values being $\log\varepsilon(\mathrm{O}) = 8.77$ for 25 Mon and $\log\varepsilon(\mathrm{O}) = 8.84$ for HR 7389 (Table 4). By means of illustration, Fig. 3 compares the observed and synthetic spectra at wavelengths of 6153–6160 Å, which are in fairly good agreement. We can see from Table 4 that the oxygen abundances are only slightly higher than the solar values: by 0.08 dex and 0.15 dex, respectively, for 25 Mon and HR 7389. According to Takeda [20], the non-LTE corrections to the oxygen abundances of both 25 Mon and HR 7389 do not exceed −0.04 dex. Erspamer and North [8] derived a substantially higher oxygen overabundance for HR 7389, equal to 0.65 dex.

Sodium. The sodium abundances for 25 Mon and HR 7389 were calculated using only the NaI λ6154.23 line, which yielded $\log\varepsilon(\mathrm{Na}) = 6.55$ and 6.50, respectively. The sodium abundances of 25 Mon and HR 7389 are 0.25 dex and 0.20 dex higher than the solar value (Table 4). The sodium overabundance derived for HR 7389 by Erspamer and North [8], 0.18 dex, is similar to our own estimate.

Silicon. The silicon abundances of 25 Mon and HR 7389 (Table 2) were calculated using several SiI lines and one SiII line, with this last line yielding a $\log\varepsilon(\mathrm{Si})$ value that was approximately 0.50 dex higher than the mean abundance for all the SiI lines for both stars. The mean weighted abundances $\log\varepsilon(\mathrm{Si})$ for the lines of both neutral and ionized silicon (Table 4) are very close to the solar values: −0.03 dex for 25 Mon and −0.07 dex for HR 7389. Similar results were obtained for HR 7389 by Erspamer and North [8].

Calcium. Our calcium abundance for 25 Mon is rather high ($\log\varepsilon(\mathrm{Ca}) = 6.96$), while that for HR 7389 is somewhat lower ($\log\varepsilon(\mathrm{Ca}) = 6.62$). This yields overabundances relative to the solar value of 0.62 dex for 25 Mon and somewhat lower (0.28 dex) for HR 7389 (Table 4). We can see from Table 2 that the CaI lines we observed in the spectra of both stars have rather high equivalent widths. As we noted above, the abundances derived from strong lines are more subject to uncertainty in the microturbulence velocity. Figure 2 shows that the microturbulence velocities $\xi_t = 3.6$ km/s for 25 Mon and $\xi_t = 3.3$ km/s for HR 7389 derived based on the CaI lines are higher than the final values we adopted for the calculations (Table 3). Recalculation of the calcium abundances using $\xi_t = 3.6$ km/s and $\xi_t = 3.3$ km/s yielded the lower values $\log\varepsilon(\mathrm{Ca}) = 6.79$ for 25 Mon and $\log\varepsilon(\mathrm{Ca}) = 6.42$ for HR 7389. In this case, the corresponding overabundances are 0.45 dex for 25 Mon and 0.08 dex for HR 7389. This suggests that 25 Mon displays a calcium overabundance relative to the solar value, while the calcium abundance of HR 7389 is only slightly higher than or close to the solar value. Erspamer and North [8] obtained a calcium overabundance of 0.14 dex for HR 7389. Based on CaI lines in the violet, Berthet [3] derived a calcium abundance for 25 Mon of $\log\varepsilon(\mathrm{Ca}) = 6.52$.

Iron. Our estimates of the iron abundances for 25 Mon and HR 7389 are $\log\varepsilon(\mathrm{Fe}) = 7.72$ and $\log\varepsilon(\mathrm{Fe}) = 7.73$, respectively, which are approximately 0.24 dex higher than the solar value. Non-LTE

Table 5. Masses, radii, luminosities, and ages of the giants 25 Mon, HR 7389, 20 Peg, and 30 LMi

Parameters	25 Mon	HR 7389	20 Peg	30 LMi
$M/M_\odot$	2.45 ± 0.47	1.87 ± 0.21	2.36 ± 0.30	2.47 ± 0.17
$\log(R/R_\odot)$	0.79 ± 0.15	0.50 ± 0.05	0.73 ± 0.05	0.75 ± 0.06
$\log(L/L_\odot)$	1.85 ± 0.31	1.24 ± 0.12	1.79 ± 0.15	1.88 ± 0.13
t, 10^8 years	5.3 ± 2.0	4.6 ± 2.1	4.9 ± 1.4	4.8 ± 1.0

corrections do not exceed +0.07 dex [19]. According to the data of Berthet [3, Table 2], even if we exclude blended lines [14], the iron abundance of 25 Mon is $\log\varepsilon(\mathrm{Fe}) = 8.05$, which exceeds our estimate by approximately 0.30 dex. Erspamer and North [8] obtained a nearly solar iron abundance for HR 7389, differing from the solar value by only +0.02 dex.

Nickel. We estimated the nickel abundances of 25 Mon and HR 7389 to be the same, $\log\varepsilon(\mathrm{Ni}) = 6.62$, which is 0.40 dex higher than the solar value. Berthet [3] derived a higher value for 25 Mon ($\log\varepsilon(\mathrm{Ni}) = 6.79$). Erspamer and North [8] obtained a $\log\varepsilon(\mathrm{Ni})$ value for HR 7389 that was only 0.02 dex higher than the solar, as was the case for iron.

Barium. We estimate the barium abundances of 25 Mon and HR 7389 to be $\log\varepsilon(\mathrm{Ba}) = 2.50$ and $\log\varepsilon(\mathrm{Ba}) = 2.40$, respectively, which exceed the solar value by 0.32 dex for 25 Mon and 0.22 dex for HR 7389. The estimate of Berthet [3] for 25 Mon, $\log\varepsilon(\mathrm{Ba}) = 2.54$, is close to our value. Erspamer and North [8] estimated $\log\varepsilon(\mathrm{Ba})$ for HR 7389 to be 0.33 dex higher than the solar value.

6. COMPARISON WITH EVOLUTIONARY COMPUTATIONS

We used the values of T_{eff} and $\log g$ (Table 3) to estimate the masses of 25 Mon and HR 7389, as well as the stars 20 Peg ($T_{\mathrm{eff}} = 6970$ K, $\log g = 3.35$) and 30 LMi ($T_{\mathrm{eff}} = 7210$ K, $\log g = 3.86$) studied by us earlier [9, 10] via a comparison with the evolutionary computations of Claret [21]. The resulting estimates are collected in Table 5, which also presents the associated errors in the masses due to the errors in T_{eff} and $\log g$. Figure 4 shows the positions of these stars relative to the evolutionary tracks for stars of various mass, according to [22]. Once we have estimated the masses of the stars, we can determine their radii and luminosities using the relations

$$\log(R/R_\odot) = 2.22 + 1/2\log(M/M_\odot) - 1/2\log g,$$
$$\log(L/L_\odot) = -15.045 + 2\log(R/R_\odot) + 4\log T_{\mathrm{eff}}.$$

The resulting R and L values are also presented in Table 5, together with the ages t for 25 Mon, HR 7389, 20 Peg, and 30 LMi, based on the computations of Claret [22].

We can see from Table 5 that the more evolved stars 25 Mon, 20 Peg, and 30 LMi have similar masses, radii, and luminosities, which are higher than the corresponding values for the less evolved star HR 7389.

7. DISCUSSION

The fourth column of Table 4 presents a comparison of the abundances $[X] = \log\varepsilon(\mathrm{El})_* - \log\varepsilon(\mathrm{El})_\odot$ in the atmospheres of 25 Mon and HR 7389 according to our estimates and the solar abundances of Lodders [18].

First and foremost, the most reliably determined abundance value—that of iron—is similar for the two stars and 0.25–0.26 dex higher than the solar value. The differences between the $\log\varepsilon(\mathrm{Fe})$ values for the

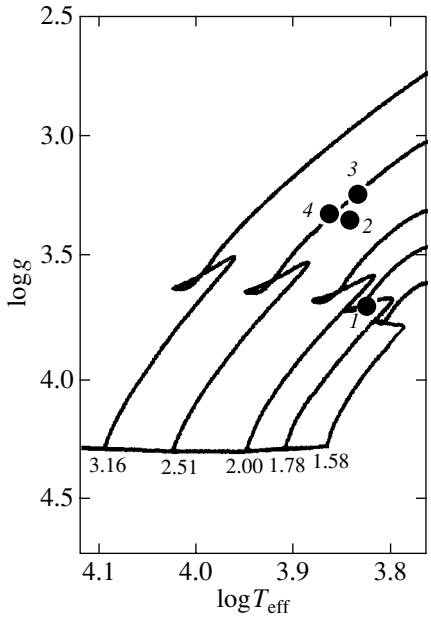

Fig. 4. Positions of the stars (*1*) HR 7389, (*2*) 20 Peg, (*3*) 25 Mon, and (*4*) 30 LMi according to their T_{eff} and $\log g$ values relative to the evolutionary tracks of Claret [22].

giants 20 Peg [9] and 30 LMi [10] previously studied by us and the solar iron abundance are somewhat lower—+0.16 dex and +0.04 dex, respectively.

The carbon abundance exceeds the solar value by a similar amount: +0.23 dex for 25 Mon and +0.16 dex for HR 7389. Recall that the $\log\varepsilon(C)$ values for 20 Peg and 30 LMi likewise differ from the solar value by a comparable amount: by 0.21 dex and 0.19 dex, respectively.

As we noted above, our estimates of the nitrogen abundances of both 25 Mon and HR 7389 were not fully trustworthy; nevertheless, we can conclude that the $\log\varepsilon(N)$ value for 25 Mon is 0.31 dex higher than the solar value, while and this abundance for HR 7389 is close to the solar value (−0.09 dex). A similar result for the nitrogen abundance is observed for 20 Peg (an excess of 0.37 dex), while a nearly solar abundance is observed for 30 LMi (−0.02 dex). Note that no previous estimates of the nitrogen abundances of stars of this type are available.

The oxygen abundances $\log\varepsilon(O)$ of 25 Mon and HR 7389 are 0.08 dex and 0.15 dex higher than the solar value, respectively; we obtained similar results for 20 Peg (+0.14 dex) and 30 LMi (+0.07 dex).

According to our estimates, the sodium abundance of both stars exceed the solar value, by 0.25 dex (25 Mon) and 0.20 dex (HR 7389), while this difference is only +0.07 dex for 20 Peg, and only −0.04 dex for 30 LMi. Note that the accuracy of the estimates is lower for 25 Mon and HR 7389, since these estimate were obtained using only one line.

The silicon abundances of 25 Mon (−0.03 dex) and HR 7389 (−0.07 dex) are close to solar, as is also true of 30 LMi (+0.03 dex), while 20 Peg displays a $\log\varepsilon(Si)$ overabundance of 0.31 dex.

The calcium abundance of 25 Mon is noteworthy, as it exceeds the solar value, and also the values for the other three stars, by 0.62 dex. The difference is somewhat lower for HR 7389: +0.28 dex. The abundances $\log\varepsilon(Ca)$ for 20 Peg (+0.10 dex) and 30 LMi (+0.04 dex) are closest to the solar value.

A similar situation is observed for the nickel abundance: the differences of $\log\varepsilon(Ni)$ from the solar value are +0.40 dex for 25 Mon and HR 7389, +0.10 dex for 20 Peg, and +0.12 dex for 30 LMi.

The estimated barium overabundances were 0.32 dex for 25 Mon, 0.22 dex for HR 7389, and 0.90 dex for 20 Peg; no barium lines were observed 30 LMi.

As we noted above, three of our studied stars—25 Mon, 20 Peg, and 30 LMi—are known as giants showing signs of metallicity [5] and were studied earlier by Berthet [3, 4]. A comparison of the results of [3, 4] and our own indicates that, many elements display higher abundances in the results of Berthet [3, 4] than in our own estimates. One probable origin for this difference is that the line list used by Berthet [3, 4] includes line blends along with single lines [14]. This is especially important for iron lines of 25 Mon.

Note that, according to our estimates, HR 7389, which is a normal giant [5], did not show the smallest deviations from the elemental abundances found for the giant 25 Mon, which possess signs of metallicity [5].

To see how our results fit in with the results of the study by Erspamer and North [8] of 18 giants with signs of metallicity and 17 normal giants, we plotted 25 Mon, HR 7389, 20 Peg, and 30 LMi on the plot presented in Fig. 10 of [8]. The C, O, Na, Si, Ca, Fe, Ni, and Ba abundances for these four stars are within the ranges found in [8]. Unfortunately, Erspamer and North studied only one star from our program—HR 7389; they found that giants with signs of metallicity display, on average, higher abundances of at least eight elements compared to normal giants: Al, Ca, Ti, Cr, Mn, Fe, Ni, and Ba. Thus, in general, our results are consistent with the results of [8].

8. CONCLUSIONS

The main results of our study of the giant with signs of metallicity 25 Mon [5] and the normal giant HR 7389 [5] are as follows.

We have determined the effective temperatures, gravitational accelerations, and microturbulence velocities $T_{\rm eff} = 6700$ K, $\log g = 3.24$, and $\xi_t = 3.1$ km/s for 25 Mon, and $T_{\rm eff} = 6630$ K, $\log g = 3.71$, and $\xi_t = 2.6$ km/s for HR 7389.

We have determined the abundances of nine elements: C, N, O, Na, Si, Ca, Fe, Ni, and Ba. For both stars, the abundances of all these elements proved to be either slightly higher than or close to the solar values.

Regarding elements C, O, one can suppose that the $\log\varepsilon(C)$ values for both stars only slightly (by 0.23 dex for 25 Mon and 0.16 dex for HR 7389) exceed the solar value, while $\log\varepsilon(O)$ is even closer to the solar value (+0.08 dex for 25 Mon and +0.15 dex for HR 7389). Our nitrogen abundances are relatively uncertain, but indicate that the $\log\varepsilon(N)$ values for 25 Mon and HR 7389 are not lower than the solar value.

The iron abundances for 25 Mon and HR 7389 are enhanced by 0.25 dex and 0.26 dex, respectively. The sodium abundances for both stars (+0.25 dex for 25 Mon, +0.20 dex for HR 7389), calcium abundance for HR 7389 (+0.28 dex), and barium abundance for HR 7389 (+0.22 dex) exceed the solar value by similar amounts; $\log\varepsilon(Ba)$ for 25 Mon exceeds the solar value by 0.32 dex.

The largest observed overabundance is 0.62 dex, for the calcium abundance of 25 Mon.

The overabundance of nickel is the same for both 25 Mon and HR 7389, and equal to 0.40 dex.

The silicon abundances were nearly equal to the solar value: −0.03 dex for 25 Mon and −0.07 dex for HR 7389.

Overall, we did not find any fundamental differences in the atmospheric elemental abundances of 25 Mon and HR 7389.

We used the $T_{\rm eff}$ and $\log g$ values and the evolutionary tracks of [22] to determine the masses, radii, luminosities, and ages of 25 Mon ($M/M_\odot = 2.45$, $\log(R/R_\odot) = 0.79$, $\log(L/L_\odot) = 1.85$, $t = 4.9 \times 10^8$) and HR 7389 ($M/M_\odot = 2.36$, $\log(R/R_\odot) = 0.50$, $\log(L/L_\odot) = 1.24$, $t = 4.6 \times 10^8$), as well as the two stars studied by us earlier in [9, 10] 20 Peg ($M/M_\odot = 2.36$, $\log(R/R_\odot) = 0.73$, $\log(L/L_\odot) = 1.79$, $t = 4.9 \times 10^8$) and 30 LMi ($M/M_\odot = 2.47$, $\log(R/R_\odot) = 0.73$, $\log(L/L_\odot) = 1.88$, $t = 4.8 \times 10^8$). The stars 25 Mon, 20 Peg, and 30 LMi were found to be more evolved than HR 7389.

REFERENCES

1. T. M. Rachkovskaya, Izv. Krymsk. Astrofiz. Obs. **80**, 3 (1988).
2. D. W. Kurtz, Astrophys. J., Suppl. Ser. **32**, 651 (1976).
3. S. Berthet, Astron. Astrophys. **227**, 156 (1990).
4. S. Berthet, Astron. Astrophys. **251**, 171 (1991).
5. B. Hauck, Astron. Astrophys. **155**, 371 (1986).
6. S. Berthet, Astron. Astrophys. **253**, 451 (1992).
7. M. Kunzli and P. North, Astron. Astrophys., Suppl. Ser. **127**, 277 (1998).
8. D. Erspamer and P. North, Astron. Astrophys. **398**, 1121 (2003).
9. T. M. Rachkovskaya, Astron. Zh. **79**, 841 (2002) [Astron. Rep. **46**, 760 (2002)].
10. T. M. Rachkovskaya, Astron. Zh. **80**, 48 (2003) [Astron. Rep. **47**, 865 (2003)].
11. *Bright Star Catalogue,* 5th Revised Ed. Dorrit Hoffleit Department of Astronomy, Yale University, Wayne H. Warren, Jr., ST Systems Corporation National Space Science Data Center, NASA Goddard Space Flight Center, 1991 (elec. version).
12. B. Hauck and M. Mermilliod, Astron. Astrophys., Suppl. Ser. **129**, 431 (1998).
13. T. M. Rachkovskaya, Astron. Zh. **77**, 264 (2000) [Astron. Rep. **44**, 227 (2000)].
14. F. Kupka, N. Piskunov, T. A. Ryabchikova, *et al.*, Astron. Astrophys., Suppl. Ser. **138**, 119 (1999).
15. W. L. Wiese, M. W. Smith, and B. M. Glennon, NSRDS—NBS 4, **1**, 34 (1966).
16. I. F. Bikmaev, T. A. Ryabchikova, H. Bruntt, *et al.*, Astron. Astrophys. **389**, 537 (2002).
17. R. L. Kurucz, CD-ROM No. 13 (Smithsonian Astrophysical Observatory, Cambridge, MA, 1993).
18. K. Lodders, Astrophys. J. **591**, 1220 (2003).
19. I. Rentzsch-Holm, Astron. Astrophys. **312**, 966 (1996).
20. Y. Takeda, Publ. Astron. Soc. Jpn. **49**, 471 (1997).
21. A. Claret, Astron. Astrophys., Suppl. Ser. **109**, 441 (1995).

Translated by D. Gabuzda

Astronomy Reports, Vol. 49, No. 9, 2005, pp. 724–738. Translated from Astronomicheskiĭ Zhurnal, Vol. 82, No. 9, 2005, pp. 814–829.

Shear Viscosity and Oscillations of Neutron Star Crust

A. I. Chugunov and D. G. Yakovlev

Ioffe Physicotechnical Institute, St. Petersburg, Russia

Received November 30, 2004; in final form, February 17, 2005

Abstract—We calculate the electron shear viscosity of dense matter (determined by Coulomb electron collisions) in a wide range of parameters typical for white dwarf cores and neutron star crusts. In the density range from $\sim 10^3$ g/cm^3 to 10^7–10^{10} g/cm^3 we consider the matter composed of widely abundant astrophysical elements, from H to Fe. For higher densities, 10^{10}–10^{14} g/cm^3, we employ the ground-state nuclear composition, taking into account finite sizes of atomic nuclei and the distribution of proton charge over the nucleus. Numerical values of the viscosity are approximated by an analytic expression convenient for applications. Using the approximation of plane-parallel layer, we study frequencies, eigenmodes, and viscous damping times of oscillations of high multipolarity, $l \sim 500$–1000, localized in the outer crust of a neutron star. For instance, at $l \sim 500$ oscillations have frequencies $f \gtrsim 40$ kHz and are localized not deeper than about 300 m from the surface. When the crust temperature decreases from 10^9 K to 10^7 K, the dissipation time of these oscillations (with a few radial nodes) decreases from $\sim$1 year to 10–15 days.

1. INTRODUCTION

The shear viscosity of dense stellar material (with densities $\rho \lesssim 10^{14}$ g/cm^3) is important for a number of astrophysical problems, including the computations of the viscous damping of oscillations of white dwarves and the envelopes of neutron stars. The total shear viscosity can be presented as a sum of various matter components. In the case of the outer crust of a neutron star or the core of a white dwarf, it is determined by electrons and ions: $\eta = \eta_e + \eta_i$; it is necessary to add a contribution due to free neutrons, η_n, in the inner crust of a neutron star. The electrons are strongly degenerate and form an ideal Fermi gas, while the ions are fully or partially ionized and form strongly nonideal Coulomb fluid or Coulomb crystal. Under these conditions, the electrons become the most important carriers of heat, charge (see, for example, [1]), and momentum, and the main process determining kinetic coefficients (thermal conductivity, electrical conductivity, and viscosity) is the scattering of electrons by ions (atomic nuclei).

The shear viscosity of the dense stellar material determined by electron–ion scattering has been considered in a number of papers. For example, the electron viscosity of a strongly nonideal Coulomb fluid was calculated in [2–4] from variational principle. The results of these computations are in good agreement. However, they were carried out without including the quasi-order of ions, which is important near the melting point. Inclusion of this quasi-order in a fluid together with multiple-phonon process of electron scattering in a crystal led to the disappearance of appreciable (by a factor of two to four) jumps in the electrical and thermal conductivities [1].

Previous computations of the viscosity were carried out in the Born approximation. However, the non-Born corrections are important when calculating the electrical and thermal conductivities of matter containing chemical elements with high charge numbers Z (see, for example, [1]). We include these corrections and show that they are equally important for calculations of the viscosity.

When studying oscillations of the envelopes of neutron stars, it is necessary to know the viscosity of matter with the density of $\rho \lesssim 10^{14}$ g/cm^3. When $\rho \sim 10^{13}$ g/cm^3, the dimensions of atomic nuclei become comparable to the distances between them, and it is necessary to take into account the distribution of proton charge within the nuclei. This effect was included in the electrical- and thermal-conductivity computations of [5, 6] by introducing the form factor for the atomic nuclei. No such computations have been carried out for the viscosity.

In the current study, we have performed computations of the shear viscosity taking into account non-Born corrections and the form factor of the nuclei, the quasi-order in a Coulomb fluid, and multiphonon process in a Coulomb crystal. The results are approximated by analytical formulas that are convenient for astrophysical applications.

Various types of oscillation modes can be excited in neutron stars. Generally speaking, these oscillations carry important information about the internal

1063-7729/05/4909-0724$26.00

structure of neutron stars. Specific types of oscillations (such as r modes) can be accompanied by the radiation of gravitational waves. Interest in studies of neutron-star oscillations has been continuously growing. Since neutron stars are relativistic objects, theoretical studies of their oscillations must be carried out in the framework of general relativity. The relativistic theory of oscillations was developed in a series of papers by Thorne and coauthors [7–12]. In particular, the rapid ($\sim$1 s) damping of p-mode oscillations with multipolarity $l = 2$ due to gravitational-wave radiation was demonstrated in [9]. Exact inclusion of general-relativistic effects is labor-intensive, but, in many cases, it is possible to use the relativistic Cowling approximation [13]. A similar analysis of various oscillation modes and mechanisms for their dissipation is carried out in [14]. We also note the recent review of Stergioulas [15], which contains an extensive bibliography. As a rule, oscillations with low values of l have been considered in the literature.

Although neutron stars are in the final stage of stellar evolution, they can be seismically active for many reasons. Possible mechanisms for the generation of oscillations have been widely discussed in the astrophysical literature (see, for example, [14, 15] and references therein). Much attention has recently been paid to r modes—vortex oscillations that can be generated in rapidly rotating neutron stars and are accompanied by powerful gravitational radiation. In addition, oscillations can be excited in neutron stars, for example, during X-ray bursts (nuclear explosions on the surfaces of accreting neutron stars), the bursting activity of magnetars (anomalous X-ray pulsars and soft gamma-ray repeaters; see, for example, [16]), and glitches (sudden changes of spin periods) of ordinary pulsars.

In this paper, we study the damping of oscillations in the context of illustrating the results of viscosity computations. We therefore choose the simplest example—p-mode oscillations that are localized in the outer crust due to a high value of the orbital number $l \gtrsim 500$.

2. SHEAR VISCOSITY OF DENSE STELLAR MATERIAL

2.1. Parameters of Equilibrium Dense Material

The state of strongly degenerate electrons can conveniently be described using their Fermi momentum $p_{\rm F}$ or wave number $k_{\rm F}$:

$$p_{\rm F} \equiv \hbar k_{\rm F} = \hbar \left(3\pi^2 n_{\rm e}\right)^{1/3} = m_{\rm e} c x_{\rm r},$$

where $\hbar$ is Planck's constant, $m_{\rm e}$ and $n_{\rm e}$ are the mass and number density of electrons, $x_{\rm r} \approx 1.009\,(\rho_6 Z/A)^{1/3}$ is the relativistic parameter of the electrons, Ze and A are the charge and atomic number of the ions (nuclei), and ρ_6 is the density in units of 10^6 g/cm^3. The electron degenerating temperature is

$$T_{\rm F} = \left(\epsilon_{\rm F} - m_{\rm e}c^2\right)/k_{\rm B}$$
$$\approx 5.93 \times 10^9 \left(\sqrt{1+x_{\rm r}^2} - 1\right)\ {\rm K},$$

where $k_{\rm B}$ is Boltzmann's constant and

$$\epsilon_{\rm F} \equiv m_{\rm e}^* c^2 = m_{\rm e} c^2 \sqrt{1+x_{\rm r}^2}$$

is the Fermi energy of electrons. In our study, we consider matter with $T \ll T_{\rm F}$ and $T \lesssim 5 \times 10^9$ K (the latter is required in order to avoid dissociation of the atomic nuclei).

Further, we will use the Fermi velocity of the electrons:

$$v_{\rm F} \equiv c\beta_{\rm r} = p_{\rm F}/m_{\rm e}^*.$$

The electrostatic screening of a test charge by the degenerate electrons is described by the Thomas-Fermi wave number $k_{\rm TF}$ (the inverse screening radius):

$$k_{\rm TF}^2 = 4\pi e^2 \frac{\partial n_{\rm e}}{\partial \mu} \approx \frac{\alpha}{\pi\beta_{\rm r}} \left(2k_{\rm F}\right)^2,$$

where $\mu \approx \epsilon_{\rm F}$ is the chemical potential of electrons and $\alpha = e^2/\hbar c \approx 1/137.036$ is the fine-structure constant.

The state of the system of ions is described by the classical Coulomb coupling parameter

$$\Gamma = \frac{Z^2 e^2}{a k_{\rm B} T} \approx \frac{22.75 Z^2}{T_6} \left(\frac{\rho_6}{A}\right)^{1/3},$$

where $a = (3/4\pi n_{\rm i})^{1/3}$ is the radius of the ion sphere; $n_{\rm i} = n_{\rm e}/Z$, the number density of ions; and T_6, the temperature in units of 10^6 K. When $\Gamma \ll 1$, the ions form a nearly ideal Boltzmann gas. If $\Gamma \gtrsim 1$, they form a strongly nonideal Coulomb fluid. Finally, when $\Gamma > \Gamma_{\rm m}$ (corresponding to temperatures $T < T_{\rm m}$), the ions crystallize. The crystallization of a classical system of ions corresponds to $\Gamma_{\rm m} \approx 175$ (see, for example, [17]).

Quantum effects in the system of ions become important when $\Theta \equiv T/T_{\rm p} \ll 1$, where

$$T_{\rm p} = \hbar\omega_{\rm p}/k_{\rm B} \approx 7.832 \times 10^6 (Z/A)\rho_6^{1/2}\ {\rm K}$$

is the ion plasma temperature, $\omega_{\rm p} = \left(4\pi Z^2 e^2 n_{\rm i}/m_{\rm i}\right)^{1/2}$ is the ion plasma frequency, $m_{\rm i} = A m_{\rm u}$ is the mass of an ion, and $m_{\rm u} = 1.6605 \times 10^{-24}$ g is the atomic mass unit.

2.2. General Formalism

In the case of isotropic matter, the viscous-stress tensor has the simple form

$$\sigma'_{\alpha\beta} = \eta\left(\frac{\partial U_\alpha}{\partial x_\beta} + \frac{\partial U_\beta}{\partial x_\alpha} - \frac{2}{3}\delta_{\alpha\beta}\nabla\cdot\mathbf{U}\right) + \zeta\delta_{\alpha\beta}\nabla\cdot\mathbf{U}, \quad (1)$$

where $\mathbf{U}$ is the hydrodynamical velocity of the matter, η is the shear viscosity, and ζ is the bulk viscosity (this last quantity is especially important for the uniform compression and rarefaction of matter).

Generally speaking, crystalline matter is anisotropic, and expression (1) for the viscous-stress tensor may not be formally applicable. However, in dense matter, ions crystallize with the formation of a high-symmetry face or body centered cubic lattice. In this case, the viscous-stress tensor for a monocrystal is determined by three independent coefficients (see, for example, [18]), and can be written in the form (1) with an additional term of the form $\kappa\delta_{\alpha\beta}\partial U_\alpha/\partial x_\alpha$ (the sum over α is not carried out). The quantity $\mathbf{U}$ should be understood as the velocity field for shifts of the ions in their lattice sites. When studying any transport processes on scales exceeding the characteristic monocrystal size, the matter can be considered to be isotropic. As in all the literature concerned with the kinetics of the crystalline matter of white dwarves and neutron stars without magnetic fields, we will restrict our analysis to this case (assuming $\kappa = 0$).

The shear viscosity of the envelopes of neutron stars and the cores of white dwarves is primarily determined by the strongly degenerate electrons. It is convenient to present this viscosity in the form

$$\eta_\mathrm{e} = \frac{n_\mathrm{e} p_\mathrm{F} v_\mathrm{F}}{5\nu_\mathrm{e}},$$

where $\nu_\mathrm{e} = 1/\tau_\mathrm{e}$ is the effective electron collision frequency, which is related to the effective electrons relaxation time τ_e. If the electron scattering is determined by several independent processes, these can be studied separately, and the total collision frequency will be the sum of the partial ones. For the dense matter of white dwarf cores and envelopes of neutron stars,

$$\nu_\mathrm{e} = \nu_\mathrm{ei} + \nu_\mathrm{imp} + \nu_\mathrm{ee},$$

where ν_ei, ν_imp, and ν_ee correspond to electron scattering by ions, impurity atoms, and electrons, respectively. The dominant process is electron–ion scattering, to which the current paper is dedicated. Electron–ion scattering also determines the thermal and electrical conductivities of dense matter (see, for example, [1]). With small variations, the formalism proposed by Potekhin *et al.* [1] is also applicable for computations of the viscosity.

In crystalline matter, the electron–ion interaction can adequately be described in terms of the emission and absorption of phonons [19]. This description can be realized using an ion dynamical structure factor [2].

The frequency of electron–ion collisions (ei scatterings) can be written as

$$\nu_\mathrm{ei} = 12\pi\frac{Z^2 e^2 \Lambda_\mathrm{ei} n_\mathrm{i}}{p_\mathrm{F}^2 v_\mathrm{F}} = \frac{4Z\epsilon_\mathrm{F}}{\pi\hbar}\alpha^2\Lambda_\mathrm{ei}, \quad (2)$$

where Λ_ei is the effective Coulomb logarithm, which can be calculated using the variational method (see, for example, [19]). When using the simplest trial function in the Born approximation for a strongly nonideal ion plasma ($\Gamma \gtrsim 1$), one obtains

$$\Lambda_\mathrm{ei} = \int_{q_0}^{2k_\mathrm{F}} q^3 u^2(q)\left(1 - \frac{q^2}{4k_\mathrm{F}^2}\right) \times \left[1 - \frac{1}{4}\left(\frac{\hbar q}{m_\mathrm{e}^* c}\right)^2\right] S_\eta(q)\,dq, \quad (3)$$

where q_0 is the minimum momentum transfered in an ei scattering event; $q_0 = 0$ for the liquid phase and $q_0 = q_\mathrm{B}$ in the crystalline phase, where $q_\mathrm{B} = (6\pi n_\mathrm{i})^{1/3}$ is the radius of a sphere of the same volume as the Brillouin zone. The value $q_0 = q_\mathrm{B}$ was intended to select umklapp processes (i.e., those involving variations in the electron momentum $\gtrsim\hbar q_\mathrm{B}$) in an ei scattering event. At temperatures that are not too low, the contribution of such processes to the Coulomb logarithm Λ_ei,

$$T \gtrsim T_\mathrm{u} \sim T_\mathrm{p} Z^{1/3}\alpha/3\beta_\mathrm{r},$$

is much higher than the contribution of normal processes occurring when $q < q_\mathrm{B}$ (see, for example, [20]). However, at low temperatures ($T \lesssim T_\mathrm{u}$), umklapp processes are "frozen" and the viscosity is determined by normal processes. We will neglect this effect below, restricting our consideration to temperatures $T \gtrsim T_\mathrm{u}$.

The function $u(q)$ in (3) describes the Coulomb interaction between an electron and an atomic nucleus, as discussed in Section 2.3. The factor in square brackets describes the kinematic effect of the backward scattering of the relativistic electrons (see, for example, [21]); $S_\eta(q)$ is an effective static structure factor that takes into account ion correlations. This factor coincides with the effective structure factor determining the electrical resistivity of the dense matter, which was computed and approximated in [22]. Note that the structure factor of a strongly nonideal Coulomb fluid is known only in the classical limit ($\Theta \gg 1$). We also define a *simplified* structure factor, based on the following approximations:

• Neglecting quasi-ordering in ion positions in the Coulomb fluid (see, for example, [1]).

• Single-phonon approximation for the inelastic structure factor of the Coulomb crystal (see, for example, [20]).

We will call the viscosity calculated using the simplified structure factor the *simplified* viscosity. Note that previous computations of the shear viscosity by Flower and Itoh [2, 3] and Nandkumar and Pethick [4] were carried out for a Coulomb fluid using the simplified structure factor.

To take into account corrections to the Born approximation, we also multiply the integrand by the ratio of the exact and Born cross sections for Coulomb scattering. This method was proposed in [23] and was used to calculate the transport coefficients by Potekhin *et al.* [1, 24].

The effective frequency of electron scattering by impurities (assuming that the impurity atoms randomly occupy some of the sites of the crystal lattice) is similar to the frequency of scattering by ions [see (2)]:

$$\nu_{\rm imp} = \frac{12\pi e^4}{p_{\rm F}^2 v_{\rm F}} \sum_{\rm imp} \left(Z - Z_{\rm imp}\right)^2 n_{\rm imp}\Lambda_{\rm imp},$$

where $Z_{\rm imp}$ is the charge number of the impurity ion and the Coulomb logarithm $\Lambda_{\rm imp}$ is calculated using (3), but assuming the impurity atoms are only weakly correlated (corresponding to the structure factor $S_{\rm imp} \equiv 1$, while the screening of the impurities is taken into account in the factor $u(q)$). In the simplest model with Debye screening (with a screening radius of $q_{\rm Simp}^{-1}$),

$$\Lambda_{\rm imp} = \frac{1}{2}\left(1 + 3\beta_{\rm r}^2\xi^2 + 2\xi + 2\xi\beta_{\rm r}^2\right) \times \ln\left(\frac{1+\xi}{\xi}\right) - \frac{3}{2}\beta_{\rm r}^2\xi - \frac{1}{4}\beta_{\rm r}^2 - 1,$$

where $\xi = q_{\rm Simp}/(2k_{\rm F})$ and $q_{\rm Simp}^2 = k_{\rm TF}^2 + k_{\rm imp}^2$. Here, $k_{\rm imp}$ is the wave number for the Debye screening of the test charge by impurities (the inverse correlation length of the impurities). This weakly influences the result ($k_{\rm TF} \gg k_{\rm imp}$), and can be estimated as $k_{\rm imp} = (4\pi n_{\rm imp}/3)^{1/3}$, where $n_{\rm imp}$ is the number density of the impurities. Scattering on impurities is important at low temperatures, when scattering on the crystal lattice is suppressed by quantum effects.

The expression for the frequency of electron-electron collisions $\nu_{\rm ee}$ was obtained by Flowers and Itoh [2]. Their result can be written in the form

$$\nu_{\rm ee} = \frac{5\pi^2\alpha^2 k_{\rm B}^2 T^2}{2m_{\rm e}^* c^2\hbar}\left(\frac{k_{\rm F}}{k_{\rm TF}}\right)\left(1 + \frac{6}{5x_{\rm r}^2} + \frac{2}{5x_{\rm r}^4}\right) \quad (4)$$
$$\approx 4.473\times 10^{11}\left(\frac{k_{\rm F}}{k_{\rm TF}}\right)\left(\frac{n_0}{n_{\rm e}}\right)^{1/3} T_8^2\ {\rm s}^{-1},$$

where the latter expression is presented for an ultrarelativistic electron gas ($x_{\rm r} \gg 1$), $n_0 \approx 0.16$ fermi^{-3} is the number density of nucleons in the atomic nuclei, and T_8 is the temperature in units of 10^8 K.

2.3. The Form Factor of the Atomic Nuclei

The function $u(q)$ describing the Coulomb interaction between an electron and an ion in (3) has the form

$$u(q) = \frac{F(q)}{q^2|\varepsilon(q)|},$$

where $\varepsilon(q)$ is the static longitudinal dielectric function of the degenerate electron gas [25], which describes the electronic screening of the ion field. Here,

$$F(q) \equiv \frac{1}{Z}\int en_{\rm p}(\mathbf{r})\exp(i\mathbf{r}\cdot\mathbf{q})dV \quad (5)$$
$$= \frac{4\pi e}{Z}\int_0^{r_{\rm p}} \frac{n_{\rm p}(r)\sin(qr)}{q} r dr$$

is the nuclear form factor characterizing the distribution of proton charge within the atomic nucleus. The integration in (5) is carried out over the atomic nucleus, $n_{\rm p}(\mathbf{r})$ is the local number density of protons, and $r_{\rm p}$ is the radius of the proton core. In white dwarves and the outer envelopes of neutrons stars ($\rho \lesssim 10^{11}$ g/cm^3), the atomic nuclei can be taken to be pointlike, $F(q) \equiv 1$. At densities $\rho \lesssim 10^{13}$ g/cm^3, the proton charge can with good accuracy be taken to be uniformly distributed throughout the nucleus. In this case, it is a good approximation to write the form factor as

$$F(q) = \frac{3}{(qr_{\rm p})^3}\left[\sin(qr_{\rm p}) - qr_{\rm p}\cos(qr_{\rm p})\right], \quad (6)$$

where $r_{\rm p}$ is the radius of the proton core in the atomic nucleus. When $\rho \gtrsim 10^{13}$ g/cm^3, the proton-density profile differs strongly from a step function, and the form factor (6) becomes unacceptable. In this case, we determined the nuclear form factor using the model of the ground-state matter with smoothed dependences of the parameters on the density of the matter [26].

2.4. Analytical Approximation for the Viscosity

We have obtained an analytical approximation for the Coulomb logarithm of *ei* scattering using the method of *the effective electron–ion scattering potential* proposed in [1] for the electrical and thermal conductivities. The properties of matter with the density of $\rho \lesssim 10^{10}$ g/cm^3 were studied in [1], where

the form factor of the atomic nuclei was taken to be unity. Later, Gnedin *et al.* [27] extended this method to higher densities. As we noted above, the effective structure factors for the viscosity and electrical conductivity coincide. This simplifies generalization of the effective-potential method for the approximation of the shear viscosity. Following [27], we write in place of $u^2(q)S_\eta(q)$ in (3)

$$\left[u^2(q)S_\eta(q)\right]_{\rm eff} = \frac{1}{\left(q^2+q_{\rm S}^2\right)^2} \times \left[1-e^{-s_0q^2}\right] e^{-s_1q^2} G_\eta D. \quad (7)$$

The factor $\left(q^2+q_{\rm S}^2\right)^{-2}$ corresponds to Debye screening of the Coulomb interaction with the effective screening radius $q_{\rm S}^{-1}$; the term in square brackets describes the ion correlations. The functions G_η and D describe ion quantum effects. The factor $\exp\left(-s_1q^2\right)$ added in [27] takes into account the influence of the atomic-nucleus form factor. The numerical values of the shear viscosity obtained based on the exact theory are reproduced for the same parameters as the electrical and thermal conductivities in [27]:

$$s \equiv \left(\frac{q_{\rm S}}{2k_{\rm F}}\right)^2 = (s_{\rm i}+s_{\rm e})e^{-\beta_Z};$$

$$\beta_Z = \pi\alpha Z\beta_{\rm r}; \quad s_{\rm i} = s_{\rm D}(1+0.06\Gamma)e^{-\sqrt{\Gamma}};$$

$$s_{\rm D} = (2k_{\rm F}r_{\rm D})^{-2};$$

$$w \equiv (2k_{\rm F})^2 s_0 = \frac{u_{-2}}{s_{\rm D}}\left(1+\frac{\beta_Z}{3}\right);$$

$$w_1 \equiv (2k_{\rm F})^2 s_1 = 14.73x_{\rm nuc}^2 \times \left(1+\frac{Z}{13}\sqrt{x_{\rm nuc}}\right)\left(1+\frac{\beta_Z}{3}\right);$$

$$G_\eta = \left(1+0.122\beta_Z^2\right)\left(1+0.0361\frac{Z^{-1/3}}{\Theta^2}\right)^{-1/2};$$

$$D = \exp\left[-0.42u_{-1}\sqrt{\frac{x_{\rm r}}{AZ}}\exp(-9.1\Theta)\right],$$

where $s_{\rm e} \equiv k_{\rm TF}^2/(2k_{\rm F})^2 = \alpha/\pi\beta_{\rm r}$ is the electron-screening parameter, $r_{\rm D} = a/\sqrt{3\Gamma}$ is the ionic Debye radius, $x_{\rm nuc}$ is the ratio of the mean-square radius of the distribution of the protons in the atomic nucleus and the radius of the ion sphere, and $u_{-1} \approx 2.8$ and $u_{-2} \approx 13$ are the parameters of the phonon spectrum in the Coulomb crystal. Note that the function G_η coincides with the function G_σ from [27].

After integrating in (3) with the effective potential (7), we obtain

$$\Lambda = \left[\Lambda_0(s, w+w_1) - \Lambda_0(s,w_1)\right] G_\eta D,$$

where the functions

$$\Lambda_0(s,w) = \Lambda_1(s,w) - \left(1+\beta_{\rm r}^2\right)\Lambda_2(s,w) + \beta_{\rm r}^2\Lambda_3(s,w),$$

with

$$2\Lambda_1(s,w) = \ln\frac{s+1}{s} + \frac{s}{s+1}\left(1-e^{-w}\right) - (1+sw)e^{sw}\left[E_1(sw) - E_1(sw+w)\right],$$

$$2\Lambda_2(s,w) = \frac{e^{-w}-1+w}{w} - \frac{s^2}{s+1}\left(1-e^{-w}\right) - 2s\ln\frac{s+1}{s} + s(2+sw)e^{sw}\left[E_1(sw) - E_1(sw+w)\right],$$

$$2\Lambda_3(s,w) = 3s^2\ln\frac{1+s}{s} + \frac{1}{2}\frac{2s^3-4s^2-3s+1}{1+s} - \frac{s^3}{(1+s)}e^{-w} + \frac{e^{-w}}{w} + \frac{(2sw-1)\left(1-e^{-w}\right)}{w^2} - s^2(3+sw)e^{sw}\left(E_1(sw) - E_1(sw+w)\right).$$

Here, $E_1(x) \equiv \int_x^\infty y^{-1}e^{-y}dy$ is the exponential integral (see, for example, [28]). The maximum error in the approximation for the viscosity does not exceed 20%.

2.5. Main Properties of the Shear Viscosity

Let us discuss the results of our computations of the shear viscosity without taking into account the freezing out of umklapp processes (Section 2.2). Figure 1 presents the temperature dependence of the shear viscosity for a carbon plasma with density $\rho = 10^4$ g/cm^3. The upper horizontal scale plots the nonideality parameter Γ of the plasma. Since the charge number is fairly low, $Z = 6$, the non-Born corrections are modest, and are not visible on the scale of Fig. 1. All the data presented in the figure except for the dot-dashed curves correspond to the scattering of electrons by ions of single type.

The bold points in the figure show the numerical results. The solid curve is the analytical approximation for the viscosity. The dashed curve shows the viscosity computed using the simplified structure factor (Section 2.2). The large jumps in this "simplified" viscosity at the melting point are clearly visible. These jumps (by a factor of two to four) are present for all chemical elements and all plasma parameters. Modification of the structure factor (Section 2.2) increases the accuracy of the computations in the liquid and solid phases, and makes the viscosity jumps insignificant for all elements. This makes it possible to introduce a single approximation for both phases (Section 2.4).

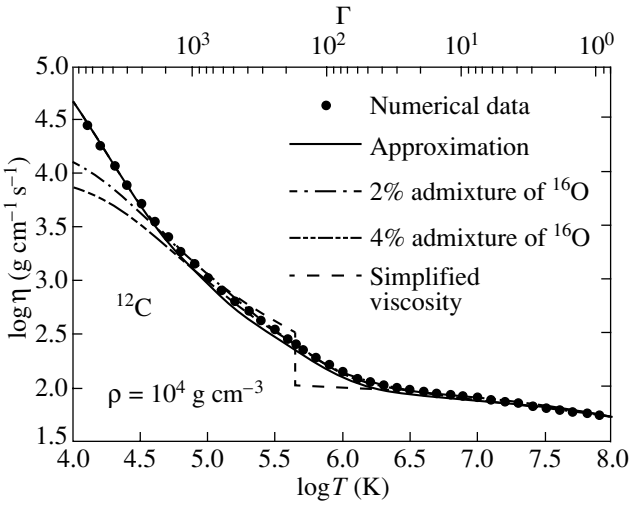

Fig. 1. Temperature dependence of the shear viscosity for a carbon plasma with density $\rho = 10^4$ g/cm^3. The solid curve shows the analytical approximation of the viscosity. The bold points present the results of the numerical calculations. The dashed curve shows the "simplified" viscosity, which demonstrates a jump at the melting point. The dot-dashed curves correspond to matter with ^{16}O impurities with concentration of 2 and 4%.

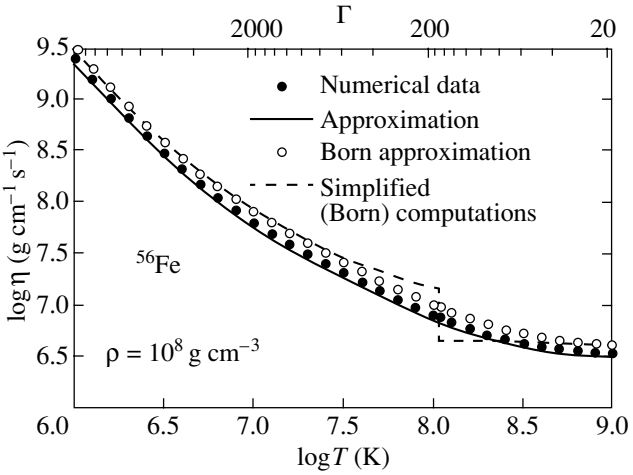

Fig. 2. Temperature dependence of the shear viscosity for an iron plasma with density $\rho = 10^8$ g/cm^3. The solid curve shows the analytical approximation of the viscosity. The bold points present the results of the numerical computations. The hollow circles correspond to the Born approximation. The dashed curve presents the "simplified" viscosity computed in the Born approximation.

However, appreciable viscosity jumps are present at the melting point in our computations for high densities, where zero point oscillations of ions become important. We assume, as did Potekhin *et al.* [1] for the electrical and thermal conductivity, that these jumps are a consequence of using the classical structure factor in the ion fluid under conditions when quantum effects are important (while quantum effects are included in the solid phase). Since the numerical data used to construct the analytical approximation include both the liquid and solid phases, the general analytical approximation shifts the viscosity in the liquid phase to the viscosity in the solid phase. We suppose that, for an ionic fluid at high densities, this approximation is more exact than our original numerical data. It will be possible to verify this in the future, when the ionic structure factors in a fluid are calculated taking into account quantum effects.

The dot-dashed curves in Fig. 1 demonstrate the influence of scattering by charged impurities. We considered oxygen impurities with concentrations of 2 and 4%. The presence of these impurities weakly manifested at high temperatures, but dominates at low temperatures, $T \ll T_p$, when scattering of electrons by phonons in the Coulomb crystal is strongly suppressed by quantum effects.

Figure 2 presents the temperature dependence of the shear viscosity for an iron plasma with density $\rho = 10^8$ g/cm^3. The upper horizontal scale plots the plasma nonideality parameter Γ. The bold points present our numerical results, while the solid curve shows the approximation. The dashed curve depicts the computations using the simplified structure factor neglecting non-Born corrections. As in Fig. 1, the simplified viscosity displays jumps at the melting point, while the new results pass smoothly through this point. The charge number of iron ($Z = 26$) is high enough for the non-Born corrections to be appreciable. To demonstrate this effect, the hollow circles in Fig. 2 show the results of numerical computations of the viscosity in the Born approximation. We can see that the non-Born corrections reduce the viscosity by approximately 20%.

Figure 3 depicts the density dependence of the shear viscosity for hydrogen, helium, carbon, and iron plasmas at a temperature of $T = 10^7$ K. Let us consider the densities typical for the cores of white dwarves and the outer envelopes of neutron stars. The bold points show the numerical results, and the curves are the approximations. The strong dependence of the plasma viscosity on the chemical composition is due to the dependence of the frequency of electron–ion collisions on the charge number Z. In contrast to the thermal conductivity (see, for example, [1]), the influence of electron-electron collisions on the viscosity is insignificant at the considered densities, even for hydrogen.

Figure 4 demonstrates the density dependence of the shear viscosity of the plasma in the range from 10^6 to 10^{15} g/cm^3 for the three temperatures $T = 10^7, 10^8, 10^9$ K. The ground state nuclear composition with smoothed parameters was used. The points

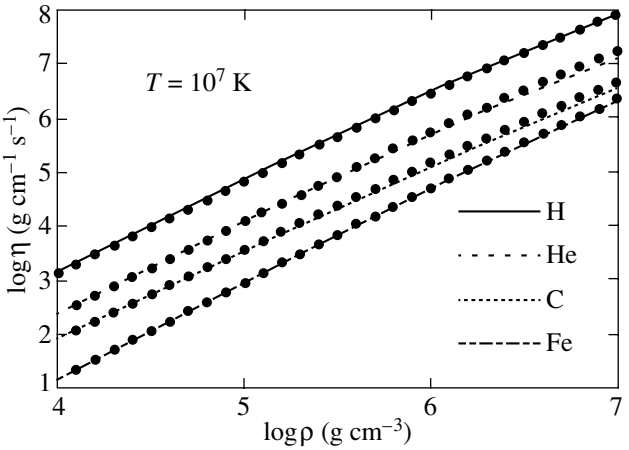

Fig. 3. Shear viscosity of a plasma at temperature $T = 10^7$ K as a function of the density for various chemical compositions (H, He, C, and Fe). The bold points show the numerical results and the curves show the analytic fit.

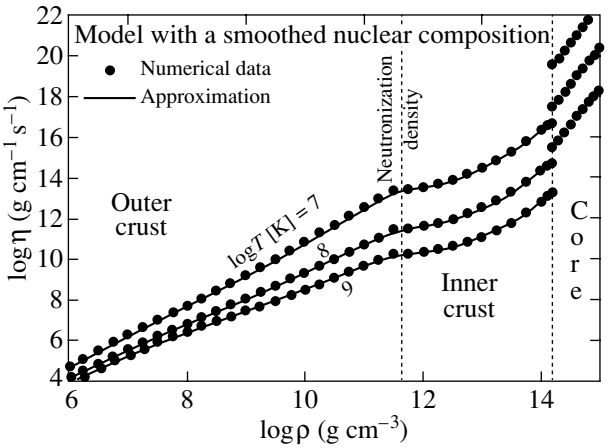

Fig. 4. Shear viscosity of the ground state matter as a function of the density ρ for the three temperatures $T = 10^7, 10^8, 10^9$ K. The solid curves show the analytical approximation of the viscosity. The bold points represent the results of our numerical computations. The vertical dotted lines indicate the neutron drip density and the boundaries of the crust and core of a neutron star ($\rho = 1.5 \times 10^{14}$ g/cm^3 in our computations). The electronic viscosity in the stellar core determined by the scattering of electrons by degenerate protons is presented for comparison.

show the numerical results, and the curves are the approximations. In contrast to the thermal conductivity [1], the shear viscosity decreases strongly with growing temperature. Note that the ratio ρ/η grows with increasing density in the outer crust of a neutron star. These results are important when computing the damping of oscillations in the crust of a neutron star (see Section 3.3).

For illustrative purposes, the plot is continued beyond the crust into the stellar core (densities $\rho \geq 1.5 \times 10^{14}$ g/cm^3). In the core, we used the equation of state of the matter presented in [29]. It is assumed that the core material consists of neutrons, protons, and electrons and is not superfluid. The electronic viscosity in the core of such a star is primarily determined by the scattering of electrons by the degenerate protons. The corresponding collision frequency is obtained analogously to the rate of electron-electron collisions [see (4)], and is equal to

$$\nu_{\rm ep} = \pi^2 \alpha^2 \left(\frac{k_{\rm F}}{q_0}\right) \frac{(k_{\rm B}T)^2 m_{\rm p}^{*2}}{\hbar p_{\rm F}^3} c$$

$$\approx 1.434 \times 10^{12} \left(\frac{k_{\rm F}}{q_0}\right) T_8^2 \left(\frac{m_{\rm p}^*}{m_{\rm p}}\right)^2 \frac{n_0}{n_{\rm e}} \ {\rm s}^{-1},$$

where $m_{\rm p} \approx 1.672 \times 10^{-24}$ g is the proton mass and $m_{\rm p}^*$ is its effective mass, which differs from $m_{\rm p}$ due to multiple-frequency effects (it is assumed that $m_{\rm p}^* = 0.7 m_{\rm p}$). The Debye-screening parameter in the stellar core is equal to

$$q_0^2 = 4\pi \sum_j e_j^2 \frac{\partial n_j}{\partial \mu_j},$$

where the sum is taken over all types of charged particles (electrons and protons); e_j, n_j, and μ_j are the charge, number density, and chemical potential of particles of sort j. Due to the strong suppression of scattering by the proton degeneracy, the electronic viscosity in the core grows by approximately a factor of 1000 compared to its value in the crust.

3. P MODES OF OSCILLATIONS OF A NEUTRON STAR CRUST

This section is dedicated to a study of the p modes of the oscillations (i.e., oscillations in which perturbations of the pressure dominate over the buoyant force) with high orbital numbers (multipolarity), $l \gtrsim 500$, localized in the outer crust of a nonrotating neutron star.

3.1. General Formalism

3.1.1. Flat Metric for the Envelope of a Nonrotating Neutron Star

The standard spacetime metric for a nonrotating neutron star [30] can be written as

$$ds^2 = c^2 e^{2\Phi} d\tilde{t}^2 - e^{2\lambda} dr^2 - r^2 d\Omega^2, \qquad (8)$$

where $d\Omega^2 = d\theta^2 + \sin^2\theta d\varphi^2$, $\tilde{t}$ is the time coordinate, r is the radial coordinate, θ and φ are the polar and azimuthal angles, and the functions $\lambda(r)$ and $\Phi(r)$ determine the curvature of spacetime. In the

case of interest to us of the thin envelope, we can neglect variation of the functions $\lambda(r)$ and $\Phi(r)$ on the scale of the crust and use the value at the stellar surface:

$$e^{2\Phi(R)} = e^{-2\lambda(R)} = 1 - \frac{2GM}{c^2 R},$$

where M is the gravitational mass of the neutron star. Neglecting variations in r in the envelope compared to the stellar radius R (in the approximation of a thin envelope layer), we can rewrite (8) in the form

$$ds^2 = c^2\left(1 - \frac{R_\mathrm{G}}{R}\right)d\tilde{t}^2 - \left(1 - \frac{R_\mathrm{G}}{R}\right)^{-1} dr^2 - R^2 d\Omega^2,$$

where $R_\mathrm{G} = 2GM/c^2 \approx 2.953(M/M_\odot)$ km is the gravitational radius. Introduction of the local time t and local depth z, specified by the relations

$$t = \tilde{t}\sqrt{1 - R_\mathrm{G}/R}, \quad z = (R - r)/\sqrt{1 - R_\mathrm{G}/R}, \tag{9}$$

we come to a flat coordinate system that is the same for the entire neutron-star crust:

$$ds^2 = c^2 dt^2 - dz^2 - R^2 d\Omega^2. \tag{10}$$

This metric coincides with the metric of a thin spherical layer in a flat spacetime.

3.1.2. Equilibrium Structure of the Neutron Star Crust

The structure of the neutron star is determined by the equation of hydrostatic equilibrium, including the effects of general relativity (the Tolman-Oppenheimer-Volkov equation; see, for example, [30]). This equation is greatly simplified in the envelope, and can be rewritten in the planar coordinate system (9):

$$c_\mathrm{s}^2 \frac{d\rho_0}{dz} = \frac{dP_0}{dz} = g\rho_0, \tag{11}$$

where P_0 and ρ_0 are the equilibrium pressure and density, $c_\mathrm{s}^2 \equiv \partial P_0/\partial\rho_0$ is the square of the local sound speed, and

$$g = \frac{GM}{R^2\sqrt{1 - R_\mathrm{G}/R}}$$
$$\approx 1.327 \times 10^{14}\frac{M}{M_\odot}\left(\frac{10\,\mathrm{km}}{R}\right)^2 \Big/ \sqrt{1 - R_\mathrm{G}/R}\ \frac{\mathrm{cm}}{\mathrm{s}^2}$$

is the gravitational acceleration.

The computations used the equation of state for a fully degenerate electron gas with electrostatic correction to the pressure. The chemical composition of the matter was determined using a model with a smoothed equilibrium nuclear composition. We also used a polytropic model for the envelope, in which the pressure is determined by the degenerate electrons, which are taken to be relativistic at all densities, and the matter is assumed to consist of ^{56}Fe nuclei.

3.1.3. Oscillation Equation

In the outer envelopes of neutrons stars, the main contribution to the pressure is produced by the degenerate electrons. Therefore, when considering the p modes of the oscillations, we can use a single equation of state to describe the equilibrium configuration of the star and perturbations.

Let us write the Euler equation in a planar metric (10):

$$\frac{\partial \mathbf{U}}{\partial t} + (\mathbf{U}\cdot\nabla)\mathbf{U} = -\frac{\nabla P}{\rho} + \mathbf{g},$$

where P is the pressure of the matter. The continuity equation must also be satisfied:

$$\frac{\partial \rho}{\partial t} + \nabla(\rho\mathbf{U}) = 0.$$

Taking the velocity $\mathbf{U}$ to be small and introducing Euler perturbations of the pressure $\delta P = P - P_0$ and density $\delta\rho = \rho - \rho_0$, we obtain the linearized Euler equation

$$\frac{\partial \mathbf{U}}{\partial t} = \frac{\delta\rho}{\rho_0^2}\nabla P_0 - \frac{1}{\rho_0}\nabla\delta P$$

and the continuity equation

$$\frac{\partial \delta\rho}{\partial t} + \nabla(\rho_0\mathbf{U}) = 0, \tag{12}$$

while the equation of state for the perturbations can be rewritten in the form

$$\delta P = c_\mathrm{s}^2\delta\rho. \tag{13}$$

We will consider irrotational motion and write the velocity in the form $\mathbf{U} = \nabla\phi$, where ϕ is the velocity potential, which is a scalar function of coordinates and time. Formally, the function ϕ is determined with accuracy to within an arbitrary function of time, which we choose so that the Euler equation can be rewritten [using (11) and (13)]

$$\frac{\partial\phi}{\partial t} = -\frac{\delta P}{\rho_0} = -c_\mathrm{s}^2\frac{\delta\rho}{\rho_0}. \tag{14}$$

Differentiating (14) with respect to the local time t and taking into account (12) and (11) yields

$$\frac{\partial^2\phi}{\partial t^2} = c_\mathrm{s}^2\Delta\phi + \mathbf{g}\cdot\nabla\phi, \tag{15}$$

where we have introduced the Laplace operator

$$\Delta \approx \frac{\partial^2}{\partial z^2} + \frac{1}{R^2}\left(\frac{\partial^2}{\partial \theta^2} + \frac{1}{\sin^2\theta}\frac{\partial^2}{\partial \varphi^2}\right).$$

An equation that coincides with (15) was obtained by Lamb [31] for atmospheric oscillations. The variables in (15) can be separated if we write

$$\phi = e^{\imath\omega t} Y_{lm}(\Omega) F(r),$$

where ω is the oscillation frequency, $Y_{lm}(\Omega)$ are spherical harmonic functions (see, for example, [32]), and $F(z)$ is an unknown function of depth that is determined by the equation

$$\frac{d^2F}{dz^2} + \frac{g}{c_s^2}\frac{dF}{dz} + \left(\frac{\omega^2}{c_s^2} - \frac{l(l+1)}{R^2}\right)F = 0. \quad (16)$$

The first boundary condition for this equation,

$$\text{function } F(z) \text{ is bounded as } z \to 0, \quad (17)$$

follows from the requirement that the amplitude of the oscillations at the stellar surface be finite. The second boundary condition is imposed artificially. In the current study, we solved equations that were applicable only in the thin crust of the star. Therefore, the oscillations should become damped with depth. For simplicity, we formally move this boundary condition to infinity along z and will monitor the true region of localization of the oscillations (see Section 3.3). In this case, the boundary condition can be written

$$F(z) \to 0 \text{ as } z \to \infty. \quad (18)$$

Together with the boundary conditions (17) and (18), Eq. (16) specifies the eigenfrequencies and modes of the oscillations. Moreover, the following asymptotics are valid at large and small depths:

$$F(z) \propto \begin{cases} 1 - \omega^2 z/g & z \to 0, \\ \exp\left(-\sqrt{l(l+1)}z/R\right) & z \to \infty. \end{cases} \quad (19)$$

Perturbations of the pressure and density are expressed in terms of the function $\phi(\mathbf{r})$ using relation (14):

$$\delta P = -\imath\omega\rho_0\phi, \quad \delta\rho = \frac{\delta P}{c_s^2} = -\imath\frac{\omega\rho_0}{c_s^2}\phi.$$

Due to the boundary condition (17), variations of the pressure and density, δP and $\delta\rho$, are zero at the stellar surface (since $\rho_0(R) = 0$). We can see from these last expressions that the number of zeros of the velocity potential with depth (k) coincides with the number of nodes of the pressure and density variations. Further, we will call k the *number of radial nodes of the mode*.

The displacement vector for a matter element in the case of oscillations can be written in the form

$$\boldsymbol{\xi} \equiv \int \mathbf{U} dt = -\frac{\imath}{\omega}\nabla\cdot\phi.$$

The z component of this vector is

$$\xi_z = -\frac{\imath}{\omega}Y_{lm}(\theta,\varphi)\frac{dF}{dz},$$

and the magnitude of the horizontal displacement can be estimated as

$$|\xi_h| \approx \frac{l}{\omega R}|F(z)|.$$

The quantities $lF(z)/R$ and dF/dz appear on equal footing in (16). Therefore, horizontal and radial displacements should have the same order of magnitude for the oscillations considered.

Oscillations of a polytropic envelope in a plane-parallel approximation were studied earlier by Goch [33] assuming that the equation of state of the unperturbed matter and the perturbations are described by polytropes with different indices. In the limiting case of equal polytropic indices n, his result can be presented as follows: the mode containing k radial nodes has the eigenfrequency

$$\omega_k^2 = \frac{g}{R}\sqrt{l(l+1)}\left(\frac{2k}{n}+1\right) \quad (20)$$
$$\approx 10^8 g_{14}\left(\frac{10\text{ km}}{R}\right)\sqrt{l(l+1)}\left(\frac{2k}{n}+1\right)\text{ s}^{-2},$$

while the velocity potential is specified by the function

$$F_k(z) = \exp\left(-\sqrt{l(l+1)}\frac{z}{R}\right) \times L_k^{(n-1)}\left(2\sqrt{l(l+1)}\frac{z}{R}\right),$$

where $L_k^{(n-1)}(x)$ is a generalized Laguerre polynomial (see, for example, [28]) and g_{14} is the gravitational acceleration at the stellar surface in units of 10^{14} cm/s^2. Note that the eigenfrequencies agree with the simple estimate $\omega^2 \sim g/a$, where $a \sim R/l$ is the characteristic scale for the localization of the oscillations.

Note that the mode with $k = 0$ does not have any radial nodes. It corresponds to the vanishing Langragian variation of the pressure and density [$\nabla\cdot\mathbf{U} = 0$, see (26)]; its parameters do not depend on the adiabatic index. Adding the condition $\nabla\cdot\mathbf{U} \equiv \Delta\phi = 0$ to (15), it is easy to show that this mode, which is described by the function $F(z) = \exp\left(-\sqrt{l(l+1)}z/R\right)$ and has the frequency

$$\omega_0^2 = \frac{g}{R}\sqrt{l(l+1)} \quad (21)$$
$$\approx 10^8 g_{14}\left(\frac{10\text{ km}}{R}\right)\sqrt{l(l+1)}\text{ s}^{-2},$$

exists for any equation of state. Therefore, the frequency ω_0 will further be used to make the eigenfrequencies of the oscillations dimensionless.

The frequencies ω computed here refer to the coordinate system of the stellar envelope [see (9)] and can easily be transformed to the frequencies $\widetilde{\omega}$ as detected by a distant observer:

$$\widetilde{\omega} = \omega\sqrt{1 - R_G/R}.$$

3.2. Viscous Damping of the Oscillations

In this section, we consider the damping of oscillations with velocity potentials of the form $e^{i\omega t}Y_{lm}(\Omega)F(r)$ in a spherically symmetrical star under the action of shear viscosity. We take the spacetime metric to be flat. This treatment is applicable to the oscillations studied in Section 3.1, since the flat metric (10), which coincides with the metric for a thin spherical layer in a flat spacetime, can be introduced in the region, where oscillations are localized. As a result, it is sufficient to consider the oscillation damping time in a flat metric and transform this time [in accordance with (9)] into the frame of a distant observer.

We define the oscillation damping time τ as

$$\tau = E/|dE/dt|, \qquad (22)$$

where

$$E = \int \varepsilon dV = \int \rho\frac{|U|^2}{2}dV \qquad (23)$$

is the total energy of the oscillations and

$$\varepsilon = \frac{1}{4}\left(\rho_0|U|^2 + \frac{c_s^2}{\rho_0}|\delta\rho|^2\right)$$

is the energy density of the oscillations at a given point averaged over the period (see, for example, [34]). The additional factor of $1/2$ in the expression for ε is required due to the averaging over the oscillation period. The integration is carried out over the entire volume of the star (in practice, over the region where the oscillations are localized). We neglect the perturbation of the gravitational potential. The last equality in (23) is determined by the equality of the mean kinetic and potential energies in the case of small harmonic oscillations. Note that a number of authors have considered the damping time for the oscillation amplitude rather than the damping time for the oscillation energy (22).

When calculating the energy using (23), the angular integration can be carried out analytically:

$$E = \frac{1}{2}\int_0^R \rho\left[\left(F'\right)^2 + \frac{l(l+1)}{r^2}F^2\right]r^2dr.$$

The period-averaged rate of viscous dissipation of the energy is (see, for example, [34])

$$\frac{dE}{dt} = -\frac{1}{4}\int \sigma'_{ik}\left(\frac{\partial U_i^*}{\partial x_k} + \frac{\partial U_k^*}{\partial x_i}\right)dV, \qquad (24)$$

where the viscous-stress tensor $\sigma'_{\alpha\beta}$ is given by (1). As in the computation of the oscillation energy E, the additional factor of $1/2$ is required owing to the averaging over the oscillation period. It is easy to see that the rate of dissipation of energy separates into a sum of terms associated with shear and bulk viscosities. We will only consider the dissipation determined by the shear viscosity. The integration over the angular variables in (24) can be carried out analytically (see the Appendix).

3.3. Discussion of the Numerical Results

As an example, we choose a "canonical" model for a neutron star with a mass of $M = 1.4\,M_\odot$ and a radius of $R = 10$ km. For this model,

$$\omega_0 \approx 1.56\times10^5\left(\frac{l(l+1)}{10^4}\right)^{1/4}\ \mathrm{s}^{-1},$$

and for a distant observer

$$\widetilde{\omega}_0 \approx 0.766\omega_0 \approx 1.19\times10^5\left(\frac{l(l+1)}{10^4}\right)^{1/4}\ \mathrm{s}^{-1}.$$

The thickness of the outer crust of such a star ($\rho < 4\times10^{11}$ g/cm^3 before the neutron drip point) is ≈410 m.

The eigenfrequencies of the oscillations were found via a series of iterative trials, testing for the coincidence of the mode number with the number of radial nodes.

3.3.1. Eigenfrequencies of the Oscillations

The dependence of the eigenfrequencies of the oscillations specified by (16) with the boundary conditions (17) and (18) on l is presented in Figs. 5 and 6. As we indicated above, the frequency of the fundamental mode, which does not have any radial nodes, is determined by (21) for all l.

With decreasing l, the oscillations penetrate deeper regions of the outer crust, where the equation of state is softened due to the relativistic nature of the electron gas and beta captures. This gives rise to a gradual decrease in the dimensionless eigenfrequencies of the oscillations. As in the model with the polytropic equation of state [see (20)], the distance between the squares of the dimensionless eigenfrequencies for a fixed l is nearly constant. The weak approach of the frequencies with growth in the number of radial nodes is due to the penetration of the oscillations to

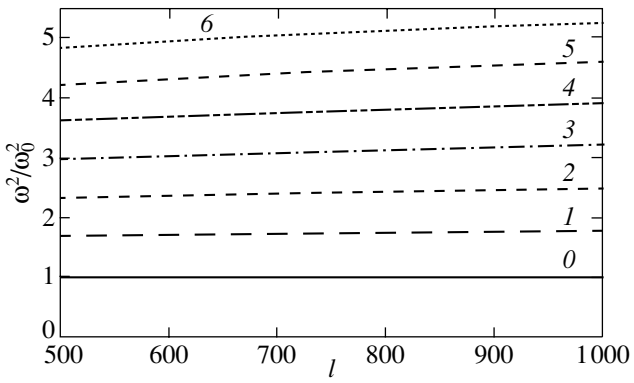

Fig. 5. Eigenfrequencies of oscillations localized in the crust of a "canonical" neutron star. The numerical values are normalized to the frequency ω_0 given by (21). The numbers next to the curves indicate the number of radial nodes.

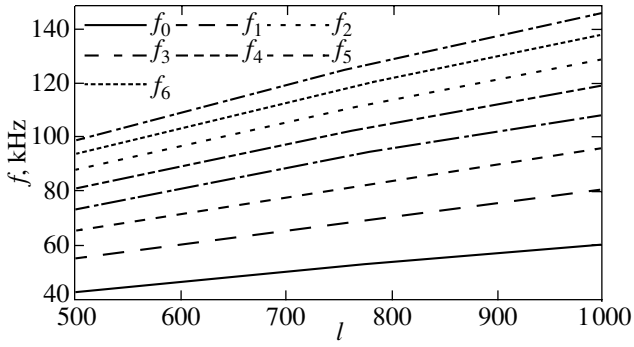

Fig. 6. Frequencies of oscillations localized in the crust of a "canonical" neutron star as detected by a distant observer. The subscript of f denotes the number of radial nodes.

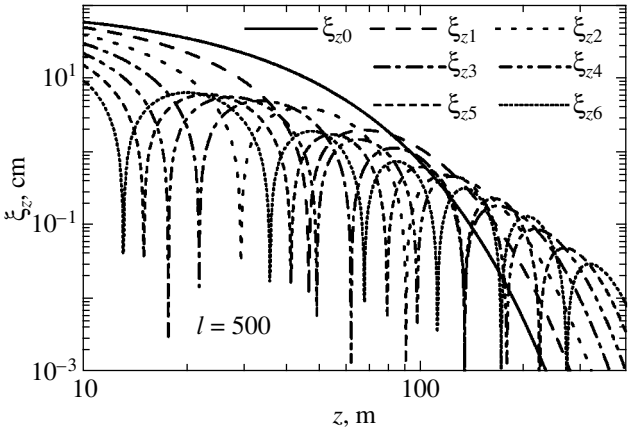

Fig. 7. Root-mean-square (in the angular variables) amplitude of the radial displacements of matter for modes with $l = 500$. The subscript of ξ indicates the number of radial nodes. The root-mean-square amplitude of the radial displacements at the stellar surface has been set equal to 1 m.

deeper layers of the star, where the equation of state is softened. When $l \sim 500$, the main oscillation energy is localized in the region 50 m $\lesssim z \lesssim$ 400 m, where the equation of state of the degenerate, relativistic electron gas is described well by the profile of the sound speed. Therefore, the estimate (20) for the eigenfrequencies obtained in the polytropic model for the envelope with polytropic index $n = 3$ is valid (with accuracy to within several percent).

3.3.2. Modes of the Oscillations

Figure 7 presents profiles of the radial displacements of the matter for modes with $l = 500$. The mean squared amplitude of the radial displacements of the stellar surface was taken to be 1 m. Since we are considering linear oscillations, this quantity is an arbitrary (sufficiently small) constant that normalizes the solution. It is easy to determine from Fig. 7 the magnitude of the radial displacements in the star for any other amplitude of the radial displacements at the surface. With growth of the depth z, there is a decrease in the amplitude of the radial displacements ξ_z, associated with oscillations. At $z \gtrsim 300$ m, the decrease becomes monotonic and gradually emerges onto the exponential asymptotic (19). This makes it reasonable to speak of the localization of the oscillations in the outer crust of the star.

This effect is manifested even more clearly in the energy density of the oscillations. Figure 8 presents the dependence of the total energy density ε averaged over the angular variables as a function of the depth z for oscillations with $l = 500$. The amplitude of the mode is normalized in the same way as in Fig. 7. In our approximation, the energy density of the oscillations is proportional to the square of the normalized amplitude of the radial displacements of the surface. The depicted modes are localized in the outer crust of the neutron star. The energy density of the oscillations varies comparatively weakly within the "critical" depth $z \lesssim 100$–200 m, after which it falls off exponentially. The energy density decreases by more than two orders of magnitude toward the boundary between the outer and inner crust of the star.

As was noted in Section 3.3.1, when $l \sim 500$, the oscillation frequencies are reproduced well by a polytropic model for the crust. The situation is somewhat different for the eigenmodes. Normalization at the stellar surface is not expedient for these modes, since this model poorly reproduces the structure of the star at low depths $z \lesssim 40$ m. Consequently, such normalization leads to large errors at the depths of interest to us, $z \lesssim 100$–200 m, where the main oscillation energy is concentrated. Therefore, we need some kind of special normalization to compare modes. Figure 9

(like Fig. 8) depicts the angle-averaged energy density of the oscillations ε as a function of z. The symbols show the results of the numerical computations, while the curves show profiles in the polytropic model, normalized so as to being the results into agreement in the region, where oscillations are localized. We can see that the polytropic model for the outer crust satisfactorily reproduces the energy density of the oscillations at depths of 60 m $\lesssim z \lesssim$ 500 m for modes with $l \sim 500$.

3.3.3. Damping of the Oscillations

In the further computations, the neutron-star crust was taken to be isothermal. This approximation describes well the intrinsic temperature profile: the temperature is nearly independent of depth due to the high thermal conductivity of the degenerate electron gas. In our computations, the frequency and damping time of the oscillations did not depend on the normalization amplitude (the amplitude of the radial displacements of the surface).

Figures 10, 11, and 12 present the dependence of the damping time τ of the oscillations (for a distant observer) on l for canonical neutron star with crust temperatures of $T = 10^7$, 10^8, and 10^9 K.

The strong temperature dependence of the oscillation damping time is due to the appreciable decrease in the viscosity with increasing temperature (Fig. 4).

The oscillation damping time can be estimated based on the characteristic parameters of the oscillations:

$$\tau \sim \varepsilon/\dot{\varepsilon} \sim \rho U^2 \Big/ \eta \left(\frac{U}{\lambda}\right)^2 \sim \lambda^2 \frac{\rho}{\eta},$$

where $\dot{\varepsilon}$ is the local viscous-dissipation rate and U and λ are the characteristic velocity and scale for variations of this quantity in the region of localization of the oscillations.

Let us consider Fig. 11 in more detail. Oscillations with $l \sim 500$ are localized at $z \lesssim 100$ m (Fig. 8), which corresponds to densities $\rho \lesssim 10^{10}$ g/cm^3. Under these conditions, the ratio ρ/η is $\sim$3 s/cm^2 (Fig. 4) and grows with increasing l (due to the decrease of the density in the region of localization of the oscillations). We present further estimates for modes with $l \sim 500$. The scale for variations in the velocity can be estimated as $\lambda \sim R/l$. Note that this scale decreases for high modes (with a large number of radial nodes), accelerating the damping of the oscillations. For the fundamental mode (without any radial nodes), the damping time (transformed to the frame of a distant observer) can be estimated as

$$\tau \sim 1.2 \times 10^4 (500/l)^2 \text{ s} \approx 120(500/l)^2 \text{ day},$$

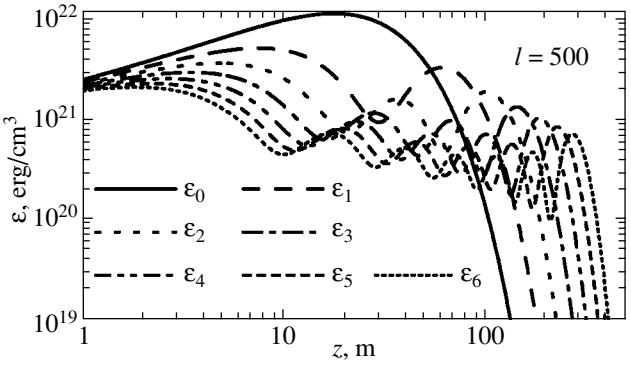

Fig. 8. Angle-averaged total energy density of the oscillations ε for modes with $l = 500$. The subscript of ε indicates the number of radial nodes. The mean squared amplitude of the radial displacements at the stellar surface has been set equal to 1 m.

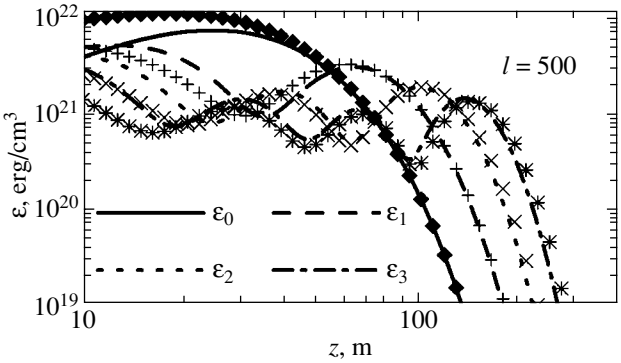

Fig. 9. Angle-averaged total energy density of the oscillations ε for modes with $l = 500$. The subscript indicates the number of radial nodes. The curves show the computed values for the polytropic model, and the symbols show the numerical results for the exact equation of state.

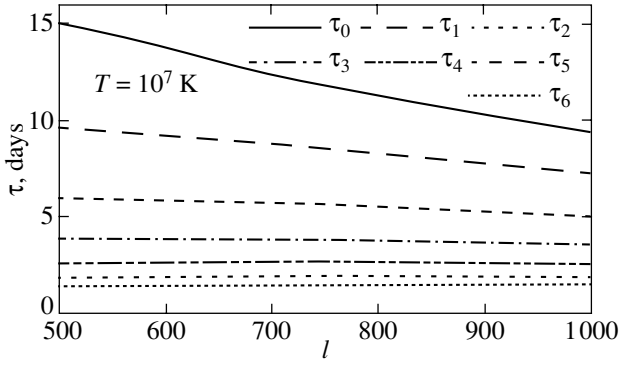

Fig. 10. Damping time of the oscillations for a distant observer as a function of l for a neutron star with a crust temperature of $T = 10^7$ K. The subscript of τ corresponds to the number of radial nodes.

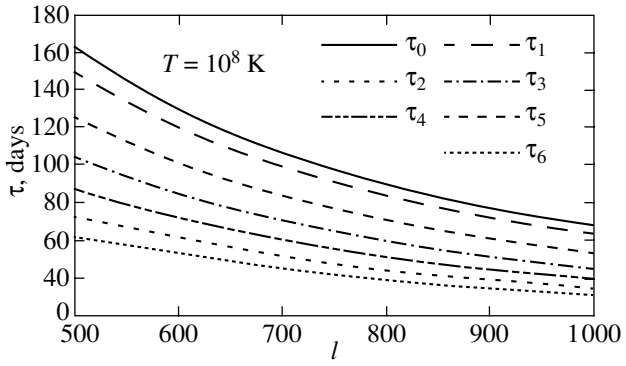

Fig. 11. Same as Fig. 10 but for a crust temperature $T = 10^8$ K.

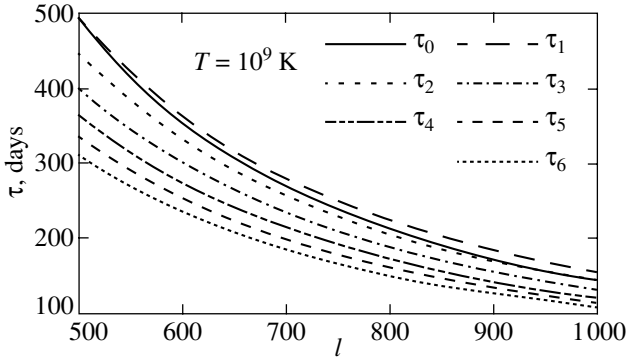

Fig. 12. Same as Fig. 10 but for a crust temperature $T = 10^9$ K.

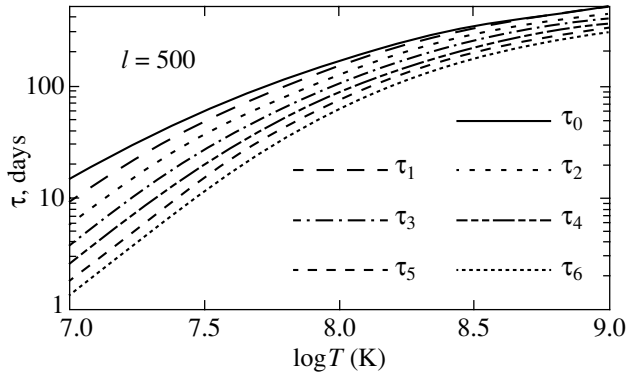

Fig. 13. Damping time of the oscillations as a function of the crust temperature of the neutron star for modes with $l = 500$. The subscript indicates the number of radial nodes. The numerical results are presented in the frame of a distant observer.

in good agreement with the numerical results for $l \sim 500$. The damping time drop weaker than $\propto l^{-2}$ is due to the growth in the ratio ρ/η for higher l, due to the decrease of the density in the region of localization of the oscillations.

For the outer crust of a star with a temperature of $T = 10^9$ K, the ratio ρ/η does not depend very strongly on the density ρ. Therefore, the oscillation damping time well obeys the law $\tau \propto l^{-2}$.

The dependence of the damping time on the crust temperature is presented in Fig. 13, where we have chosen modes with $l = 500$ as an example. The damping time grows by approximately two orders of magnitude as the temperature varies from 10^7 to 10^8 K. When the temperature increases by another order of magnitude, the damping time grows further by a factor of three. This is due to the nonlinear drop in the viscosity with growth in the temperature (Fig. 4).

There exist many other damping mechanisms in addition to the viscous damping of oscillations of a neutron star considered here [14]. For example, damping due to the radiation of gravitational and electromagnetic waves (due to oscillations of the stellar matter with a frozen-in magnetic field) are often studied. In our case, these mechanisms are inefficient due to the high multipolarity considered, $l \gtrsim 500$. When l is high, we expect gravitational or electromagnetic radiation to be generated by an ensemble of closely spaced coherent elementary radiating regions, which radiate in antiphase and cancel each other out. Formally, the weakness of this radiation is manifested by the presence of large factors $(2l+1)!!$ in the denominators of the expressions for the radiation intensities (see, for example, [35, 36]). Analysis shows that the damping of the oscillations we consider here is determined to a substantial extent by the shear viscosity.

A detailed analysis of the evolution of the pulse shapes of some radio pulsars provides evidence that high-multipole oscillations are, indeed, excited in them (see, for example, the recent study [37]). However, reliable observational data on the existence of such oscillations have not yet been obtained.

4. CONCLUSIONS

We have carried out computations of the shear viscosity of the dense stellar matter for a broad range of parameters that are typical for the cores of white dwarves and the envelopes of neutron stars. We considered matter consisting of important astrophysical elements from H to Fe at densities from 10^2–10^4 g/cm^3 to 10^7–10^{10} g/cm^3. At higher densities, 10^{10}–10^{14} g/cm^3, we considered matter with an equilibrium nuclear composition taking into account

the finite size of the atomic nuclei and the distribution of proton charge within the nuclei. Under the conditions described above, the viscosity is determined by the Coulomb scattering of the degenerate electrons by atomic nuclei. We used the modified ion structure factor proposed by Baiko *et al.* [22] and applied by Potekhin *et al.* [1] to compute the thermal and electrical conductivities. In an ionic fluid, this modification approximately takes into account the quasi-ordering in ions positions, which reduces the scattering of electrons by the ions. In the crystalline phase, the new structure factor takes into account multiphonon processes, which are important near the melting temperature $T_{\rm m}$. The new results near the melting point differ appreciably from those of Flowers and Itoh [2, 3] obtained for a Coulomb fluid. The numerical results were approximated by an analytical expression that is convenient for astrophysical applications.

We investigated the frequencies and modes of oscillations localized in the outer crust of a neutron star in a plane–parallel approximation. A polytropic model for the crust can reproduce the eigenfrequencies of the oscillation modes with multipolarity $l \sim 500$ reasonably well. The viscous-damping time for the oscillations was also computed. There is a sharp decrease in the damping time with increasing temperature of the neutron-star crust. For example, for a neutron star with mass $M = 1.4\,M_\odot$, radius $R = 10$ km, and a crust temperature of $T = 10^8$ K, the damping time for the fundamental mode with $l = 500$ is ∼160 day. When the temperature decreases to $T \sim 10^7$ K, the damping time falls to ∼15 day.

In our computations, we used a model of the ground state matter for the neutron star crust with a smoothed dependence of the parameters of the atomic nuclei on the density of the matter. More accurate computations would require the use of an exact model for the equilibrium nuclear composition, in which this composition was varied with depth in the crust in a jumpwise fashion (there arises a series of weak phase transitions of the first kind at specific depths). The presence of these jumps could strengthen the damping of the oscillations. We plan on considering this problem in a future study.

ACKNOWLEDGMENTS

The authors thank D. Gough for reprints of his papers related to oscillations of polytropic stellar envelopes, and W. Dziembowski, who pointed out these works to us. We are also grateful to K.P. Levenfish and A.Yu. Potekhin for useful discussions. This work was supported by a student grant of the Non-Profit Foundation "Dynasty" and the International Center for Fundamental Physics in Moscow, the Russian Foundation for Basic Research (RFFI-IAU grant no. 03-02-06803 and project no. 05-02-16245), and the Program of Support for Leading Scientific Schools of Russia (NSh-1115.2003.2).

APPENDIX

INTEGRATION OF THE LOCAL RATE OF VISCOUS DISSIPATION OF ENERGY OVER THE ANGULAR VARIABLES

When calculating the angular integral in (24), it is convenient to introduce the notation

$$\widetilde{\sigma}_{ik} \equiv \frac{\partial U_i}{\partial x_k} + \frac{\partial U_k}{\partial x_i}.$$

Then, the part of (24) that is associated with the shear viscosity can be written as

$$\frac{dE}{dt} = -\frac{1}{4}\int\limits_0^R \eta r^2 dr \int \left[\widetilde{\sigma}_{ik}\widetilde{\sigma}^*_{ki} - \frac{4}{3}\left|\nabla \mathbf{U}\right|^2\right] d\Omega \qquad (25)$$

$$= -\frac{1}{4}\int\limits_0^R r^2 \eta \left(I_1 - \frac{4}{3} I_2\right) dr,$$

where $d\Omega$ is an element of solid angle,

$$I_1 \equiv \int \widetilde{\sigma}_{ik}\widetilde{\sigma}^*_{ki} d\Omega \quad \text{and} \quad I_2 \equiv \int \left|\nabla \mathbf{U}\right|^2 d\Omega.$$

Here, we have assumed that the unperturbed star is spherically symmetrical, so that the shear viscosity η does not depend on the angular variables. The integrals I_1 and I_2 were computed analytically for velocities of the form $\mathbf{U} = \nabla\phi$, where the velocity potential is $\phi = e^{i\omega t} Y_{lm}(\theta, \varphi) F(r)$.

The integral I_1 can be computed if we write the components of the tensor $\widetilde{\sigma}_{ik}$ in spherical coordinates (see, for example, [34]). After this, the integration over the angles can be carried out analytically (using the properties of the function $Y_{lm}(\theta, \varphi)$; see, for example, [32]). This yields

$$I_1 = 4\Bigg\{ \left(F''\right)^2 + 2\frac{1 + l(l+1)}{r^2}\left(F'\right)^2 - 6\frac{l(l+1)}{r^3}F'F + l(l+1)\frac{1 + l(l+1)}{r^4}F^2 \Bigg\}$$

$$\approx 4\Bigg\{ \left(F''\right)^2 + 2\frac{l(l+1)}{R^2}\left(F'\right)^2 + l(l+1)\frac{l(l+1)}{R^4}F^2 \Bigg\},$$

where the last equality is valid in the plane-parallel layer approximation.

Let us now consider the integral I_2. For this, we write the divergence of the velocity:

$$\nabla\mathbf{U} = \Delta\phi = \left(\frac{1}{r^2}\frac{\partial}{\partial r}r^2\frac{\partial F}{\partial r}Y_{lm}(\theta,\varphi) + F\Delta_\Omega Y_{lm}(\theta,\varphi)\right)e^{\imath\omega t} \quad (26)$$

$$= \left(F'' + \frac{2F'}{r} - \frac{l(l+1)}{r^2}F\right)Y_{lm}(\theta,\varphi)e^{\imath\omega t},$$

where Δ_Ω is the angular part of the Laplacian. The integral I_2 can easily be calculated:

$$I_2 = \left(F'' + \frac{2F'}{r} - \frac{l(l+1)}{r^2}F\right)^2 \approx \left(F'' - \frac{l(l+1)}{R^2}F\right)^2,$$

where this last equality is valid in the plane-parallel layer approximation. As expected, expression (25) does not depend on the azimuthal number m (due to the spherical symmetry of the unperturbed star). It can be shown that it is nonnegative for all allowed values $l = 0, 1, 2, \ldots$.

REFERENCES

1. A. Y. Potekhin, D. A. Baiko, P. Hansel, and D. G. Yakovlev, Astron. Astrophys. **346**, 345 (1999).
2. E. Flowers and N. Itoh, Astrophys. J. **206**, 218 (1976).
3. E. Flowers and N. Itoh, Astrophys. J. **230**, 847 (1979).
4. R. Nandkumar and C. J. Pethick, Mon. Not. R. Astron. Soc. **209**, 511 (1984).
5. N. Itoh, Y. Kohyama, N. Matsumoto, and M. Seki, Astrophys. J. **285**, 758 (1984).
6. N. Itoh, H. Hayashi, and Y. Kohyama, Astrophys. J. **418**, 405 (1993).
7. K. S. Thorne and A. Campolattaro, Astrophys. J. **149**, 591 (1967).
8. R. Price and K. S. Thorne, Astrophys. J. **155**, 163 (1969).
9. K. S. Thorne, Astrophys. J. **158**, 1 (1969).
10. K. S. Thorne, Astrophys. J. **158**, 997 (1969).
11. A. Campolattaro and K. S. Thorne, Astrophys. J. **159**, 847 (1970).
12. J. R. Ipser and K. S. Thorne, Astrophys. J. **181**, 181 (1973).
13. P. N. McDermott, H. M. Van Horn, and J. F. Scholl, Astrophys. J. **268**, 837 (1983).
14. P. N. McDermott, H. M. Van Horn, and C. J. Hansen, Astrophys. J. **325**, 725 (1988).
15. N. Stergioulas, Living Rev. Relativ. **6**, 3 (2003).
16. V. M. Kaspi, *Young Neutron Stars and Their Environments*, Ed. by F. Camilo and B. M. Gaensler (Astron. Soc. Pac., San Francisco, 2004), p. 231.
17. H. DeWitt, W. Slattery, D. Baiko, and D. Yakovlev, Contrib. Plasma Phys. **41**, 251 (2001).
18. L. D. Landau and E. M. Lifshitz, *Theory of Elasticity* (Nauka, Moscow, 1968; Pergamon Press, Oxford, 1986).
19. J. M. Ziman, *Electrons and Phonons* (Clarendon, Oxford, 1960; Inostrannaya Literatura, Moscow, 1962).
20. D. A. Baiko and D. G. Yakovlev, Pis'ma Astron. Zh. **21**, 784 (1995) [Astron. Lett. **21**, 702 (1995)].
21. V. B. Berestetskii, E. M. Lifshitz, and L. P. Pitaevskii, *Quantum Electrodynamics* (Fizmatlit, Moscow, 2001; Pergamon Press, Oxford, 1982).
22. D. A. Baiko, A. D. Kaminker, A. Y. Potekhin, and D. G. Yakovlev, Phys. Rev. Lett. **81**, 5556 (1998).
23. D. G. Yakovlev, Astron. Zh. **64**, 661 (1987) [Sov. Astron. **31**, 347 (1987)].
24. A. Y. Potekhin, G. Chabrier, and D. G. Yakovlev, Astron. Astrophys. **323**, 415 (1997).
25. B. Jancovici, Nuovo Cimento **25**, 428 (1962).
26. A. D. Kaminker, C. J. Pethick, A. Y. Potekhin, *et al.*, Astron. Astrophys. **343**, 1009 (1999).
27. O. Y. Gnedin, D. G. Yakovlev, and A. Y. Potekhin, Mon. Not. R. Astron. Soc. **324**, 725 (2001).
28. M. Abramowitz and I. A. Stegun, *Handbook of Mathematical Functions*, Ed. by M. Abramowitz and I. A. Stegun (Dover, New York, 1971; Nauka, Moscow, 1979).
29. M. Prakash, T. L. Ainsworth, and J. M. Lattimer, Phys. Rev. Lett. **61**, 2518 (1988).
30. S. L. Shapiro and S. A. Teukolsky, *Black Holes, White Dwarves, and Neutron Stars: the Physics of Compact Objects* (Wiley, New York, 1983; Mir, Moscow, 1985), Vols. 1, 2.
31. H. Lamb, Proc. R. Soc. A **84**, 551 (1911).
32. D. A. Varshalovich, A. N. Moskalev, and V. K. Khersonskii, *Quantum Theory of Angular Momentum* (Nauka, Leningrad, 1975; World Sci., Singapore, 1988).
33. D. O. Gough, *Astrophysical Fluid Dynamics*, Ed. by J.-P. Zahn and J. Zinn-Justin (Elsevier, Amsterdam, 1993), p. 399.
34. L. D. Landau and E. M. Lifshitz, *Fluid Mechanics* (Fizmatgiz, Moscow, 2001; Pergamon Press, Oxford, 1987) .
35. E. Balbinski and B. F. Schutz, Mon. Not. R. Astron. Soc. **200**, 43 (1982).
36. P. N. McDermott, M. P. Savedoff, H. M. Van Horn, *et al.*, Astrophys. J. **281**, 746 (1984).
37. J. Clemens and R. Rosen, Astrophys. J. **609**, 340 (2004).

Translated by D. Gabuzda

Astronomy Reports, Vol. 49, No. 9, 2005, pp. 739–746. Translated from Astronomicheskiĭ Zhurnal, Vol. 82, No. 9, 2005, pp. 830–837.

Resonance Scattering in a Line in the Presence of a Weak External Magnetic Field

D. N. Rachkovskiĭ

Crimean Astrophysical Observatory, Nauchnyĭ, Crimea, Ukraine

Received May 5, 2004; in final form, February 17, 2005

Abstract—The theory required to calculate the phase matrix for resonance scattering in the presence of a magnetic field is set out. Interference effects between radiation from individual magnetic sublevels of the atom are taken into account. Errors in the algorithms used to calculate the phase matrix published earlier by other authors are identified. © *2005 Pleiades Publishing, Inc.*

1. INTRODUCTION

Weak magnetic fields of the order of several Gauss can be measured directly—for example, using magnetographs—only with great difficulty. The strength of a weak magnetic field can be estimated using the Hanle effect: the depolarization of atomic resonance radiation by a weak external magnetic field. Limits on the magnetic-field strength can be placed based on the absence of linear polarization in this radiation or deviations of the degree of polarization from the theoretically expected value.

The theory of the Hanle effect has been developed by many authors; we note here only those works that we will reference further below. Stenflo [1, 2], House [3–5], and M. Landi Degl'Innocenti and E. Landi Degl'Innocenti [6] considered the Hanle effect, taking into account only interference effects. In the calculations presented below, we likewise limited our analysis to the influence of interference between radiation from different magnetic sublevels of the atom. In particular, depolarization due to collisions with atoms is not considered.

The theory presented here essentially corresponds to that worked out by Stenflo [1, 2] and House [3–5], although we present a more complete set of formulas. We also derive certain necessary phase factors, without which some of the formulas presented by Stenflo [1] and House [3] for certain spectral lines yield inexact results. In contrast to the approach of Stenflo [1], our algorithm for calculating the phase matrix enables us to calculate this matrix for each frequency within a spectral-line profile, not only separately for the center and wings. We show using a numerical example that the computations obtained using our formulas and those obtained using the formulas presented in the work of M. Landi Degl'Innocenti and E. Landi Degl'Innocenti [6] virtually coincide for the line center.

2. THEORY

Our starting point will be the formalism of Hamilton [7], but assuming the presence of a weak external magnetic field. We will take the quantization axis Z to be in the direction of the external magnetic field **H**. Figure 1 shows the basic coordinate system X, Y, Z and the unit vectors x_f, y_f, and x_s, y_s associated with the incident and scattered radiation, denoted by the vectors **F** and **S**.

The probability that a photon in the direction **F**

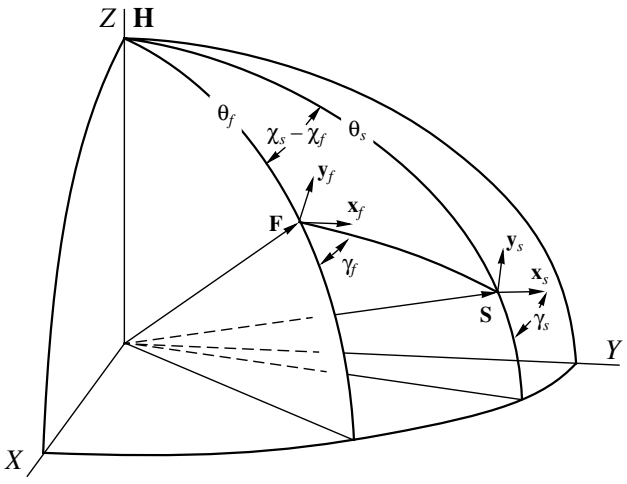

Fig. 1. Angular characteristics of the incident ($\mathbf{F}(\theta_f, \chi_f, \gamma_f)$) and scattered ($\mathbf{S}(\theta_s, \chi_s, \gamma_s)$) radiation. The vectors $\mathbf{x}_f, \mathbf{y}_f$ and $\mathbf{x}_s, \mathbf{y}_s$ lie in planes perpendicular to the vectors **F** and **S**, respectively, and determine the polarization of the radiation.

1063-7729/05/4909-0739$26.00

with polarization corresponding to the vector $\mathbf{e}^{(f)}$ is scattered into the direction $\mathbf{S}$ with the polarization $\mathbf{e}^{(s)}$ is given by the formula

$$W(\mathbf{S},\mathbf{e}^{(s)},\mathbf{F},\mathbf{e}^{(f)}) = \sum_{k,p}\left|\sum_m\left(\mathbf{e}^{(s),*}\mathbf{P}^{(s)}_{m,p}\right)\left(\mathbf{e}^{(f)}\mathbf{P}^{(f)}_{k,m}\right)\right|^2, \quad (1)$$

where the indices k,p denote the magnetic quantum numbers for the initial and final states, respectively, and m denotes the quantum number for the intermediate state.

It follows from (1) that radiation with different pairs of quantum numbers k,p is phase-independent, so that the corresponding Stokes parameters are additive.

We will characterize the radiation using the circular-polarization vectors

$$\mathbf{e}^{(f),(s)}_{\pm} = \mp\frac{\mathbf{x}_{f,s}\mp i\mathbf{y}_{f,s}}{\sqrt{2}}. \quad (2)$$

We represent the instantaneous electric vector of the radiation in terms of circularly and linearly polarized components:

$$\mathbf{E} = E_+\mathbf{e}_+ + E_-\mathbf{e}_- = E_x\mathbf{x} + E_y\mathbf{y}. \quad (3)$$

Here, E_+, E_- and E_x, E_y are certain complex amplitudes of the electric vector. The relation between these quantities can be written

$$\begin{pmatrix}E_+\\E_-\end{pmatrix} = \begin{pmatrix}-1 & -i\\ 1 & -i\end{pmatrix}\begin{pmatrix}E_x\\E_y\end{pmatrix}\Big/\sqrt{2},$$

$$\begin{pmatrix}E_x\\E_y\end{pmatrix} = \begin{pmatrix}-1 & 1\\ i & i\end{pmatrix}\begin{pmatrix}E_+\\E_-\end{pmatrix}\Big/\sqrt{2}.$$

Using (1), we can write for some specific pair of quantum numbers k,p

$$\begin{pmatrix}E_+\\E_-\end{pmatrix}^{(s)} = \sum_m\begin{pmatrix}\left(\mathbf{e}^{(s),*}_+\mathbf{P}^{(s)}_{m,p}\right)\\ \left(\mathbf{e}^{(s),*}_-\mathbf{P}^{(s)}_{m,p}\right)\end{pmatrix} \times\left(\left(\mathbf{e}^{(f)}_+\mathbf{P}^{(f)}_{k,m}\right),\left(\mathbf{e}^{(f)}_-\mathbf{P}^{(f)}_{k,m}\right)\right)\begin{pmatrix}E_+\\E_-\end{pmatrix}^{(f)}. \quad (4)$$

We have for the vectors $\mathbf{P}^{(s)}_{m,p}, \mathbf{P}^{(f)}_{k,m}$

$$\mathbf{P}^{(f)}_{k,m} = \sqrt{g}_{k,m}\mathbf{e}_{m-k}, \quad \mathbf{P}^{(s)}_{m,p} = \sqrt{G}_{m,p}\mathbf{e}_{p-m}. \quad (5)$$

For permitted dipole transitions, the quantities $m-k$ and $p-m$ take on the values $\pm1, 0$.

The coefficients $g_{k,m}$ and $G_{m,p}$ are calculated in accordance with [8]. We present here a table of values of the coefficients $g_{k,m}, G_{m,p}$:

	$J\to J-1$	$J\to J+1$
$m_J\to m_J\pm1$	$\frac{1}{2}(J\mp m_J)(J\mp m_J-1)$	$\frac{1}{2}(J\pm m_J+1)(J\pm m_J+2)$
$m_J\to m_J$	$(J+m_J)(J-m_J)$	$(J+m_J+1)(J-m_J+1)$

	$J\to J$
$M_J\to m_J\pm1$	$\frac{1}{2}(J\mp m_J)(J\pm m_J+1)$
$m_J\to m_J$	m_J^2

Here, J and m_J are the quantum numbers for the level from which the emission or absorption transition is initiated. We denote

$$q_f = m-k, \quad q_s = p-m. \quad (6)$$

Let us find the relation between the vectors $\mathbf{x}_{f,s}, \mathbf{y}_{f,s}$ and $\mathbf{X}$, $\mathbf{Y}$, $\mathbf{Z}$ for the basic coordinate system (Fig. 1):

$$\mathbf{x}_n = (\cos\chi_n\cos\theta_n\cos\gamma_n - \sin\chi_n\sin\gamma_n)\mathbf{X} + (\sin\chi_n\cos\theta_n\cos\gamma_n + \cos\chi_n\sin\gamma_n)\mathbf{Y} - \sin\theta_n\cos\gamma_n\mathbf{Z}, \quad (7)$$

$$\mathbf{y}_n = (-\cos\chi_n\cos\theta_n\sin\gamma_n - \sin\chi_n\cos\gamma_n)\mathbf{X} + (-\sin\chi_n\cos\theta_n\sin\gamma_n + \cos\chi_n\cos\gamma_n)\mathbf{Y} + \sin\theta_n\sin\gamma_n\mathbf{Z}, \qquad n = f, s.$$

Using (2), (5), and (7) for the products $\mathbf{e}_\alpha^{(n)}\mathbf{P}_q^{(n)}$, we can obtain

$$\mathbf{e}_\alpha^{(s),*}\mathbf{P}_{q_s}^{(s)} = \sqrt{G_{q_s}}e^{-i(\alpha\gamma_s+q_s\chi_s)}d_{q_s,\alpha}(\theta_s), \quad (8)$$

$$\mathbf{e}_\alpha^{(f)}\mathbf{P}_{q_f}^{(f)} = \sqrt{g_{q_f}}(-1)^{q_f}e^{i(\alpha\gamma_f-q_f\chi_f)}d_{-q_f,\alpha}(\theta_f),$$
$$\alpha = \pm 1, \qquad q = 0, \pm 1.$$

The dependence of $d_{q,\alpha}(\theta)$ on the angle θ will be omitted below.

We thus have

$$d_{q,\alpha} = \frac{1}{2}(1 + q\alpha\cos\theta) \quad q, \alpha = \pm 1,$$
$$d_{q,\alpha} = \frac{\alpha}{\sqrt{2}}\sin\theta \quad q = 0, \alpha = \pm 1.$$

Substituting (8) into (4) yields

$$\begin{pmatrix} E_+ \\ E_- \end{pmatrix}^{(s)} = \sum_m \sqrt{g_{k,m}G_{m,p}}e^{-i(q_s\chi_s+q_f\chi_f)} \quad (9)$$
$$\times \begin{pmatrix} e^{-i\gamma_s}d_{q_s,+} \\ e^{i\gamma_s}d_{q_s,-} \end{pmatrix}$$
$$\times (-1)^{q_f}(e^{i\gamma_f}d_{-q_f,+}, e^{-i\gamma_f}d_{-q_f,-}) \begin{pmatrix} E_+ \\ E_- \end{pmatrix}^{(f)}.$$

Relation (9) can be written succinctly in the form

$$E_\alpha^{(s)} = w_{\alpha\beta}E_\beta^{(f)},$$

where the indices α, β run over the values ± 1. We have for the elements of the matrix $w_{\alpha,\beta}$

$$w_{\alpha,\beta} = \sum_m \sqrt{g_{k,m}G_{m,p}}e^{-i(q_s\chi_s+q_f\chi_f+\alpha\gamma_s-\beta\gamma_f)}$$
$$\times d_{q_s,\alpha}d_{-q_f,\beta}(-1)^{q_f}.$$

For brevity in writing (9), we introduce the vectors

$$\mathbf{E}^{(s),(f)} = \begin{pmatrix} E_+ \\ E_- \end{pmatrix}^{(s),(f)},$$

$$\mathbf{l}_{q_s}^{(s)} = e^{-iq_s\chi_s}\begin{pmatrix} e^{-i\gamma_s}d_{q_s,+} \\ e^{i\gamma_s}d_{q_s,-} \end{pmatrix},$$

$$\mathbf{l}_{q_f}^{(f)} = (-1)^{q_f}e^{-iq_f\chi_f}\begin{pmatrix} e^{i\gamma_f}d_{-q_f,+} \\ e^{-i\gamma_f}d_{-q_f,-} \end{pmatrix}.$$

Relation (9) then takes the form

$$\mathbf{E}^{(s)} = \mathbf{w}\mathbf{E}^{(f)}, \quad (10)$$

where

$$\mathbf{w} = \sum_m \sqrt{g_{k,m}G_{m,p}}\mathbf{l}_{q_s}^{(s)}\tilde{\mathbf{l}}_{q_f}^{(f)}. \quad (11)$$

Let us now turn from the amplitude E_α to the complex Stokes parameters $\mathbf{I}_+$:

$$\mathbf{E}_+ = (\overline{E_+E_+^*}, \overline{E_-E_-^*}, \overline{E_+E_-^*}, \overline{E_-E_+^*}). \quad (12)$$

An overline in (12) denotes averaging over an ensemble of oscillations of the electric vector. The relation between the incident and scattered radiation can be formally written

$$\mathbf{I}_+^{(s)} = \mathbf{w} \otimes \mathbf{w}\mathbf{I}_+^{(f)} = \mathbf{W} \cdot \mathbf{I}_+^{(f)}.$$

Substituting (3) into (12), it is straightforward to determine the matrix element

$$W_{i,j} = w_{a(i),a(j)}w_{b(i),b(j)},$$

where the rows $\mathbf{a}$ and $\mathbf{b}$ are defined to be

$$\mathbf{a} = (1, -1, 1, -1), \qquad \mathbf{b} = (1, -1, -1, 1). \quad (13)$$

The translation from the parameters $\mathbf{I}_+$ to the Stokes parameters

$$\mathbf{I}_X = (\overline{E_xE_x^*}, \overline{E_yE_y^*}, 2\mathrm{Re}\overline{E_xE_y^*}, -2\mathrm{Im}\overline{E_xE_y^*})$$
$$= (I_x, I_y, U, V)$$

is brought about by the transformation

$$\mathbf{I}_X = \mathbf{L} \cdot \mathbf{I}_+, \qquad \mathbf{I}_+ = \mathbf{L}^{-1} \cdot \mathbf{I}_X, \quad (14)$$

where

$$\mathbf{L} = \frac{1}{2}\begin{pmatrix} 1 & 1 & -1 & -1 \\ 1 & 1 & 1 & 1 \\ 0 & 0 & 2i & -2i \\ -2 & 2 & 0 & 0 \end{pmatrix},$$

$$\mathbf{L}^{-1} = \frac{1}{2}\begin{pmatrix} 1 & 1 & 0 & -1 \\ 1 & 1 & 0 & 1 \\ -1 & 1 & -i & 0 \\ -1 & 1 & i & 0 \end{pmatrix}.$$

Thus far, we have considered the case of linear unit vectors $x_f, y_f; x_s, y_s$ oriented arbitrarily relative to the scattering plane. Of special interest is the case when the unit vectors lie in or perpendicular to the scattering plane. In this case, if we calculate the phase matrix with and without a magnetic field, we can estimate the influence of the magnetic field on the polarization of the scattered radiation. The transition to the limiting case of no magnetic field in this coordinate system serves as an additional test of the correctness of the calculations.

We can see from an examination of the spherical triangle FHS in Fig. 1 that, in order for the x_f and x_s axes to lie in the scattering plane, we must have

$$\gamma_f = \pi - F, \qquad \gamma_s = S,$$

where F and S are the angles of the spherical triangle FHS at the corresponding vertices, which are given by the formulas

$$F = \arctan \frac{\sin(\chi_s - \chi_f)\sin\theta_s}{\cos\theta_s \sin\theta_f - \sin\theta_s \cos\theta_f \cos(\chi_s - \chi_f)}, \quad (15)$$

$$S = \arctan \frac{\sin(\chi_s - \chi_f)\sin\theta_f}{\cos\theta_f \sin\theta_s - \sin\theta_f \cos\theta_s \cos(\chi_s - \chi_f)}.$$

Since γ_f and γ_s lie in the interval $(0, \pi)$, formula (15) uniquely defines the quadrant in which the angles F, S lie.

Let us now turn to the means for finding the indices of the matrix $\mathbf{w}$ in (11). The choice of the indices k, m, p in (11) must take into account the selection rules. No simple, transparent formulas can be obtained. However, we can formulate a straightforward procedure for computating these indices.

As was noted above, transitions with different pairs of indices k, p are phase-independent. Therefore, calculations for a specific pair k, p must be carried out right to the determination of the Stokes parameters of the scattered radiation. Let J_L, J_U be the orbital quantum numbers of the lower and upper levels, respectively. We can take into account interference effects in (10) in a convenient way by distinguishing three types of transitions:

1. The initial and final magnetic quantum numbers coincide, $k = p$. In this case, we can write out expression (10) as follows:

$$\mathbf{E}^{(s)} = \sum_{i=-J_L}^{J_L} \left(\sqrt{g_{i,i+1}G_{i+1,i}}\mathbf{l}_-^{(s)}\tilde{\mathbf{l}}_+^{(f)} + \sqrt{g_{i,i}G_{i,i}}\mathbf{l}_0^{(s)}\tilde{\mathbf{l}}_0^{(f)} + \sqrt{g_{i,i-1}G_{i-1,i}}\mathbf{l}_+^{(s)}\tilde{\mathbf{l}}_-^{(f)} \right)\mathbf{E}^{(f)}. \quad (16)$$

2. The initial and final quantum numbers differ by unity, $p = k \pm 1$. In this case,

$$\mathbf{E}^{(s)} = \sum_{i=-J_L}^{J_L} \left(\sqrt{g_{i,i}G_{i,i\pm1}}\mathbf{l}_\pm^{(s)}\tilde{\mathbf{l}}_0^{(f)} + kz\sqrt{g_{i,i\pm1}G_{i\pm1,i\pm1}}\mathbf{l}_0^{(s)}\tilde{\mathbf{l}}_{\pm1}^{(f)} \right)\mathbf{E}^{(f)}, \quad (17)$$

where kz is a certain sign factor, which we will discuss further below.

3. The initial and final quantum numbers differ by two, $p = k \pm 2$. In this case, we have

$$\mathbf{E}^{(s)} = \sum_{i=-J_L}^{J_L} (\sqrt{g_{i,i\pm1}G_{i\pm1,i\pm2}}\mathbf{l}_\pm^{(s)}\tilde{\mathbf{l}}_\pm^{(f)})\mathbf{E}^{(f)}. \quad (18)$$

When summing over the index i in (16)–(18), the product $g_{i,l}G_{l,j}$ must be set equal to zero if $|i| > J_U$ or $|j| > J_L$. Note that certain terms in (16)–(18) may be absent.

These formulas enable us to calculate the phase matrix of the scattered radiation without taking into account the influence of the magnetic field. The coincidence of the form of the phase matrix with the form presented by Chandrasekhar [9] served as a test of these computations. It turned out that this condition is not fulfilled for all lines with different $J_L J_U$. We found that it is necessary to choose the sign of the terms for transitions $p = k \pm 1$ in some definite way.

For example, for lines corresponding to changes in the quantum numbers $\Delta J = \pm 1$, the terms in (17) must have different signs. For lines with $\Delta J = 0$, the terms (17) must have the same sign, except when $2J$ is odd and simultaneously $|k| = |p| = 1/2$. We propose an empirical formula to determine the sign of the second term in (17):

$$kz = (-1)^{[(2J+1+|m_k|+|m_p|)(|\Delta J|+1)+\Delta J]}. \quad (19)$$

Let us briefly describe how we derived this sign rule. In the work of Hamilton [7], the quantization axis is chosen to coincide with the direction of the incident radiation. Since transitions $k = p \pm 1$ are not realized in this case, we suppose that the signs in (17) can be different. When choosing the unit vectors of the system to be associated with the scattering plane, the phase matrix has the form [9]

$$\mathbf{I}_X^{(s)} = \frac{1}{8\pi}\left[3E_1 \begin{pmatrix} \cos\theta^2 & 0 & 0 \\ 0 & 1 & 0 \\ 0 & 0 & \cos\theta \end{pmatrix} + E_2 \begin{pmatrix} 1 & 1 & 0 \\ 1 & 1 & 0 \\ 0 & 0 & 0 \end{pmatrix} \right] \mathbf{I}_X^{(f)},$$

$$V^{(s)} = \frac{3}{8\pi}E_3 \cos\theta V^{(f)}, \quad (20)$$

$$I_X^{(s)} = (I_l, I_r, V, U),$$

where θ is the angle between the incident and scattered rays.

In the phase matrix determined by (20), terms with indices (1,3) and (3,1) are equal to zero. We wrote a program to change the signs of all components of transitions $k = p \pm 1$. When the matrix term with indices (1,3) vanishes, the corresponding system of signs was stored. The condition that the empirically calculated coefficients E_1, E_2 coincided with the theoretical values served as an additional criterion.

The next step in our computations is taking into account the frequency dependence in (11). This dependence is given, for example, by Stenflo [1], but we present it here for the sake of completeness and due to the need to refer to it in our subsequent analysis.

We can allow for this frequency dependence by introducing the following factor in formula (11):

$$\frac{1}{\omega_{m,p} - \omega - \frac{1}{2} i\gamma_m},$$

where γ_m is the decay constant for the upper level m,

$$\omega_{m,p} = \omega_0 + \Delta\omega_{m,p},$$

$$\Delta\omega_{m,p} = (mg_U - pg_L)\omega_L H, \qquad \omega_L = e/2cm_e,$$

$$g = 1 + \frac{J(J+1) + S(S+1) - L(L+1)}{2J(J+1)}.$$

We can thus write (11) in the form

$$\mathbf{w} = \frac{C}{\omega_0 + \Delta\omega_{m,p} - \omega - \frac{i}{2}\gamma_m} \times \sum_m \sqrt{g_{k,m} G_{m,p}}\, \mathbf{l}^{(s)}_{p-m} \tilde{\mathbf{l}}^{(f)}_{m-k}, \tag{21}$$

where C is a constant that does not depend on k, p, which can be determined via normalization after summing all the independent Stokes parameters.

When computing the Stokes parameters based on (21), the frequency factor will appear via the product

$$\varphi(\omega) = \frac{1}{(\omega_0 + \Delta\omega_{m,p} - \omega - \frac{i}{2}\gamma_m)} \times \frac{1}{(\omega_0 + \Delta\omega_{m',p} - \omega + \frac{i}{2}\gamma_{m'})}.$$

Taking into account the thermal motion of the atoms, we must replace ω by $\omega + \Delta\omega$ in this expression, then integrate over $\Delta\omega$ from $-\infty$ to $+\infty$. We thus obtain

$$f(\omega) = \int_{\infty}^{\infty} e^{-(\frac{\Delta\omega}{\Delta\omega_D})^2} \varphi(\omega - \Delta\omega) \frac{\Delta\omega}{\Delta\omega_D}.$$

Denoting

$$a_m = \frac{\gamma_m}{2\Delta\omega_D}, \qquad v_{m,p} = \frac{(\omega - \omega_0) - \Delta\omega_{m,p}}{\Delta\omega_D}$$

and integrating, we find

$$f_{m,m'}(\omega) = \frac{c}{(2a - i(v_{m,p} - v_{m',p}))} \times [\mathcal{H}(v_{m,p}, a) + \mathcal{H}^*(v_{m',p}, a)], \tag{22}$$

where we have introduced the notation

$$\mathcal{H}(v, a) = H(v, a) - 2iF(v, a),$$

where $\mathcal{H}(v, a)$ is the complex Voigt function.

Using transitions of the type $k = p$ as an example, we propose the following procedure to take into account the frequency dependence.

1. We store the sequence of magnetic quantum numbers m for the upper level. Let these numbers be m_1, m_2, m_3.

2. We successively determine the matrices

$$\mathbf{w}^{(m_1)} = \sqrt{g_{k,m1} G_{m1,p}}\, \mathbf{l}^{(s)}_{p-m_1} \tilde{\mathbf{l}}^{(f)}_{m_1-k},$$
$$\mathbf{w}^{(m_2)} = \sqrt{g_{k,m_2} G_{m_2,p}}\, \mathbf{l}^{(s)}_{p-m_2} \tilde{\mathbf{l}}^{(f)}_{m_2-k},$$
$$\mathbf{w}^{(m_3)} = \sqrt{g_{k,m_3} G_{m_3,p}}\, \mathbf{l}^{(s)}_{p-m_3} \tilde{\mathbf{l}}^{(f)}_{m_3-k}.$$

If some of these matrices are zero, this has no meaning here.

3. Using (22), we construct the frequency matrix

$$\mathbf{f} = \begin{pmatrix} f_{m_1,m_1} & f_{m_1,m_2} & f_{m_1,m_3} \\ f_{m_2,m_1} & f_{m_2,m_2} & f_{m_2,m_3} \\ f_{m_3,m_1} & f_{m_3,m_2} & f_{m_3,m_3} \end{pmatrix}.$$

If there are two terms or one term in (16), some of the elements of the matrix $\mathbf{f}$ can be set equal to zero.

4. Finally, the element $W_{i,j}$ of the phase matrix for a transition $k = p$ in the system of Stokes parameters I_+ will be given by the formula

$$W_{i,j} = \sum_{k_1} \sum_{k_2} f_{k_1,k_2} w^{(k_1)}_{a(i),a(j)} w^{(k_2),*}_{b(i),b(j)},$$

$$k_1, k_2 = m_1, m_2, m_3.$$

The vectors $\mathbf{a}, \mathbf{b}$ are given by (13).

The full phase matrix in the system of complex Stokes parameters $\mathbf{I}_+$ is equal to

$$\mathbf{W} = \sum_k (\mathbf{W}_{p=k} + \mathbf{W}_{p=k+1} + \mathbf{W}_{p=k-1} + \mathbf{W}_{p=k-2} + \mathbf{W}_{p=k+2}),$$

$$|k| \le J_L.$$

Thus, the relationship between the incident and scattered radiation can be written in the form

$$\mathbf{I}_X^{(s)} = \mathbf{P}_R \cdot \mathbf{I}_X^{(f)}, \qquad (23)$$

where

$$\mathbf{P}_R = \mathbf{L} \cdot \mathbf{W} \cdot \mathbf{L}^{-1}.$$

The formulas presented above enable computation of the phase matrix for resonance scattering in the presence of a weak magnetic field. Stenflo [1, 2], House [3], and M. Landi Degl'Innocenti and E. Landi Degl'Innocenti [6] also present theory for calculating the phase matrix in an approximation analogous to our own. It is of interest to compare the results of computations carried out using these methods.

We will turn first to the work of M. Landi Degl'Innocenti and E. Landi Degl'Innocenti [6], who present rather complex analytical formulas defining the phase matrix. There is no dependence on the frequency of the radiation in these formulas; they apparently correspond to scattering at the line center. We will not present these formulas here, only noting that they are appreciably simplified when the direction of the magnetic field is chosen to coincide with the Z axis, as we have done.

It is convenient to chose the unit vectors x_f, x_s to coincide with the scattering plane, in which case the effect of the external magnetic field on the polarization of the scattered radiation is clearly visible.

We denote $\mathbf{P}_L$ to be the phase matrix calculated in accordance with [6]. This expression for the phase matrix was obtained in the system of Stokes parameters $\mathbf{I}_Q = [I, Q, U, V]$, while our results were obtained for the Stokes parameters in the form $\mathbf{I}_X = [I_x, I_y, U, V]$. Accordingly, we must carry out certain transformations.

In [6], the x_f, x_s axes are directed along meridians, so that we must carry out rotations of the x_f, y_f and x_s, y_s coordinate systems by $\pi - F$ and S, respectively (Fig. 1). The angles F, S are determined by formula (15). Upon rotation through the angle S, the Stokes parameter $\mathbf{I}_Q$ transforms as

$$\mathbf{I}'_Q = \mathbf{G}(S) \cdot \mathbf{I}_Q,$$

where

$$\mathbf{G}(S) = \begin{pmatrix} 1 & 0 & 0 & \\ 0 & \cos 2S & \sin 2S & 0 \\ 0 & -\sin 2S & \cos 2S & 0 \\ 0 & 0 & 0 & 1 \end{pmatrix}.$$

We must also carry out the transition from the parameters $\mathbf{I}_Q$ to $\mathbf{I}_X$ and back; this transition is given by

$$\mathbf{I}_Q = \mathbf{T} \cdot \mathbf{I}_X, \qquad \mathbf{I}_X = \mathbf{T}_{-1} \cdot \mathbf{I}_Q,$$

where

$$\mathbf{T} = \begin{pmatrix} 1 & 1 & 0 & 0 \\ 1 & -1 & 0 & 0 \\ 0 & 0 & 1 & 0 \\ 0 & 0 & 0 & 1 \end{pmatrix},$$

$$\mathbf{T}_{-1} \begin{pmatrix} 0.5 & 0.5 & 0 & 0 \\ 0.5 & -0.5 & 0 & 0 \\ 0 & 0 & 1 & 0 \\ 0 & 0 & 0 & 1 \end{pmatrix}.$$

Thus, in order to compare with our results, we must calculate

$$\mathbf{I}_X^{(s)} = \mathbf{T}_{-1} \cdot \mathbf{G}(S) \cdot \mathbf{P}_L \cdot \mathbf{G}(-\pi + F) \cdot \mathbf{T} \cdot \mathbf{I}_X^{(f)}. \qquad (24)$$

Before turning to an analysis of the methods used by Stenflo [1] and House [3–5] to compute the phase matrix, we must compare the notation for the quantum numbers used there and in our own study. We have the following set of correspondences:

Our study	Stenflo [1]	House [3–5]
J_L, J_U, k, m, p	$J_a = J_f, J_b, \mu_a, m, \mu_f$	J, J'', M, M'', M'

Let us now turn to the method used by Stenflo to calculate the phase matrix [1]. The initial formula has the form

$$\omega_{\alpha\beta} \sim \sum\nolimits_{J_b,m} (-1)^{r_{ab}+r_{fb}} \times \sqrt{f_{ab}f_{fb}}\sqrt{(2J_a+1)(2J_f+1)} \times \begin{pmatrix} J_b & J_f & 1 \\ -m & -\mu_f & -q \end{pmatrix} \times \begin{pmatrix} J_b & J_a & 1 \\ -m & -\mu_a & -q' \end{pmatrix} (-1)^{q-q'} \Phi_{m\mu_f}(\nu)\varepsilon_q^{\alpha *}\varepsilon_{q'}^{\beta}. \quad (25)$$

We are considering scattering under the condition $J_a = J_f$ and without summing over the orbital quantum number J_b. The absolute value of expression (25) must be taken. Since the indices $r_{ab}, r_{fb,}(q-q')$ do not depend on the magnetic quantum number m [1, 2], the sign factors in (25) can be omitted. Expression (25) is analogous to our expression (21); therefore, computations carried out using (25) will differ from our own only if the signs of individual components in (25) differ from the corresponding signs in (21). The signs of the components in (25) are determined by the product

$$\sqrt{2J_a+1}\sqrt{2J_f+1} \times \begin{pmatrix} J_b & J_f & 1 \\ -m & -\mu_f & -q \end{pmatrix} \begin{pmatrix} J_b & J_a & 1 \\ -m & -\mu_a & -q' \end{pmatrix}, \quad (26)$$

which is proportional to the expression $\sqrt{g_{k,m}G_{m,p}}$ we have used. Applying the formulas for the $3j$ symbols [10], we compared the signs of components for transitions $p = k$ and $p = k \pm 1$ obtained using (26) and using our formula (19). In order for these signs to be in agreement, it is necessary to change the sign of one of the components of the $p = k \pm 1$ transition in (26).

Thus, the phase matrix determined in [1] is slightly incorrect.

We will now carry out an analogous analysis for the signs of the components of the phase matrix presented by House [3]. The formula for the probability that a photon with linear polarization $\bar{e}^{\alpha}$ is reradiated with linear polarization $\bar{e}^{\alpha'}$ has the form [3]

$$W \sim \left| \sum_{M''} f_{M',M''} g_{M,M''}^{M'',M'} \varepsilon_{M-M''}\varepsilon'_{M''-M'} \right|^2.$$

We have written here only that part of this expression that determines the interference of the line components. In this expression, $f_{M',M''}$ determines the frequency dependence of the components, and does not affect their signs. In our notation, the product $\varepsilon_{M-M''}\varepsilon'_{M''-M'}$ is equal to

$$\varepsilon_{M-M''}\varepsilon'_{M''-M'} = (\mathbf{x}_f \mathbf{e}_{n-k})(\mathbf{x}_s \mathbf{e}_{p-n})$$

and likewise has the same sign for all components.

Let us now write an expression for $g_{M,M''}^{M'',M'}$:

$$g_{M,M''}^{M'',M'} = (-1)^{J''-M''+J-M'} \times \begin{pmatrix} J'' & 1 & J \\ -M'' & (M''-M) & M \end{pmatrix} \times \begin{pmatrix} J & 1 & J'' \\ -M' & (M'-M'') & M'' \end{pmatrix}. \quad (27)$$

When analyzing the signs of this expression, it is convenient to move to the notation for the indices and symbols used by Stenflo [1]. Replacing J'', J, M'', M', M in (27) with $J_b, J_a, m, \mu_f, \mu_a$, respectively, and manipulating the $3j$ symbols, we obtain

$$g_{M,M''}^{M'',M'} = (-1)^{1+(m-\mu_f)} \times \begin{pmatrix} J_b & J & 1 \\ -m & \mu_a & -q' \end{pmatrix} \begin{pmatrix} J_b & J & 1 \\ -m & \mu_f & -q \end{pmatrix}. \quad (28)$$

The factor $(-1)^{1+(m-\mu_f)}$ in (28) provides correct signs for transitions $k \longrightarrow k \pm 1$ and incorrect signs for transitions $k \longrightarrow k$, since the signs of all components should be the same for transitions $k \longrightarrow k$.

3. SOME COMPARATIVE RESULTS

In order to illustrate the derivations described above with numerical computations, we computed the dependence of the degree of polarization of the scattered radiation on the strength of the external magnetic field. The Stokes parameters of the incident radiation were taken to be $I_X = (1, 1, 0, 0)$. We chose a line with quantum numbers for the upper and lower levels $J_U = 1.5, J_L = 0.5$. This line has transitions of both type $k = p$ and type $k = p \pm 1$. As we showed above, the theoretical formula given by Stenflo [1] incorrectly determines the relative signs of the components of a $k = p \pm 1$ transition. The theoretical formula applied by House [3] incorrectly determines the signs of the components of a transition $k = p$.

We also carried out the same computations using the analytical formulas presented by M. Landi Degl'Innocenti and E. Landi Degl'Innocenti [6]. There is no averaging of the frequency factor over the thermal motions of the radiating atoms in [6]. The frequency factor depends on the decay parameter γ. We

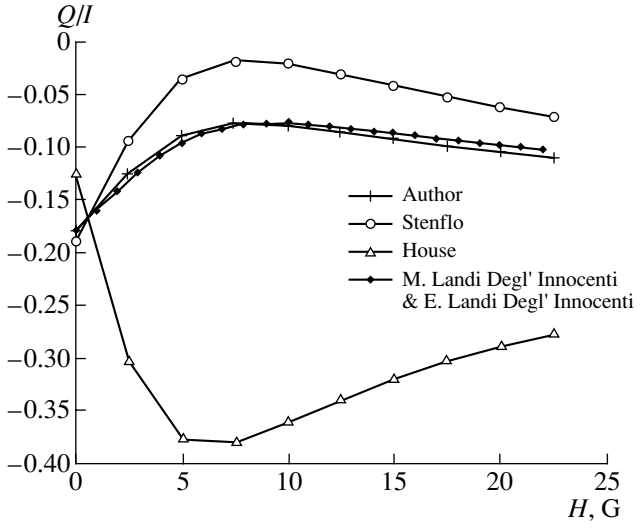

Fig. 2. Comparison of the degree of linear polarization of the scattered radiation as a function of the strength of the external magnetic field according to the results of various authors. The line $J_U = 1.5, J_L = 0.5$ is considered, with $I_f = (1, 1, 0, 0)$, $\gamma_f = 0$, $\theta_f = 30^\circ$, $\chi_f = 0^\circ$, $\gamma_s = 0$, $\theta_s = 70^\circ$, and $\chi_s = 30^\circ$. The Voigt parameter is $a = 0.003$, and the decay parameter is $\gamma = 10^{-8}$. The curves marked "Stenflo" and "House" were obtained using our own program, but taking into account the supposed errors.

adopted the value $\gamma = 10^8$; this quantity is denoted $A_{J',J}$ in [6]. In the theory we have developed, this corresponds to the Voigt parameter $a = \gamma/2\Delta\omega_D$. When $\Delta\omega_D = 1.53 \times 10^{10}$ ($T_{\text{eff}} \approx 5000$ K), $a = 0.00328$.

The results of the computations are presented in Fig. 2. We can see that there is good agreement between our computations and the computations carried out using the analytical formulas of [6]. This agreement is preserved if $\gamma/a = \Delta\omega_D^{(T=5000\text{ K})}/\pi$. The coincidence of the curves begins to be disrupted for other values for this ratio.

We can also see in Fig. 2 appreciable discrepancies between our results and those computed using the formulas presented by Stenflo [1] and House [3]. Note that, since the computations were carried out using our formulas, the curves denoted "Stenflo" and "House" in Fig. 2 can only conditionally be considered the results for the corresponding theories of these authors. These curves only demonstrate the influence of possible errors in the signs of the amplitudes of certain quantum transitions in the formulas used by these authors.

4. CONCLUSION

We have developed a detailed algorithm for computing the phase matrix for resonance scattering in the presence of a weak external magnetic field. The frequency dependence of the phase matrix is exactly taken into account. A specific numerical example (for the line center) shows good agreement between our computations and those obtained using the theoretical formulas published in [6]. Computations of the phase matrix using the algorithms proposed in [1] and [3] will yield inexact results due to certain errors in the signs of the amplitudes of some quantum transitions.

REFERENCES

1. J. O. Stenflo, Astron. Astrophys. **338**, 301 (1998).
2. J. O. Stenflo, *Solar Magnetic Fields—Polarized Radiation Diagnostic* (Kluwer, Dordrecht, 1994).
3. L. L. House, J. Quant. Spectrosc. Radiat. Transf. **10**, 909 (1970).
4. L. L. House, J. Quant. Spectrosc. Radiat. Transf. **10**, 1171 (1970).
5. L. L. House, J. Quant. Spectrosc. Radiat. Transf. **11**, 367 (1971).
6. M. Landi Degl'Innocenti and E. Landi Degl'Innocenti, Astron. Astrophys. **192**, 374 (1988).
7. D. Hamilton, Astrophys. J. **106**, 457 (1947).
8. S. E. Frish, *Optical Spectra of Atoms* (Fiz.-Mat. Literatura, Moscow, 1963) [in Russian].
9. S. Chandrasekar, *Radiative Transfer* (Clarendon, Oxford, 1950; Inostrannaya Literatura, Moscow, 1953).
10. L. D. Landau and E. M. Lifshitz, *Quantum Mechanics: Non-Relativistic Theory* (Fiz.-Mat. Literatura, Moscow, 1963; Pergamon Press, Oxford, 1977).

Translated by D. Gabuzda

Astronomy Reports, Vol. 49, No. 9, 2005, pp. 747–754. Translated from Astronomicheskiĭ Zhurnal, Vol. 82, No. 9, 2005, pp. 838–846.

Sign Reversals of the Polarization of the Microwave Emission of Sunspot Radio Sources

T. I. Kal'tman[1], A. N. Korzhavin[1], and Yu. T. Tsap[2]

[1] *Special Astrophysical Observatory, Russian Academy of Sciences, Nizhniĭ Arkhyz, Karachaevo-Cherkesskaya Republic, 357169 Russia*

[2] *Crimean Astrophysical Observatory, National Academy of Sciences of Ukraine, Nauchnyĭ, Crimea, 98409 Ukraine*

Received July 13, 2004; in final form, February 17, 2005

Abstract—Thermal cyclotron emission features from a sunspot-associated source in a solar active region are considered in the framework of a three-level temperature model with a hot layer. The images of the source have a complex fine structure, with rings with different brightness temperatures and different signs of circular polarization. The proposed model suggests the possibility of a double or multiple reversal of the sign of polarization, as well as a significant increase of the fluxes in the 3–4 cm range, as is typical of active regions associated with proton flares. Energetic particles of the halo cannot provide the required temperatures of the layers. Alternative heating mechanisms are discussed. © *2005 Pleiades Publishing, Inc.*

1. INTRODUCTION

Observations indicate that the microwave emission of solar active regions (ARs) is determined by sources that are associated with sunspots, flocculi, coronal arches, etc. [1–3]. At the same time, it is not always possible to identify these radio sources with optical, ultraviolet, or X-ray objects. For instance, decimeter-wavelength halos, which represent vast, diffuse regions of enhanced radio emission, cannot be unambiguously distinguished in other wavelength ranges. Searches for generic connections between various structures in ARs based on the characteristic features of their emission are clearly of interest.

Sunspot-associated sources display the most contrast at 3–4 cm. Microwave observations with high angular resolution show that their structures resemble either horseshoes or rings [4–6]. The degree of polarization in the short-wave range can reach 100%. Typical brightness temperatures T_b are $(0.5–2.5) \times 10^6$ K, reaching $(4–6) \times 10^6$ K in some cases. There is no doubt that the emission of the sunspot component is dominated by thermal cyclotron emission at the first four harmonics of the gyrofrequency (see, e.g., [3, 7, 8]).

The decimeter-wavelength halo covers the entire AR, with its emission (with $T_b = (2–5) \times 10^6$ K) dominating at 10–20 cm [9, 10]. The spectral index grows beginning from $\lambda = 4$ cm, but the spectrum is not very steep, as a rule, having spectral indices from one to two. Attempts to interpret this component as thermal emission encounter serious difficulties. The best-grounded alternative hypothesis is that nonthermal electrons that generate gyrosynchrotron emission are responsible for the halo emission [2]. This suggests that there is a large-scale magnetic trap at heights $\sim 10^5$ km that can accumulate energetic electrons, like the Earth's radiation belts.

Reversals of the sign of circular polarization of the microwave emission are observed fairly frequently in powerful ARs and can be multiple when the entire wavelength range is considered [10–14]. Peterova and Korzhavin [14] distinguished such ARs as a separate subclass of sunspot-associated sources. As before, the origin of the sign reversals remains unclear; they are usually attributed to the propagation of electromagnetic waves through regions with quasi-transverse magnetic fields [7]. However, in at least some cases, the spectrum of the polarized emission and its independence of location in the AR structure suggest that the ordinary emission dominates due to the conditions under which the emission is generated in the source [15]. The relevance of this approach also follows from observations of the low-lying, bright, compact sources of emission above sunspots, which display a thermal bremsstrahlung spectrum [14]. Therefore, the preferred approach for individual cases is that first proposed by Gel'freĭkh *et al.* [15], in which the polarization sign reversal is due to the presence of local high-temperature regions in the source (see also [16]).

Hot plasma layers can be formed by many processes, such as the interaction of "precipitating" nonthermal halo particles with dense layers of the lower

1063-7729/05/4909-0747$26.00

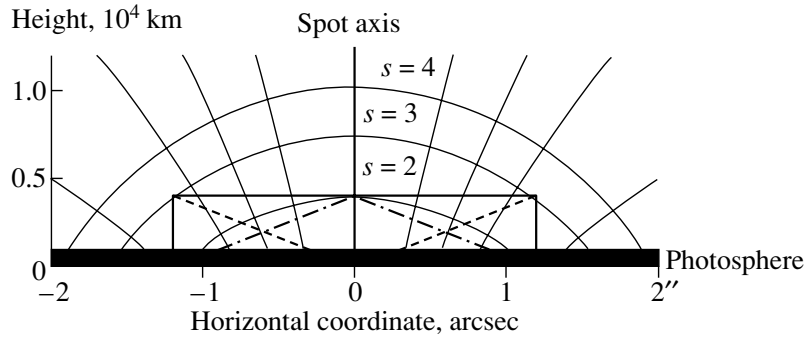

Fig. 1. Schematic of the region of emission of a sunspot-associated source. The temperature of the hot layer at a height of $(1–4) \times 10^3$ km varies from 1.5×10^6 to 8×10^6 K.

corona and upper chromosphere. This scenario is quite similar to that used to interpret the hard X-ray and microwave emission of solar flares [17]. We also cannot exclude the possibility of more efficient dissipation of the magnetic field or magnetohydrodynamic waves near the transition layer [18]. In this connection, we point out that attempts to relate the reversal layer to the horizontal part of a hot coronal loop above the source [19] are unconvincing. Since the loop feet are concentrated in the sunspot region, the loop tops are hardly able to cover the sunspot component, having at the same time a strong magnetic field ($\gtrsim$500 G).

In this work, which is a continuation of [20], we present follow-up studies of the properties of the AR microwave emission. The next section describes the main features of a model for a sunspot-associated source with a hot layer. We discuss the adopted restrictions and main theoretical premises. Section 3 is dedicated to the results of our numerical calculations, while Section 4 considers the problem of heating of the hot plasma layer. The main results are formulated in the conclusion.

2. MODEL FOR A SUNSPOT-ASSOCIATED SOURCE WITH A TEMPERATURE GRADIENT

To calculate the radio emission of a unipolar spot, we used a temperature model that is simpler than the model of [21] (Fig. 1). It includes a cool transition zone with a kinetic temperature of $T = 10^4$ K, shown as a black strip above the photosphere; a layer of hot plasma, whose temperature ($T = (1.5–8) \times 10^6$ K) was varied for a family of models; and the corona region ($T = 1.5 \times 10^6$ K). We chose the parameters so that the ordinary wave ($\lambda \approx 3$ cm, the second harmonic of the gyrofrequency) was generated in a layer with a higher temperature than the extraordinary wave (the third harmonic). Three possible shapes of the hot layer were specified: (1) a cylinder (solid lines of the rectangle in Fig. 1), which included the emission region for the second harmonic for $\lambda = 3$ cm; (2) a cone (dashed line); and (3) a "cap" (dashed–dot line). We either assumed a constant electron density ($n = (0.3–1) \times 10^{10}$ cm^{-3}) or determined this density from the condition of constant pressure ($n = 1.5 \times 10^{16}/T$ cm^{-3}).

We assumed a dipolar sunspot magnetic field, with $B = 3100$ G at the photosphere level. The vertical dipole was placed at a depth of 2×10^4 km below the solar surface. A region of 30×30 thousand km was calculated in steps of 200 km. The sunspot longitude was varied over the entire solar disk.

The optical depth τ_{js} of the gyroresonant layer at the harmonics $s = 2–4$ for the mode j propagating at an angle θ to the magnetic field **B** was found from the formula [7]

$$\tau_{js} = \frac{s^{2s}}{2^s s!}\frac{\pi e^2}{m_e c^2}\beta_T^{2s-2} L_B n\lambda \sin^{2s-2}\theta \qquad (1)$$
$$\times \frac{(\sqrt{u}\sin^2\theta + 2\cos^2\theta \pm \sqrt{u\sin^4\theta + 4\cos^2\theta})}{u\sin^4\theta + 4\cos^2\theta \pm \sqrt{u}\sin^2\theta\sqrt{u\sin^4\theta + 4\cos^2\theta}}.$$

Here, we use the standard notation and take $\beta_T = v_T/c$ to be the ratio of the thermal velocity of the electrons to the speed of light; $L_B = B(dB/dl)^{-1}$ is the characteristic scale of the magnetic-field variations and $u = \omega_B^2/\omega^2$. Plus signs on the right-hand side of (1) correspond to the extraordinary wave ($j = 1$), and minus signs, to the ordinary wave ($j = 2$).

We calculated the optical depth for the emission of the ordinary wave at the first harmonic using the formula [7]

$$\tau_{21} = \pi\frac{\omega}{c}\beta_T^2 \sin^4\theta \frac{(1 + 2\cos^2\theta)^2}{(1 + \cos^2\theta)^3} L_B. \qquad (2)$$

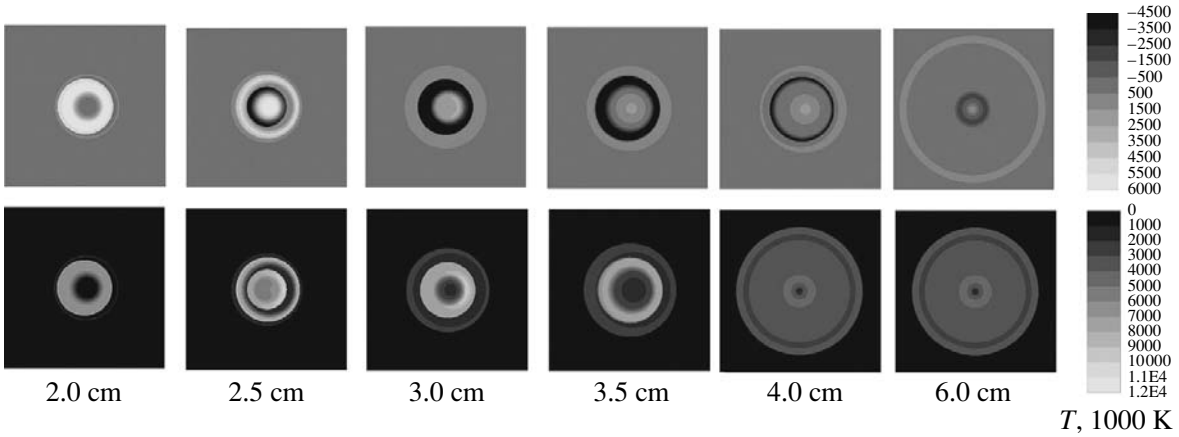

Fig. 2. Two-dimensional maps of the distribution over the source of the difference (upper row) and sum (lower row) of the brightness temperatures of the ordinary and extraordinary emission modes at 2.0, 2.5, 3.0, 3.5, 4.0, and 6.0 cm, calculated for the family of models with the temperature of the cylindrical hot layer equal to 6×10^6 K.

Expressions (1) and (2) are valid only for a rarefied magnetized plasma ($u \ll 1$, $\omega_L^2/\omega^2 \ll 1$) with a refractive index close to unity. Therefore, in our model calculations, we restricted our consideration to gyroresonant emission in the microwave range ($\lambda = 1$–10 cm). Note also that, in the bremsstrahlung mechanism, the optical depth is inversely proportional to the temperature ($\tau_j \propto T^{-3/2}$) and the bremsstrahlung contribution to the emission can be neglected for $T > 10^6$ K [22].

We obtained the brightness temperatures for the extraordinary (T_{b1}) and ordinary (T_{b2}) waves taking into account emission and absorption at the first four gyrolevels, taking the corresponding kinetic temperatures T_s at the points of intersection with the considered beam. Thus, the main formula simplified to [8]

$$T_{b1} = T_2(1 - e^{-\tau_{1,2}})e^{-\tau_{1,3}-\tau_{1,4}} + T_3(1 - e^{-\tau_{1,3}})e^{-\tau_{1,4}} + T_4(1 - e^{-\tau_{1,4}}),$$

$$T_{b2} = T_1(1 - e^{-\tau_{2,1}})e^{-\tau_{2,2}-\tau_{2,3}} + T_2(1 - e^{-\tau_{2,2}})e^{-\tau_{2,3}} + T_3(1 - e^{-\tau_{2,3}}).$$

The first and second subscripts on the right-hand sides of these equations denote the emission mode j and the gyrolevel number s.

We used the Rayleigh–Jeans approximation to translate from brightness temperatures T_b to the corresponding fluxes F:

$$F = \frac{k}{\lambda^2}\int T_b d\Omega, \qquad (3)$$

where k is Boltzmann's constant and $d\Omega = \sin\Theta d\Theta d\alpha$ is an element of the source solid angle.

The hot layers can make a substantial contribution to the soft X-ray radiation of ARs. Therefore, before carrying out the numerical calculations, we must determine the constraints imposed on the thermodynamic parameters of the plasma in these structures. We addressed this problem using solar observations obtained with the GOES satellite.

According to results obtained using the technique of Thomas *et al.* [23], a cylindrical region with a radius of 12 000 km and a thickness of 3000 km heated to $T = 6 \times 10^6$ K will emit a 1–8 Å flux of less than 7×10^{-4} erg m^{-2} s^{-1} if the density of thermal electrons is $n \lesssim 4.5 \times 10^{10}$ cm^{-3}. This flux is at the sensitivity limit of the receiver. In turn, the minimum detectable flux for the GOES detector with a passband of 0.5–4 Å is approximately 3×10^{-6} erg m^{-2} s^{-1}; applied to the model with a cylindrical layer, this corresponds to an electron density of 1.5×10^{10} cm^{-3}. Since the emission measure for a conical or cap-shaped hot layer is even smaller, the contribution of the hot layer to the total flux of soft X-ray radiation from all ARs can be neglected when $n \lesssim 10^{10}$ cm^{-3} and $T \sim 6 \times 10^6$ K.

3. RESULTS OF NUMERICAL CALCULATIONS

As an example, Fig. 2 presents the distributions over the source of the sum and difference of the brightness temperatures of the ordinary and extraordinary modes of the microwave emission for a cylindrical hot layer with $T = 6 \times 10^6$ K. This temperature was chosen because it best matches the observations. Calculations were carried out for a spot near the equator in the western part of the

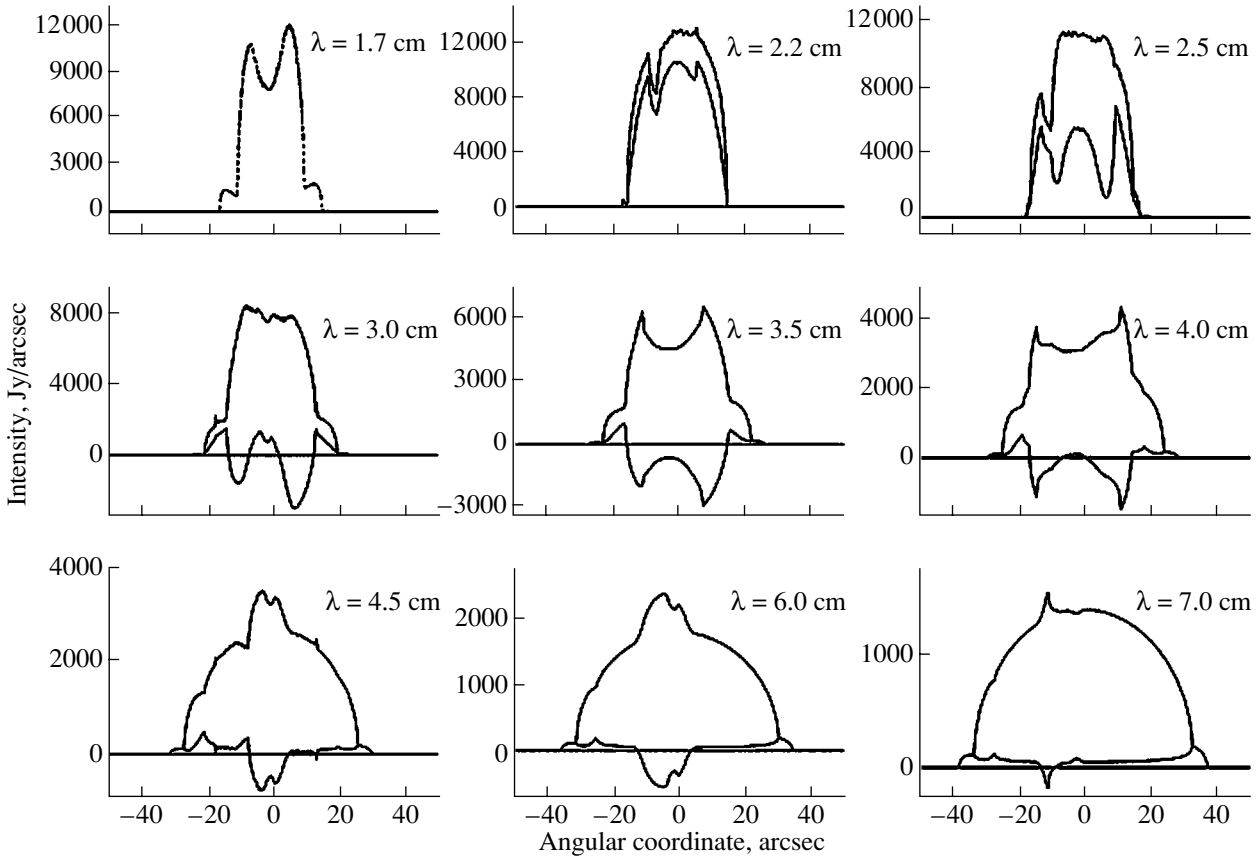

Fig. 3. Strip scans of the intensity and polarization of the source emission at longitude 20°, calculated in the model with a cylindrical hot layer ($T = 6 \times 10^6$ K).

solar disk at longitude 20°. The maps for different wavelengths were reduced to a common temperature scale for the difference ($\Delta T_b = T_{b2} - T_{b1}$) and sum ($T_\Sigma = T_{b1} + T_{b2}$) of the brightness temperatures. In the two-dimensional maps in Fig. 2, the source consists of ring-shaped regions with various brightness temperatures T_b and values of ΔT_b with alternating signs. If the source is shifted from the center to the limb of the solar disk, the rings begin more and more to resemble horseshoes.

Figure 3 shows strip scans of the intensity and polarization of a sunspot-associated source with a cylindrical hot layer recalculated from the two-dimensional maps. To obtain these scans, we integrated over only coordinate α in (3). We can see that these distributions have a complex alternating-sign structure with sharp changes in wavelength; this may be consistent with the observations of Bogod and Tokhchukova [12]. In the 3–7 cm range, some of the polarized emissions become negative (inverted) with the predominant ordinary mode.

Thus, the examples of two- and one-dimensional maps of a sunspot-associated source presented in Figs. 2 and 3 testify to a strong wavelength dependence for these images. Additional calculations show that the source images also depend strongly on the chosen geometry for the hot layer (cylindrical, conical, cap-shaped). This shape is unlikely to be stationary under the conditions in the solar atmosphere; therefore, the corresponding variations of the one-dimensional source images with wavelength and time may be relevant for interpretations of the observations described in [12].

Figure 4 shows the calculated spectra of the total flux and degree of polarization of the emission for a family of models with different temperatures of a (a) cylindrical, (b) conical, and (c) cap-shaped hot layer. All these plots are given for a spot located at the disk center. According to Fig. 4, the sign alternation of the polarization at 3–6 cm is manifest to some extent in all the models and can be multiple. We especially emphasize that the emission spectra for the models with cylindrical layers (Fig. 4a) have a characteristic peak at 2–3 cm; in contrast to the other

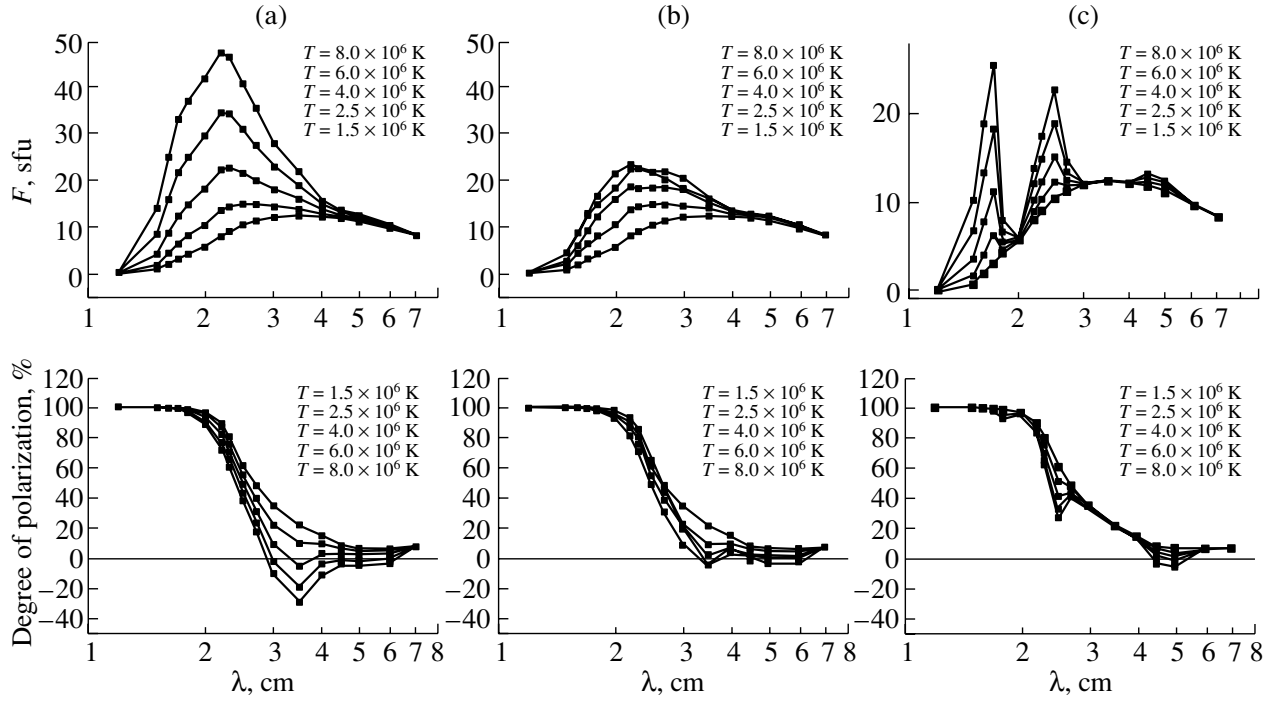

Fig. 4. Total flux (upper row) and degree of polarization (lower row) of the emission as functions of the wavelength for a source at the disk center for a family of models with different temperatures for (a) cylindrical, (b) conical, and (c) cap-shaped hot layers.

layer shapes, the peak height appreciably increases with increasing temperature of the layer. In this case, the inverted polarized flux at 3–4 cm also grows with temperature. The calculated spectra for a conical layer (Fig. 4b) have a flat maximum and the least pronounced polarization reversal. The most complex spectra are those for models with a cap-shaped hot layer (Fig. 4c), which display three maxima, at 1.7, 2.5, and 4.6 cm. A detailed analysis shows that these are due to the relative increase of the effective area of the gyrosheets penetrating the hot layer, which make the main contribution to the extraordinary emission at the second and third harmonics, as well as to the ordinary emission at the first harmonic.

Additional calculations established that the motion of a sunspot-associated source over the solar disk does not produce substantial changes in the pattern described above (Fig. 5). It is also of interest that the maximum of the polarized-flux spectrum is shifted toward shorter wavelengths with decreasing height of the layer, and toward longer wavelengths with increasing height.

4. MECHANISMS FOR HEATING THE HOT-LAYER PLASMA

Let us consider the heating of plasma by fast electrons captured in a magnetic trap (halo). When scattered into the loss cone, these electrons lose their energy due to Coulomb collisions near the loop feet.

According to our current understanding, there are three modes of pitch-angle diffusion of the captured electrons into the loss cone: weak, moderate, and strong [17]. Particles escape from the magnetic trap most efficiently in the moderate diffusion mode. The distinctive feature of this mode is that the distribution function of the captured electrons is almost isotropic. In this case, we have for the total flux of the passing particles at the loop feet [17]

$$\frac{dN}{dt} \approx \frac{\mathcal{N}v}{\sigma L},$$

where N and $\mathcal{N}$ are the numbers of the passing and captured electrons, respectively, σ is the mirror ratio, L is the loop length, and v is the mean velocity of the electrons. Then, assuming $\mathcal{N} = 10^{34}$–10^{35}, $\sigma = 10$, $L = 10^{10}$ cm, and $v = 6 \times 10^8$ cm/s ($\approx$10 keV), we estimate the total flux of electrons escaping from the trap to be $dN/dt \lesssim 6 \times (10^{32}$–$10^{33})$ s^{-1}—one or two orders of magnitude lower than typical values adopted for solar flares [24].

Following Somov and Syrovatskiĭ [25], we represent the spectrum of the passing electrons that penetrate the lower corona and transition layer beginning

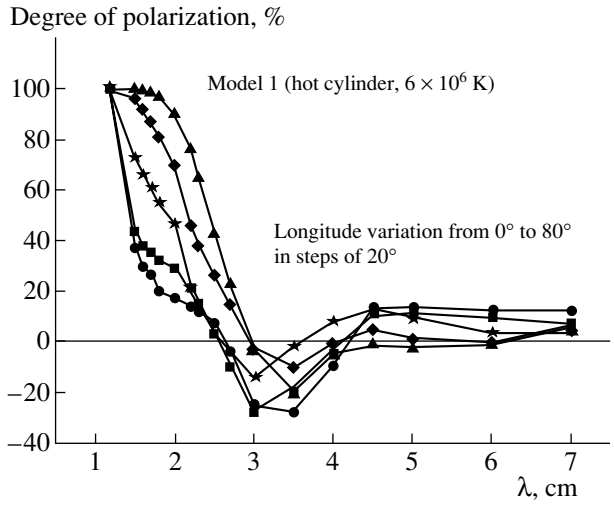

Fig. 5. Longitude variations of the spectrum of the degree of polarization of a sunspot-associated source in the model with a cylindrical hot layer ($T = 6 \times 10^6$ K). The longitude varies from 0° to 80° in steps of 20°.

from some adopted height $s = 0$ as

$$N(E,0) = KE^{-(\gamma+1/2)}\Theta(E - E_0), \qquad (4)$$

where K is a normalization factor and $\Theta(x)$ is the Heavyside function. If $\gamma > 2$, the energy flux of the accelerated electrons is

$$F(0) = \int_{E_0}^{\infty} EvN(E,0)dE = \frac{K}{\gamma - 2}\sqrt{\frac{2}{m}}E_0^{2-\gamma}. \quad (5)$$

In turn, since the change of the energy of a fast electron due to Coulomb collisions with the background plasma is

$$\frac{dE}{ds} = -\frac{an}{E}, \qquad (6)$$

where $a = 3 \times 10^{-12}$ eV^2 cm^2, then, assuming a uniform "target," the energy flux of the electrons is

$$F(s) = \int_{E_0'}^{\infty} EvN(E,s)dE, \qquad (7)$$

where $E_0' = \sqrt{E_0^2 - 2asn}$.

We obtain from the continuity equation

$$\frac{\partial}{\partial s}\left[vN(E,s)\right] + \frac{\partial}{\partial E}\left[\frac{dE}{ds}vN(E,s)\right] = 0,$$

and from (7)

$$N(E,s) = KE^{1/2}(E^2 + 2asn)^{-(\gamma+1)/2} \qquad (8)$$
$$\times\, \Theta(\sqrt{E^2 + 2asn} - E_0).$$

Substituting (8) to (7) and using (5) and (6) yields

$$\frac{F(s)}{F(0)} = \frac{\gamma - 2}{2}B\left(\frac{3}{2}, \frac{\gamma - 2}{2}\right)\left(\frac{s_0}{s}\right)^{(\gamma-2)/2}, \qquad (9)$$

where $B(x,y)$ is the beta function, $s = E^2/(2an)$, and $s \geq s_0 = E_0^2/(2an)$. Then, according to (9), the flux of thermal energy released from the propagation of electrons to depth s is

$$\delta Q = F(0) - F(s) \qquad (10)$$
$$= F(0)\left[1 - \frac{\gamma - 2}{2}B\left(\frac{3}{2}, \frac{\gamma - 2}{2}\right)\left(\frac{s_0}{s}\right)^{(\gamma-2)/2}\right],$$

where $B/2 = 0.785$, 0.333, 0.196, 0.137 for $\gamma = 3$, 4, 5, 6, respectively. In particular, for $s = 2s_0$ and $\gamma = 4$, we find from (10) that $\delta Q \approx 0.7F(0)$; i.e., the accelerated electrons crossing the depth $s \sim s_0$ lose almost all their energy. In this case, the determining contribution to plasma heating is made by low-energy electrons with $E \simeq E_0$.

Using (4), we can represent the total flux of accelerated electrons as

$$\frac{dN}{dt} = A\int_{E_0}^{\infty} N(E,0)vdE = \frac{AK}{\gamma - 1}\sqrt{\frac{2}{m}}E_0^{1-\gamma}, \quad (11)$$

where A is the cross sectional area of the electron beam. Substituting (5) into (11) yields

$$\frac{dN}{dt} = A\frac{\gamma - 2}{\gamma - 1}\frac{F(0)}{E_0}. \qquad (12)$$

Let us estimate the minimum density $n_{\min}$ of the background plasma that is able to provide an efficient transfer of energy from the accelerated electrons to thermal particles via Coulomb collisions. Taking $s_0 = 10^8$ cm and $E_0 = 3$–10 keV, we find $n_{\min} = E_0^2/2as_0 = 10^{10}$–$10^{11}$ cm^{-3}, consistent with the restrictions adopted in the previous section.

Estimates show that, in the case of hot and relatively rarefied plasma, radiative losses are considerably smaller than heat-conductive losses, for which

$$F_T = \eta T^{5/2}\frac{dT}{ds} \approx 10^{-6}\frac{T^{7/2}}{s}\ \text{erg/cm}^2\,\text{s}. \qquad (13)$$

Then, using the energy-balance equation $F_T \approx F(0)$ with $T = 6 \times 10^6$ K, $s = 10^8$ cm, and $E_0 = 3$–10 keV, we find from (12) and (13) that $dN/dt = 3 \times (10^{35}$–$10^{36})$ s^{-1}.

The resulting estimates of dN/dt considerably exceed the values that follow from the coronal magnetic-bottle model and are comparable to the typical values invoked to interpret the hard X-ray radiation of solar flares [24]. In addition, the value of dN/dt is obviously underestimated, since we have not taken into consideration energy losses due to plasma

"evaporation," which are also are quite substantial. Indeed, we can estimate the energy flux due to the evaporation of the hot plasma layer as

$$F_{ev} \approx nkTs.$$

Hence, according to (13), we have

$$\frac{F_T}{F_{ev}} \approx 7 \times 10^9 \frac{T^{5/2}}{ns^2}. \quad (14)$$

Setting in (14) $n = 10^{10}$–10^{11} cm^{-3}, $T = 6 \times 10^6$ K, and $s = 10^8$ cm, we obtain $F_T/F_{ev} = 0.6$–6; i.e., plasma evaporation can play a fairly important role in the energy balance. This also testifies that the energy of the accelerated electrons alone is usually not sufficient to produce high-temperature plasma layers in the lower corona and transition region of the Sun. However, their role can considerably increase during powerful flare activity [26].

MHD waves generated by convective motions in the photosphere can also be responsible for heating. In this case, the energy flux of acoustic waves is rather small [27]; therefore, these modes are not able to make an important contribution to the production of high-temperature plasma layers. At the same time, Alfvén waves with periods of 10–40 s can certainly provide coronal temperatures [27]. It is natural to attribute their efficient dissipation in the transition region to an increase of the magnetic-field gradient, which creates favorable conditions for the realization of phase mixing or the resonant absorption of waves. An important role for the reconnection of magnetic lines should likewise not be excluded.

5. DISCUSSION AND CONCLUSIONS

We have used numerical modeling to consider the effect of thin, hot plasma layers on the properties of the thermal gyroresonant emission of sunspot-associated sources. We have also analyzed mechanisms that can result in the formation of high-temperature layers in the upper chromosphere and lower corona of the Sun.

Our results suggest that images of a sunspot-associated source should resemble either rings or horseshoes, depending on the source's location on the solar disk. This suggests that these features could be detected in observations with high angular resolution ($\sim 1'$). In this case, an alternation of the sign of polarized emission within the source should be manifest; in our model, this is especially pronounced at 2.5–3.5 cm.

We have shown that, for a cylindrical layer, the fluxes of microwave emission at 2–4 cm increase considerably with increasing temperature, as is characteristic of proton events. We have established the possibility of double, and even multiple, reversals of the polarization sign for hot layers with various shapes. Thus, our model agrees fairly well with the observations and can be applied to the interpretation of sources with dominant ordinary wave emission [10–14].

Our analysis neglected the condition of hydrostatic equilibrium; at first glance, this seems a quite crude approximation. However, this assumption is consistent with the observational data obtained with TRACE, which show that up to 70% of coronal loops display high-velocity plasma flows that propagate at close to the sound speed [28]. In our opinion, this testifies to nonstationary energy release at the feet of coronal loops, which results in a violation of hydrostatic equilibrium. This conclusion is supported by the results of Aschwanden [29], which indicate that the heating of coronal loops is localized at their feet.

In the context of a coronal magnetic-bottle model, we have analyzed the formation of a hot layer associated with the precipitation of energetic electrons captured in a magnetic trap (halo) in the lower corona of the Sun. According to our estimates, the energy of the electrons is not sufficient to provide the required temperatures. Note that, even in fairly powerful flares, the high-velocity electrons are not always capable of providing the observed thermodynamic parameters of the flare plasma [30–32]. The flux of acoustic energy is rather small; therefore, in our opinion, Alfvén modes or microflare processes due to magnetic reconnection are most likely responsible for the possible temperature inversion in the lower corona and upper chromosphere.

ACKNOWLEDGMENTS

This work was supported by INTAS (grant no. 00-181) and the Russian Foundation for Basic Research (project no. 03-02-17528).

REFERENCES

1. G. B. Gelfreikh, in *Three-Dimensional Structure of Solar Active Regions*, Ed. by C. Alissandrakis and B. Schmieder (Astron. Soc. Pac., San Francisco, 1998); Astron. Soc. Pac. Conf. Ser. **155**, 110 (1998).
2. T. I. Kaltman, A. N. Korzhavin, N. G. Peterova, *et al.*, in *Three-Dimensional Structure of Solar Active Regions*, Ed. by C. Alissandrakis and B. Schmieder (Astron. Soc. Pac., San Francisco, 1998); Astron. Soc. Pac. Conf. Ser. **155**, 140 (1998).
3. S. M. White and M. R. Kundu, Sol. Phys. **174**, 31 (1997).
4. C. E. Alissandrakis and M. R. Kundu, Astrophys. J. Lett. **253**, L49 (1982).
5. K. R. Lang and R. F. Willson, Astrophys. J. Lett. **255**, L111 (1982).
6. N. Gopalswamy, J. P. Raulin, M. R. Kundu, *et al.*, Astron. Astrophys. **316**, L25 (1996).

7. V. V. Zheleznyakov, *Radio Radiation of the Sun and Planets* (Nauka, Moscow, 1964) [in Russian].
8. E. Ya. Zlotin, Astron. Zh. **45** (3), 585 (1968) [Sov. Astron. **12** (3), 464 (1968)].
9. G. B. Gel'freĭkh, Izv. Ross. Akad. Nauk, Ser. Fiz. **59**, 90 (1995).
10. Sh. B. Akhmedov, V. M. Bogod, V. N. Borovik, *et al.*, Issled. Geomagn. Aeron. Fiz. Solntsa **62**, 172 (1982).
11. Sh. B. Akhmedov, V. M. Bogod, V. N. Borovik, *et al.*, Izv. Spets. Astrofiz. Obs., Astrofiz. Issled. **25**, 105 (1987).
12. V. M. Bogod and S. Kh. Tokhchukova, Pis'ma Astron. Zh. **29**, 305 (2003) [Astron. Lett. **29**, 263 (2003)].
13. N. G. Peterova, A. A. Golovko, and M. N. Stoyanova, Astron. Zh. **74**, 466 (1997) [Astron. Rep. **41**, 409 (1997)].
14. N. G. Peterova and A. N. Korzhavin, Bull. Spec. Astrophys. Obs. **44**, 71 (1998).
15. G. B. Gel'freĭkh, A. N. Korzhavin, and G. F. Shemyakin, *Radio Astronomical Observations of the Solar Eclipse of May 20, 1996*, Ed. by G. B. Gel'freĭkh and N. G. Peterova (Nauka, Moscow, 1972), p. 50 [in Russian].
16. Ya. Zlotnik, Radiophys. Quantum Electron. **44**, 53 (2001).
17. A. V. Stepanov and Y. T. Tsap, Sol. Phys. **211**, 135 (2002).
18. D. Tsiklauri and V. M. Nakariakov, Astron. Astrophys. **379**, 1106 (2001).
19. E. Ya. Zlotnik and O. A. Sheĭner, in *Current Problems of Solar and Stellar Activity*, Ed. by V. V. Zaitsev (IPF RAN, Nizhni Novgorod, 2003), Vol. II, p. 308 [in Russian].
20. T. I. Kal'tman and A. N. Korzhavin, in *Current Problems of Solar and Stellar Activity*, Ed. by V. V. Zaitsev and L. V. Yasnov (NIIRF SPbGU, St. Petersburg, 2002), p. 51 [in Russian].
21. G. B. Gel'freĭkh and A. N. Korzhavin, *Physics of Sunspots*, Ed. by V. E. Stepanov (Nauka, Moscow, 1976), p. 94 [in Russian].
22. C. E. Alissandrakis, M. R. Kundu, and P. Lantos, Astron. Astrophys. **82**, 30 (1980).
23. R. Thomas, R. Starr, and C. J. Crannell, Sol. Phys. **95**, 323 (1985).
24. J. A. Miller, P. J. Cargill, A. G. Emsile, *et al.*, J. Geophys. Res. **102**, 14631 (1997).
25. B. V. Somov and S. I. Syrovskiĭ, Usp. Fiz. Nauk **120**, 217 (1976) [Sov. Phys. Usp. **19**, 813 (1976)].
26. T. P. Borisevich, G. N. Il'in, A. N. Korzhavin, *et al.*, Kosm. Issled. **42**, 1 (2004) [Cosmic Res. **42**, 561 (2004)].
27. G. B. Gel'freĭkh, Yu. T. Tsap, Yu. G. Kopylova, *et al.*, Pis'ma Astron. Zh. **30**, 540 (2004) [Astron. Lett. **30**, 489 (2004)].
28. M. J. Aschwanden, in *SOLMAG 2002*, Ed. by H. Sawaya-Lacoste (Noordwijk, Netherlands, 2002), ESA SP-505, p. 191.
29. M. J. Aschwanden, Astrophys. J. Lett. **559**, L171 (2001).
30. S. Urpo, N. M. Bakhareva, V. V. Zaitsev, and A. V. Stepanov, Sol. Phys. **154**, 317 (1994).
31. A. Czaykowska, D. Alexander, and B. De Pontieu, Astrophys. J. **552**, 849 (2001).
32. Yu. T. Tsap, Yu. G. Kopylova, and N. S. Nesterov, Kin. Fiz. Neb. Tel **18**, 3 (2002).

Translated by G. Rudnitskiĭ

Astronomy Reports, Vol. 49, No. 9, 2005, pp. 755–766. Translated from Astronomicheskiĭ Zhurnal, Vol. 82, No. 9, 2005, pp. 847–859.

Integrated Characteristics of the Radial Magnetic Field in Solar Active Regions during Quiet and Flare-Productive Phases of Their Evolution

O. V. Chumak[1] and H.-Q. Zhang[2]

[1]*Sternberg Astronomical Institute, Moscow State University, Universitetskiĭ pr. 13, Moscow, 119992 Russia*

[2]*National Astronomical Observatories, Chinese Academy of Sciences, Beijing, 100012 China*

Received September 30, 2004; in final form, February 17, 2005

Abstract—This paper presents a statistical study of various integrated parameters of solar active regions, such as the distance between the polarity centroids, the inclination of the magnetic axis, the flux imbalance between the polarities, and the interosculation parameter of the magnetic fluxes of opposite polarities. The study is based on observations of the longitudinal photospheric magnetic field. We analyze ten active regions for which an appreciable volume of data with good spatial resolution are available. The distributions of the above parameters with field strength are very different for quiet and flare-productive active regions and for quiet and flare-active evolutionary phases of the same active region. Some distributions exhibit substantial and characteristic variations during the development of certain flare processes. The first moments of the distributions reflect specific features in the configuration of the photospheric magnetic fields and are correlated with the level of eruptive processes in the active regions. © *2005 Pleiades Publishing, Inc.*

1. INTRODUCTION

Studies of solar active regions (ARs) are of great practical and general scientific importance. ARs are a basic and fundamental element of solar activity. The investigation of ARs is an important problem, not only from the standpoint of numerous applications, but also in the context of understanding the phenomenon of solar and stellar activity as a whole. Moreover, solar ARs present a unique opportunity for studying plasmas under physical states that cannot be realized in the laboratory. Strong local magnetic fields are the basic pattern-forming element of solar ARs. Studies of the physics of the processes underlying the origin and dynamics of magnetic-flux structures in an AR provide clues to the evolution of ARs and their production of geo-efficient factors. It is thus natural that analyses of relationships between the structural morphology of the photospheric magnetic fields in solar ARs and their flare activity and coronal-eruptive activity have been the subject of numerous studies over the past several decades.

In simple cases, the magnetic fields of ARs are essentially dipolar and display very small local twists of the field vector. The magnetic fields in such ARs are nearly potential, i.e., their energy is nearly minimum. In complex cases, an AR presents a complicated pattern of magnetic fluxes on various scales and with various strengths. The photospheric cross sections of major fluxes are manifest in white light as sunspots in various evolutionary stages. This almost chaotic landscape is constantly changing due to the emergence of new flux, the disappearance of old flux, and slow or fast movements of sunspots and pores in various directions. The magnetic fields of ARs with such complex morphologies only rarely represent a low-energy potential field. The complex structure and fast dynamics result in the formation of structures that can be qualitatively described as twisted, sheared, etc. Such structures provide evidence for strong departures from potentiality, the storage of excess energy in the magnetic fields, and the presence of major current systems in them.

It is usually believed that the mechanism for the release of the energy stored in such fields is magnetic reconnection. This mechanism can ensure a rapid conversion of magnetic energy into kinetic and thermal energies. Details of the energy accumulation and the subsequent energy release are now understood fairly well. A magnetic energy of the order of 10^{29}–10^{32} erg, required for flares, is accumulated in nonpotential fields with considerable field-aligned currents (see, e.g., [1–4]). The origin and dynamics of such configurations in the chromosphere is directly dependent on specific morphological and kinematic features of the photospheric magnetic fields in the ARs. It is therefore clear that investigations of the state of the magnetic fields in ARs at the photospheric level and analyses of magnetic-field stability against flares are of paramount importance.

Numerous studies have shown that the frequency and intensity of solar flares correlate fairly well with

the size and complexity of the AR in which they develop [5, 6]. The flare productivity is also related to the presence of rapidly emerging fresh magnetic flux (see, e.g., [7–10]) and overall restructuring of the magnetic fields [11, 12]. However, there is no exact correlation: some regions give rise to major flares when they have their simplest morphology, and far from all ARs with complex morphologies produce such flares [6, 13]. Thus, one problem is that nobody has discovered a set of rules or signatures that unambiguously relate specific features of the photospheric magnetic-field configuration with violent ejections of thermal and kinetic energy in the chromosphere and corona.

Most recent studies have concentrated on the magnetic shear transverse to the inversion line of the radial field component [14, 15] (see also references therein) and the spatial and temporal correlations between this shear and the occurrence of X-ray flares. However, results obtained by different observers for different ARs often disagree, due to both technical and fundamental reasons. Technical reasons include the relatively low accuracy with which the transverse component of the field can be measured, the dependence of the final spectral and polarimetric observational results on seeing conditions and instrumental factors, the 180° ambiguity, etc. [16, 17]. These technical difficulties can be successfully overcome (see, e.g., [14]). However, it is very difficult to overcome fundamental difficulties, which are associated, first and foremost, with the weak spatial correlations between flare processes and structural features or local variations in the photospheric fields [18].

In our view, these weak correlations indicate that various fine-structure features of the diverse morphologies do not represent the basic origin and source of flares, but instead may serve as a triggering mechanism that releases the energy stored in magnetic fields on scales comparable to the size of the entire AR. If this is the case, it does not matter which of the trigger mechanisms will operate at a given time and where it will operate; it is only important whether a sufficient amount of energy is accumulated in the field and how stable the corresponding configurations are against such local disturbances.

In this context, it seems reasonable to pay greater attention to a more detailed study of various integrated parameters of ARs rather than to the local dynamics and fine-structure morphology of the field. These parameters should directly or indirectly reflect the overall excess of accumulated energy on the scale of the entire AR and the stability of the entire magnetic-field configuration in the AR against local disturbances. For example, such parameters include quantities describing the departures of the photospheric magnetic field from a potential field. Note, however, that the results of investigations of this sort have thus far remained inconclusive [19–21]. This could be due to a somewhat inadequate choice of characteristic parameters and analysis techniques. Our own experience [22] has demonstrated that similar approaches are fairly promising in addressing the above problems. Here, we will demonstrate this by considering observational data on the line-of-sight components of the magnetic fields in ten ARs.

2. OBSERVATIONAL DATA

The magnetometric observations of solar ARs were carried out at the Beijing Astronomical Observatory of the Chinese Academy of Science in 1989–2001. The observations were obtained using the Solar Magnetograph (with an aperture of 350 mm), which is part of the Solar Multichannel Telescope, which comprises a system of four separate solar instruments with a common parallactic mounting [23, 24].

The solar magnetograph is used to obtain data on the magnetic fields (full vectors) and line-of-sight velocities in ARs on a regular basis. Observations have been carried out since 1987 in the FeI (5324.19 Å) and Hβ (4861.34 Å) lines. The instrument is a so-called video magnetograph, in which a narrowband birefringent filter replaces the spectrograph. The Beijing video magnetograph is distinguished for its high sensitivity and high spatial and temporal resolutions.

The magnetograph has undergone several reconstructions since 1987. Currently, the telescope's field of view projected onto the CCD array (512 × 512 pixels) is $4' \times 5.5'$ (more accurately, $3.75' \times 5.45'$, or 163 Mm × 237 Mm), making it possible to study a substantial part of an AR rather than only a fragment. Thus, one pixel of the CCD array corresponds to approximately $0.4'' \times 0.7''$, or an area on the Sun (near the disk center) of $\sim 1.8 \times 10^{15}$ cm^2 = 1.8×10^5 km^2 = 0.180 Mm^2 = 0.06 millionths of the hemisphere. The area on the Sun that corresponds to the entire CCD array is 38 631 Mm^2. Time resolutions as high as 1 min are possible. The actual accuracy is ±10 G for the line-of-sight and ±15 . . . ±25 G for the transverse components of the magnetic field. More detailed information on the Solar Multichannel Telescope of the Beijing Astronomical Observatory can be found in [23, 24] and other publications of the Beijing Astronomical Observatory of the Chinese Academy of Sciences.

More than 300 magnetograms of the line-of-sight component of the magnetic field at the FeI 5324 Å wavelength were selected for reduction over all ten ARs. Only data for the selected ARs obtained under conditions of excellent or good seeing were chosen for analysis. Information on solar flares in the ARs were

obtained from the corresponding issues of the *Solar Geophysical Data*.

Solar flares represent a complex phenomenon that is accompanied by an abrupt release of nonpotential energy in the upper layers of the solar atmosphere. Their spatial and temporal parameters are traditionally referenced to the chromospheric ejections of energy that can be observed in Hα. However, they are also frequently observed as impulsive events in hard X-ray emission and/or sharp enhancements in soft X-rays (SXRs) and are accompanied by high-energy particle fluxes [2, 24] (see also references in [2]). Here, we regard flares primarily as SXR events, particularly marking the onset of the flare according to the GOES SXR data in the NOAA Space Environment Center's listings of events (*Solar Geophysical Data,* 1989–2002). This is mainly because these events are well documented in terms of their amplitude, time, and spatial position, with virtually no gaps in the observation series.

To avoid edge effects, we analyzed observational data obtained at longitudes within ±60° of the central meridian; a normal correction for latitude and longitude projection effects was applied, so that all magnetic-field values, lengths, and areas were reduced to the disk center. This made it possible to compare parameters for different ARs and different states of the same AR in a unified, physically independent heliographic coordinate system.

3. PARAMETERS ANALYZED

A number of integrated parameters appropriate for quantitative descriptions of the current state of an AR based on magnetometric and Doppler observations were suggested in [25–27]. The numerical values of these parameters depend on the corresponding magnetic-field strength. It is well known that several types of magnetic fields can coexist in an AR, viz., background fields with various levels of organization, the fields of decaying old ARs, the fields of newly emerging magnetic fluxes, etc. Any of these fields has its own flux distribution, in accordance with the magnetic-field strength and the spatial topology of the magnetic fluxes. The state of an AR is determined by a complex interplay of all these fields coexisting in the AR. Moreover, the observational data are subject to noise due to various types of errors. It is desirable that the contributions of all the fields present in the AR be taken into account with corresponding weights in the calculated integrated parameters and that the contribution of random errors be minimized.

We present here some results of examining the properties of the radial photospheric magnetic fields in ten solar ARs derived from the integrated characteristics of these fields. We consider the following four parameters quantifying the current integrated properties of the magnetic fields in the AR:

(1) the distance (in Mm) between the centroids of the polarities in the AR weighted by the field strength, Rns;

(2) the angle (in degrees) between the vector **Rns** (the magnetic axis of the AR) and the local parallel, Fi;

(3) the interosculation parameter of the magnetic fluxes, or the complexity parameter of the AR, $Hu = (Rn + Rs)/Rns$;

(4) the flux imbalance, $Ov = (Fs + Fn)/Fc$.

Here, Fn and Fs are the magnetic fluxes (in Wb) of northern- and southern-polarity fields, respectively, determined from the radial component of the magnetic field; $Fa = |Fn| + |Fs|$; $Rn = (Nn)^{1/2}$ and $Rs = (Ns)^{1/2}$ are the equivalent linear sizes (in Mm) of the N and S polarities; and Nn and Ns are the areas of the N and S polarities. More detailed information on these and some other integrated parameters, together with a description of the procedures used to extract them from the observational data, can be found in the already cited papers [22, 25–27], as well as in [28].

Our choice of precisely these four parameters out of the numerous possible integrated characteristics of ARs was dictated by the results of our previous studies (see [22, 28] etc.). We found that, if we consider only the radial magnetic field of an AR, these four parameters are the most variable and sensitive to changes in the field. Furthermore, these parameters have a number of other useful properties: (1) they can be derived from the most reliable observational data (the radial field); (2) they are derived via summation and averaging, i.e., the operations normally used to suppress random errors and enhance the signal-to-noise ratio (we intentionally did not use parameters based on data of different accuracies and on numerical differentiation, subtraction, division, etc., such as radial currents, helicities, and others, which lead to substantial increases in the random errors); (3) since the four parameters are geometric (Rns, Fi) or dimensionless (Hu, Ov) characteristics of the AR magnetic field, they are basically insensitive to variations in the observed output signal due to changes in atmospheric conditions during an observation. This allowed us to avoid complex, sometimes questionable, and not very trustworthy procedures for correcting the calculated parameters for seeing conditions.

We note here the basic properties of the parameters considered that are required to understand the results presented in Section 4 below.

Theoretically, the distance between the polarities in the AR averaged using the radial magnetic field as a weighting factor, Rns, can range from zero to

200 Mm or so (the characteristic length on the Sun specified by the field of view of the recording system; see the preceding section). In fact, as we will see below, Rns ranges from 10 to 100–120 Mm. It is obvious that, if we compare ARs with similar net magnetic fluxes, larger field gradients and more complex magnetic-flux topologies can be expected in ARs for which this parameter is smaller. Among the advantages of this parameter are its clear meaning, simple computability, good variability, and high stability against noise. One drawback is that it does not incorporate the net magnetic flux of the AR: a highly developed AR with a complex configuration and a simple pair of pores can give the same value for this parameter. Therefore, comparisons between various ARs based on this parameter alone are of limited interest. It makes sense to consider this parameter for a single AR in the course of its evolution, provided that the net flux is relatively stable, or in combination with other parameters, such as the net flux.

The angle between the magnetic axis of the AR and the local parallel has been considered by many researchers. Noteworthy among recent studies is the fundamental investigation by Wang [29] (see references for preceding studies therein). Wang [29] investigated the statistical relationship between this angle and the net flux, latitude, distance between the polarities, etc. Our technique for calculating the angle Fi is somewhat different from that employed by Wang, but these differences are not important, and our results are consistent with his statistical conclusions. Our procedure for calculating Fi as the arctangent of the inclination to the local parallel, Rns, proves to be less affected by random errors. This parameter and Rns have nearly the same advantages and disadvantages. In the context of our problem, it makes sense to consider this parameter (or Rns) for a given AR either along when tracing the evolution of this AR or jointly with other integrated characteristics.

The interosculation parameter of the magnetic fluxes, or the complexity parameter of the AR configuration, Hu, that we introduced shares all the advantages of Rns, but is virtually free of drawbacks. Since the area and magnetic flux of some polarity in the AR are related by fairly simple power laws [30], the equivalent linear dimension of this polarity enables us to consider both the magnitude and degree of concentration of its flux. At the same time, the ratio of the sum of the equivalent linear dimensions of the polarities to the weighted mean distance between their centroids can be used to determine the degree of interosculation for magnetic fields of opposite polarities. This parameter is easy to determine and stable to variations in the seeing, and can be fairly reliably obtained even from data with moderate spatial resolution. In addition, this parameter can be used to compare the degrees of complexity of different ARs, via comparison of the degree of interosculation of magnetic fields of opposite polarities. In this respect, it can be viewed as a fairly universal structural parameter of the AR reflecting the topological complexity of its magnetic fluxes. This parameter is dimensionless and, theoretically, it can range from zero to infinity. Zero corresponds to infinitely large Rns and infinity to zero Rns. The geometrical meaning of Hu suggests that values between zero and approximately 0.5 correspond to well-separated bipolar configurations, or β configurations, according to the Mt. Wilson magnetic classification of ARs. Values in the range 0.5–1.0 correspond to $\beta\gamma$ configurations; values from 1.0 on up, to $\gamma\delta$ and δ configurations of varying degrees of complexity. In practice, as we will see below, Hu assumes values ranging from 0.1 for quiet ARs to about 10.0 for preflare states in most flare-productive regions. The high sensitivity of this parameter to any changes in the magnetic field, the ability to interpret its values in a clear and obvious way, and its relative universality and stability against noise make it a convenient tool for absolute and relative estimates of the structural complexity of ARs. We will give particular attention to this parameter below.

The relative magnetic-flux imbalance between the two polarities—the parameter Ov—provides a quantitative estimate of the degree of closure of the magnetic fluxes within an AR. As can be seen from its definition above, this parameter is also dimensionless and can range from +1.0 to −1.0. These limiting values correspond to unipolar configurations, while values near zero correspond to ARs with well-balanced fluxes. Any intermediate value yields a quantitative estimate of the degree of openness of the AR; i.e., the degree to which it is connected to other ARs by magnetic fluxes.

We calculated all these parameters for each AR at 50-G intervals to obtain the field-strength distributions of the parameters. Next, we calculated the first four moments of each of these distributions,

$$Mx = \frac{1}{n}\sum_{j=0}^{n-1} x_j,$$

$$Dx = \left[\frac{1}{n-1}\sum_{j=0}^{n-1}(Mx - x_j)^2\right]^{1/2},$$

$$Sx = \frac{1}{n}\sum_{j=0}^{n-1}\left[\frac{x_j - Mx}{Dx}\right]^3,$$

$$Kx = \frac{1}{n}\sum_{j=0}^{n-1}\left[\frac{x_j - Mx}{Dx}\right]^4 - 3,$$

Table 1. Main data for non-flare-productive ARs

NOAA	HSOS	Date	Time (UT)	X	Y	Fa, 10^{-14} Wb	MC
5572	89159	08.07.1989	2:03	22.7	−16.8	4.453	B
6239	90200	01.09.1990	4:54	−21.9	15.2	1.503	A
6878	91209	17.10.1991	2:52	−3.9	−25.8	2.458	B
7555	93101	02.08.1993	5:41	13.7	10.9	1.563	B
7568	93112	28.08.1993	2:59	18.3	10.5	0.28	B
7737	94057	24.06.1994	1:32	7.5	−16.7	0.449	B
7896	95050	07.08.1995	4:36	26.1	1.5	2.361	B
7901	95053	24.08.1995	5:29	7.3	4.2	0.324	B

Table 2. Means and standard deviations for the four parameters

NOAA	$MRns$	MFi	MHu	MOv	$DRns$	DFi	DHu	DOv
6239	77.9	24.5	0.188	−0.161	24.87	13.20	0.231	0.453
7555	63.5	297.2	0.264	−0.012	29.68	9.38	0.303	0.172
7896	45.5	11.7	0.281	−0.014	13.66	6.80	0.339	0.359
5572	46.6	178.3	0.348	0.308	19.13	53.57	0.326	0.323
6878	96.5	206.1	0.166	−0.135	28.29	55.17	0.187	0.241
7901	37.4	33.3	0.342	−0.064	14.83	20.49	0.412	0.152
7737	50.2	160.2	0.222	−0.109	19.83	52.03	0.216	0.171
7568	59.8	84.7	0.12	0.153	25.60	14.79	0.109	0.291
Mean	59.7		0.241	−0.004	22	28.2	0.265	0.27
St. dev.	19.5		0.082	0.15	6.02	21.4	0.097	0.106

thus extracting 16 parameters from each magnetogram. Here, Mx is the average over the distribution for each parameter, Dx is the standard deviation, which provides an estimate for the departure of a given parameter from its mean value in the given distribution, and Sx is the third moment, which describes the asymmetry of the distribution—its value indicates the direction and magnitude of the displacement of the maximum relative to the mean, or the degree of asymmetry of the distribution relative to its maximum. A Gaussian distribution has zero asymmetry, so that Sx can be regarded as the degree of deviation of our distribution from a normal distribution. Finally, Kx is the fourth moment, or excess, which also differs from zero for non-Gaussian distributions or distributions consisting of several Gaussian distributions. This quantity describes the sharpness of the peak or the degree to which a given distribution is elongated.

It is noteworthy that the dependence of the radial component of the field Bz on the height z in a force-free approximation can be represented by the simple expression $Bz(z) = B_0 J_0(kR)\exp(-lz)$, where B_0 is the field at the photospheric level, $J_0(kR)$ the zeroth-order Bessel function, R the radius in a cylindrical coordinate system (R, ϕ, z), and l a scaling constant [3]. If $l = k$, the field is potential (the shear angle vanishes). As l varies from k to 0, the shear increases from 0 to $\pi/2$, and the field becomes progressively more twisted. This expression for $Bz(z)$ indicates that, for a given k and l, any fixed value of $Bz(z)$ will be observed at higher altitudes, the greater B_0. In other words, our field-strength distributions for the parameters can also be interpreted, in a sense, as their height distributions.

The variation in the rotation of the magnetic axis, Fi, with field strength can be treated as a shear on the scale of the entire AR. The mean value of this angle, MFi, is not as important as its standard deviation DFi. It is this quantity that characterizes the range

Table 3. Asymmetries and excesses for four parameters

NOAA	$SRns$	SFi	SHu	SOv	$KRns$	KFi	KHu	KOv
6239	−2.021	−0.397	2.111	−0.068	4.077	−1.271	4.225	−1.571
7555	0.022	−2.075	1.415	1.491	−0.393	2.448	1.428	1.445
7896	−2.243	−0.311	2.401	−1.298	4.921	−0.838	6.205	0.632
5572	−0.591	−2.292	1.055	−0.306	−0.023	5.016	0.447	−1.209
6878	−2.332	−3.346	1.458	0.148	5.998	9.582	1.332	−0.83
7901	−0.852	0.997	2.049	−0.661	0.362	0.613	3.966	−0.687
7737	−1.186	−2.621	2.104	−1.158	1.071	5.181	4.841	0.742
7568	−0.298	1.507	1.719	−0.242	−0.354	0.319	2.438	0.251
Mean	−1.19	−1.07	1.79	−0.26	1.96	2.63	3.11	−0.15
St. dev.	0.91	1.77	0.45	0.87	2.61	3.73	2	1.07

of variation of the angle, and can serve as an indicator for excess magnetic energy stored on the scale of the whole AR. This angle does not vary uniformly with growth of the field. The field strength (height) at which these variations reach large amplitudes is of particular importance. If the variations in this angle are large in the presence of strong fields (the asymmetries SFi have large magnitudes), this can provide an additional indicator for the growth of nonpotential energy in strong fields.

The mean value of the polarity-interosculation parameter, MHu, quantitatively characterizes the structure of the AR and reflects the magnitudes of gradients and the topological complexity and overall instability of the magnetic configuration, while its standard deviation, DHu, describes the range of variations in the structural complexity with field strength (height). Large positive asymmetries of this parameter, SHu, represent evidence for high complexity and instability of the magnetic configuration in the presence of strong fields. Large excesses KHu also testify to the presence of strong anomalies in the distribution $Hu(B)$ and, therefore, to instability of the magnetic structure of the AR.

The interpretation of $MRns$, $DRns$, $SRns$, $KRns$, MOv, DOv, SOv, and KOv is also fairly obvious, and we will not dwell on this here. Our experience in handling data on the radial field has demonstrated that the first and second moments are especially significant. The third and fourth moments are less informative in our problem, although they also can provide useful information about the state of the AR magnetic field in some cases. We restrict our discussion here to these remarks and will now proceed to presenting the results.

4. SOME RESULTS

In this section, we describe some of the most interesting and typical results obtained in our analysis of the field-strength distributions of all four parameters considered above and their first four moments, for all ten ARs. We first examine the distributions and their moments for eight ARs with low flare productivity during their quiet evolutionary phases. We present the typical form of these distributions and typical values for their moments for quiet ARs. These results are needed for comparison with their counterparts for flare-productive ARs. The field-strength distributions of the parameters of two flare-productive ARs are presented for relatively quiet and active evolutionary phases; we also show the variations in the parameters during a flare.

4.1. Quiet ARs

We will use the field-strength distributions of the above parameters and the typical values of their moments for non-flare-productive ARs as a basis for comparison studies of various states and various ARs with both high and moderate flare productivity. Table 1 presents the data for eight quiet ARs; the columns contain (1) the international number of the AR (according to NOAA, Boulder); (2) the number adopted for this AR at the Huairou Solar Observing Station (Beijing), where the observations were carried out; (3) and (4) the date and time of observation; (5) and (6) the coordinates of the AR relative to the center of the solar disk; (7) the net magnetic flux Fa in units of 10^{14} Wb; and (8) the magnetic class of the AR at the observation time, according to the *Solar Geophysical Data* [31].

Table 2 gives the mean values and standard deviations of the four parameters for all eight ARs.

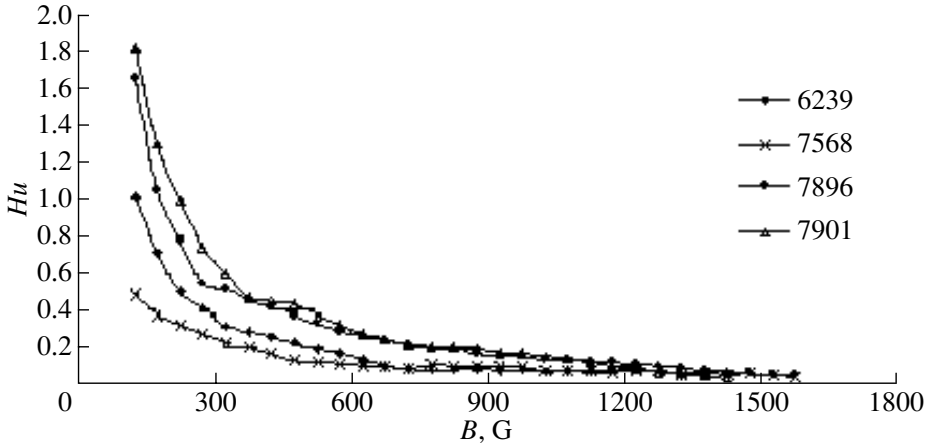

Fig. 1. Typical distributions $Hu(B)$ in non-flare-productive ARs.

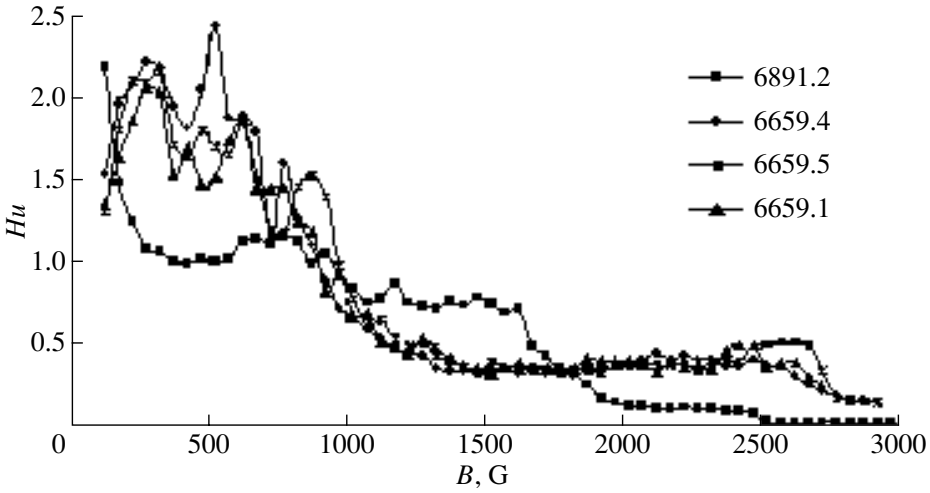

Fig. 2. Distributions $Hu(B)$ in flare-productive ARs during quiet evolutionary phases.

The columns contain the number of the AR, and the mean values of the parameters for these ARs together with their standard deviations. The next-to-last row of the table contains the parameters averaged over all eight ARs and the last row, the corresponding standard deviations. The quantity MFi is an exception, since such values have no meaning in view of the specificity of the angular measurements; however, the second and higher moments have their usual meaning.

We can see from Table 2 that the field-strength-weighted mean distances between the polarities in non-flare-productive ARs are, on average, about 60 Mm and range between approximately 40 and 80 Mm.

The mean value of the dimensionless complexity parameter, MHu, is 0.24 ± 0.08. Thus, magnetic class B (see Table 1) corresponds to MHu values from approximately 0.15 to 0.35. Values $MHu < 0.15$ represent magnetic class A, although the correspondence between the range of variation in MHu and a magnetic class is not unambiguous, in view of the qualitative and purely subjective nature of the magnetic classification [31]. These ranges will likely overlap, and the correspondence is meaningful only in the context of certain statistical-mean values. The fifth column in Table 2 shows that all eight ARs are well balanced in magnetic flux, with the mean imbalance being as small as -0.004. However, deviations from flux balance are significant in some individual regions.

Table 3 has the same structure as Table 2 and presents data on the asymmetries and excesses of the four parameters for the same eight ARs. The first column is analogous to the first columns of Tables 1 and 2, columns 2–5 contain the asymmetries, and columns 6–9 contain the excesses. The last two rows of Table 3 present the mean values and standard

Table 4. Mean values and standard deviations for AR 6659 (June 8, 1991)

Time (UT)	$MRns$	MFi	MHu	MOv	$DRns$	DFi	DHu	DOv
3:44	27.3	307.0	0.804	−0.451	10.28	74.15	0.696	0.426
4:11	28.7	310.5	0.761	−0.458	10.66	62.11	0.694	0.418
4:40	27.9	312.7	0.753	−0.455	10.65	61.49	0.618	0.417
5:06	26.7	287.1	0.848	−0.436	10.63	64.92	0.721	0.424
5:42	27.0	293.2	0.753	−0.452	9.68	70.95	0.581	0.413
6:14	25.5	286.9	0.946	−0.432	11.12	68.57	0.825	0.417
8:08	32.4	296.7	0.683	−0.583	12.18	67.56	0.858	0.406
Mean	28	299.2	0.792	−0.467	10.7	67.1	0.713	0.417
St. dev.	2.2	10.9	0.085	0.052	0.8	4.6	0.101	0.007

Table 5. Mean values and standard deviations for AR 6891 (October 25, 1991)

Time (UT)	$MRns$	MFi	MHu	MOv	$DRns$	DFi	DHu	DOv
1:23	69.1	152.8	0.505	0.297	52.9	30.28	0.572	0.563
2:17	71.4	150.7	0.545	0.224	59.3	31.63	0.497	0.574
3:06	48.1	235.5	0.831	0.009	35.0	50.15	0.773	0.408
5:18	42.4	222.9	0.809	0.021	25.2	47.93	0.653	0.431
5:35	47.8	203.7	0.675	0.185	28.6	49.54	0.626	0.556
6:10	36.8	213.4	0.776	0.089	21.4	46.08	0.574	0.497
7:12	36.2	214.9	0.843	−0.003	13.5	45.40	0.583	0.494
8:08	40.9	221.3	0.816	0.079	24.1	47.09	0.63	0.507
Mean	49.1	202	0.725	0.113	32.5	43.5	0.614	0.504
St. dev.	13.8	32.2	0.134	0.111	15.9	7.9	0.08	0.061

deviations of these moments for all eight ARs. Although eight ARs certainly cannot constitute a fully representative sample, they nevertheless can give us an idea of the mean variability of these parameters in quiet ARs.

Figure 1 shows the field-strength distribution of Hu for four of the eight ARs. Since the distributions for the other four ARs are similar and lie between the upper and lower curves, they are not plotted here to avoid cluttering the figure. We can see that Hu decreases rapidly and fairly smoothly with the field strength. For weak fields, high values of Hu are frequently observed. This is due to the fact that the areas of the two polarities are well mixed in the case of weak fields and, as a rule, are balanced on the scales of ARs (Ov is nearly zero). At the same time, since the magnetic-field energy is proportional to the square of the field strength, such fields do not contribute significantly to the flare process. Therefore, it would be desirable to cut off such weak fields in order to make the parameters more sensitive to the variations in strong fields. However, the question is the cutoff level, which could be chosen based on either theoretical considerations or via fitting for flare-active ARs. These two approaches are not contradictory, and the choice of a specific value ultimately depends on the formulation of the problem. It is only important that this level be explicitly indicated in a particular study and remain unchanged during the course of the analysis. Here, we adopted a cutoff level of 100 G and calculated all parameters using this value.

4.2. Flare-Productive ARs

In this study, we analyzed two flare-productive ARs observed at the Beijing Astronomical Observatory (Huairou) in 1991: AR 6659, observed from

Table 6. First two moments during the flare period of AR 6659 (June 9, 1991)

Time (UT)	$MRns$	MFi	MHu	MOv	$DRns$	DFi	DHu	DOv
1:06	18.96	252.10	2.285	−0.467	21.30	115.19	2.265	0.424
3:52	31.77	302.97	1.091	−0.459	13.71	73.40	1.035	0.407
4:25	32.19	305.64	0.869	−0.435	14.15	68.69	0.854	0.385
5:14	31.92	310.37	0.814	−0.461	13.53	62.23	0.832	0.402
5:29	33.72	307.66	0.658	−0.442	12.36	57.61	0.671	0.36
6:13	32.59	300.82	0.991	−0.446	12.88	71.12	1.042	0.377
6:51	34.71	305.49	0.801	−0.522	13.86	61.64	1.145	0.396
7:27	32.55	289.76	0.857	−0.493	12.92	88.42	1.093	0.388
8:01	32.64	307.61	0.744	−0.505	12.94	66.92	0.775	0.395
Mean	31.23	298.05	1.012	−0.47	14.19	73.91	1.081	0.393
St. dev.	4.69	18.24	0.494	0.03	2.73	17.92	0.470	0.018

June 3 to 9 and from June 12 to 16, and AR 6891, observed from October 22 to November 4.

According to the NOAA data, six flares of X-ray class X (five with classes X > 12.5), 31 flares of class M, and about 70 flares of class C were recorded in AR 6659 from June 1–15. Based on these data, we estimate the X-ray Flare Index (XRI) of this AR to be >81.1, making it the most flare-productive active region of the past two solar cycles, even exceeding the productivity of AR 5395 in March 1989, whose flare activity is well known for its geophysical repercussions (XRI = 57.0, according to the same data). Although AR 6891 did not display the absolute highest flare productivity, five class-X flares (1.9–6.1), about 30 class-M flares, and about 80 class-C flares were observed in this active region, according to the NOAA data.

We analyzed 113 magnetograms for AR 6659 and 156 for AR 6891. Unfortunately, the distribution of these data in observation time prevented us from tracing all the variations in the parameters studied in the preflare and flare periods in detail. Nevertheless, we obtained some results that we believe to be interesting.

4.2.1. Quiet Phase

It is known that periods of relatively low activity in flare-productive ARs alternate with powerful series of flares. The periods of reduced activity are of particular interest, since the energy accumulation and preparation for the next active phase seem to occur during these periods. In the ARs we consider, such periods occurred on June 8 for AR 6659 and on October 25 for AR 6891. To analyze this evolutionary phase of the AR, we selected magnetograms obtained at times of lowerest activity during these periods. The results are gathered in Tables 4 and 5 and in Fig. 2.

As in Fig. 1, the field strength (in Gauss) in Fig. 2 is plotted along the horizontal axis and the dimensionless parameter Hu along the vertical axis. To save room, we do not present the distributions of other parameters. Only four distributions are shown in Fig. 2 for the same reasons as in Fig. 1. A comparison of Figs. 1 and 2 shows substantial differences in the distribution of this parameter. The most important of these are the presence of local extrema at different field strengths and a generally higher level of Hu at all field strengths.

Tables 4 and 5, which present the first two moments of the parameters considered for the quiet phases of AR 6659 and AR 6891, demonstrate these differences quantitatively and in more definite form. The third and fourth moments are somewhat less informative, and are not given here in view of space limitations.

Comparing Tables 2, 4, and 5, we find that the higher the flare productivity, the lower the mean value $MRns$; in principle, this seems reasonable, but is not obvious a priori. The mean values of the complexity parameter, MHu, are higher, the higher the flare productivity of the AR. The mean values of the imbalance parameter, MOv, do not exhibit any correlation with the flare activity. The standard mean deviations of the angle DF demonstrate a clear relationship with the capacity of the AR for flare activity and display good internal accuracy (see the last rows of these tables). The standard mean deviations of the complexity parameter, DHu, along with its mean values, MHu, correlate well with the potential flare productivity of

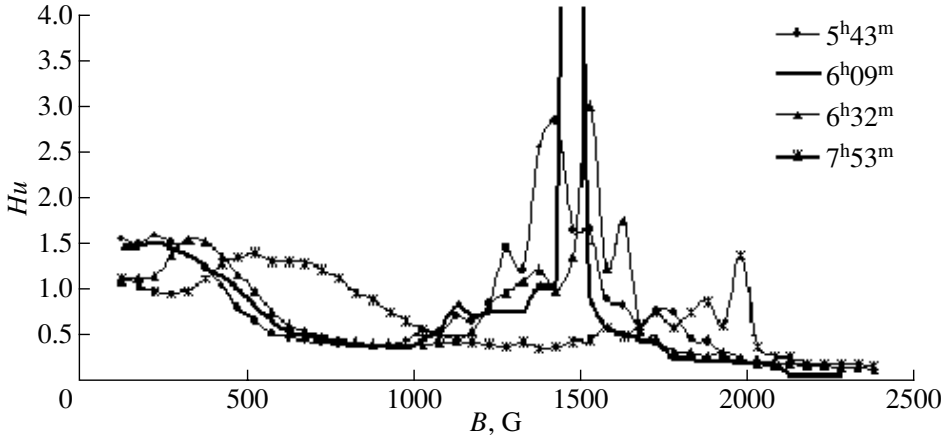

Fig. 3. Sequence of changes in the distribution $Hu(B)$ during the flare in AR 6891 on October 30, 1991.

the AR, with the spread in individual values being small (see the same tables). The parameter DOv—the standard mean deviation of the flux imbalance between the polarities—does not exhibit any relationship to the capacity of the AR for flare activity and displays a small spread in the individual values.

4.2.2. Active Phase

A clear growth in the amplitudes of the local extrema in the parameter distributions signals the termination of the quiet phase. If these extrema are observed at large field strengths and Hu is generally high, this heralds the onset of especially powerful flare events. A series of such complex distributions accompanies the entire flare-active phase.

As an example, Table 6 presents the first two moments for our four parameters in the flare-productive phase in AR 6659 (July 9, 1991). During the observations (first column of Table 6), this AR gave rise to one flare of class X10 (B3), one flare of class M19 (N1), and several minor flares of class C (SF). The XRI was 10.25 for this period. For comparison, this index was only 0.1 during an observational period of similar length on July 8 (Tables 4, 5), during a quiet phase.

A comparison of Tables 4 and 6 demonstrates that (1) the mean values $MRns$ somewhat increased during the flare-productive phase (compared to the quiet phase), remaining, however, within the standard deviation; (2) the mean values MFi and MOv remained virtually unchanged; (3) the mean values MHu clearly increased during the flare-productive phase and ranged approximately from 0.6 to 1.6. We can also conclude that the standard deviations $DRns$, DFi, and DHu were obviously higher and DOv lower during the flare-productive phase than during the quiet phase.

Figure 3 presents part of the sequence of distributions $Hu(B)$ during the relatively powerful flare of class X2.5 (3B) in AR 6891 on October 30, 1991. The onset of the flare (according to the NOAA data) was recorded at 6^h11^m, its maximum at 6^h21^m, and its end at 9^h03^m. This sequence of diagrams describing the development of the event is, to all appearances, quite typical and demonstrates all the main phases of changes in $Hu(B)$ during major flares.

We can see from Fig. 3 that, at 5^h43^m, approximately half an hour before the onset of the flare, an appreciable local peak of height $Hu = 2.84$ appeared in the $Hu(B)$ distribution in the range 1300–1600 G. By two minutes before the onset of the flare, this maximum had shifted to $B = 1475$ G and $Hu = 10.9$. Later, 11 min after the flare maximum (at 6^h32^m), this peak was characterized by values of $B = 1525$ G and $Hu = 3.02$, and then by values of $B = 1975$ G and $Hu = 1.38$ at 7^h53^m (the last available observation).

The time variations in MHu are illustrated by Table 7 (they do not appear as impressive when represented in terms of mean values). We can see that DHu displays a more pronounced response to the flare. Note that local features in the time variations of the other parameters presented in Table 7 also emerge almost synchronously (DOv seems to be the only exception). This confirms the conclusion [32] that the flux imbalance between the polarities is not linked to flare activity.

The third and fourth moments (asymmetry and excess), which are not presented in Table 7, also display strong variations. In particular, the excess KHu was an order of magnitude higher at 6^h09^m than at other times. Therefore, variations in the higher moments of the parameter distributions can also characterize the development of particular flare situations, although they are less informative in terms of their statistical mean values.

Table 7. The first two moments of the parameter distributions during the class-X2.5 flare in AR 6891 (November 30, 1991)

Time (UT)	$MRns$	MFi	MHu	MOv	$DRns$	DFi	DHu	DOv
5:42	39.47	141.52	0.811	0.404	25.04	98.33	0.633	0.429
6:09	51.28	141.75	0.826	0.427	33.22	84.13	1.587	0.454
6:32	48.83	104.23	0.774	0.554	21.14	94.38	0.573	0.471
7:18	40.89	166.94	0.717	0.271	18.51	80.59	0.384	0.453
7:53	41.02	159.34	0.686	0.309	16.55	79.21	0.408	0.458
Mean	44.31	142.81	0.763	0.393	22.92	87.31	0.717	0.453
St. dev.	5.36	24.20	0.061	0.111	6.59	8.55	0.501	0.015

5. CONCLUSIONS

To conclude, let us summarize the principal results of our study.

(1) Quiet ARs differ from flare-productive ones in the form and first moments of the distributions of their field-strength parameter.

(2) The distributions of the net flux, $Fa(B)$, and of the flux imbalance between the polarities, $Ov(B)$, do not exhibit any pronounced and unambiguous relationship with the flare process, nor do their first moments.

(3) The distributions of the magnetic-axis inclination, $An(B)$, and of the structural complexity parameter, $Hu(B)$, clearly discriminate between quiet and flare-productive ARs. Substantial changes in the form of these distributions and in their first moments begin several hours before the flare and reach their maxima during the flare.

While carrying out this study, we analyzed numerous field-strength distributions for the four considered parameters for several dozen ARs. Space limitations have forced us to omit numerous interesting features that appear in these distributions during the preflare phase and the flare itself, some of which we describe in [28]. The observational data that were available to us did not enable us to follow the time variations of the parameters in detail during all development phases of the flare process in solar ARs. For this reason, the results presented here should be considered preliminary. Further investigations based on higher-resolution observational data are needed.

However, the results obtained indicate that our approach is fairly promising as a means of finding links between particular configuration features of the photospheric magnetic field and major releases of thermal and kinetic energy in the chromosphere and corona. We believe that some details of these links could be clarified using the results obtained based on our approach. We also hope that such results will be useful in practical contexts, for example, in the development of short-term forecasts for certain geoefficient factors of solar activity.

ACKNOWLEDGMENTS

We are grateful to the staff members of the Huairou Solar Observing Station, National Astronomical Observatories of China, for magnetometric observations. This work was supported by the Chinese Academy of Sciences and the National Natural Science Foundation of China. Our particular thanks for discussions, valuable remarks, and constant attentive interest in this study go to Prof. V.N. Obridko.

REFERENCES

1. K. Tanaka and Y. Nakagawa, Sol. Phys. **33**, 187 (1973).
2. E. Tansberg-Hahsen and A. G. Emslie, *The Physics of Solar Flares* (Cambridge Univ. Press., Cambridge, 1988).
3. E. R. Priest, *Solar Magnetohydrodynamics* (Reidel, Dordrecht, 1982; Mir, Moscow, 1985).
4. T. R. Metcalf, J. Litao, A. N. McClymont, *et al.*, Astrophys. J. **439**, 474 (1995).
5. C. Sawyer, J. W. Warwick, and J. T. Dennett, *Solar Flare Prediction* (Colorado Assoc. Univ. Press, Boulder, 1986).
6. P. S. McIntosh, Sol. Phys. **125**, 251 (1990).
7. B. Schmieder *et al.,* Sol. Phys. **150**, 199 (1994).
8. T. Wang, A. Xu, and H. Zhang, Sol. Phys. **155**, 99 (1994).
9. D. P. Choudhary, A. Ambastha, and G. Ai, Sol. Phys. **179**, 133 (1998).
10. N. Nitta, L. van Driel-Gesztelyi, K. D. Leka, and K. Shibata, Adv. Space Res. **17**, 201 (1996).
11. V. S. Gorbachev, S. R. Kel'ner, B. V. Somov, and A. S. Shvarts, Astron. Zh. **65**, 601 (1988) [Sov. Astron. **32**, 308 (1988)].
12. T. Wang, Q. Jiong, and Z. Hongqi, Astron. Astrophys. **336**, 359 (1998).

13. S. R. Patty and M. J. Hagyard, Sol. Phys. **103**, 111 (1986).
14. J. Wang, Z. Shi, H. Wang, and Y. Lü, Astrophys. J. **456**, 861 (1996).
15. H. Li, T. Sakurai, K. Ichimoto, and S. Ueno, Publ. Astron. Soc. Jpn. **52**, 465 (2000).
16. D. L. Mickey *et al.*, Sol. Phys. **168**, 229 (1996).
17. B. J. LaBonte, D. L. Mickey, and K. D. Leka, Sol. Phys. **189**, 1 (1999).
18. J. Chen, H. Wang, H. Zirin, and G. Ai, Sol. Phys. **154**, 261 (1994).
19. M. J. Hagyard, J. B. J. Smith, D. Teuber, and E. A. West, Sol. Phys. **91**, 115 (1984).
20. A. Ambastha, M. J. Hagyard, and E. A. West, Sol. Phys. **148**, 277 (1993).
21. H. Wang, M. W. J. Ewell, H. Zirin, and G. Ai, Astrophys. J. **424**, 436 (1994).
22. O. V. Chumak *et al.*, Astron. Astrophys. Trans. **22** (3), 335 (2003).
23. G. Ai, Publ. Beijing Astron. Obs. **9**, 27 (1987).
24. N. Nitta, Astrophys. J. **491**, 402 (1997).
25. O. V. Chumak and Z. N. Chumak, Kin. Fiz. Neb. Tel **3** (3), 7 (1987).
26. O. V. Chumak, Tr. Astrofiz. Inst. Akad. Nauk Kaz. SSR **51**, 65 (1992).
27. O. V. Chumak, É. V. Kononovich, and S. A. Krasotkin, Izv. Ross. Akad. Nauk, Ser. Fiz. **62**, 1879 (1998).
28. O. V. Chumak and H. Zhang, in *Solar Variability as an Input to the Earth's Environment,* Ed. by A. Wilson (ESA Publ. Division, Noordwijk, 2003), ESA SP-535, p. 75.
29. H. Wang, Sol. Phys. **215**, 281 (2003).
30. O. V. Chumak and H. Zhang, Chin. J. Astron. Astrophys. **3** (2), 175 (2003).
31. *Solar Geophysical Data. Explanation of Data Reports,* No. 515 (Suppl.), 21 (1987).
32. L. M. Green, P. Démoulin, C. H. Mandrini, and L. Van Driel-Gesztelyi, Sol. Phys. **215**, 307 (2003).

Translated by A. Getling

Astronomy Reports, Vol. 49, No. 9, 2005, pp. 767–770. Translated from Astronomicheskiĭ Zhurnal, Vol. 82, No. 9, 2005, pp. 860–864.

Plasma Motion in Coronal Loops

A. A. Vedenov, M. M. Molodensky, V. L. Merzlyakov, and L. I. Starkova

Institute of Terrestrial Magnetism, Ionosphere, and Radiowave Propagation, Russian Academy of Sciences, Troitsk, Moscow oblast, 142190 Russia

Received July 25, 2004; in final form, February 17, 2005

Abstract—Three-dimensional images of solar coronal loops are constructed based on Hα observations obtained on June 15, 1982, and EUV data obtained by TRACE on November 6, 1999. Our analysis of these structures shows that coronal-plasma motion in crossed fields can form loops, in accordance with the theoretical model proposed by Kazarov and Molodenskiĭ. In general, the singular points in the magnetic fields of the active regions considered and the footpoints of the loops agree in location.

1. INTRODUCTION

Plasma motion in coronal loops can be explained by either plasma drifting in crossed fields [1] or interactions between the currents in filaments and the magnetic fields of active regions [2]. According to [3, 4], the onset of rapid motions is associated with the passage of a current through a potential barrier, which results in a "fold"-type catastrophe. Depending on the conditions under which this transition takes place, either finite or infinite motions of material are possible in the filaments [5].

We chose Hα loops as targets for our study of these drift motions. In their analysis of such loops located near the limb, Starkova and Shilova [6] found that the plasma moves along a loop from one footpoint to the other; i.e., between two regions of opposite magnetic polarity.

2. MODEL OF THE MAGNETIC FIELD

Post-flare loop systems are associated with active regions. The configuration of the magnetic field in such regions is determined by subphotospheric sources and coronal currents.

A subphotospheric source can be modeled as a two-dimensional dipole whose magnetic moment is directed normal to the boundary of the photosphere. The coronal current is localized near the polarity-inversion line, and the equilibrium of the current is due to the balance between the repulsive force produced by the reflected current and the Lorentz force $\frac{1}{c}[\mathbf{I} \times \mathbf{B}]$, where $\mathbf{I}$ is the current and $\mathbf{B}$ is the magnetic field of the active region [3].

The vector potential of the current (including the reflected current) in the active region studied has a z component only:

$$A = A_z = \frac{I}{c} \ln \left(\frac{r_1}{r_2} \right)^2, \qquad (1)$$

where r_1 and r_2 are the distances from the given point to the currents 1 and 2, respectively.

3. THE DRIFT MOTION

Changes in the magnitude or location of the current make the vector potential (1) time-dependent. If the magnetic field is frozen in, a change in the vector potential $\delta\mathbf{A}$ results in a displacement of the plasma normal to the magnetic field $\mathbf{B}$ [3]:

$$\boldsymbol{\xi}_\perp = \frac{[\mathbf{B} \times \delta\mathbf{A}]}{B^2}. \qquad (2)$$

We constructed the velocity field $\boldsymbol{\xi}_\perp$ corresponding to the vector potential A for a given system of field lines (Fig. 1). The field configuration contains five singular points—two saddle points and three nodes. Formally, upon the substitution $\mathbf{B} \to \boldsymbol{\xi}$, centers are replaced with nodes, all saddle points are rotated by $\pi/4$, and the dipole $\mathbf{M}$ is rotated by $\pi/2$. It is curious that precisely saddle points—regions where $|\xi_\perp|$ is maximum—rather than nodes or centers turn out to be the "sources" of this vector field.

Note that $\boldsymbol{\xi}_\perp$ grows as saddle point 1 is approached (Fig. 1). The motions in the neighborhood of the saddle point were calculated in [7, 8], where it was shown that the drift motions are localized within an area of $\approx 1.5'' \times 1.5''$.

If the current varies (decreases) with time, both saddles rise; at some value of the coronal current I_1, saddle 2 intersects the photosphere (shown by the

1063-7729/05/4909-0767$26.00

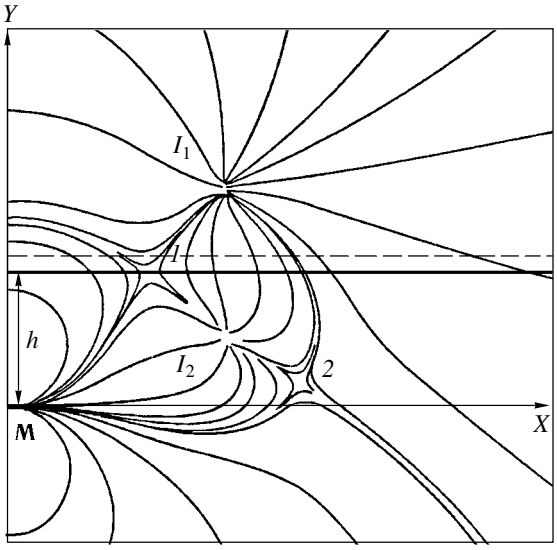

Fig. 1. Drift-velocity (displacement) field $\boldsymbol{\xi}_\perp$ in the z plane, which is perpendicular to the coronal current I_1 and the reflected current I_2 and runs through a subphotospheric two-dimensional dipole **M** located at the coordinate origin. The saddle points are labeled by the numbers *1* and *2*. The heavy solid line a distance h from the dipole marks the photospheric boundary. The dashed line corresponds to the chromospheric level.

heavy line in Fig. 1). As can be seen from (2), the regions of the most rapid motions in the chromosphere can exchange their roles in this case: ejections of matter may first emerge from the neighborhood of saddle 1, after which this saddle rises into the corona, where there is no dense matter or observable motion; further, saddle 2 may undergo a similar evolution. Therefore, a motion that originates in a region of some polarity at the footpoint of a loop may repeat itself some time later in the region of the opposite polarity at the footpoint of another loop system.

An analysis of motions in the model considered indicates that two situations can be realized if the current does not exceed the critical value, i.e., if it does not pass through the potential barrier. The first situation takes place if the coronal, and reflected currents have similar values: $I_2 \approx -I_1$. In this case, saddle point 2 (Fig. 1) remains below the photosphere and there is only one source for the motion of the chromospheric material. As a result, a loop with unidirectional motion forms.

Another scenario is realized if the current magnitudes are substantially different. In this case, both saddle 1 and 2 (Fig. 1) will simultaneously end up above the photosphere. In our model, this is the case when $I_2 \approx -2I_1$. The emergence of two sources should give rise to flows from both footpoints of the loop simultaneously. However, this scenario requires that the motions be so rapid that the reflected current has no time to react to the coronal current.

As an example, we consider the postflare loop system in Active Region 203 (according to the numbering adopted in the *Solnechnye dannye* bulletin [9]) of June 15, 1982. Figure 2 presents a filtergram obtained at 13:30 UT using the *Opton* interference–polarization filter on the Tower Solar Telescope of the Institute of Terrestrial Magnetism, Ionosphere, and Radiowave Propagation (IZMIRAN). The filter has a 0.25-Å pass band and is shifted $\delta\lambda = \pm 1$ Å from the center of the Hα line. The H$\alpha + 1$ Å filtergram recorded simultaneous motions of matter from two chromospheric regions (from both loop footpoints at once). The H$\alpha + 0.25$ Å filtergram displayed the entire loop system. This filtergram was used to obtain the geometric parameters of the loops.

Figure 3 shows the five main loops. To reconstruct the three-dimensional structure, we determined the heliographic coordinates of some points of the loops (Fig. 3). The shape of a loop was reconstructed using the technique described in [10], assuming that each loop lies in a plane and that its apex is located along the perpendicular line running from the midpoint of the segment connecting the footpoints of the loop.

A three-dimensional representation of the loop system is given in Fig. 4. The stereoscopic image was obtained by applying a 5° latitude shift. Analysis of the three-dimensional image enabled us to trace the trajectories of the matter flows in the loops over the time interval studied. In this way, we found that the velocity vector is directed away from the footpoints of the three long loops. The planes in which the loops lie form a fan (Fig. 4) and are inclined to the surface by angles of 23°–45°.

The short and long loops are bent in different directions (Fig. 3), so that the line-of-sight projections of the velocities directed from the footpoints are different. The right-hand parts of the short loops can be seen in the H$\alpha - 1$ Å filtergram (Fig. 2). Therefore, the motions in the short loops are simultaneous and are directed from the footpoints upward.

In some cases, other techniques can be used to obtain a stereoscopic image of a loop system. For example, the methods developed by Vedenov (see, e.g., [11]) are applicable. In particular, the appearance of the well-known system of coronal loops observed by TRACE (http://vestige.lmsal.com/TRACE/POD/TRACEpodarchive.html) on November 6, 1999 is very complex. If, however, we assume that most of the loops lie on a cylindrical surface, we can obtain a stereoscopic image of this system (Fig. 5).

In general, additional information about the object studied is needed to reconstruct its three-dimensional

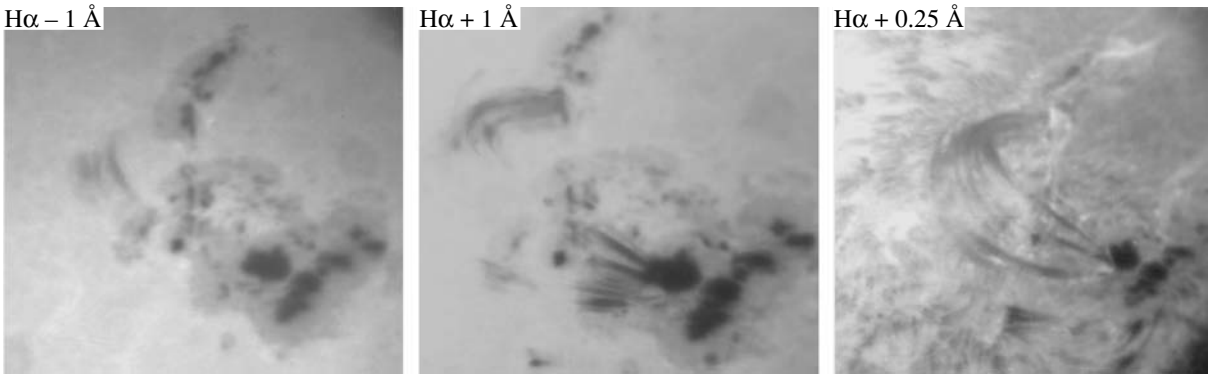

Fig. 2. Filtergrams of Active Region 203 obtained on June 15, 1982 in the blue ($H\alpha - 1$ Å) and red ($H\alpha - 1$ Å, $H\alpha + 0.25$ Å) wings of the $H\alpha$ line.

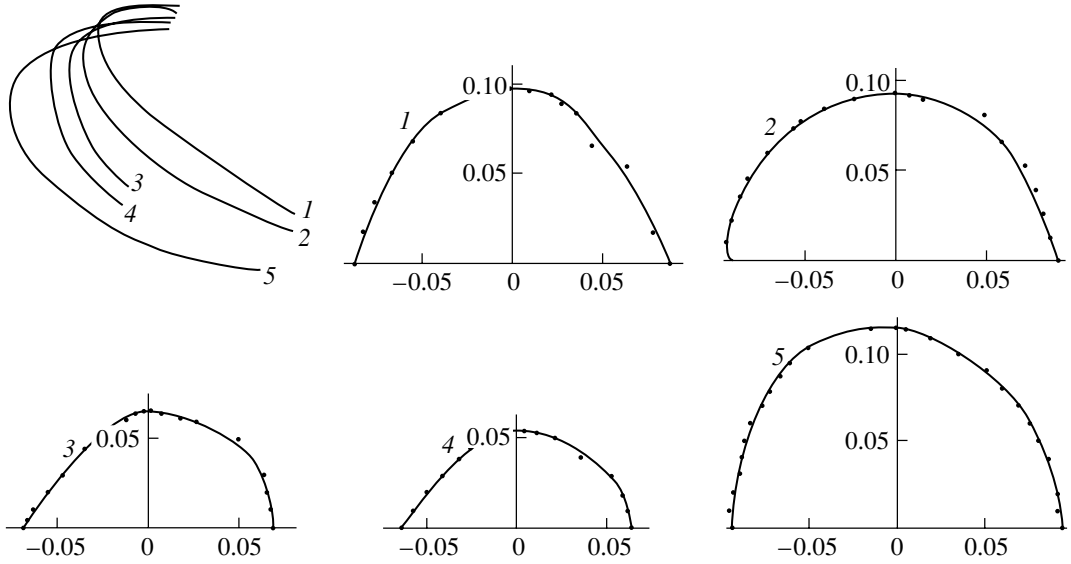

Fig. 3. Schematic representation of the five main $H\alpha$ loops in Active Region 203 after the flare of June 15, 1982, and their reconstructed configurations. The axes are scaled in solar radii.

structure from a two-dimensional image. Our above assumption about the shape of each individual loop [10] served as such supplementary information.

This assumption is not necessary, however. The data for the model described in [1] can also be used. As is noted above, Fig. 1 shows integrated curves of the vector displacement field $\xi_\perp$; these curves represent the trajectories of the chromospheric material if its velocity $\mathbf{v} = \mathbf{v}_\perp + \mathbf{v}_\parallel$ is such that $v_\parallel \ll v_\perp$. This condition is satisfied if the initial velocity is zero, gravity and inertia can be neglected, and only the plasma drift in the crossed fields need be taken into account [12].

In addition, Kazarov and Molodenskiĭ [1] consider the case when a current is present in the field of a two-dimensional dipole modeling the magnetic field near the polarity-inversion line (which corresponds to a filament), the entire structure exhibits translational symmetry $\left(\dfrac{\partial}{\partial z} \equiv 0\right)$, and an x and a y dependence are present. The surface (formed by the drift trajectories of the plasma in this case), whose equation $f(x, y) = \text{const}$ does not contain z, is a cylindrical surface (not necessarily with a circular generatrix). However, loops appear as circular arches in some particular cases (e.g., in TRACE observations). This fact was utilized when constructing the stereoscopic pair shown in Fig. 5.

The stereoscopic images are constructed as follows. In the plane of the image, (x, y), we construct the projection of the cylindrical surface $x^2 + (y - c)^2 = \text{const}$ to which the brightness from the plane of the sky is mapped. This specifies the third (spatial) coordinate of each point. To construct the stereoscopic image, we shift the resulting structure

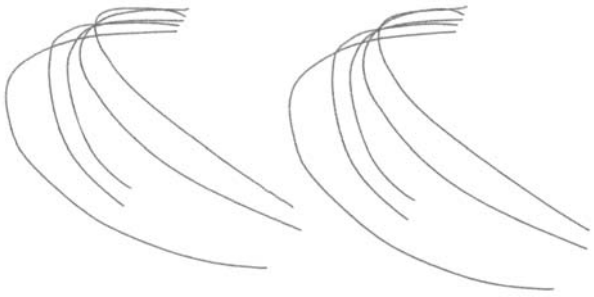

Fig. 4. Three-dimensional representation of the loops of June 15, 1982. The planes of the loops are inclined to the photospheric surface at angles of 44°, 35°, 44°, 45°, and 23°, in order of their numbering.

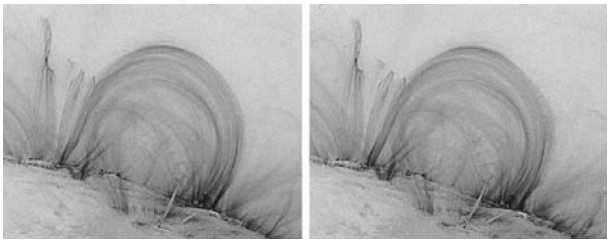

Fig. 5. Stereoscopic image of the coronal loops of October 6, 1999 (according to TRACE data).

by a distance corresponding to the base. Thus, a stereoscopic pair is formed.

The use of this technique for constructing stereoscopic images requires some spatial margin for shifting the observation point by the base length. To this end, we moved the observed object closer to the plane of the sky.

4. CONCLUSIONS

Our analysis of the loop system shown in Fig. 2 reveals two regions of acceleration. Despite the apparent complexity of Active Region 203 [9], its dynamics can be satisfactorily described using a relatively simple model (Fig. 1).

However, a different situation is also possible. In particular, Moore *et al.* [13] studied a region in which a major flare occurred on June 25–26, 1992. The magnetic-field configuration after the flare was highly complex. The postflare loops formed two different systems, one with a vertical orientation and a strong inclination to the surface (30°). This situation requires a more complex field configuration and sources of motion than the situation considered in Section 2.

The types, number, and disposition of the singular points can be determined from the observed loop structures based on the model considered [1]. This, in turn, makes it possible to reconstruct the topology of the magnetic and the induction electric field of the active region [14].

REFERENCES

1. D. Yu. Kazarov and M. M. Molodenskii, Astron. Zh. **69**, 1282 (1992) [Sov. Astron. **36**, 654 (1992)].
2. M. M. Molodenskii and B. P. Filippov, Astron. Zh. **64**, 825 (1987) [Sov. Astron. **31**, 430 (1987)].
3. M. M. Molodenskii and B. P. Filippov, Astron. Zh. **64**, 1079 (1987) [Sov. Astron. **31**, 564 (1987)].
4. B. Vrsnak, V. Ruzdjak, B. Brajsa, and A. Dzubar, Sol. Phys. **116**, 45 (1988).
5. M. M. Molodenskii, B. P. Filippov, and N. S. Shilova, Astron. Zh. **69**, 181 (1992) [Sov. Astron. **36**, 92 (1992)].
6. L. I. Starkova and N. S. Shilova, Kin. Fiz. Neb. Tel, No. 6, 28 (1985).
7. E. R. Priest and T. G. Forbes, Astron. Astrophys. Rev. **10**, 313 (2002).
8. V. S. Imshennik and S. I. Syrovatskii, Zh. Éksp. Teor. Fiz. **52**, 990 (1973).
9. Soln. Dannye, No. 6, 16 (1982).
10. R. E. Louhhead, J.-L. Wang, and G. Blows, Astrophys. J. **274**, 883 (1983).
11. A. A. Vedenov, Usp. Fiz. Nauk **164**, 967 (1994) [Phys. Usp. **37**, 889 (1994)].
12. M. M. Molodenskii and V. L. Merzlyakov, Pis'ma Astron. Zh. **28**, 314 (2002) [Astron. Lett. **28**, 272 (2002)].
13. R. L. Moore, B. Schmieder, D. H. Hathaway, and T. D. Tarbell, Sol. Phys. **176**, 153 (1997).
14. M. M. Molodenskii and S. I. Syrovatskii, Astron. Zh. **54**, 1293 (1977) [Sov. Astron. **21**, 734 (1977)].

Translated by A. Getling